Asociación Argentina de Geofísicos y Geodestas

GEOACTA

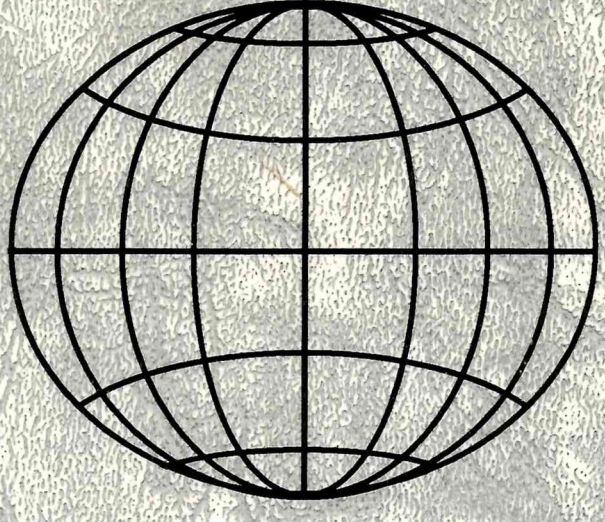

VOLUMEN 22
1997

ISSN 0326-723

Asociación Argentina de
Geofísicos y Geodestas

GEOACTA

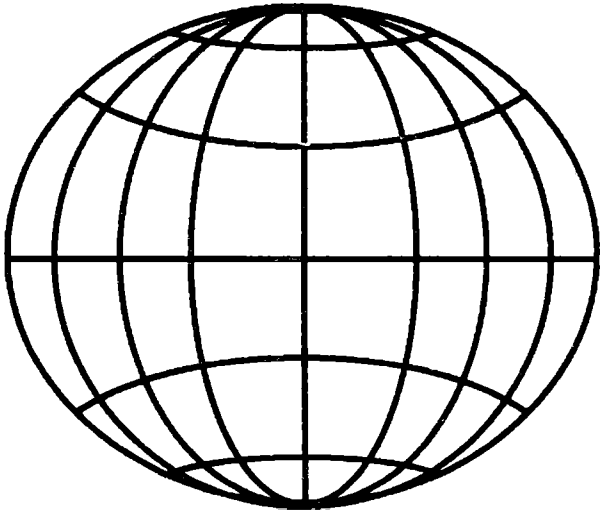

VOLUMEN 22
1997

ISSN 0326-723

GEOACTA, 22, 1997

Isostatic systems -and tectonic mechanisms present in Argentina.
Antonio Introcaso 1
On the dissipation of an upper oceanic front
Alejandro I. Camerlengo and Mónica I. Demmler 20
El calculo del agua precipitable y algunas de sus aplicaciones en Argentina
Graciela A. Catuogno e Inés Velasco 30
Aspectos cualitativos en el comportamiento de fof2 en la anomalía de invierno en la región f2 de la ionósfera.
Ana Martínez Pulido 47
Absolute palaeoreconstructions of continents based on palaeomagnetic poles and virtual geomagnetic poles?
Haroldo Vizan and Carlos Alberto Vasquez 59
Variability and motion of the Brazil-Malvinas front
Alejandro A. Bianchi and Silvia L. Garzoli 74
The andean elevation in Argentina-Chile at 39° south latitude from gravity data
María Cristina Pacino 91
Spectral decomposition of a long Rossby wave after reflection on an equatorial western boundary
Alejandro Camerlengo and Mónica Inés Demmler 103
Geomagnetism as an independent science
Luiz Muniz Barreto 122
Response of the ocean mixed layer, off the east coast of peninsular Malaysia during the north-east and south-west monsoons
Mohd Nasir Saadon and Alejandro Camerlengo 134
Sea level characteristics in Puerto Quequén
María Cintia Piccolo and Gerardo M. E. Perillo 144
Stability condition for Arakawa' s *B* grid
Alejandro I. Camerlengo and Mónica I. Demmler 155
Mejoramiento en el ajuste orbital de satelites GPS
A. Meza , J. C. Usandivaras and C. Brunini 165

GEOACTA, 22,1-19, 1997

ISOSTATIC SYSTEMS AND TECTONIC MECHANISMS PRESENT IN ARGENTINA

Antonio Introcaso
Facultad de Cs. Exactas e Ingeniería , Universidad Nacional de Rosario
Instituto de Física de Rosario (CONICET)

ABSTRACT

It is well known the diversity of geological structures present in Argentina. This makes it possible to analyze the vertical mobility throughout five selected cases in which different isostatic systems act. They are: Airy (+), (-) for an Andean section compensated on 33° S; Airy (-), (+) for the decompensated Salado basin; regional (or Vening-Meinesz's) to explain - although partially - the imperfect compensation of the Córdoba ranges; Airy and Pratt (thermal) systems combined to explain the Andean section compensated on 25° S; and Rudzki (+), (-) to explain - in part - the decompensation of the 50°20' S Austral basin section.

At the same time, we have considered the following mechanisms: shortening (on the Andes and Córdoba Ranges); thermal expansion (that we add to the Andean section on 25° S); stretching, thermal deactivation and load subsidence and load subsidence on the Salado and Austral basins.

By analyzing not only the compensation level but also either the most adequate isostatic system or the involved mechanisms, a better understanding of the origin and evolution of each structure can be achieved.

RESUMEN

Es bien conocida la diversidad de estructuras geológicas presentes en Argentina. Ello hace posible analizar el movilismo vertical a través de cinco casos seleccionados en los cuales operan diferentes sistemas isostáticos; a saber: Airy (+), (-) para una sección Andina compensada en 33° S; Airy (-), (+) para la cuenca descompensada del Salado; regional (o de Vening-Meinesz) para explicar - aunque sólo parcialmente - la compensación imperfecta de la Sierra de Córdoba; Airy y Pratt (térmica) combinadas para explicar la sección andina compensada en 25° S; y Rudzki (+), (-) para explicar en parte la descompensación de la sección en 50° 20' S de la cuenca austral.

Hemos contemplado al mismo tiempo los siguientes mecanismos aportamientos (en los andes y en la Sierra de Córdoba); expansión térmica (que agregamos a la sección andina en 25° S); estiramientos, desactivación térmica y subsidencia por carga en las cuencas del Salado y Austral.

Analizando no sólo el grado de compensación sino además tanto el sistema isostático más adecuado como los mecanismos involucrados, puede lograrse un mejor conocimiento de la génesis y evolución de cada estructura.

1. INTRODUCTION

The different isostatic systems demand to compensate the heterogenities of the masses located on the upper part of the crust, with equivalent masses below them. These masses, called compensating masses, are located at different depths, sometimes reaching deep levels in the upper mantle. The beginning and evolution of the different geological structures are entailed to:(1) the isostatic system characteristics, and (2) the compensation level that was reached. It is because of this, that it is important to recognize (1) and (2) while analyzing a structure by means of geophysical data, particularly by means of gravity. We start by describing the different isostatic systems mentioned in this paper, using the idea of dipolar distribution.

Dipole moment: It is known that two magnetic masses -m, +m making up a dipole originate a potential on external points ($r_1 \sim r_2$; r_1(or r_2)>>d) (Fig. 1):

$$V_p=\eta\nabla\left(\frac{1}{r}\right) z=\eta\,(\partial/\partial n)\,\left(\frac{1}{r}\right) \qquad (1)$$

where η is the magnetic moment: m x d. If we take gravitational masses -m and +m instead of magnetic masses, the expression (1) will become:

$$V_p=M(\partial/\partial n)\,\left(\frac{1}{r}\right)$$

where M = m x d: dipole moment.

From a dipole unit we can generalize the case of the potential of double layer. However, we concentrate our attention on the dipole moment related to different isostatic mechanisms treated in this paper. If we have a column with topographic mass +m and compensation mass -m and density σ separated by a distance d, (Fig. 2), we will have a distribution with dipole moment:

$$M=m\times d=\left(\left(\sigma\times s\times h\right)/s\right)\times d=\sigma\times h\times d=\frac{h}{2}+T_n+\frac{R}{2}$$

The condition d → 0 is relatively well satisfied if d is small compared with the distance to the station.

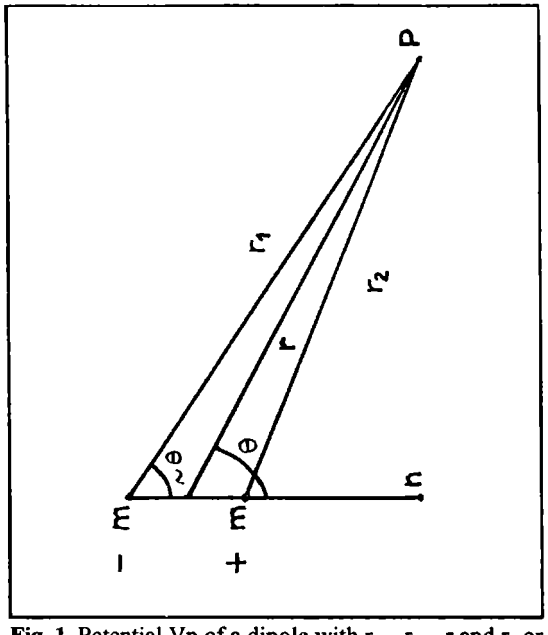

Fig. 1. Potential Vp of a dipole with $r_1 \sim r_2 \sim r$ and r_1 or $r_2 >> d$

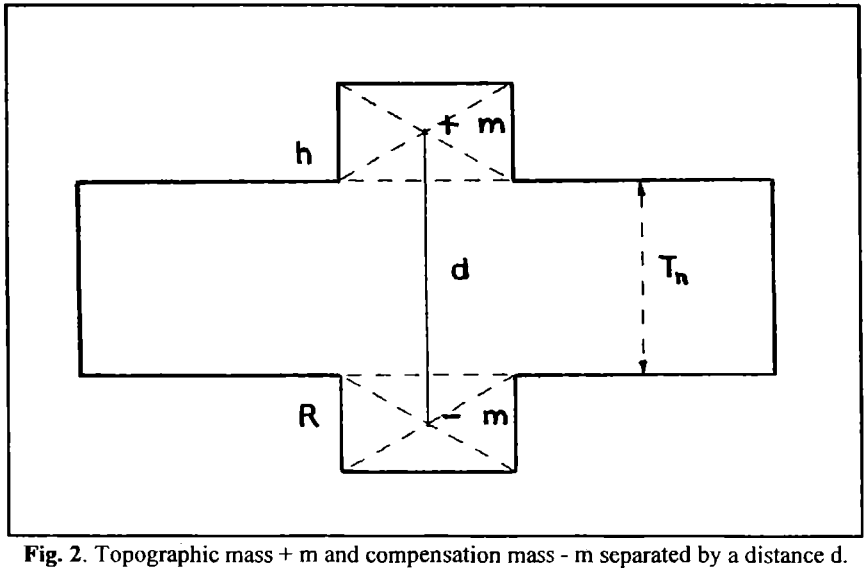

Fig. 2. Topographic mass + m and compensation mass - m separated by a distance d.

2. ISOSTATIC SYSTEMS

For different reductions we will have (Heiskanen and Moritz, 1965):(a) Pratt-Hayford: d=(h+H)/2; (b_1) Airy-Heiskanen (continent):d=Tn+(h+R)/2; (b_2) Airy-Heiskanen (ocean): d'=T_n-(h'+R')/2; (c) Rudzki (inversion): d=h (Fig. 3).

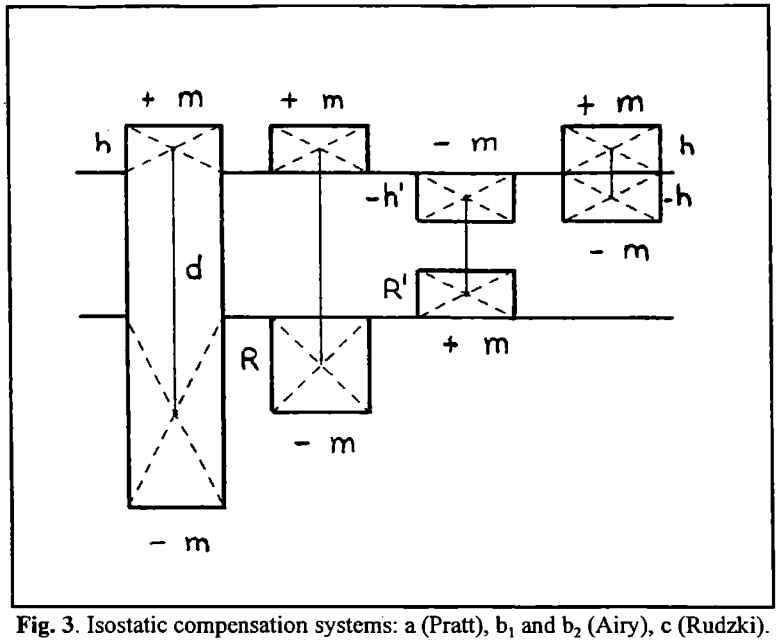

Fig. 3. Isostatic compensation systems: a (Pratt), b_1 and b_2 (Airy), c (Rudzki).

We have already analyzed the dipole moment ,ή = σ.h.d for continental areas. Instead of this, for oceanic areas we will have:

$$\mu = -h'(\sigma - \sigma_\omega)\, d'$$

where σ_ω is the water density. In the case of a sedimentary basin:

$$\mu = -h'(\sigma - \sigma_s)\, d'$$

where σ_S is the sediments' density.

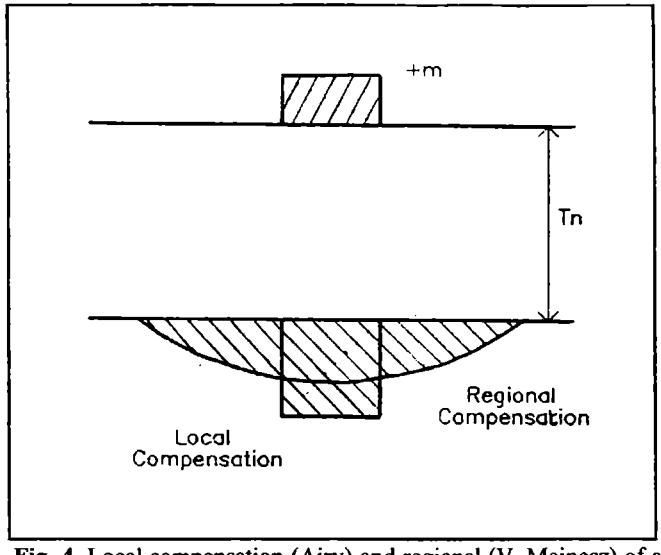

Fig. 4. Local compensation (Airy) and regional (V. Meinesz) of a topographic mass + m.

We have just considered the case of compensated columns. The regional (flexural) system of Vening-Meinesz distributes the compensation on a root of less amplitude, although distributed in the same way that the flexure and elastic beam suffers when loaded with a mass + m (Fig. 4). Next, we will see mechanisms that - keeping the isostatic equilibrium - originate uplifting and subsidence.

3. UPPER MANTLE MATERIALS HEATING AND COOLING

This mechanism keeps the isostatic equilibrium at the bottom of the normal lithosphere expanding (uplifting) the upper mantle column in presence of anomalous heating and depressing it in case of cooling. We assume the following initial conditions: "normal" crustal thickness: T_n= 30 km; thermal lithospheric thickness: L= 100 km; crustal density: σ_C=2.9 g/cm^3; upper mantle density: σ_m= 3.3 g/cm^3; thermal expansion coefficient: α=3x10^{-5} 1/°C. So, the upper mantle density variations $\Delta\sigma$ each ± 100 °C of the thermal anomaly, ΔT will be:

$$\Delta\sigma=\pm\sigma\alpha\Delta T=\pm 3.3\times 10^{-5}\times 100^{\circ}C\,1/^{\circ}C\,g/cm^3=\pm 0.01\,g/cm^3$$

The expression that leads the ascension or descent of the 70 km mantle column that supports a crust 30 km thick and keeps pressures at a depth of 100 km is:

$$70(1-(3.30/(3.30\pm n\Delta\sigma)))$$

where n=1,2,3,4 and 5; and $\Delta\sigma$ = 0.01 g/cm^3. Fig. 5 shows the elevations ρ_e and depressing ρ_d of the lithospherical column in presence of anomalous heating (density defects) and cooling (density excesses).

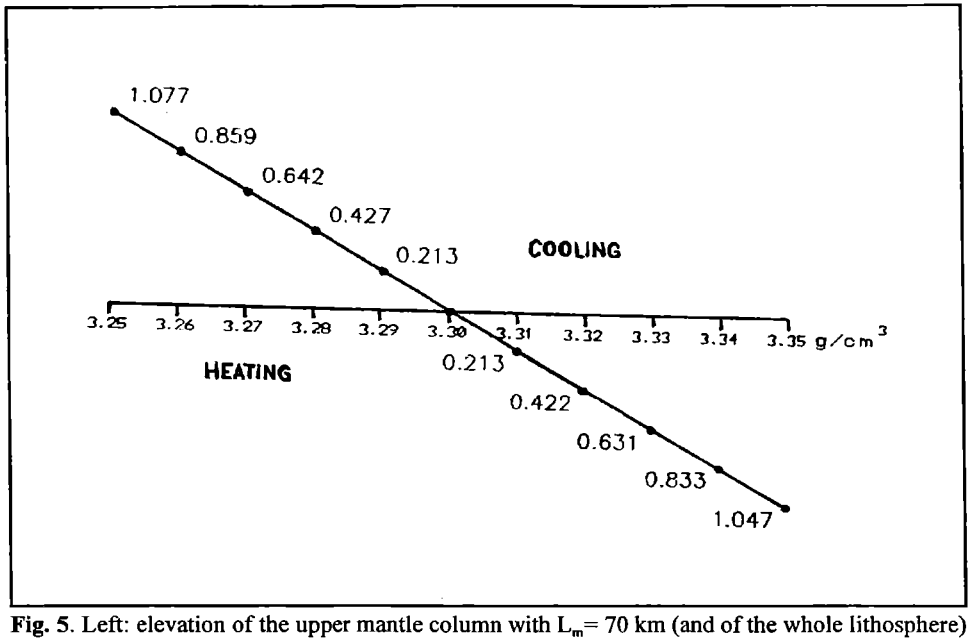

Fig. 5. Left: elevation of the upper mantle column with L_m= 70 km (and of the whole lithosphere) 100 km thick, in presence of density increasing by heating. Right: Depressing of the same column in presence of cooling.

4. CRUSTAL ATTENUATION AND THICKENING

This mechanism keeps the isostatic equilibrium at the crust, producing subsidence in the case of attenuation and elevation in the case of thickening. In order to study these effects, we assume the following initial conditions: σ_c= 2.9 g/cm^3; σ_m= 3.3 g/cm^3; crustal thickness T_i=30 km ± nx5 km, where n is varying from 1 to 4 in the case of attenuation (with n=4: T_n= 10 km; below this value in 9.375 (= 30 / 3.2) the crust could break (Le Pichon et al., 1981). In the case of thickening, n varies from 1 to 7 (for n=7: T_n= 65 km which is the case of many Andean segments (Introcaso et al.,1992). The expression used here is:

$$\rho'=5n(1-2.9/3.3))=\pm n0.606$$

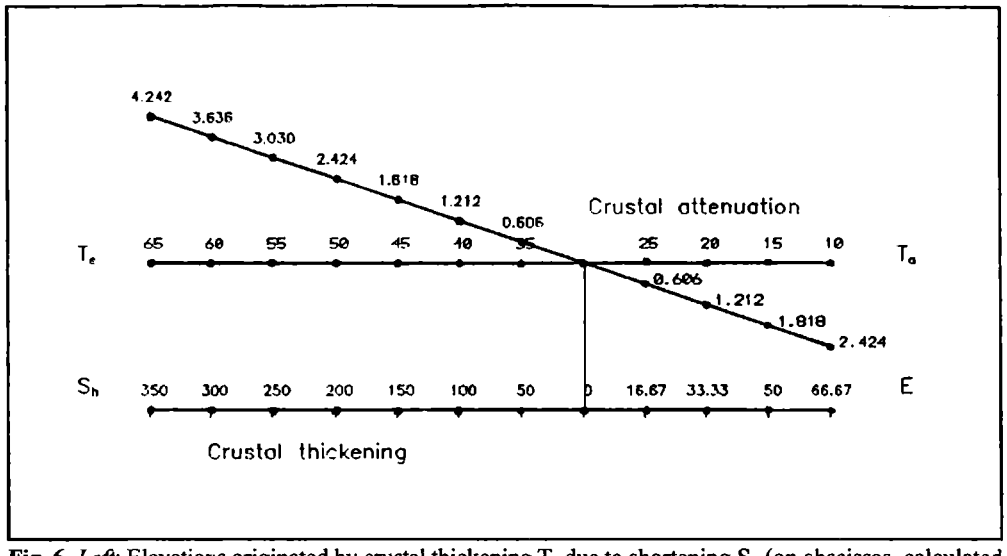

Fig. 6. *Left*: Elevations originated by crustal thickening T_e due to shortening S_h (on abscissas, calculated with a crustal width $\acute{\omega}_0$= 300 km). *Right*: Subsidence originated by crustal attenuation T_a on abscissas due to stretching S_t with a width $\acute{\omega}'_0$ = 100 km.

Fig. 6 shows the mentioned changes. All the columns show equality of pressure at a depth of 60.758 km, reached by the maximum thickening. We should also consider the mechanisms that thicken and attenuate the crust. Thickening is usually entailed with shortening Sh (for example on the Andes). So, for a width $\acute{\omega}_0$= 300 km, the shortened sector:

$$S_h=(\varpi_0\times(T_e-T_n))/T_n=(300\times(T_e-30))/30$$

where T_n= 30 km, T_e=T_i= 30 + 5n. For example, if T_e is 65 km, it will become S_h= (300 x 35) / 30= 350 km. It is also usual to entail crustal attenuation with stretching S_t. If the stretched sector width is $\acute{\omega}'_0$= 100 km, stretching will be:

$$S_t=(\varpi_0\times(T_n-T_a))/T_n=(100\times(30-T_a))/30$$

where T_n= 30 km, T_a=T_i=30-5n. For example, if T_a is 15 km, it will become S_t= (100 x 15) / 30 = 50 km.

5. CRUSTAL DENSITY CHANGES

Increasing of crustal density keeping T_n and σ_m produces subsidence, while decreasing of crustal density without changes in T_n and σ_m produces elevations. In both processes the isostatic equilibrium is kept in the Airy System. At the maximum reached depth (density 2.95 g/cm^3) every column equals pressures.

With the following initial conditions: T_n= 30 km (constant), σ_m= 3.3 g/cm^3 (constant) and varying σ_c according to σ'_c = (2.9 + n 0.01) g/cm^3, with n= 1, 2, ..., 5 we will have the variation graphic (Fig. 7).

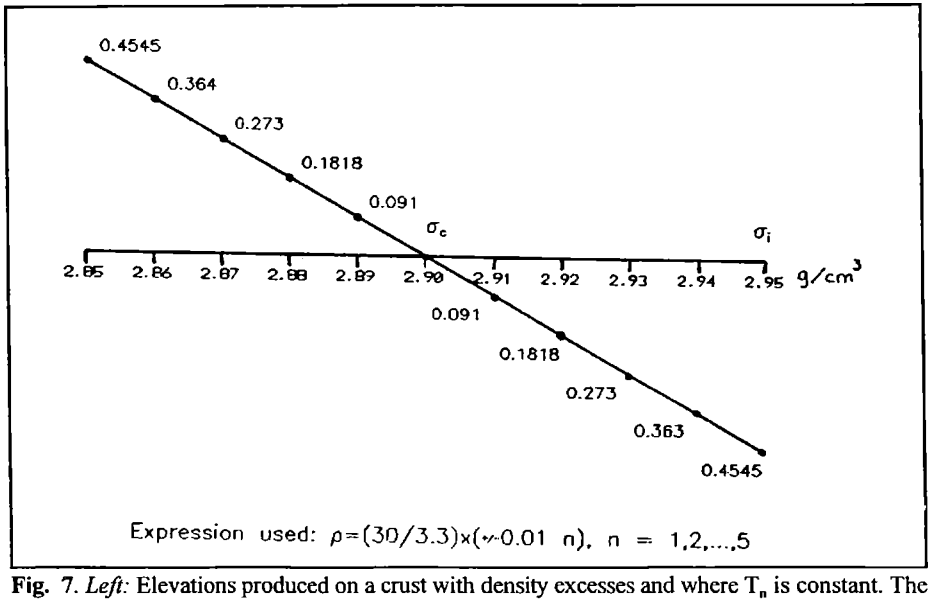

Fig. 7. *Left:* Elevations produced on a crust with density excesses and where T_n is constant. The crust lies on a mantle in which σ_m is constant. *Right*: Subsidence produced on a crust with density excesses, where T_n and σ_m are constant.

6. SUBSIDENCE BY SEDIMENTARY LOAD

One of the mechanisms contributing to the evolution (subsidence) of a sedimentary basin is the load of sediments. The process - controlled by isostasy under the Airy

hypothesis - needs to have an initial trench produced, for example, by stretching.

With the following initial conditions obtained from Fig. 6, paragraph b): S_0 varying between 0.606 km; 1.212 km; 1.818 km and 2.424 km, the basin would develop to its whole fulfilling of sediments with density σ_S= 2.35 g/cm^3 descending respectively to 2.10 km; 4.21 km; 6.315 km and 8.42 km (Fig. 8). We have used the expression proposed by Introcaso (1980):

$$S_T = S_0 / (1 - \sigma_S / \sigma_m)$$

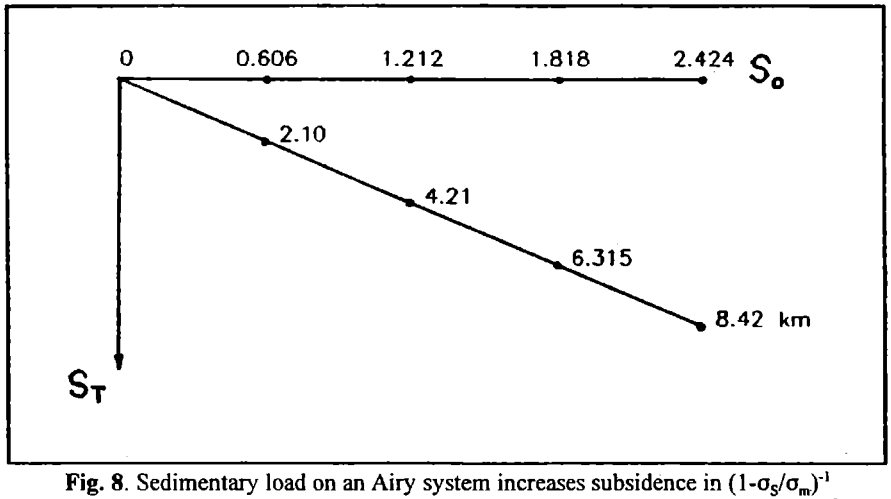

Fig. 8. Sedimentary load on an Airy system increases subsidence in $(1-\sigma_S/\sigma_m)^{-1}$.

We have found and analyzed some examples in Argentina (see locations at Fig. 9) where the isostatic behavior is adapted - at least partially - to the different compensation hypothesis we have pointed out. They are:

♦ Andes Cuyanos where - as the isostatic anomalies indicate - compensation would take place in a system like b_1 (Fig. 3) (Airy-Heiskanen, + m_T-m_R) at the bottom of the crust and agreeing with seismic data; + m_T-m_R= 0.

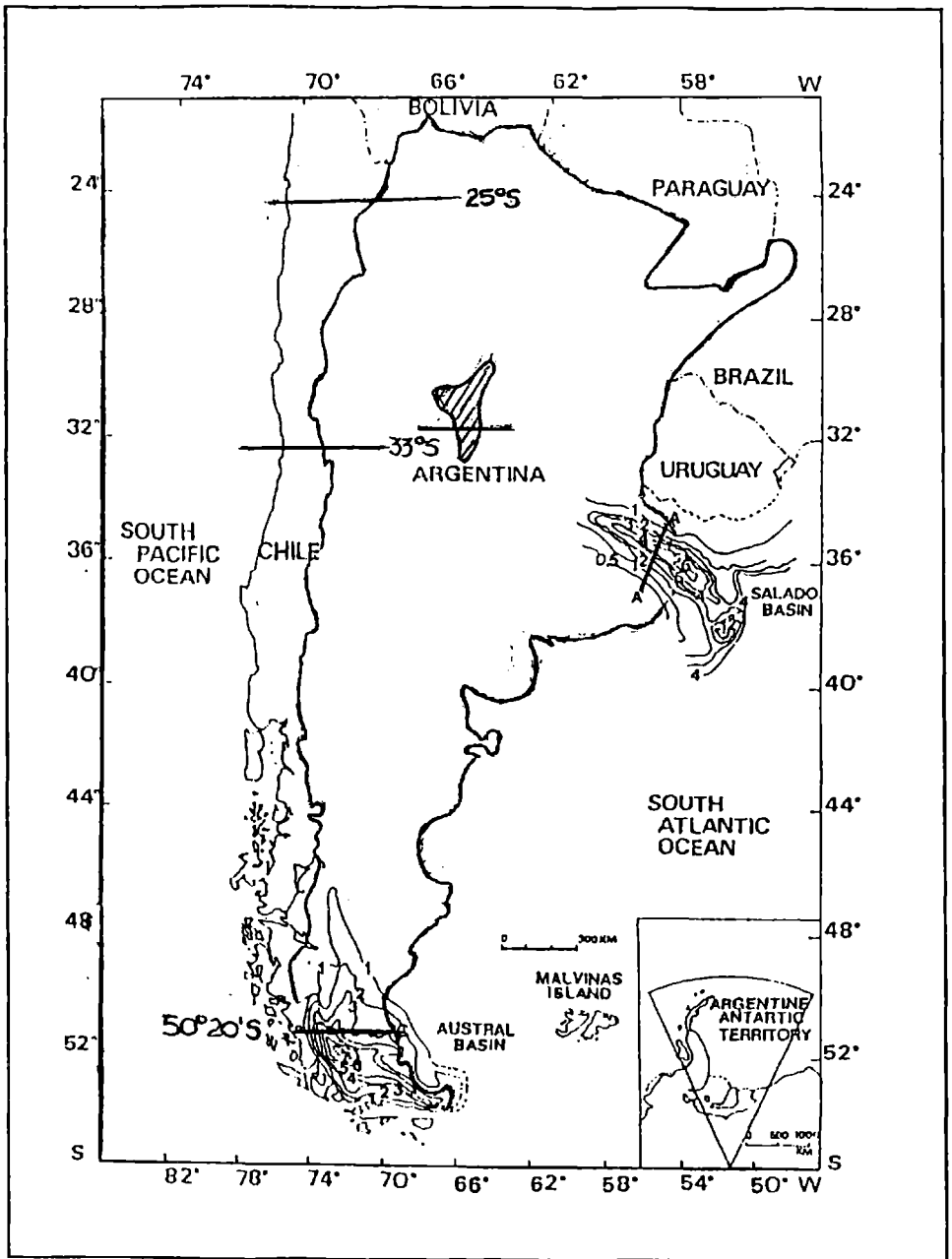

Fig. 9. Location of the five analyzed gravity sections

♦Central Andes where compensation - pointed out by small isostatic anomalies - would take place at a depth of 140 km involving a combination of systems (a) Pratt-Heyford, and (b) Airy-Heiskanen (Fig. 3). So, the Andean exceeding mass + m_T is compensated by means of the deficits originated by the crustal root -m_R and the thermal root -m_c; m_T-m_C-m_R = 0 (Fig. 10).

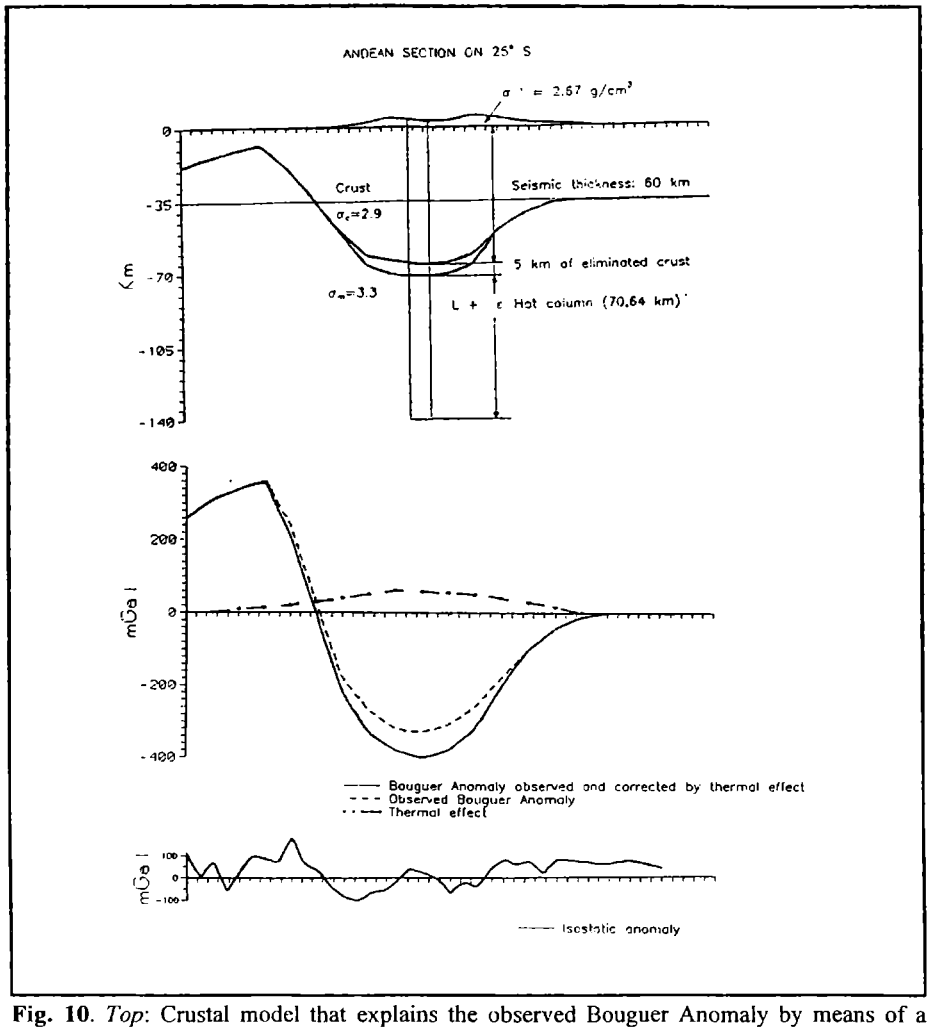

Fig. 10. *Top*: Crustal model that explains the observed Bouguer Anomaly by means of a combination of a 25 km crustal root (agreeing with the maximum seismic depth of 60 km) and thermal expansion on the lithospheric mantle. *In the middle*: Observed Bouguer Anomaly (ABo) and Bouguer Anomaly observed and corrected by the thermal effect. *Bottom*: Isostatic Anomaly. Source: Introcaso, A. (1993).

♦ Salado basin, whose significatively positive isostatic anomaly in the Airy system (-m,+ m), would indicate decompensation -m+ m > 0, excess of crustal density, or a combination of both.

♦ Northwards the Austral basin, whose isostatic anomaly in the Airy system is positive. However, the setting of the materials located over the crystalline basement, allows us to analyze the possibility of partial compensation on the upper crust (Rudzki system +m, -m) although + m - m > 0. So, + m is integrated with the masses located over the sea level and the masses excess inside the crust, while - m involves sediments below the sea level and a probable small root.

♦ Córdoba range does not seem to respond neither to a compensation system like the Airy one nor to a regional system like the Vening-Meinesz's one. The range appears decompensated (the isostatic anomaly is positive, increasing from west to east); + m - m > 0.

Fig. 11 shows columns that equal pressures at a depth of 120 km. They constitute models to begin the analysis of different structures of Argentina treated in this paper. In every case, the analysis of isostatic compensation must be done together with the genetic mechanisms and evolutions involved in the compensation systems. They must be consistent with the studied structures.

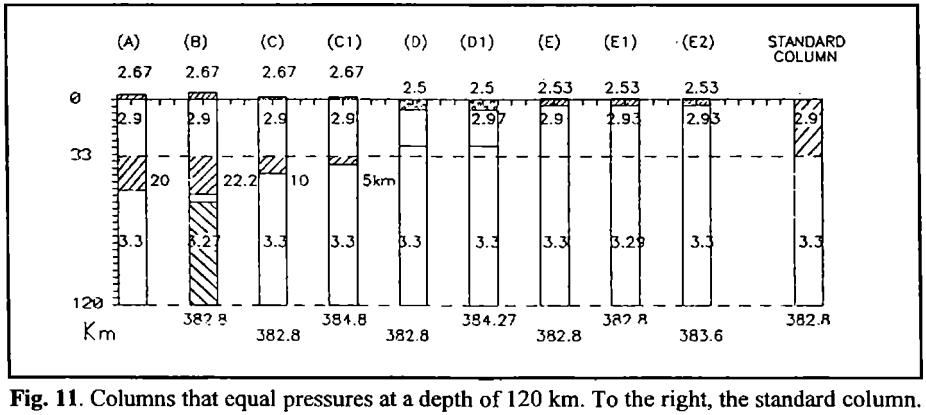

Fig. 11. Columns that equal pressures at a depth of 120 km. To the right, the standard column. All the columns have been thought to begin the study of the following sections: Andes on 33° S (Column A); Andes on 24° S (Column B); Córdoba Range (Columns C, isostatically compensated and C1 undercompensated); Salado Basin (Columns D isostatically compensated and D1 overcompensated); Austral Basin (columns E and E1 isostatically compensated). The densities: 2.67, 2.9, etc. are expressed in g/cm^3. Below each column there are pressures (with unitary gravity) expressed in 10^5 dyn/cm^2.

So, at the Central Andes (25° S latitude; Fig. 11 column B and Fig. 10) the isostatic anomalies at the Airy system are minimum compared with the significative Bouguer anomalies (AB) whose maximum is over - 400 mGal. The seismic-crustal model presents a maximum M depth of 60 km (Schmidt, 1993). The AB inversion in a crustal system like the Airy one gives a maximum M of 65 km. But a combination of a 60 km crustal root (in agreement with the seismic model) and the lithospheric expansion by heating of the lower half of the 70 km thermal lithosphere (Isacks, 1988) satisfies the observed Bouguer anomaly (Introcaso, 1993), Mechanisms correspond to Fig. 6 and Fig. 5. Two mechanisms would so explain the Andean uplift: shortening of about 250 km (Isacks, 1988) and thermal uplifting. From an isostatic point of view, two mechanisms are acting: Airy one on the crust and thermal one (Pratt) on the lithospheric mantle.

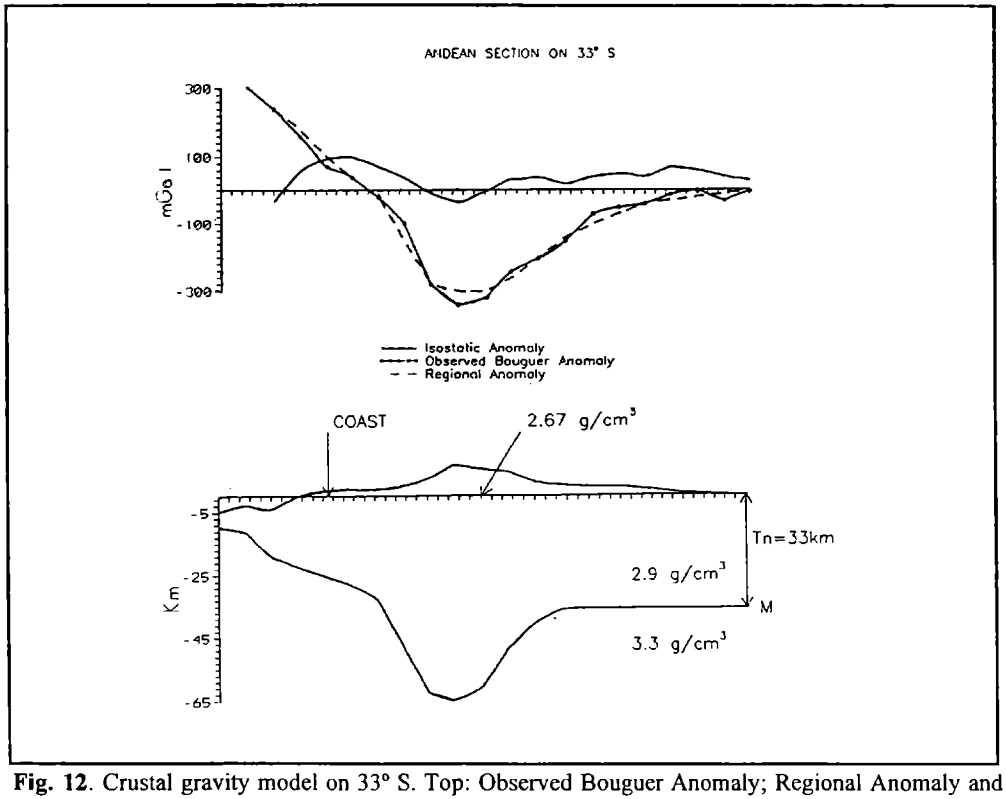

Fig. 12. Crustal gravity model on 33° S. Top: Observed Bouguer Anomaly; Regional Anomaly and Isostatic Anomaly. Bottom: Crustal model obtained by gravimetric inversion. Source: Introcaso et al. (1992).

At the Andes Cuyanos (33° S, Fig. 11 A and Fig. 12) the isostatic anomalies are also minimum, while the AB inversion with maximum values of -300 mGal produces a maximum M of 65 km, agreeing with the seismic model of Pardo-Fuenzalida (1988). Shortenings of 130 km justify the whole Andean uplifting in a process controlled by the Airy system (Introcaso et al., 1992). The involved mechanism can be seen in Fig. 6 (left).

At the Salado basin, a cross section shows a positive Bouguer anomaly with a maximum of + 55 mGal located over the basin axis (Fig. 11 D and D1 and Fig. 13). From the theoretical model of Introcaso (1993) we observe: (a) an isostatic anomaly of + 65 mGal, pointing out overcompensation or antiroot excess; (b) stretching E = 33.71 km, with β 1.5 that justifies the crustal attenuation; (c) the possibility that the gravity effect could be entailed with the crustal density excess is not discarded. The mechanisms involved can be seen in Fig. 5 (heating 3.25 g/cm^3 to cooling 3.30 g/cm^3), 6 (right), 7 (right) and 8 (for each value σ mantle).

This basin, entailed with the South Atlantic Ocean opening 125 Ma ago and classified as a model of aulacogenic evolution (Introcaso-Ramos, 1984) must continue its subsidence until the isostatic anomaly is eliminated. On the Austral basin section located at 50° 20' S (Fig. 11 E, E1 and E2 and Fig. 14) Bouguer anomalies are negative with a maximum of aprox. - 30 mGal, while the isostatic anomalies on the Airy system have values of more than + 40 mGal. This usually indicates crustal attenuation. Besides, as it was just pointed out, the setting of the load located over the bottom of the basin would imply an analysis in the Rudzki isostatic system (+ m_T over the sea level, compensated by - m_S immediately below). Such compensation is produced imperfectly. In fact, it does not exist a consistent correlation neither between wave lengths nor between the masses m_T and m_S of the basin topography. So, m_S is only 29 % of m_T according to the isostatic anomaly sign. Three mechanisms: crustal attenuation, cooling and sedimentary loading are present in this basin, with the possibility of keeping on subsiding (see Fig. 5,6 and 8). From the present model of the basin (see columns E1 and E2 in Fig. 11) that involves 4 km of sediments, subsedimentary attenuated crust, negative Bouguer anomaly, basic materials intruded in the crust, in view of the probable heating present, we have done an acceptable retroprediction from column E1, finding - for the initial conditions: attenuation by stretching ($\beta \sim 1.3$) and heating of the lithospherical mantle. Then cooling happens, with subsidence and sedimentary load, and crustal thickening by basic material intrusion. On the Córdoba range, and according to Lion-Introcaso (1987, Fig. 11 C and C1 and Fig. 15), the isostatic anomaly in the Airy system is positive (increasing eastwards until reaching + 50 mGal). So, compensating root in the Airy system (Fig. 2) is too big. On the other hand, a flexural system, or V. Meinesz (Fig. 4) with T_n= 33 km, D = 3.8 x 10^{30} dyn x cm, does not satisfy the observed Bouguer anomaly neither in amplitude (it is too small) nor in wave length.

Compression forces could retain the descending vertical movement that the Airy

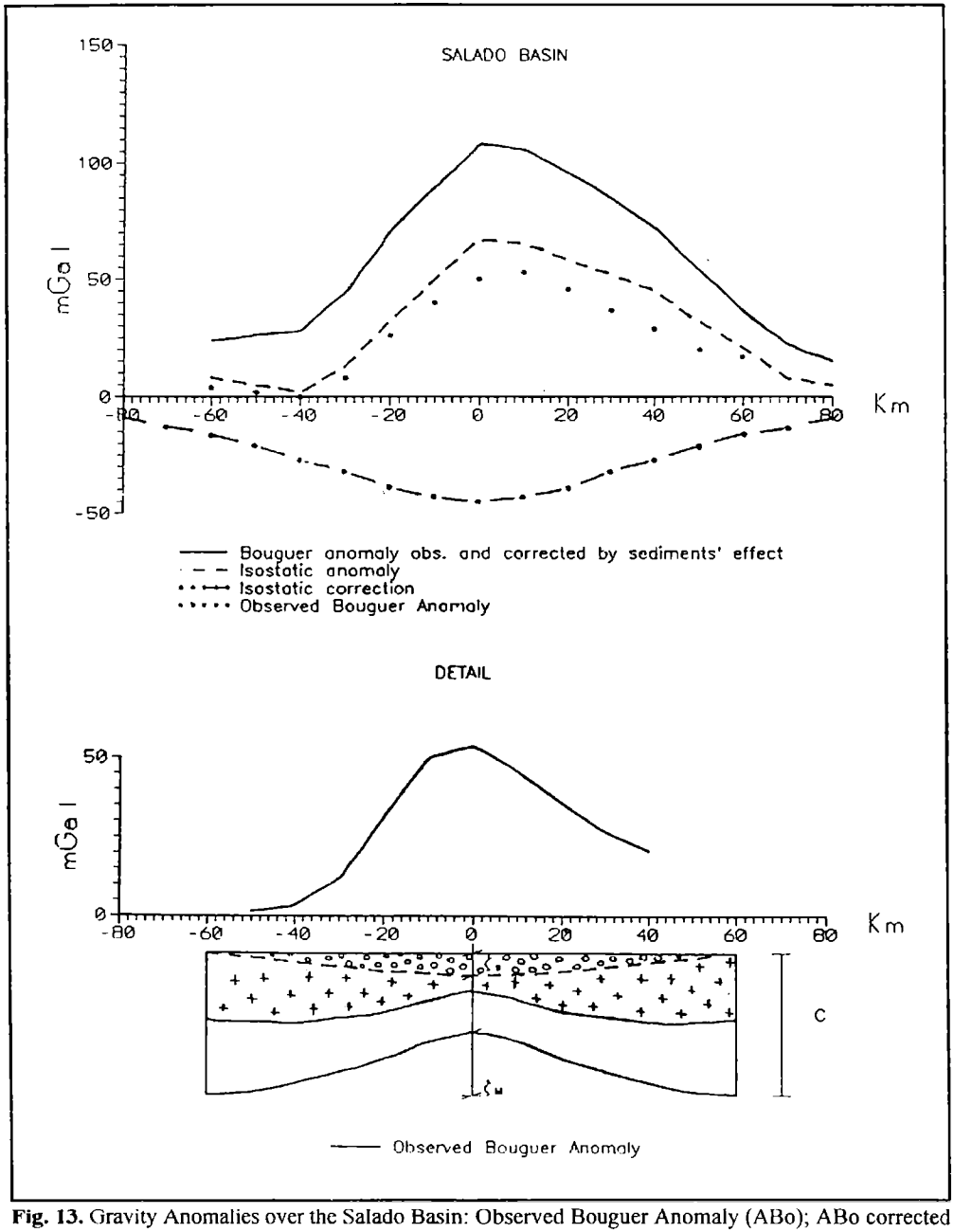

Fig. 13. Gravity Anomalies over the Salado Basin: Observed Bouguer Anomaly (ABo); ABo corrected by sedimentary filling effect (ABo + Ces); Isostatic Correction (Cl); Isostatic Anomaly (Al = ABo + Ces - Cl). Source: Introcaso and Ramos (1984). *Detail:* Crustal model of the Salado Basin ρ_M (antiroot) >> ρ_S (sedim) C: crustal thickness.

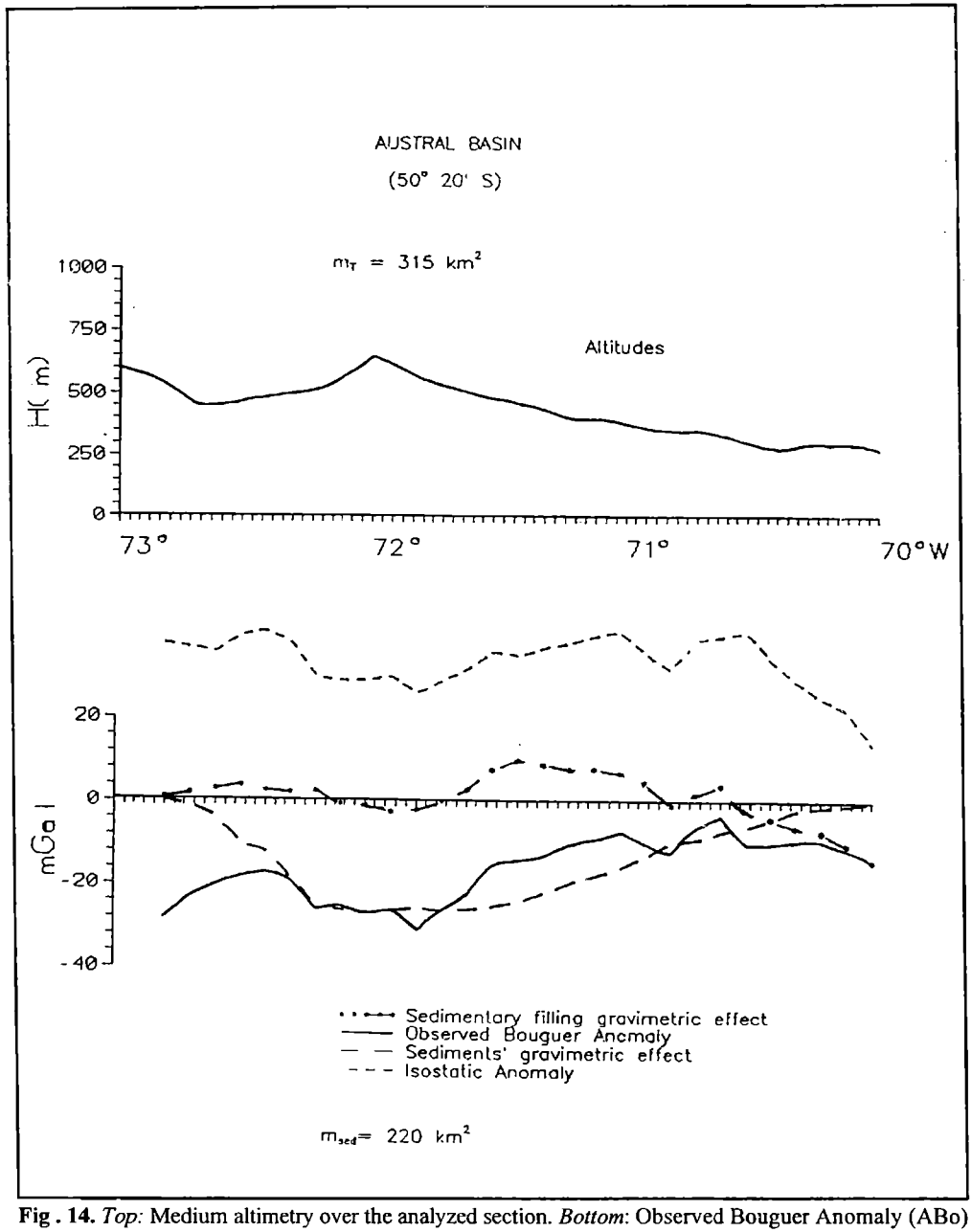

Fig . 14. *Top:* Medium altimetry over the analyzed section. *Bottom*: Observed Bouguer Anomaly (ABo) over the northern part of the Austral Basin (50°20'S). Source: Kraemer, Robles and Introcaso (unpublished). Gravimetric effect of the sedimentary filling (Egs); Bouguer Anomaly (ABo) ob served and corrected by the sediments' effect (Egs) and the crustal root on the west (Erc).

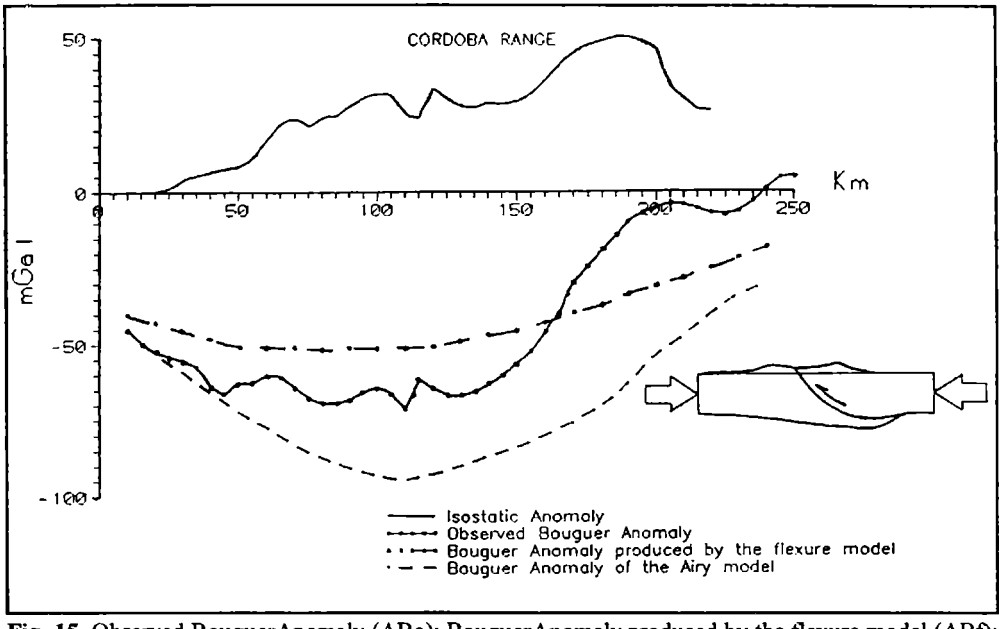

Fig. 15. Observed BouguerAnomaly (ABo); BouguerAnomaly produced by the flexure model (ABf): $\sigma = 2.7$ g/cm^3; $T_n = 35$ km; $D = 3.81 \times 10^{30}$ dyn.cm; Bouguer Anomaly of the Airy model (ABa): $T_n = 35$ km; $\Delta\sigma = 0.39$ g/cm^3; averaged altitudes on segments 60 km wide; D = 0. Source: Lion and Introcaso (1987).

system proposes, while if the flexural system is modified with $T_n = 15$ km and $D = 3.8 \times 10^{30}$ dyn x cm, the Bouguer anomaly amplitude can be reproduced, although the wave length cannot. A viscoelastic model better agrees with the observed results (Miranda, Silvia - personal communication). Isostasy regulates all the time the anomalous masses + m, - m and - m, +m distribution. So, it acts every time a mechanism tends to alter the normal masses distribution. For example, in the case of the Andes, each 10 mm of crustal thickening produced by shortening, 8.8 mm are located on the compensating root and 1.2 mm on the Andean emergent. In the same way, if the 1.2 mm were eliminated by erosion, it would be necessary to diminish the root thickness in 8.8 mm to keep the isostatic balance.

If the elevation mechanism happened to be the lithospheric expansion, as in the Central Andes, every 10 mm of elevation, the mantle heating would produce a decreasing of density of 0.5×10^{-5} g/cm^3 in presence of an anomalous heating of $\sim 5 \times 10^{-2}$ °C. In this case, the compensation depth would be the bottom of the thermal lithosphere.

Taking now the stretching as an attenuation factor, in the case of a sedimentary basin

we will also have that every 10 mm of crustal attenuation, crust would decrease 1.2 mm leaving an antiroot of 8.8 mm. Every time the sediments fill the basin there will be subsidence in a convergent process that contains repetitions, always controlled by isostasy.

The cooling of the mantle is another probable mechanism that increases subsidence. This time, the isostatic control would be at the level of the bottom of the lithospheric mantle.

7. CONCLUSIONS

We have pointed out that the explanation of the origin and evolution of the different geological structures needs: (a) To define the sign and rate of the isostatic compensation; for this purpose, the Airy system (± m, ± m) is usually used. (b) To find the type of the isostatic system or systems involved (Airy, regional or Vening-Meinesz, thermal or Pratt, etc.). (c) To analyze the previous mechanisms involved in these processes (shortenings, stretchings, etc.).

Throughout five examples of different structures in Argentina, we have carried out an analysis involving items (a), (b) and (c) just mentioned.

Only one of the models analyzed here (Andean section on 33°S) expresses - in general terms - compensation in the classical Airy system. The Andean uplift by crustal thickening can be justified by means of an only mechanism: crustal shortening of 130 km, controlled by the just pointed out isostatic system. The bottom of the crust M defined by means of seismicity and gravity, presents good consistency.

The Andean section on 25° S, also isostatically compensated, involves a combination of two isostatic systems: Airy (imperfect) on the crust, and Pratt
on the lower half of the thermal lithosphere. The crustal thickness of the gravity model is only 60 km, agreeing with the seismic results. The crustal root corresponding to that thickness justifies 85 % of the observed Bouguer anomaly with a maximum of aprox. - 340 mGal. The rest (- 60 mGal) is justified by the thermal effect on the lithospheric mantle.

To justify the origin of the Salado basin, we have proposed: crustal attenuation by stretching and increase of temperature from the base of the thermal lithosphere. For the evolution of the basin still in subsiding process - as it is shown by the positive isostatic anomaly, we have considered the following mechanisms: sediments load, upper mantle cooling and subsidence anomalous pulses related to velocity changes of the continental derive.

For the section that crosses the Austral basin at 50° 20' S, we have found a gravity exceeding (positive isostatic anomaly) that shows the possibility of subsidence. Crustal stretching, sedimentary load and cooling should be considered in the study of the basin.

The distribution of the load located over the crystalline basement suggests an imperfect compensation in the Rudzki system.

Finally, the Córdoba range presents a positive isostatic anomaly. Crustal shortening that is solved over a listric failure without a defined isostatic control, explains the range uplift. The isostatic mechanisms seem to be inhibited by strong compensation.

We point out, at last, that the isostatic anomalies should be calculated to determine the sign and level of compensation of the studied structures. But we must go further trying to find in each case the most adequate isostatic compensation system. They contain the vertical mobility mechanisms that regulate the masses distribution at depth.Other mechanisms: compressive shortenings, tractional stretchings, derived from horizontal stresses, precede the isostatic control.

REFERENCES

Heiskanen, Wand Moritz, H. 1967. Physical Geodesy. L. H. Freeman. San Francisco and London. 364 ps.

Introcaso, A. 1980. Resultados gravimétricos en la banda latitudinal de Argentina Central y países vecinos. Rev. Geofís., Inst. Panam. Geogr. Hist. 12, 5-25.

Introcaso, A. and Ramos, V. 1984. La cuenca del Salado. Un modelo de evolución aulacogénica. Actas IX Congreso Geológico Argentino 3, 2746.

Introcaso, A., Pacino, M. C. and Fraga, H. 1992. Gravity, isostasy and Andean crustal shortening between latitudes 30° and 35° S. Tectonophysics 205, 31-48.

Introcaso, A. 1993. Anomalous upper mantle beneath the Central Andes. Isostasy and Andean uplift. Symposium of Andean Geodinamics (Oxford, September 1993). Expanding Abstract.

Isacks, B. 1988. Uplift of the Central Andean Plateau and Bending of the Bolivian Orocline. J. Geophys. Res. 93 (B4), 3211-3231.

Le Pichon, X. and Sibuet. 1981. Passive margins: a model of formation. J. Geophys. Res. 86, 3708-3720.

Lion, A. and Introcaso, A. 1987. Comportamiento isostático de la Sierra de Córdoba (Rep. Arg.) Rev. de Geof. (Madrid) 43, 171-182.

Miranda, S. and Introcaso, A., 1995. Mecanismo de flexión viscoelástica en la Sierra de Córdoba (República Argentina). Análisis preliminar en 31 ° 30'S. IV Congreso Internacional da Sociedade Brasilera de Geofísica. Resúmenes expandidos Vol II, 1090-1093.

Pardo, M. and Fuenzalida, A. 1988. Estructura cortical y subducción en Chile Central. V Congreso Geológico Chileno II, F247-F265.

Schmidt, M. 1993. Kollisionsstrukturen in den Zentralen Anden: Ergebnisse refraktionsseismischer Messungen und Modellierung krustaler Deformationen. Berliner Geowiss Abh (B), BandZo, 1, 127. Selbstverlag Fachbereich Geowissenschaften, F. U. Berlin.

GEOACTA, 22, 20-29, 1997

ON THE DISSIPATION OF AN UPPER OCEANIC FRONT

Alejandro L. Camerlengo and Mónica I. Demmler
Faculty of Fisheries and Marine Science, Universiti Pertanian Malaysia, Mengabang Telipot, 21030 Kuala Terengganu, Malaysia.

ABSTRACT

This study seeks to gain some insight into the role played by horizontal friction in the dissipation of an oceanic front. For this purpose, a two layer model is used. The barotropic, or external, mode is filtered out. To simplify the equations, the wind stress terms are omitted. Two cases are considered: the coastal front and the upper ocean front. In the first case, it is shown that the larger the Ekman number, the lesser time it would take for the front to dissipate. In the second case, it is demonstrated that the average time scale of dissipation, due to horizontal friction, of an upper oceanic front is in the order of decades. Oceanic fronts do represent areas of horizontal convergence of different water masses. This convergence is due to the change of the curl of the wind stress pattern. Because of the fact that the wind stress is not considered in this study, it can be concluded that upper ocean fronts should be a permanent feature. This is the case of the Gulf Stream and the Kuroshio front.

RESUMEN

En el presente trabajo se estudia el papel jugado por la fricción horizontal en la disipación de un frente oceánico. A tales efectos, se ha utilizado un modelo de dos capas, en el cual el modo externo, o barotrópico, ha sido eliminado. A fin de simplificar las ecuaciones, los términos que representan la forzante del viento, no han sido incluídos en este trabajo. Se consideran dos casos: los frentes costeros y los de alta mar. En el primer caso, se demuestra que cuanto mayor es el número de Ekman, menor es el tiempo de disipación del frente costero. En el segundo caso, se demuestra que el tiempo promedio de disipación de un frente en alta mar es del orden de décadas. Los frentes de alta mar representan zonas de convergencia de masas de agua de distintas características. Dicha convergencia está asociada a las variaciones del rotor de la forzante del viento. Dado que la forzante de viento no ha sido considerada en este trabajo, se deduce que los frentes de alta mar deberán ser una característica permanente del océano. Tal es el caso de la corriente del Golfo y del frente de Kuroshio.

1. INTRODUCTION

Oceanic fronts occur on areas of increasing turbulence and convection. Their main characteristic are sharp gradients of salinity and/or temperature. It is a region of

increasing motion (Roden, 1976). Usually oceanic fronts represent the discontinuity between two different water masses where one or more of the following properties: temperature, salinity, density and velocity, are different.

Oceanic fronts occur at all depths. Fronts are also variable in time. They intensify and decay, in response to changes in the atmospheric and oceanic flow patterns. Examples of permanent oceanic fronts are the Antarctic Circumpolar Current, the Subarctic and the Subtropical oceanic fronts in the North Pacific Ocean.

Oceanics fronts differ from their atmospheric counterpart in many ways. In the atmosphere, both the temperature and the density fronts coincide. Thus, atmospheric frontal zones are extremely baroclinic (Palmen & Newton, 1969). The first attempts in the understanding and the physical interpretation of atmospheric fronts started early in this century. The classical Norwegian school was the first one which attempted to understand this meteorological phenomenon. The studies of Bjerknes (1919) and Bergeron (1928) are classical in this matter. In the case of oceanic fronts, if the temperature and the salinity fronts do have the same geographical location, the density front is weak, or nonexistent. The baroclinicity is small. Such is the case of the subtropical Pacific Ocean Front (Roden, 1974).

Frontogenesis in the North Pacific is due to differential vertical and horizontal advection of the Ekman type. A given configuration of the wind stress field may lead to frontogenesis in some regions, and to frontolysis in other areas. Furthermore, in the upper layer of the ocean, the formation and maintenance of oceanic fronts depends of the horizontal shear of the wind stress (Roden, 1977).

Camerlengo (1982) studied the large scale response of the Pacific Ocean Subarctic Front to different forms of atmospheric forcing, i.e., atmospheric fronts, extratropical cyclones, wind stress curl, etc. His results agree with Roden's (1972) observations, in the sense that the dynamic response of the subarctic front to momentum transfer is limited to the layer between the sea surface and the high stability layer. The only exception was represented by the passage of a strong extratropical cyclone, where an upwelling of the order of 20 m is observed at the wake of the cyclone. Due to the fact that the time scale of dissipation of an upper oceanic front is an integral part of ocean dynamics, a series of theoretical experiments are conducted. This is the first attempt in this regard.

2. MODEL FORMULATION

2.1. Statement of the problem

A two layer model is considered in this study. The vertically averaged equations of conservation of mass and continuity (barotropic mode) are filtered out. For this purpose, the lower layer is chosen to be infinitely deep. Therefore, the currents, in that particular layer, are set to be zero. The model equations for this study are similar to MacVean &

Woods (1980) and Camerlengo (1982).

The analysis was limited to the first layer, or the first baroclinic mode. This type of model is, sometimes, referred as the one a half layer model (Busalacchi & O'Brien, 1980). The east-west and north-south velocity components, u and v, correspond to the horizontal coordinates x and y (positive in the east and north direction, respectively).

To simplify the equations to be used, the following hypotheses are made: 1) the time scale of dissipation of the oceanic front is larger that the time scale of the perturbation produced by the wind stress; 2) the longitudinal frontal length scale is smaller than the latitudinal length scale. Thus, the derivatives with respect to x are neglected as compared to the derivatives with respect to y; 3) the oceanic front is geostrophically balanced; 4) since the meridional length scale of the oceanic front in the upper layer has an order of magnitude of ten kilometers, the f-plane approximation is used; 5) the zonal wave number, k, is much smaller than 1/L. Therefore, only long waves are considered; and, 6) the vorticity at the front, represented by $\partial u/\partial y$, is much smaller than the planetary vorticity, f.

The pressure in the upper layer, layer 1, will have the form

$$P = P_\alpha + \rho_1 g (h_1 - z) + \rho_2 g (H - h_1) \qquad (1)$$

where P_α represents the atmospheric pressure; h_1, the depth of the upper layer; ρ the water's density; H, the total depth; g, the acceleration due to the earth's gravity; and z, the vertical coordinate, which is measured from the bottom. The gradient of P_1 yields

$$\nabla P_1 = - \rho_1 g^* \nabla h_1 \qquad (2)$$

where $g^* = g (\rho_1 - \rho_2)/\rho_1$ represents the reduced gravity. As usual, the horizontal fluctuations of the atmospheric pressure are neglected. For convenience, the subindex 1, representing the upper layer, will be omitted.

2.2. Equations of motion

With the above assumptions, the equations of motion for the upper layer are:

$$\partial u/\partial t + v \partial u/\partial y - f v = A \partial^2 u/\partial y^2 \qquad (3)$$

$$\partial v/\partial t + v \partial v/\partial y + f u = - g^* \partial h/\partial t + A \partial^2 v/\partial y^2 \qquad (4)$$

$$\partial h/\partial t + \partial (vh)/\partial y = 0 \qquad (5)$$

where f, is the Coriolis parameter; A, the horizontal diffusion coefficient of momentum; h, upper layer thickness and t, time. In our study, the forcing due to the wind stress terms

are neglected in order to retain only the forcing due to the frictional terms.

This non-linear set of equations are difficult to solve. Therefore, it is assumed that the frictional effect will slowly change a steady, inviscid initial front, and a perturbation solution is presented by assuming that friction has a weak effect. For this steady oceanic front to persist, the interface, h , must be balanced initially by a zonal velocity of the form

$$u_o = - (g^*/f) \partial h_o/ \partial y \tag{6}$$

where the subscript "o" stands for the basic state.

The height of the upper (first) layer, h , has an hyperbolic profile, centered in the middle of the north-south extent of the basin, W, of the form:

$$h = h - \Delta h \tanh ((y - W/2)/L) \tag{7}$$

where h represents the mean value depth; L, the longitudinal frontal length scale; Δh, the maximum amplitude of the interface perturbation. By continuity, the meridional velocity, v , is initially set to zero.

3. ANALYSIS OF THE PROBLEM

The viscous perturbation solutions are obtained by assuming the value of A to be very small. Let

$$\begin{aligned} u &= u + u' \\ v &= v + v' \\ h &= h + h' \end{aligned} \tag{8}$$

where the perturbation variables are denoted by primes. The perturbation variables are assumed to be of order A (Pedlosky, 1979). The equations for the upper layer then become

$$\partial u'/\partial t - (v' g^*/f) \partial^2 h_o/ \partial y^2 + v'\partial u'/\partial y - f v' = - (A g^*/f) \partial^3 h_o/ \partial y^3 + A \partial^2 u'/ \partial y^2 \tag{9}$$

$$\partial v'/\partial t + v'\partial v'/\partial y + f u_o + f u' = - g^* \{ \partial h_o/ \partial y + \partial h'/ \partial y\} + A \partial^2 v'/ \partial y^2 \tag{10}$$

$$\partial h'/\partial t + \partial (h_o v')/\partial y + \partial (h' v')/\partial y = 0 \tag{11}$$

The terms $v'\partial u'/\partial y$, $v'\partial v'/\partial y$, $\partial (h' v')/\partial y$, $A \partial^2 u'/ \partial y^2$ and $A \partial^2 v'/ \partial y^2$ are of second order. Thus, they are considered negligible. The terms fu and -g*dh /dy represent

the basic state balance. In order to filter out the gravity waves, the term $\partial v'/\partial t$ is omitted (Pedlosky, 1979). With these simplifications, the above equations are reduced to linear perturbation equations of the form

$$\partial u'/\partial t - (v' g^*/f)\{\partial^2 h_o/\partial y^2 + (f^2/g^*) = -(A g^*/f)\partial^3 h_o/\partial y^3 \quad (12)$$

$$u' = -(g^*/f)\,\partial h'/\partial y \quad (13)$$

$$\partial h'/\partial t + \partial (h_o v')/\partial y = 0 \quad (14)$$

To solve this system, a single equation for v' is first needed. Replacing the value of u' in (12) yields

$$-(g^*/f)\{(\partial^2 h'/\partial y \partial t) - (v' g^*/f)\{\partial^2 h_o/\partial y^2 + (f^2/g^*)\} = -(A g^*/f)\,\partial^3 h_o/\partial y^3 \quad (15)$$

Applying the operator $(g^*/f)\,\partial(\,)/\partial y$ to (14), it follows that

$$(g^*/f)\{(\partial^2 h'/\partial t \partial y) + \partial^2 (h_o v')/\partial y^2\} = 0 \quad (16)$$

The addition of (15) and (16) yields

$$\partial^2 V/\partial y^2 - \{\partial^2 h_o/\partial y^2 + (f^2/g^*)\}/h_o V = -A\,\partial^3 h_o/\partial y^3 \quad (17)$$

where V (=v'h) is the mass transport in the upper layer. The boundary conditions are such that the meridional mass transport, V, is set to be zero at both the northern and southern boundaries. It is of interest to note that V is independent of time.

As h (y) is a known function, the coefficients of (17) are known. Therefore, this equation can be rewritten as

$$\partial^2 V/\partial y^2 - F(y)\,V = -G(y) \quad (18)$$

where

$$F(y) = \{\partial^2 h_o/\partial y^2 + (f^2/g^*)\}/h_o \quad (19a)$$

and

$$G(y) = A\,\partial^3 h_o/\partial y^3 \quad (19b)$$

In order to cover a wider range of oceanic fronts, two different meridional length scales, L, are considered. The chosen dimensions are 1 and 50 kilometers, respectively. In the first case, an approximate value of F(y) is:

$$F(y) = (f^2/g^* h_o) \tag{20}$$

while in the second case, F(y) has an approximate value of:

$$F(y) = \{\partial^2 h_o/ \partial y^2 \}/ h_o \tag{21}$$

Using the first approximation, (18) may be rewritten as:

$$\partial^2 V/ \partial y^2 - \alpha^2 V = - A \partial^3 h_o/ \partial y^3 \tag{22}$$

where $\alpha^2 = f^2 (g^* h_o)^{-1}$ is the inverse of the squared Rossby radius of deformation. For this particular case, an analytical solution can be obtained. If the Ekman number is set to be equal to 0.1, the resulting value of A is then 10 m sec. The scaling of (22) shows that the first and third terms are the largest ones, by two orders of magnitude. Therefore, (22) has the form

$$\partial^2 V/ \partial y^2 = - (2 A \Delta h/ L^3)\{[2 \sinh^2((y - 0.5 W)/L) - 1]/ \cosh^4((y - 0.5 W)/L)\} \tag{23}$$

The analytical solution of this expression is

$$V(y) = - (A \Delta h/ L) \operatorname{sech}^2 ((y - 0.5 W)/L) \tag{24}$$

The integration, with respect to time, of the continuity equation yields a perturbation expression for the interface, h', of the form

$$h' = (\partial V/ \partial y)\ t \tag{25}$$

Considering the maximum absolute value of the y-derivative of the meridional mass transport, the time scale of dissipation, T, is defined in such a way that

$$T=h' |\partial V/\partial y|^{-1}_M \tag{26}$$

where $|\partial / \partial y |_M$ represents the maximum absolute of such derivative. The value of h' is arbitrarily set up to be equal to 10 meters. For different values of A and L, different values of $|\partial V/ \partial y |_M$ may be obtained (Table 1).

However, this solution is restricted to oceanic fronts of the order of one kilometer.

As stated previously, the upper oceanic fronts have a meridional length scale of the order of ten kilometers. A new scaling of (22), using this same length scale, shows that the three terms of the equation are comparable. Thus, the full equation has to be solved.

A (m sec^{-1})	L (km)	$\lvert \partial V/\partial y \rvert_M$ (m sec^{-1})	T (sec)
10	2	$2\ 10^{-5}$	$5\ 10^{5}$
10	1	$8\ 10^{-5}$	$1.25\ 10^{5}$
1	2	$2\ 10^{-6}$	$5\ 10^{6}$
1	1	$8\ 10^{-6}$	$1.25\ 10^{6}$

Table 1. Time scale of dissipation, T, for different values of A, L, $\lvert \partial V/\partial y \rvert_M$, using equation (22).

In using a meridional length scale of 50 kilometers, (22) has the form:

$$\partial^2 V/\partial y^2 \quad - \quad (\partial^2 h_o/\partial y^2)\ (V/h_o) = - A\ \partial^3 h_o/\partial y^3 \tag{27}$$

The general solution of the corresponding homogeneous equation (27), Vc(y), is

$$Vc(y) = C_1 V_1 + C_2 V_2 \tag{28}$$

where V = h , V = h Ii h dy and C and C are arbitrary constants. The method of variation of parameters is used to solve the nonhomogeneous equation (22). This method requires the replacement of the constants C and C by two arbitrary functions, c(y) and z(y). These arbitrary functions will be determined in such a way that the particular solution, V (y), has the form

$$V(y) = \chi(y)\, V_1(y) + \zeta(y)\, V_2(y) \tag{29}$$

The arbitrary function, c and x, must satisfy certain conditions in order to satisfy the nonhomogeneous ordinary differential equation. These conditions are

$$\chi_y V_1 + \zeta_y V_2 = 0 \tag{30a}$$

$$\chi_y V_{1y} + \zeta_y V_{2y} = \psi(y) \tag{30b}$$

where χ_y, ζ_y, V_{1y} and V_{2y} represent the meridional derivatives of the functions χ , ζ,

V_1 and V_2, respectively; and ψ (y) represents the forcing function defined by

$$\psi (y) = - (2 A \Delta h / L^3) \{[2 \sinh^2((y - 0.5 W)/L) - 1]/ \cosh^4((y - 0.5 W)/L)\} \quad (31)$$

The system of equation (30) gives us a solution for the functions χ_y and ζ_y.. These values are:

$$\chi_y = - V_2 (y) \psi (y)/ W (V1,V_2) \quad (32a)$$

$$\zeta_y = - V_1 (y) \psi (y)/ W (V1,V_2) \quad (32b)$$

where the wroskian, W(V1 ,V_2), is equal to one.

The values of χ and ζ, at each grid point, are determined by numerical integration. To achieve this purpose, Simpson's rule is used. Knowing the values of χ and ζ, a final expression for the meridional mass transport, V, can be numerically evaluated at each grid point. Such an expression has the form

$$V (y) = (C_1 + \chi) V_1 (y) + (C_2 + \zeta) V_2 (y) \quad (33)$$

Again, by plotting the function $\partial V / \partial y$ versus y, a maximum absolute value of the former function may be determined for different values of A and L (Table 2).

A (m sec)	L (km)	$\lvert \partial V / \partial y \rvert_M$ (m sec^{-1})	T (sec)
1	10	5 10	10^9
1	50	7 10	10^{11}
10	10	5 10	10^8
10	50	7 10	10^{10}
100	10	5 10	10^7
100	50	7 10	10^9

Table 2. Same as table 1, but using equation (27).

3. CONCLUSIONS

Kao (1980) showed that the structure of an oceanic front in a quasi-steady state depends on the Ekman number, E. Furthermore, in that same study, it is shown that for $E << 1$, the structure of the front is insensitive to changes in the value of E.

A study dealing with the dissipation of an oceanic front due to horizontal friction has not yet been conducted. This is a first such an attempt. In our study, the value of E was allowed to vary from 10 to 10. In choosing this particular range, the cases of coastal front and upper ocean front are addressed.

Due to the fact that oceanic fronts occur in all horizontal space scales, the value of L is allowed to vary between 1 and 50 km. In the first case, we attempt to study the dissipation of coastal fronts. Therefore, the chosen value of L is in the order of 10 m (Table 1). On the other hand, in the second case, we attempt to study the dissipation of an upper ocean front (Table 2). In this case, L is chosen to be on the order of 10 m (Roden, 1976).

In the first case, A is chosen to vary between 1 and 10 m sec. Due to the almost constancy in the (chosen) value of L, the value of the Ekman number (E = A/(f L)) highly depends on the value of A. In our case, the value of E varies from 10 to 10. An uppermost value of A = 10 m sec is chosen such that E ¾ 10. It is shown that the larger the value of E, the smaller the value of T (Table 1). It is concluded that the larger the value of horizontal friction, the lesser time it would take for the coastal oceanic front to dissipate.

In the second case, we attempt to study the dissipation of an upper ocean front (Table 2). In this case, the values of A are chosen to vary between 1 and 100 m s. The resulting Ekman number varies between 10 to 10. This range in the value of E corresponds to the large scale ocean circulation (Pond & Pickard, 1978). For the smallest value of E, T would be in the order of one year.

Forcing due to the wind stress terms are neglected in this study. However, the existence of the Pacific Ocean subarctic front is a natural consequence of the convergence of two different water masses. This convergence is triggered by the wind stress pattern. The average time scale of dissipation (due to horizontal friction) of upper ocean fronts is in the order of decades (Table 2). It can concluded that upon consideration of the wind stress terms, upper ocean fronts should be a permanent feature in the ocean. This is precisely what happens in the real world. Examples of such permanent fronts are the Kuroshio front, the Gulf Stream, the subtropical and the doldrums fronts.

Acknowledgements. This study was supported by Universiti Pertanian Malaysia through contract No. 50213-94-05. The authors gratefully acknowledge comments made by anonymous reviewers. Their comments greatly helped the improvement of this paper.

REFERENCES

Bergeron, T., 1928. Tber die drei dimensional verknüpfende Wettranalyse 1. Geofys. Publ., 5, No. 6, 1-111.

Bjerkness, J., 1919. On the structure of moving cyclones. Geofys. Publ., 1, No. 2.

Busalacchi, A. J. and J. J. O'Brien, 1980. The Seasonal variability in a Model of the Tropical Pacific. J. Phys. Oceanogr., 10, 1929-1951.

Camerlengo, A. L., 1982. Large Scale Response of the Pacific Subarctic Front to Momentum Transfer: A Numerical Study. J. Physical Oceanography. 12. 1106-1121.

Kao, T. W., 1980. The dynamics of oceanic fronts. Part I: the Gulf Stream. J. Phys. Oc., 10, 483-492.

MacVean, M. K. and J. D. Woods, 1980. Redistribution of Scalars during Upper Ocean Frontogenesis: A Numerical Model. Quart. J. R. Met. Soc., 106, 293-311.

Palmen , E. & C. W. Newton, 1969: Atmospheric Circulation System. Academic Press, 602 pp.

Pedlosky, J., 1979. Geophysical Fluid Dynamics; Springer-Verlag. 624 pages.

Pond, S. and G. L. Pickard, 1978. Introductory Dynamic Oceanography. Pergamon Press, 241 pages.

Roden, G. I., 1972. Temperature and Salinity Fronts at the Boundaries of the Subarctic-Subtropical Transition Zone in the Western Pacific. J. Geophysical Research. 77. 7175-7187.

Roden, G. I., 1974. Thermohaline structure, fronts and sea-air energy exchange of the trade wind region east of Hawaii. J. Phys. Oceanogr., 4, 168-182.

Roden, G. I., 1976. On the Structure and Prediction of Oceanic Fronts, Naval Research Reviews, 29(3), 18-35.

Roden, G. I., 1977. Oceanic Subarctic fronts of the Central Pacific: structure of and Response to atmospheric forcing. J. Phys. Oc., 7, 761-778.

GEOACTA, 22, 30-46, 1997

EL CALCULO DEL AGUA PRECIPITABLE Y ALGUNAS DE SUS APLICACIONES EN ARGENTINA

Graciela A. Catuogno e Inés Velasco
Depto de Cs. de la Atmósfera, Facultad de Ciencias Exactas y Naturales,
Universidad de Buenos Aires, Ciudad Universitaria, Pab. II 1428, Buenos Aires.

ABSTRACT

Different models have been essayed for the estimation of precipitable water based on humidity data observed at ground level in order to improve the spatial and time distribution of precipitable water values, due to the fact that there are only four upper air data stations in an extended area of central and northeastern Argentina. Fields of precipitable water are analysed in relation to the development of mesoscale convective complexes. Ten years of data were processed in order to evaluate the different models. One model used only surface dew point in an adiabatic saturate atmosphere calculated from that value. The vertical profile of the dew point monthly average was used as an alternate method for calculating the precipitable water, modified in the layer between the surface and 800 hpa. by the average surface dew point gradient. When the results of the first model were compared with the values of precipitable water calculated with radiosonde data it showed a seasonal behaviour in the error estimation which reached 30% during summer. Results improved when a second method was applied. The analysis of precipitable water model showed a redistribution of water vapour in the atmosphere during the evolution of mesoscale convective complexes according to our expectation. The precipitable water field appears as an upper limit of the areal precipitation in the zone, existing exceptions for punctual cases.

RESUMEN

Con el fin de realizar un análisis espacio temporal del agua precipitable más detallado que el que permite la red de radiosondeos de Argentina y su relación con el desarrollo de sistemas convectivos de mesoescala, se ensayaron para su estimación distintos métodos que utilizan como base el punto de rocío en superficie. Uno de ellos usa solamente la temperatura de rocío de superficie y asume una atmósfera saturada a partir de ese valor. Otro modelo asume un perfil vertical medio mensual de la temperatura de rocío modificado en la capa entre superficie y 800 hPa por el gradiente medio de la temperatura de rocío calculado éste a partir de la temperatura de rocío de superficie. La región estudiada incluye cuatro estaciones de radiosondeos y 31 estaciones de superficie y se trabajó con un período de 10 años. Al comparar los valores de agua precipitable calculados con la red de radiosondeos de Argentina con los estimados por el primer método aplicado, se encontró que la diferencia mostraba un comportamiento estacional cuyo error alcanzaba a un 30% en los meses de verano. Los resultados mejoran con el segundo método de estimación aplicado. Un tercer método asume el sondeo de una estación como representativo de

la tropósfera en un área de su entorno, excepto en superficie. Al estudiar los campos de agua precipitable estimados en relación con el desarrollo de los sistemas convectivos estos mostraron una evolución similar en los distintos casos estudiados, observándose una redistribución del vapor de agua en la atmósfera durante la evolución de las tormentas. Estos campos representan el valor máximo esperable de la precipitación areal en la región, con excepciones a nivel puntual.

1. INTRODUCCION

El contenido de vapor de agua integrado verticalmente en la atmósfera es llamado vapor columnar o agua precipitable (AP) y de acuerdo con Solot (1939) puede cuantificarse por la altura que adquiriría el agua líquida que resultara condensada en una columna de aire de sección unitaria. Para su cálculo se necesita conocer la presión en superficie y el perfil vertical de humedad que se puede obtener a través de los radiosondeos. Sin embargo, como es sabido, las estaciones de radiosondeo están muy dispersas y esto motivó la elaboración de distintos modelos para estimar AP en función de algún parámetro de humedad medido en superficie. Varios intentos han sido realizados en el hemisferio Norte, Reitan (1963) propuso una regresión lineal entre la temperatura de rocío y el logaritmo natural del agua precipitable para valores mensuales y Bolsenga (1965) extrajo una relación similar sobre bases diarias. Smith (1969) demostró que las expresiones anteriores tienen un error de estimación grande y realizó un estudio sobre bases físicas, introduciendo la dependencia del agua precipitable respecto a la latitud y la estación del año. En nuestro país Vargas y Ashkenazi (1975) realizaron un estudio sobre las bases propuestas por Smith pero incluyendo la situación sinóptica para estimaciones areales. Un método alternativo de medición es el uso de los radiómetros pasivos que emplean dos o más canales de microondas y que fueron usados experimentalmente durante la última década para medir el agua precipitable. Estos instrumentos según Guiraud *et al.* (1979) son capaces de medir el contenido de vapor de agua en una columna con mayor exactitud que con un radiosonda convencional, y cuando están equipados con 6 o más canales pueden estimar también el perfil vertical de temperatura.

El contenido de vapor de agua en la atmósfera es muy variable tanto en el espacio como en el tiempo y su conocimiento es de sumo interés en relación con diferentes temas. Entre estos están los estudios de balance de radiación y de propagación de ondas electromagnéticas (Youklin *et al.*, 1965; Lowry, 1972 y, Reber y Swope, 1972). Resch (1980) y Hellings (1980) han explicado además que la variabilidad del vapor de agua es frecuentemente la principal fuente de error en la determinación de posiciones usando interferometría de microondas empleando estaciones terrestres y una fuente extraterrestre. La variabilidad del vapor de agua en el espacio y en el tiempo genera dificultades en la

simulación numérica de las circulaciones atmosféricas. Los modelos de predicción de mesoescala (Perkey, 1980) y los modelos de circulación general en latitudes bajas (Lorenc y Tibaldi, 1980) son altamente sensibles al campo de humedad inicial. Otros ejemplos están relacionados con la formación de nubes y con los flujos de calor latente y la dificultad de obtener mediciones representativas de la humedad.

El contenido del vapor de agua en la atmósfera es una cantidad fluctuante y las aplicaciones requieren un mejor conocimiento no sólo de su valor sino también de sus fluctuaciones. Los datos de agua precipitable existentes sobre la Argentina son escasos y representan evaluaciones realizadas a nivel hemisférico o global, con una base de datos muy limitada (Van Loon, 1955; Tuller, 1968 y Landsberg, 1969), que utilizaron en ocasiones relaciones empíricas con los datos de humedad en superficie (Viswanadham *et al.*, 1970; Vargas y Ashkenazi, 1975) o bien, valores medios mensuales de la red aerológica del Servicio Meteorológico Nacional (Catuogno y Velasco, 1986).

El objetivo de este trabajo es, dada la baja densidad de estaciones de radiosondeo en Argentina, obtener métodos de estimación del agua precipitable en la región para lograr una mejor resolución que permita obtener campos más detallados para su análisis en relación con el desarrollo de sistemas convectivos de mesoescala.

2. CALCULO DEL AGUA PRECIPITABLE POR DISTINTOS METODOS

Con el fin de lograr una mayor frecuencia espacio/temporal del agua precipitable que la que se obtiene con la red de estaciones aerológicas al hacer su cálculo por fórmula (Catuogno y Velasco, 1986) y poder entonces captar con más detalle las variaciones que puede experimentar el vapor de agua en la atmósfera fueron ensayados distintos métodos para estimar AP en función de un parámetro de humedad medido en superficie. En el presente trabajo se aplicó en principio el modelo descripto en OMM (1986) que usa solamente la temperatura de rocío de superficie y asume una atmósfera saturada a partir de ese valor. Este método es frecuentemente utilizado por los hidrólogos para estimar la precipitación máxima probable de una tormenta (OMM, 1986). Como alternativa se diseñó otro modelo que asume un perfil vertical medio mensual de la temperatura de rocío modificado, en la capa entre superficie y 800 hPa por el gradiente medio de temperatura de rocío, calculado éste a partir de la temperatura de rocío de superficie. Por último se aplicó un método que resulta más adecuado cuando interesa tener mayor información del agua precipitable en un área donde sólo se dispone de un radiosondeo, pero de varias estaciones de superficie. En éste caso los datos del radiosondeo se toman como representativos de la tropósfera en el área y se modifican en el nivel de superficie.

2.1. Cálculo del agua precipitable asumiendo una atmósfera adiabática saturada

Con dos muestras de datos de radiosondeos interpolados a los niveles 1000, 900, 850, 800, 700, 600, 500 y 400 hPa de las estaciones Resistencia, Córdoba y Ezeiza de la hora 1200 UTC, una representativa de la estación cálida y otra de la fría para un período de 10 años (1971-1980) se calculó por un lado el agua precipitable dividiendo a la atmósfera en 8 capas considerando los niveles de presión antes mencionados e integrando verticalmente el vapor de agua (Catuogno y Velasco, 1986), variable que se indicará en adelante como AP(R), y es además considerada como el valor más cercano al contenido total de vapor en una columna de aire de sección unitaria. Por otro lado se calculó esta variable usando solamente la temperatura de rocío de superficie (Td) y asumiendo una atmósfera adiabática saturada a partir de ese valor, variable que se representará en adelante como AP(T) dado que los valores usados para este método están en tablas. De la comparación de ambos métodos y tomando como valores verdaderos los calculados en base a los datos de radiosondeo (AP(R)) se observó que el agua precipitable calculada por tablas (AP(T)) sobreestima, en la mayoría de los casos a la calculada con datos del radiosondeo y que además esta sobreestimación tiene un comportamiento estacional. Estos resultados se evidencian en la Fig. 1 a) y b), donde se muestra el histograma de frecuencia de las diferencias entre ambos métodos para invierno y verano respectivamente. El error (E) cometido al estimar el agua precipitable por tablas es más significativo en verano (del orden del 30%) que en invierno (menor que el 1%). Por ejemplo el análisis de los datos diarios de radiosondeo de Ezeiza para el período de verano (en una muestra de 1200 casos), indica que en el 40% de los casos la diferencia AP(T)-AP(R) es mayor que 10 mm representando ésta cota un 30% del valor promedio del agua precipitable. Dentro de esta última muestra se encuentra que en el 10% de los casos la sobreestimación es mayor que 20 mm y para el 1.4% la estimación supera en más de 30 mm y sólo en el 1% de los 1200 casos se observa que esa diferencia es negativa (menor o igual que 10 mm). El análisis de los sondeos muestra que en el caso de las diferencias positivas la humedad se concentra en las capas próximas a superficie, tal como lo indican los marcados gradientes de temperatura de rocío entre 1000 y 800 hPa, obteniéndose grandes diferencias con respecto al gradiente adiabático saturado correspondiente a la temperatura de rocío de superficie e incluso respecto al gradiente medio de la temperatura de rocío (Fig. 2).

2.2. Cálculo del agua precipitable utilizando un perfil vertical medio de temperatura de rocío

Como una alternativa al método de (OMM, 1986) para el cálculo del agua precipitable se usó el perfil vertical medio mensual de la temperatura de rocío modificado en la capa entre superficie y 800 hPa por el gradiente medio de temperatura de rocío calculado éste, a partir de la temperatura de rocío de superficie, variable que se nombrará

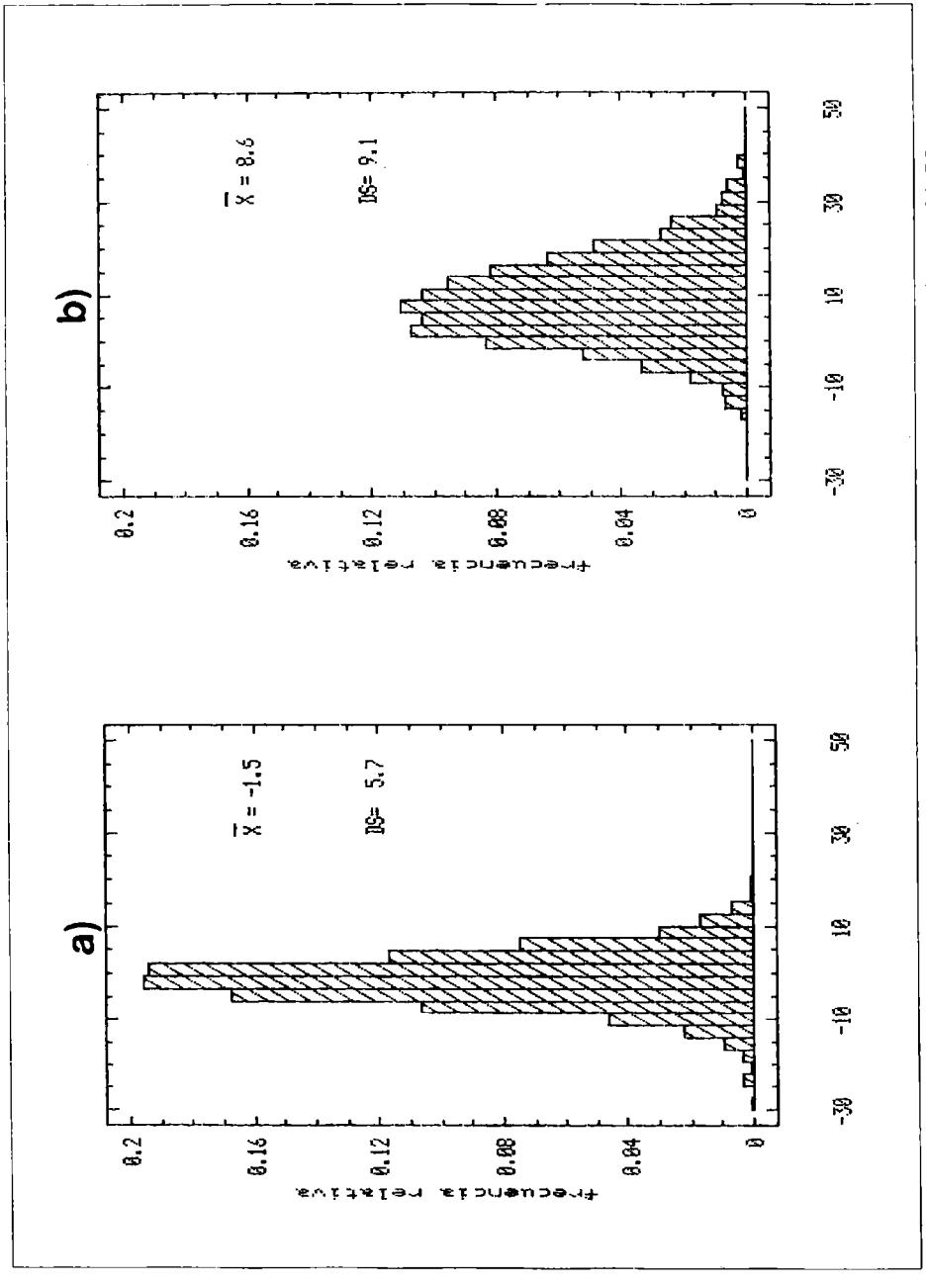

Fig.1 Histograma de Frecuencias de AP (T) - AP (R) para Ezeiza. a) Invierno; b) Verano

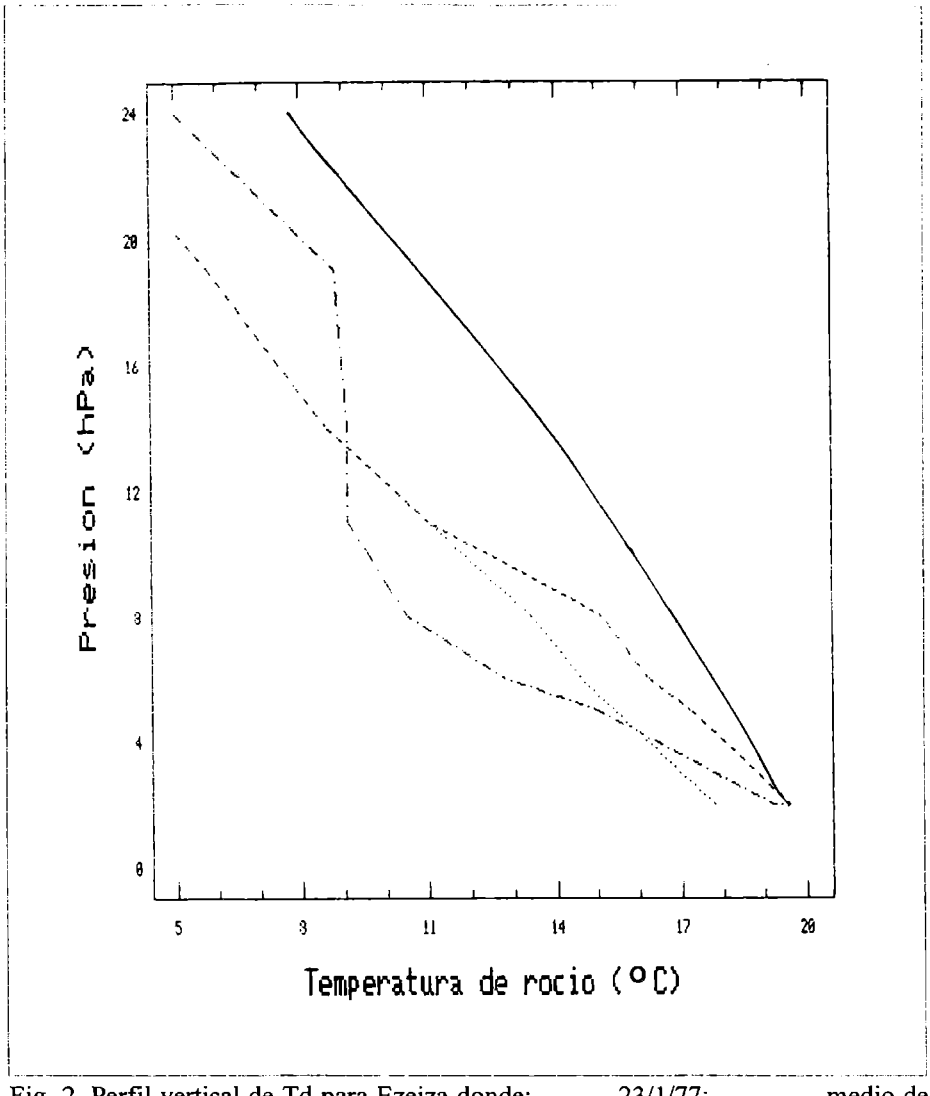

Fig. 2. Perfil vertical de Td para Ezeiza donde: -.-.-.-. 23/1/77; ..... medio de Enero; ---- medio de Enero modificado entre superficie y 850 hPa; _____ de una atmósfera adiabática saturada

en adelante como AP(P). El cálculo de AP(P) se hizo con la misma muestra anterior, para el período de verano dado que en esa estación es cuando el método anterior muestra más error. En la Fig. 3 se muestra el histograma de las diferencias entre AP(P)-AP(R). Se puede observar que las diferencias entre el valor real y el calculado en este caso se

distribuyen normalmente con media -1.9 y desviación estándar 7.6. Estos resultados indicaran que este método mejora al anterior. Sin embargo los resultados tampoco son lo suficientemente satisfactorios para que los valores estimados remplacen directamente a los valores calculados individualmente.

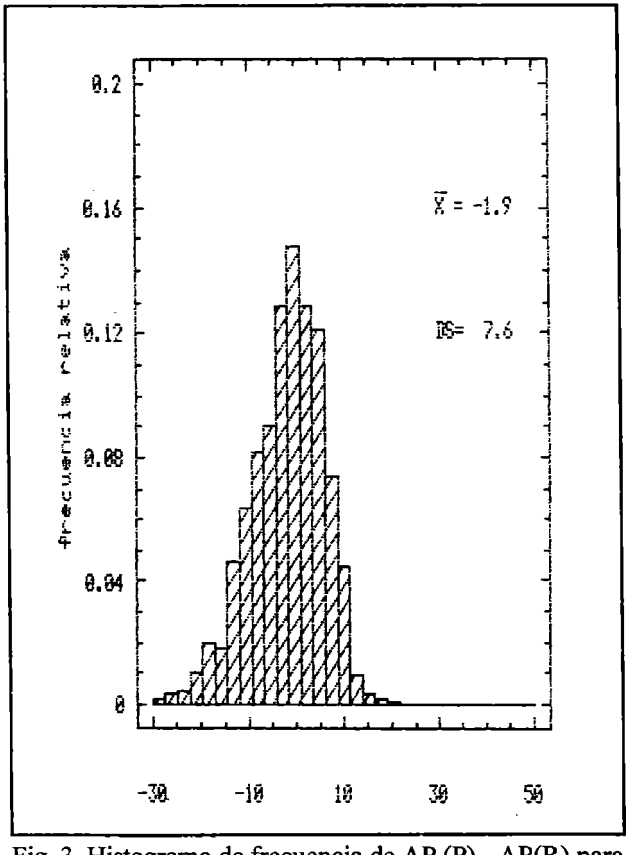

Fig. 3. Histograma de frecuencia de AP (P) - AP(R) para Ezeiza verano.

2.3. Cálculo de errores

En vista de los resultados obtenidos se procedió a realizar un análisis del peso de cada una de las variables de la fórmula del cálculo de AP adaptada según Catuogno y Velasco (1986) teniendo en cuenta sus posibles variaciones y como cada uno de ellos es reemplazado en los métodos de estimación. Para este análisis se aplicó el método de propagación de errores a la fórmula del cálculo del AP y se consideraron sólo la presión de superficie y las temperaturas de rocío de superficie, 900, 850 y 800 hPa ya que como es sabido, la mayor concentración y variación del vapor de agua se encuentra en dicha capa. En el cálculo de propagación de errores se utilizaron los valores medios de verano (diciembre, enero, febrero y marzo) de las estaciones aerológicas Ezeiza y Resistencia. Los resultados indican que las variaciones relativas de mayor peso son las que representan a la humedad en los niveles de superficie y 900 hPa (del orden del 2%), seguidas por las variaciones de ese parámetro en los niveles superiores, totalizando en conjunto un 6%. En el caso del cálculo del AP diario asumiendo una atmósfera adiabática saturada se observan desviaciones de la temperatura de rocío (Fig. 2) generalmente positivas que aumentan con la altura generando una acumulación de errores que se manifiestan produciendo una sobreestimación marcada. Si bien el peso relativo de los parámetros decrece con la altura su influencia en este caso

aumenta al aumentar notoriamente la sobreestimación de Td por el gradiente adiabático saturado. Con el segundo método si bien también se observan desviaciones de Td en los niveles superiores estas son menores y de signo alternados. En consecuencia el segundo método resultaría ser más adecuado, especialmente para su uso en cálculos estadísticos.

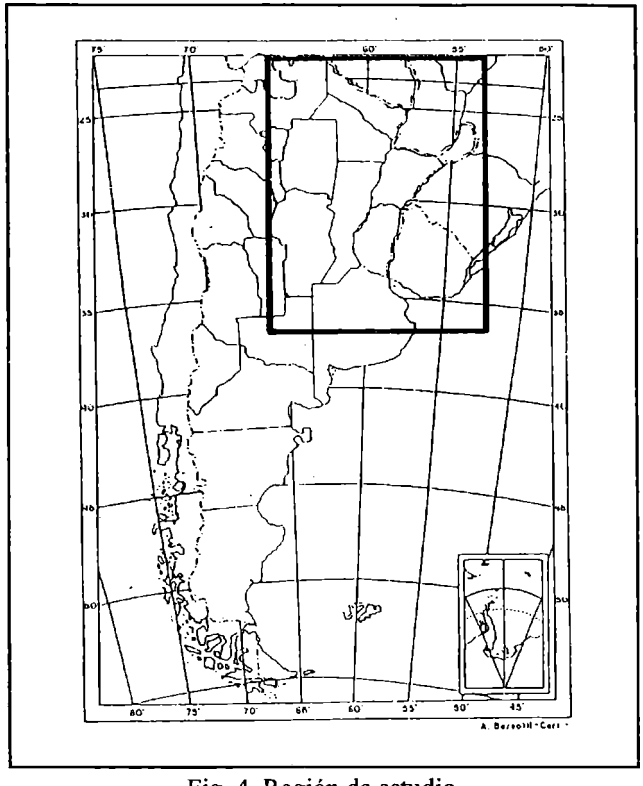

Fig. 4. Región de estudio.

2.4. Cálculo del agua precipitable considerando el sondeo de una estación representativo de un área.

En este caso, se estima el agua precipitable para cada estación de superficie, utilizando en su cálculo el perfil vertical obtenido en la estación de radiosondeo más próxima (Fig. 5), reemplazando los datos de presión y temperatura de rocío de superficie por las observaciones respectivas de cada estación sinóptica del área y aplicando la fórmula de Catuogno y Velasco (1986). Este procedimiento implica asumir condiciones homogéneas de humedad en la tropósfera del área, pero no en superficie, donde, como ya se mencionó anteriormente se observan las mayores variaciones de humedad.

3. EL AGUA PRECIPITABLE EN RELACION CON EL DESARROLLO DE MCCs

La gran separación que existe en el espacio y el tiempo entre las observaciones de radiosondeo en nuestro país conduce por un lado a la obtención de campos de humedad excesivamente suavizados y al filtrado de variaciones temporales de la humedad importantes para la detección de fenómenos de la escala sinóptica y más aún de la mesoescala. Al recurrir al uso del cálculo de este parámetro por tablas, se aumentó la

densidad espacial y temporal de datos sensiblemente, pero los campos obtenidos representaban en exceso los campos de precipitación. En vista de los resultados obtenidos se optó por calcular esta variable de acuerdo con el siguiente esquema: La región de interés (territorio argentino al este de los 65°O y al norte de los 45°S) (Fig. 4) se dividió en cuatro subregiones (Fig. 5) en las cuales se consideraron condiciones homogéneas de humedad en la tropósfera de cada una de ellas representadas por los datos de radiosondeo de Resistencia, Salta, Córdoba y Ezeiza respectivamente, pero condiciones diferentes de humedad y presión en superficie de acuerdo a los datos de las estaciones sinópticas del área respectiva. De esta forma se aumentó la densidad de datos de agua precipitable por valores más cercanos a los reales. Con esta información se analizaron los campos de AP correspondientes a seis fechas (25-27/11/82, 23-25/1/83) en las que se desarrollaron tormentas del tipo de los Complejos Convectivos de Mesoescala (MCCs), ver Fig. 6 y Tabla 1. Los campos de AP previos al desarrollo de la tormenta muestran en el oeste de la región un área de alto contenido de humedad (del orden del doble del valor promedio para la época) en tanto que en el resto de la región los valores son del orden del promedio (comparar Fig. 7a) y 8a) con 7b) y 8b)). El gradiente zonal que separa los sectores se intensifica con el tiempo y en sus flancos oriental (tormentas 1,2,3 y 4) y norte (tormenta 5) se generaron las primeras tormentas que originaron los MCCs. A medida que estos

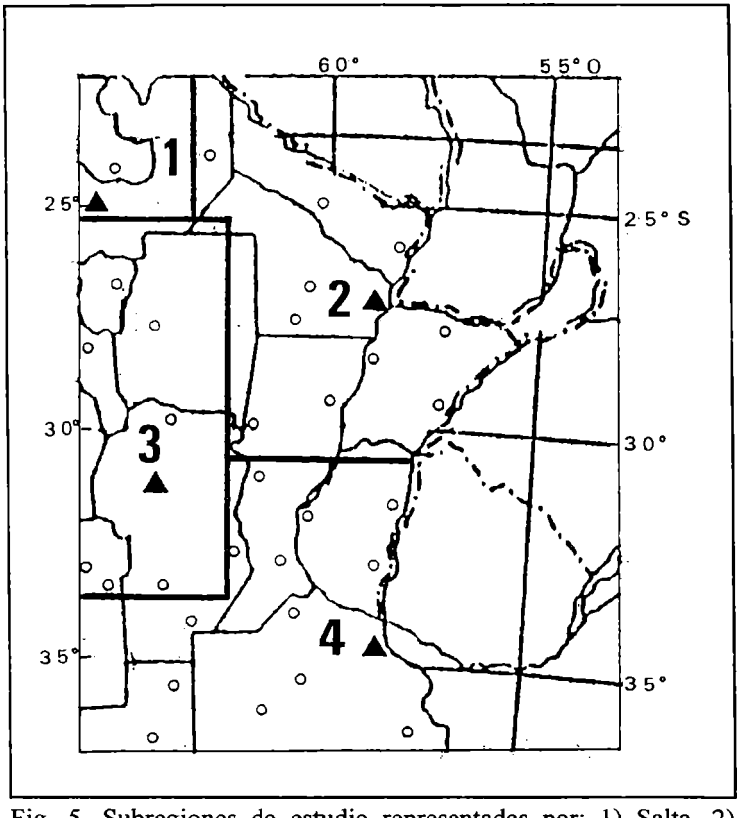

Fig. 5. Subregiones de estudio representadas por: 1) Salta, 2) Resistencia, 3) Córdoba, 4) Ezeiza.

sistemas se van desarrollando se debilitan los gradientes y se intercambian los máximos y mínimos de los campos iniciales de agua precipitable. En el entorno donde estos sistemas alcanzaron su máxima extensión se observa además de un alto contenido de humedad una distribución más homogénea tanto en extensión horizontal como vertical (Fig. 7c),8c) y 7d),8d)).

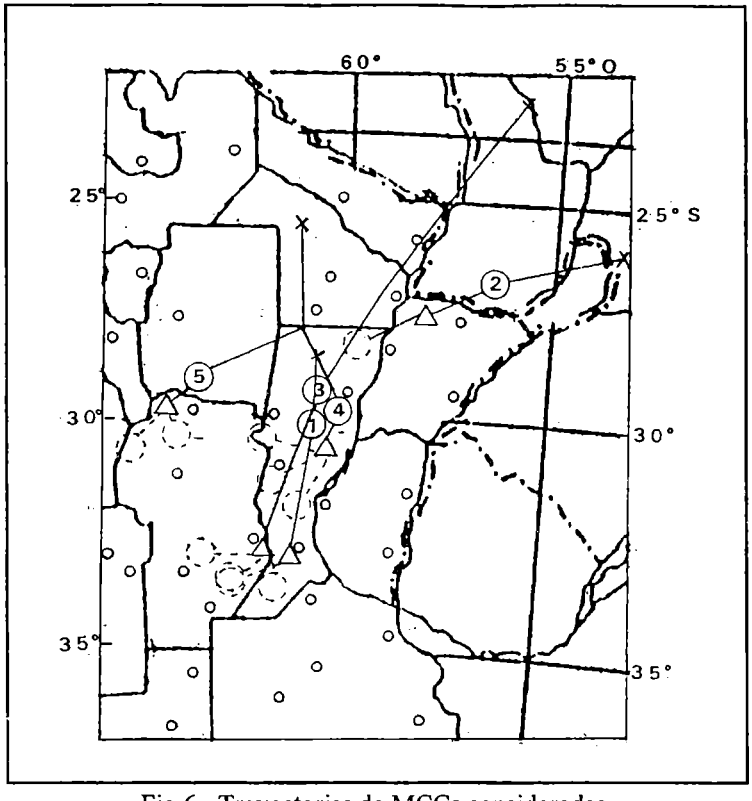

Fig.6 . Trayectorias de MCCs consideradas.

La comparación de los análisis del agua precipitable con los análisis de precipitación total producida por los dos MCCs del 25/26 de noviembre de 1982 (Velasco *et al.*, 1989) indica que en general el agua precipitable calculada por fórmula constituye una cota superior de la precipitación media areal esperable, pero estos valores pueden ser superados por la precipitación en forma muy localizada, siendo en esos casos los valores de precipitación muy cercanos a los valores máximos del AP estimada por tablas.

TABLA 1

Nº	Fecha	a)	b)	c)	d)
1	25/26-11-81	1800	0000	0600	0700
2	26-11-81	0800	0900	1300	1700
3	23/24-01-82	1100	1400	0600	2200
4	25/26-01-82	1800	2100	0200	1300
5	25/26-01-82	2300	0100	0500	1300

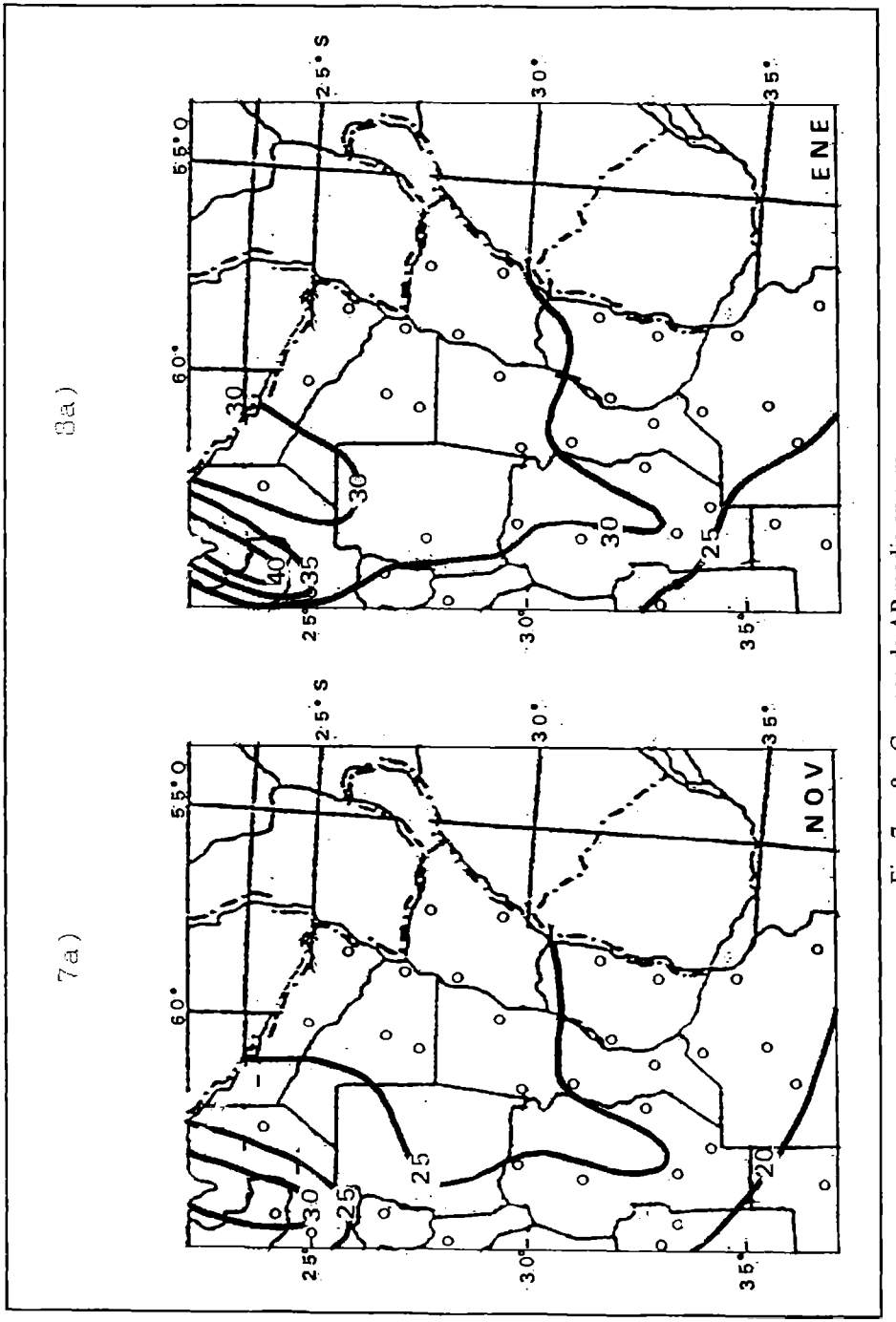

Fig. 7a y 8a. Campos de AP media en mm.

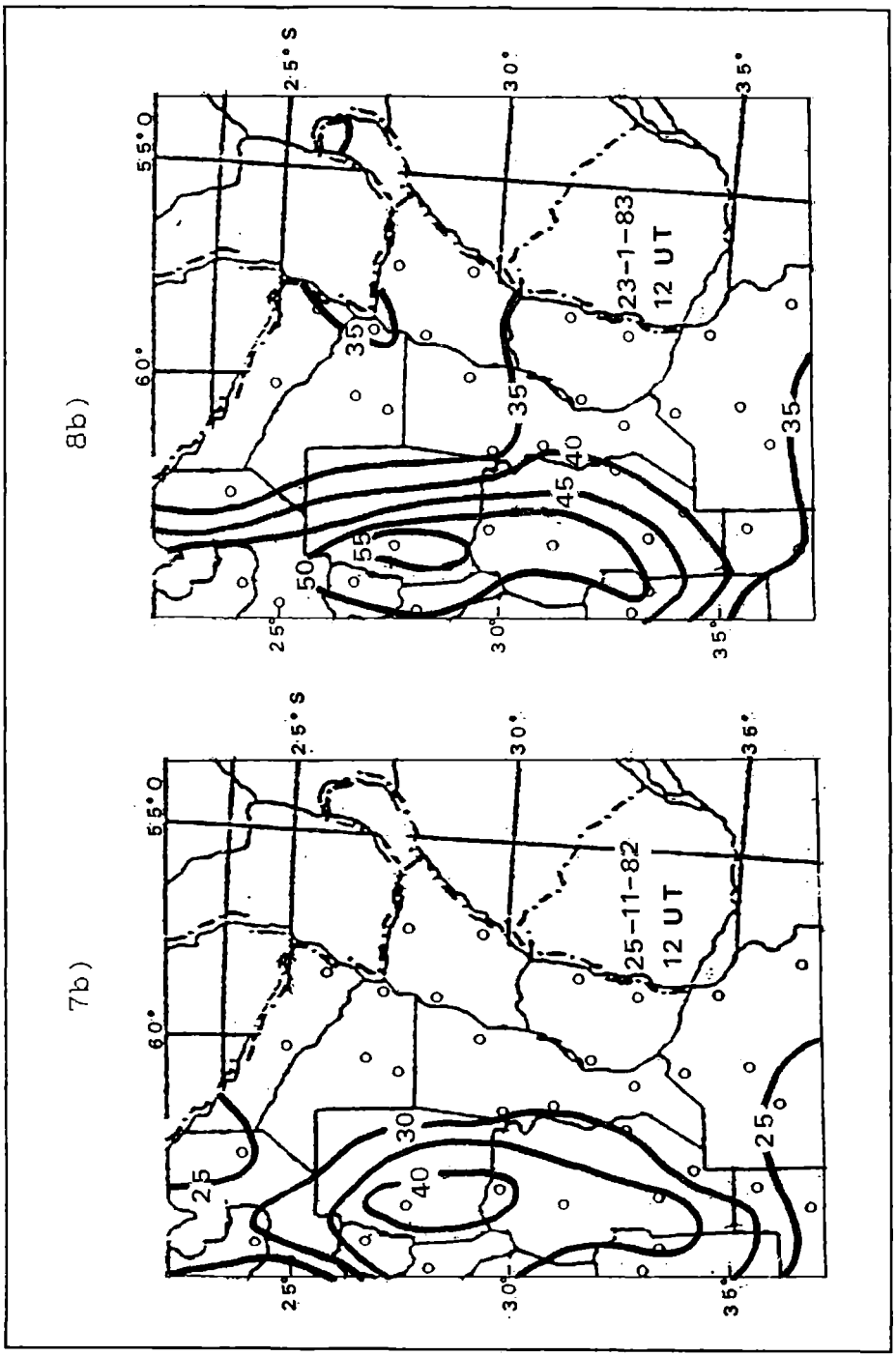

Fig. 7b y 8b. Campos de AP en mm previos al desarrollo.

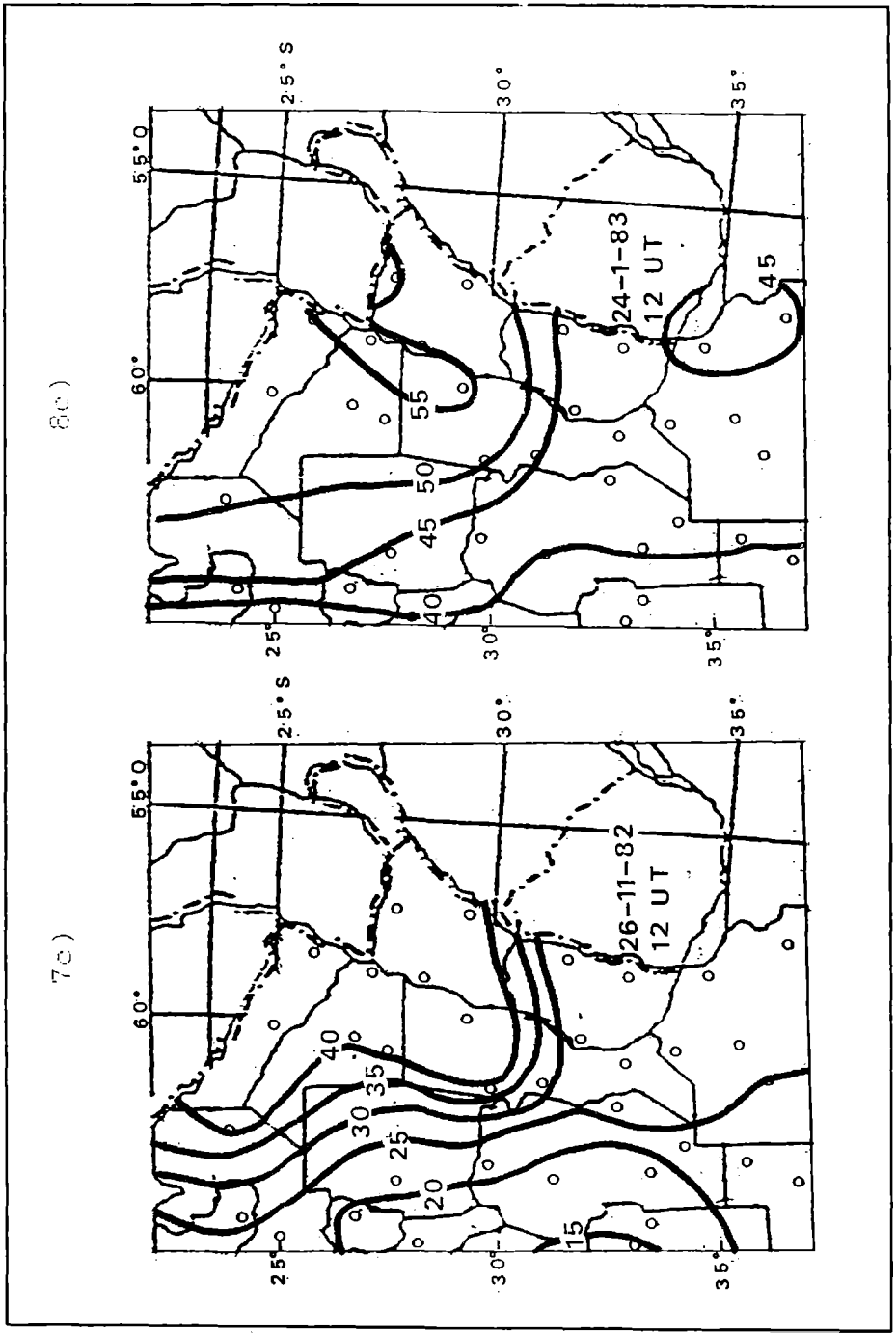

Fig. 7c y 8c. Campos de AP en mm a la hora de máxima extensión.

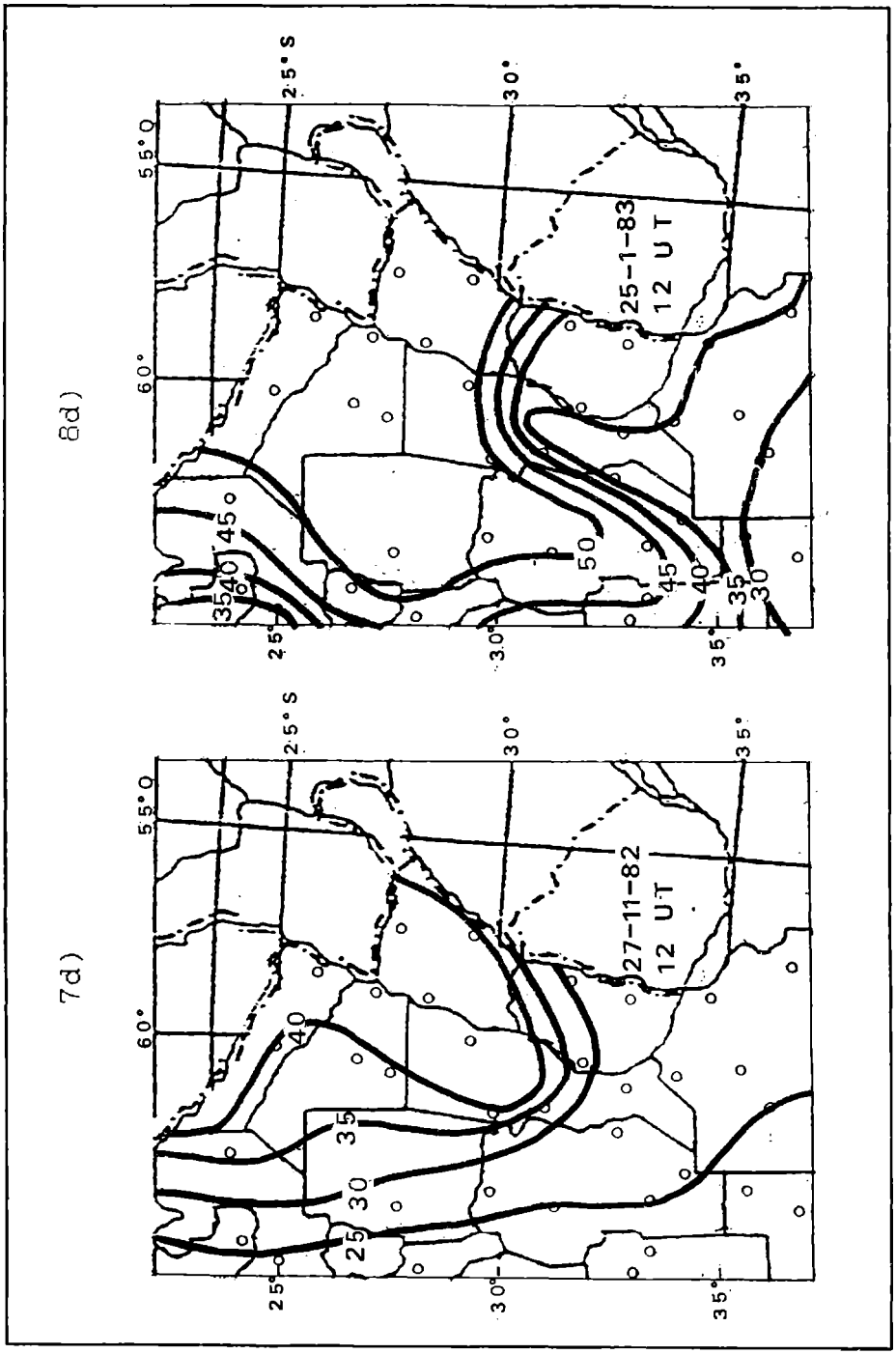

Fig. 7d y 8d. Campos de AP en mm posterior a la ocurrencia de los MCCs.

donde a), b), c) y d) indican la hora (UT) de ocurrencia de las primeras tormentas, iniciación, máxima extensión y finalización de las tormentas; que aparecen en la Fig. 6 por (C), (O), (Δ) y (x) respectivamente.

4. CONCLUSIONES

Las diferencias entre los valores de AP calculados por fórmula y los calculados usando el punto de rocío de superficie conjuntamente con tablas que asumen una atmósfera adiabática saturada, muestran un comportamiento estacional. Estas diferencias, generalmente positivas son altas durante los meses de verano, indicando excesos del orden del 30% que bajan en los meses de invierno a un 2%.

Con la idea de obtener valores más próximos a los reales en cualquier situación estos cálculos pueden mejorarse reemplazando el gradiente adiabático saturado por el gradiente medio de la temperatura de rocío. Sin embargo, ninguno de los dos métodos muestra un comportamiento que permita el ajuste de una ley a las diferencias entre los valores reales y los estimados. Esto constituye un obstáculo al fin perseguido de aumentar objetivamente la frecuencia espacial y temporal de los datos de agua precipitable, contando sólo con los datos de humedad y presión en superficie.

El análisis del peso relativo de los términos que intervienen en el cálculo por fórmula del AP indica que los parámetros de mayor influencia son los puntos de rocío en los niveles de superficie y 900 hPa y si se considera la capa entre superficie y 700 hPa los errores obtenidos serían del 5%, para una disminución de 1 hPa en la presión de superficie y un aumento de sólo 1°C en los rocíos de los niveles de superficie, 900, 850 y 800 hPa.

Finalmente para analizar con más detalle las condiciones de humedad troposférica que acompañaron el desarrollo de algunas tormentas tipo MCC se optó por considerar la región de interés subdividida en áreas tales que las condiciones de humedad por encima de la capa de superficie estaban representadas por los datos de humedad de la estación aerológica más cercana. Estos datos se combinaron con los datos de presión y humedad en superficie para obtener una mejor distribución espacial del AP. El análisis de estos datos muestra zonas de gradientes de agua precipitable muy marcados, coincidentes con el área donde se inició la formación de los MCCs. A medida que estos sistemas se desarrollaron y desplazaron, los gradientes de AP se suavizaron y se observó un aumento generalizado de la humedad de la tropósfera en toda la región noreste.

La comparación de los campos de AP con los de precipitación producidos por las tormentas estudiadas muestran a los primeros como una cota superior para la precipitación areal, pudiendo observarse sin embargo que a nivel puntual el valor de la precipitación puede superar al del agua precipitable.

Agradecimientos

A las autoridades del Servicio Meteorológico Nacional (FAA) por los datos facilitados. Este trabajo contó con el apoyo de los subsidios UBA - 19095/91 y CONICET - PIA 07812/91.

REFERENCIAS

Bolsenga, S. I., 1965: The relationship between total atmospheric water vapor and surface dew point on a mean daily and hourly basis. J. Appl. Meteor., Vol. 4, N° 3, 430- 432.

Catuogno, G. A. y Velasco I., 1986: Agua Precipitable sobre la República Argentina. Publicación del Departamento de Meteorología, FCEYN-UBA, 24 pp.

Guiraud, F. O., J. Howard and D.C. Hogg, 1979: A dual channel microwave radiometer designed for measurement of precipitable water vapor and liquid. IEEE Trans. Geosci. Electron; GE-17, 129-136.

Hellings, R. W., 1980: The effect of tropospheric fluctuations on spacecraft-tracking gravity wave experiments. Atmospheric Water Vapor, A. Deepak, T. D. Wilkerson and L. H. Ruhnke, Eds., Academic, 283-290.

Landsberg, H., 1969: Physical Climatology. Gray Dubois, 446 pp.

Lorenc, A., and S. Tibaldi, 1980: The treatment of humidity in ECMWF's data assimilation scheme. Atmospheric Water Vapor, A. Deepark, T.D. Wilkerson, and L.H. Ruhnke, Eds, Academic, 497-512.

Lowry, D.A., 1972: Climatological relationships among precipitable water , thickness and precipitation. J. Appl. Meteor., 11, 1326-1333.

OMM, 1986: Manual for Estimation of Probable Maximum Precipitation N° 332, 269 pp.

Perkey, D. J., 1980: Impact of moisture on regional-scale numerical model simulations, Atmospheric Water Vapor, A. Deepark, T.D. Wilkerson, and L. H. Ruhnke, Eds., Academic, 513-526.

Reber, E. E. y Swope, J. R., 1972: On the correlation of the total precipitable water in a column and absolute humidity at surface, J. Appl. Meteor., 11, 1322-1325.

Reitan, C. H., 1963: Surface dew point and water vapor aloft. J. Appl. Meteor., 2, 776- 779.

Resch, G.M., 1980: Water vapor - the wet blanket of microwave interferometry. Atmospheric Water Vapor. A. Deepak, T. D. Wilkerson, and L. A. Ruhnke, Eds., Academic, 265-282.

Smith, W. L., 1966: Note on the relationship between total precipitable water and surface dew point. J. Appl. Meteor., Vol 5, N° 5, 726- 727.

Solot, S. B., 1939: Computation of Depth of Precipitable Water in a Column of Air. Monthly Weather Review, Vol. 67, N°41, 100-103

Tuller, S. E., 1968: World distribution of mean, monthly and annual precipitable water. Monthly Weather Review, Vol. 96, N°11, 785-797.

Van Loon, H., 1955: A note on meridional atmospheric cross sections in the Southern Hemispheric, Notos, Weather Bur., 127-129.

Vargas, W. M. y Ashkenazi, A. R., 1975: Régimen del equivalente de vapor de agua en la atmósfera. Instituto Nacional de Ciencia y Técnica Hídricas, Informe Técnico N°2, 22 pp.

Velasco, Campetella y Catuogno, 1989: Precipitación y agua precipitable asociadas a tormentas estivales de gran extensión. Actas de la IV Reunión Argentina de Agrometeorología.
Viswanadham, Y., Ramanadham, R. y Rama Krishna, Y., 1970: Studies on Precipitable Water over Tropical Stations in Relation to Monsoon Flow. Pageogh., Vol. 79, 11, 103-119.
Younklin, R. J., LaRue, J. A. y Sanders, F., 1965: The Objective Prediction of Clouds and Precipitation Using Vertically Integrated Moisture and Adiabatic Vertical Motions. Journal of Applied Meteorology, Vol. 4, N°1, 3-17.

GEOACTA, 22, 47-58,1997

ASPECTOS CUALITATIVOS EN EL COMPORTAMIENTO DE foF2 EN LA ANOMALIA DE INVIERNO EN LA REGION F2 DE LA IONOSFERA

Ana Martínez Pulido
Laboratorio de Ionósfera, Instituto de Física, Universidad Nacional de Tucumán.

RESUMEN

Se hace un estudio cualitativo sobre la anomalía de invierno de la región F2 de la ionósfera con datos de sondeadores de estaciones de ambos hemisferios para poner de manifiesto su presencia y destacar las importantes diferencias "inter - hemisféricas". Se consideran las medianas mensuales de foF2 para un mes de invierno y uno de verano de 1980 (alta actividad solar) y 1975 (baja actividad). Los resultados muestran que la anomalía de invierno forma parte del comportamiento regular de la ionósfera del hemisferio norte, presentándose siempre. Los valores del mediodía en el invierno son más altos que los del verano. Para el hemisferio sur la presencia de la anomalía es sólo ocasional. En América del sur está ausente; y en Australia y Sudáfrica aparece solamente en períodos de alta actividad. La ionósfera de bajas latitudes, no ofrece diferencias sustanciales con la ionósfera de latitudes medias, aun cuando mantiene características específicas.

ABSTRACT

Data from both hemispheric sounders are used in order to make an ionospheric F2 region winter anomaly qualitative study, pointing out "inter - hemispheric" differences. Tacking into account a high solar activity year (1980) and a low solar activity year (1975) foF2 monthly medians for one summer month and one winter month are considered. Results show that winter anomaly is always present in the Northern hemisphere, that is, noon foF2 winter values are always greater than summer ones. For the Southern hemisphere, winter anomaly is present only occasionally. In South America it is absent, while in Australia and South Africa it appears for high solar activity periods. Low latitudes ionospheric behaviour is essentially the same that those of middle latitudes, even if it shows specific characteristics.

1. INTRODUCCION

En este artículo se realiza un estudio fundamentalmente cualitativo de la anomalía de invierno de la región F2 de la ionósfera, caracterizada por el hecho, aparentemente paradójico, de presentar, al mediodía, valores de foF2 -frecuencia crítica de la capa F2- mayores en invierno que en verano. Durante la noche la situación se revierte. Esta es una de las clásicas anomalías de esta región, algunas de cuyas características más destacadas

se irán señalando.

De todos los fenómenos anómalos que en cierta forma caracterizan el comportamiento de la región F2, esto es la anomalía ecuatorial, el mantenimiento de la capa durante la noche, etc., la anomalía de invierno tiene la particularidad de poner de manifiesto notables diferencias entre la ionósfera del hemisferio norte y la del hemisferio sur. Tan es así, que si el estudio del comportamiento de la región F2 en invierno hubiera sido iniciado por investigadores del hemisferio sur lo más probable es que no se hubiera hablado de anomalía, ya que, como se verá, su presencia en el sur es sólo ocasional.

2. ANTECEDENTES HISTORICOS

Muy poco después de la invención de las ionosondas, Kirby, Berkner y Stuart (1934) descubrieron que la frecuencia crítica (foF2) de la región F2 diurna en el invierno, excedía los valores del verano. Encontraron que por la noche esto no se observaba (la situación se "normalizaba"): entonces los valores de foF2 del verano excedían los del invierno, indicando que la anomalía de invierno es un fenómeno diurno y debe guardar alguna relación con el sol.

Estos resultados fueron tan sorprendentes para ellos que llegaron a dudar de que foF2 fuera realmente una medida digna de confianza de la densidad electrónica máxima de la ionósfera. Por el contrario, Appleton y Naismith (1935) sostuvieron que foF2 era realmente confiable y, desde hace tiempo, el hecho de que en invierno los valores diurnos de la densidad electrónica máxima en la región F2 superan los del verano, está aceptado por todos los autores (Duncan, 1968; King y Smith, 1968).

En estos primeros trabajos, e incluso en algunos más modernos, no se considera la posibilidad de que la situación en el hemisferio sur pudiera ser diferente o pudiera ser igual (ej., Rishbeth y Setty, 1961; Duncan, 1968; Mao-Fu y Newell, 1972, Chauhan *et al.*, 1980; Rawer, 1986; Rishbeth, 1989.

Este comportamiento se hizo conocido en la literatura como "anomalía de invierno" (AI), ya desde los primeros artículos, siendo claramente reflejado en la región F2, a diferencia de las otras capas ionosféricas, E y F1. También se observó (Chauhnan *et al.*, 1980) que la anomalía estacional en la densidad electrónica de la región F2 es más pronunciada que la anomalía estacional en el contenido electrónico total (CET). Esto sería consistente con lo que se acaba de decir y sugiere que la anomalía no es uniforme en la columna vertical total sino que es más dominante alrededor del máximo de concentración.

Otro aspecto interesante asociado a este fenómeno y que fue señalado desde los primeros autores (Duncan, 1968) es que el verano y las tormentas magnéticas pueden influenciar la región F similarmente al deprimir las densidades electrónicas. Esto causa turbulencia y mezclado en la baja ionósfera y en consecuencia se incrementa la abundancia de oxígeno molecular y la pérdida electrónica en la región.

3. ASPECTOS DESCRIPTIVOS

Antes de proceder con un análisis cuantitativo, resulta interesante observar algunas particularidades en el comportamiento global de la región F2 de la ionósfera que ponen de manifiesto la existencia de importantes diferencias "inter-hemisféricas", (Martínez Pulido, 1989) así como la presencia misma del fenómeno. Se ha trabajado con estaciones de latitud media y con estaciones de baja latitud, (Tabla I) analizando el comportamiento de la densidad electrónica máxima.

TABLA I
Datos de estaciones de ambos hemisferios

Estaciones	Latitud Geogr.	Latitud Geomag.	Longitud Geogr.	Longitud Geomag.
Hemisferio Sur				
Puerto Argentino	-51,7	-40,6	-57,8	10,3
Tucumán	-26,9	-15,6	-64,4	4,6
Hermanus	-34,4	-33,6	19,2	81,9
Johannesburgo	-26,1	-27,2	28,1	92,8
Canberra	-35,3	-43,7	149,0	-134,2
Vanimo	-2,7	-12,3	141,3	-147,5
Hemisferio Norte				
Dourbes	50,1	51,7	4,6	88,9
Wakkanai	45,4	35,5	141,7	-152,7
Manila	14,7	3,6	121,1	-168,8

3.1. Densidad electrónica

En la Figura 1 se ha graficado la frecuencia crítica de la región E (foE) para una estación del hemisferio norte (Wakkanai) y otra del hemisferio sur (Puerto Argentino) para dos años, uno de alta (1980) y otro de baja (1975) actividad solar. Esta Figura resulta ilustrativa sobre la "no presencia" en esta región de la anomalía de invierno.

Las Figuras 2 y 3 muestran el comportamiento de cuatro estaciones de latitud media: Dourbes y Wakkanai, por una parte y Puerto Argentino y Canberra por otra, que pertenecen dos al hemisferio norte y dos al hemisferio sur (Tabla I), bajo distintos niveles de actividad solar. Aceptando que un día "medio" puede ser representado mediante las

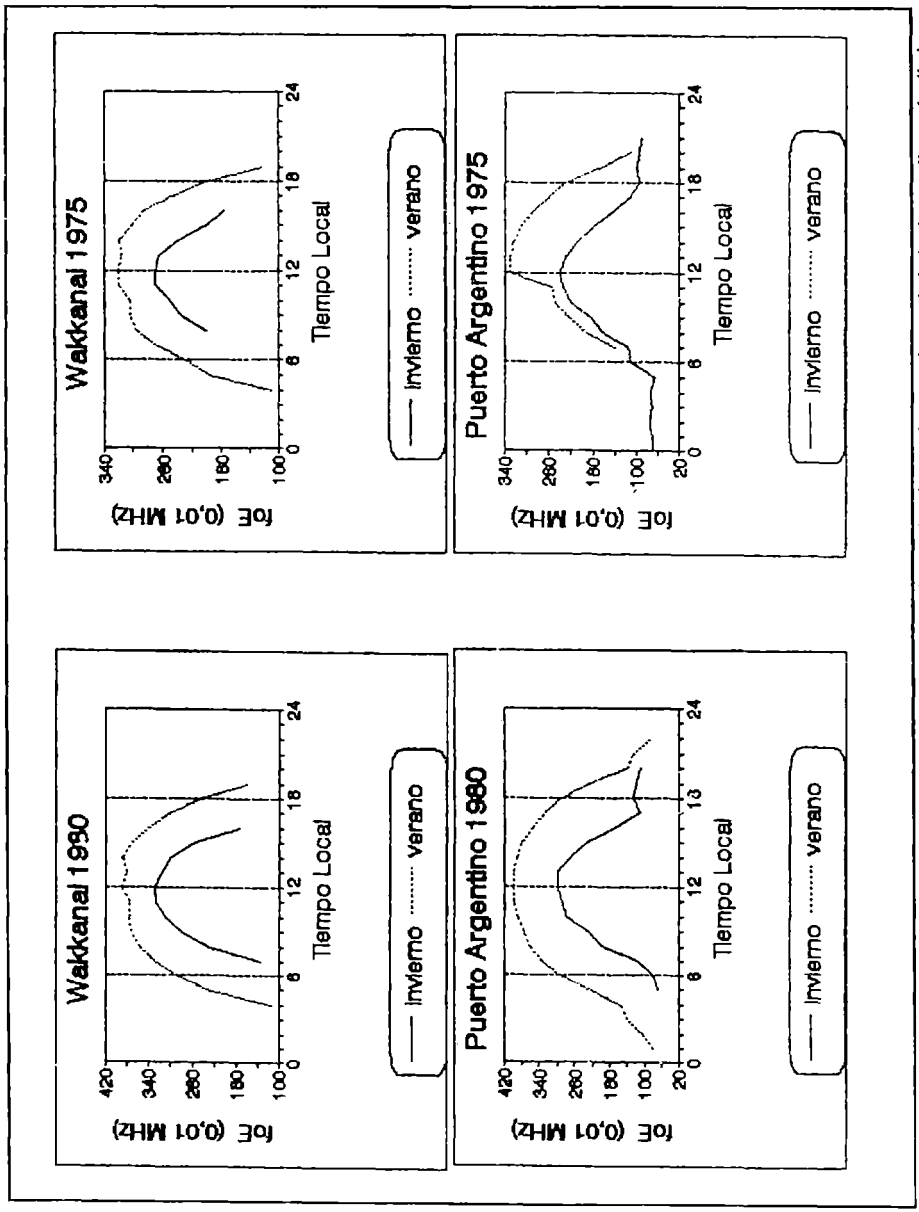

Fig. 1. Medianas mensuales de la frecuencia crítica foE en función del tiempo local para dos estaciones de latitudes medias y de distinta longitud, Wakkanai del HN y Puerto Argentino del HS. Se ha considerado que los meses de julio y enero reflejan el comportamiento del invierno (verano para el HN) y el verano (invierno para el HN), respectivamente, para el HS. El año 1980 es de alta actividad solar y 1975 de baja . Los valores de foE del verano son siempre superiores a los del invierno, esto es, la anomalía de invierno no se manifiesta a alturas de la región E.

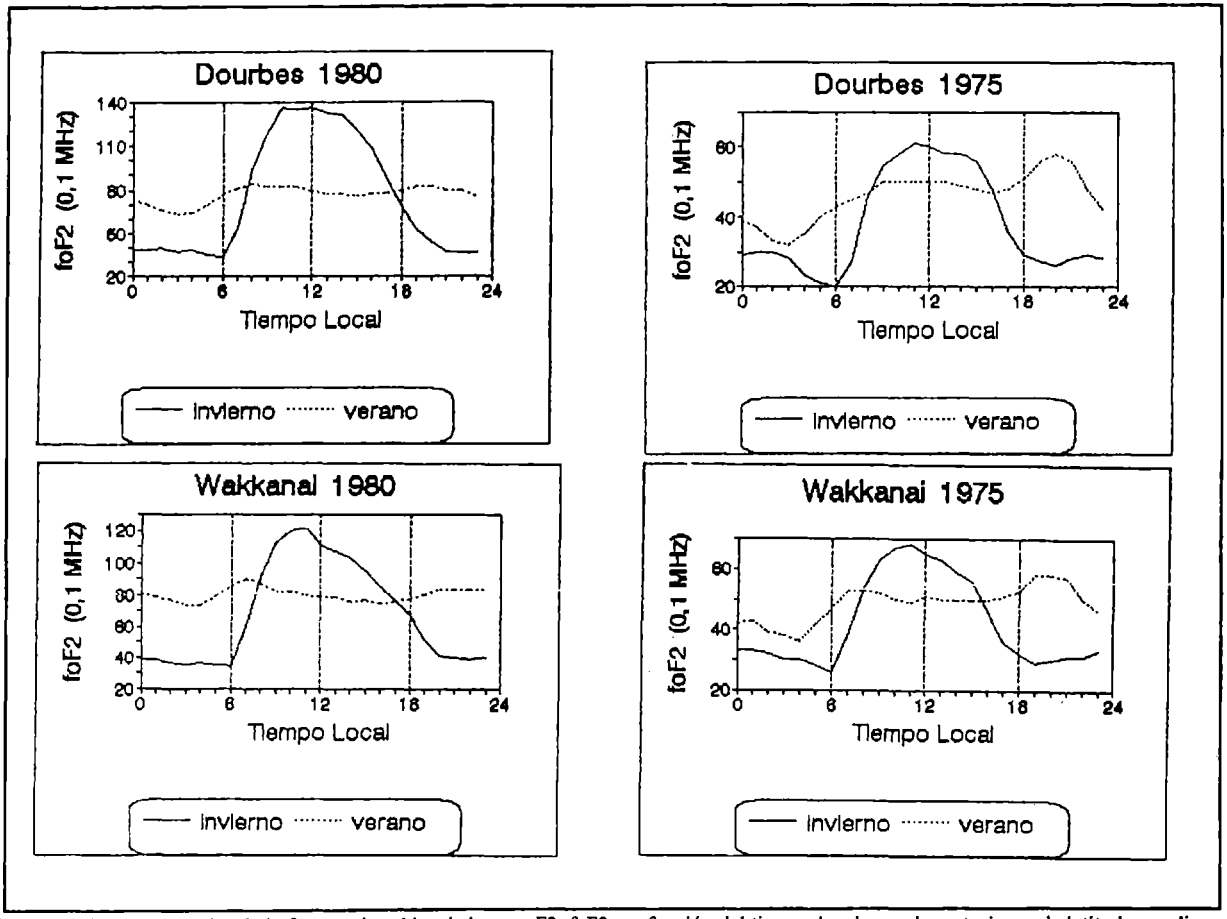

Fig. 2. Medianas mensuales de la frecuencia crítica de la capa F2, foF2, en función del tiempo local para dos estaciones de latitudes medias pero de distinta longitud pertenecientes al hemisferio norte. Se ha considerado que los meses de julio y enero reflejan el comportamiento del verano y el invierno respectivamente. El año 1980 es de alta actividad solar y el año 1975 de baja. Se observa en todos los casos que, aproximadamente, entre las 08.00 y las 17.00 hs. los valores de foF2 del invierno superan los del verano, poniendo de manifiesto la presencia de la anomalía de invierno.

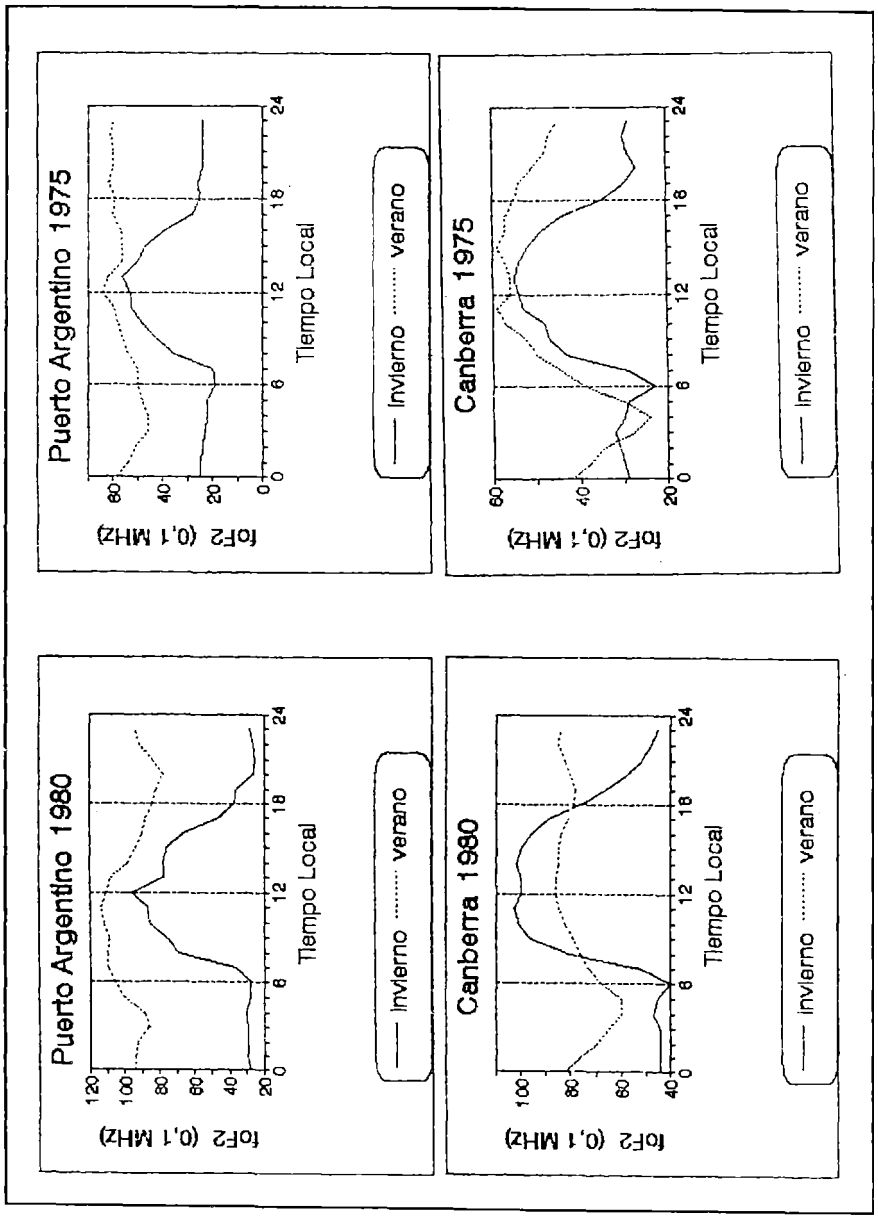

Fig. 3. Se han graficado las medianas mensuales de la frecuencia crítica de la capa F2, foF2, en función del tiempo local para dos estaciones de latitudes medias pero de distinta longitud, pertenecientes al hemisferio sur. Se ha considerado que los meses de julio y enero reflejan el comportamiento del invierno y el verano respectivamente. El año 1980 es de alta actividad solar y el año 1975 de baja. En Puerto Argentino los valores del verano son superiores a los del invierno en ambos casos, poniendo de manifiesto la ausencia de la AI. Sólo se observa la presencia de la AI para Canberra en 1980

medianas mensuales, se puede ver la variación diaria de foF2 para meses característicos del verano y del invierno local graficando julio y enero en función del tiempo local. Se prefiere tomar las medianas mensuales, en este caso, y no los promedios porque éstos son más sensibles a los valores extremos ("out layer").

En Dourbes y Wakkanai, estaciones del hemisferio norte, la anomalía existe para alta y baja actividad solar (para el año 1980, de alta actividad solar R = 154.6 y para 1975, de baja actividad, R = 15.5, siendo R número medio de manchas solares). Se observa además que los valores de foF2 del invierno para el año 1975 son superiores a los del verano a partir de las 08 hs aproximadamente, alcanzando un máximo de cercano a los 7 MHz a las 11 hs..En 1980, máxima actividad solar, la AI se manifiesta desde las 08 hasta las 17 hs. presentando un máximo de más de 12 MHz a las 11 hs. de tiempo local TL. Durante la noche la situación cambia y los valores de foF2 correspondientes al verano son superiores a los del invierno, para ambos niveles de actividad solar considerados. En general, durante el día, los valores del verano se presentan deprimidos, con máximos poco pronunciados, o casi inexistentes, lo que también constituye una característica de la AI.

En el hemisferio sur, la situación se presenta claramente diferente. Para Puerto Argentino, la anomalía está ausente siempre, tanto en 1975 como en 1980. En Canberra aparece asociada a la actividad solar alta.

3.2. Estaciones de baja latitud

Las estaciones de baja latitud, ecuatoriales y subecuatoriales, despliegan una distribución de foF2 que tiene sus propias características. Sin embargo, la AI suele estar presente también aquí, aun cuando la ionósfera de estas estaciones está bajo los fuertes efectos de la anomalía ecuatorial, cuya influencia se intensifica y se expande cuando aumenta la actividad solar.

A título de ejemplo se puede ver en la Figura 4 el comportamiento de foF2 para Tucumán. La Figura 5 muestra la frecuencia crítica, para Vanimo y Manila (Tabla I), a través de las medianas mensuales de enero y julio considerando, como anteriormente, años de alta y baja actividad solar. En Tucumán, la AI directamente no se presenta; en Manila sí lo hace, tanto para alta como para baja actividad solar, y en Vanimo (hemisferio sur) aparece con alta actividad. De esta manera, frente al fenómeno que estamos estudiando, la ionósfera de bajas latitudes no presentaría diferencias sustanciales con la ionósfera de latitudes medias.

3.3. Estaciones sudafricanas

Estas estaciones, Hermanus y Johannesburgo (Tabla I) no han sido incluidas en las secciones precedentes porque se ha presentado la siguiente dificultad: no hemos podido

acceder a los datos completos del año 1980 para la estación de Hermanus, y por lo tanto, la presentación hubiera quedado un poco "despareja". De todas formas, como el comportamiento de estas estaciones resulta de interés, entre otras cosas porque el hemisferio sur está menos estudiado que el norte, se ha resuelto incorporarlas tomando para Hermanus el año 1991 como el de alta actividad solar. El número medio anual de manchas solares para este año, es de 145,7, comparable al de 1980. La Figura 6, relativa a la frecuencia crítica foF2, indica la presencia de la AI solamente en Hermanus, para alta actividad solar.

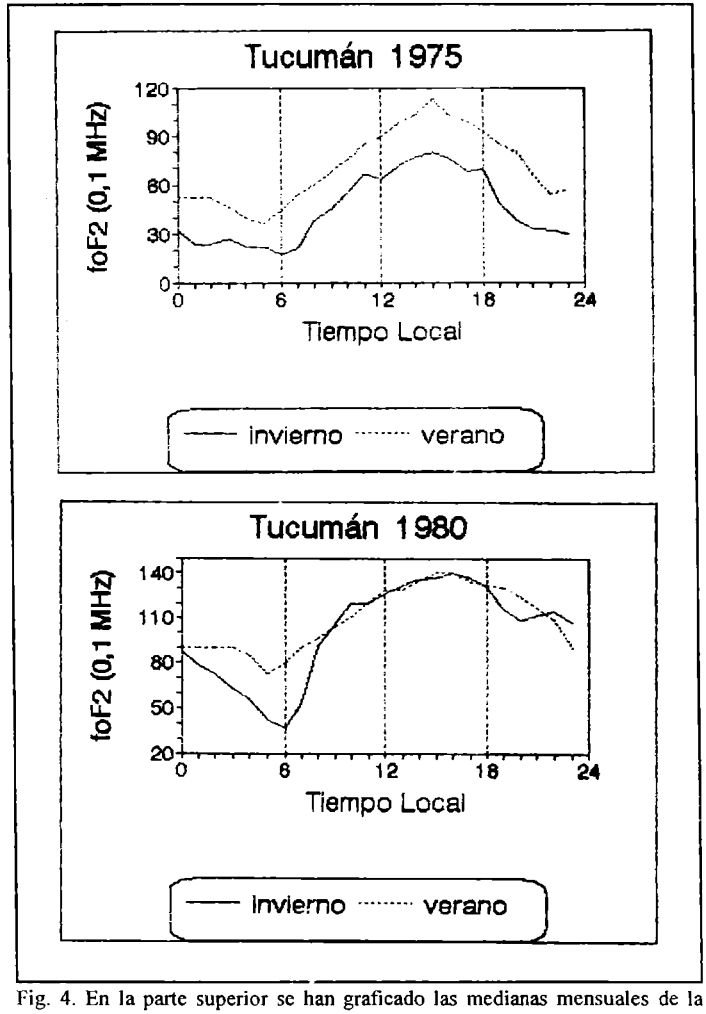

Fig. 4. En la parte superior se han graficado las medianas mensuales de la frecuencia crítica de la capa F2, foF2, y en la parte inferior las medianas mensuales de hpF2, valor aproximado para la altura del pico de concentración, en función del tiempo local para Tucumán, estación de baja latitud. Se ha considerado que los meses de julio y enero reflejan el comportamiento del invierno y el verano, respectivamente. El año 1980 es de alta actividad solar y el año 1975 de baja. Los valores de foF2 no revelan la presencia de la AI, mientras que los de hpF2 muestran un comportamiento anómalo para las alturas.

4. SUMARIO

La Tabla II resume algunos de los hechos más destacados del estudio precedente, en relación al comportamiento de la densidad electrónica máxima de la capa F2, para las estaciones de latitud media y baja que se han considerado.

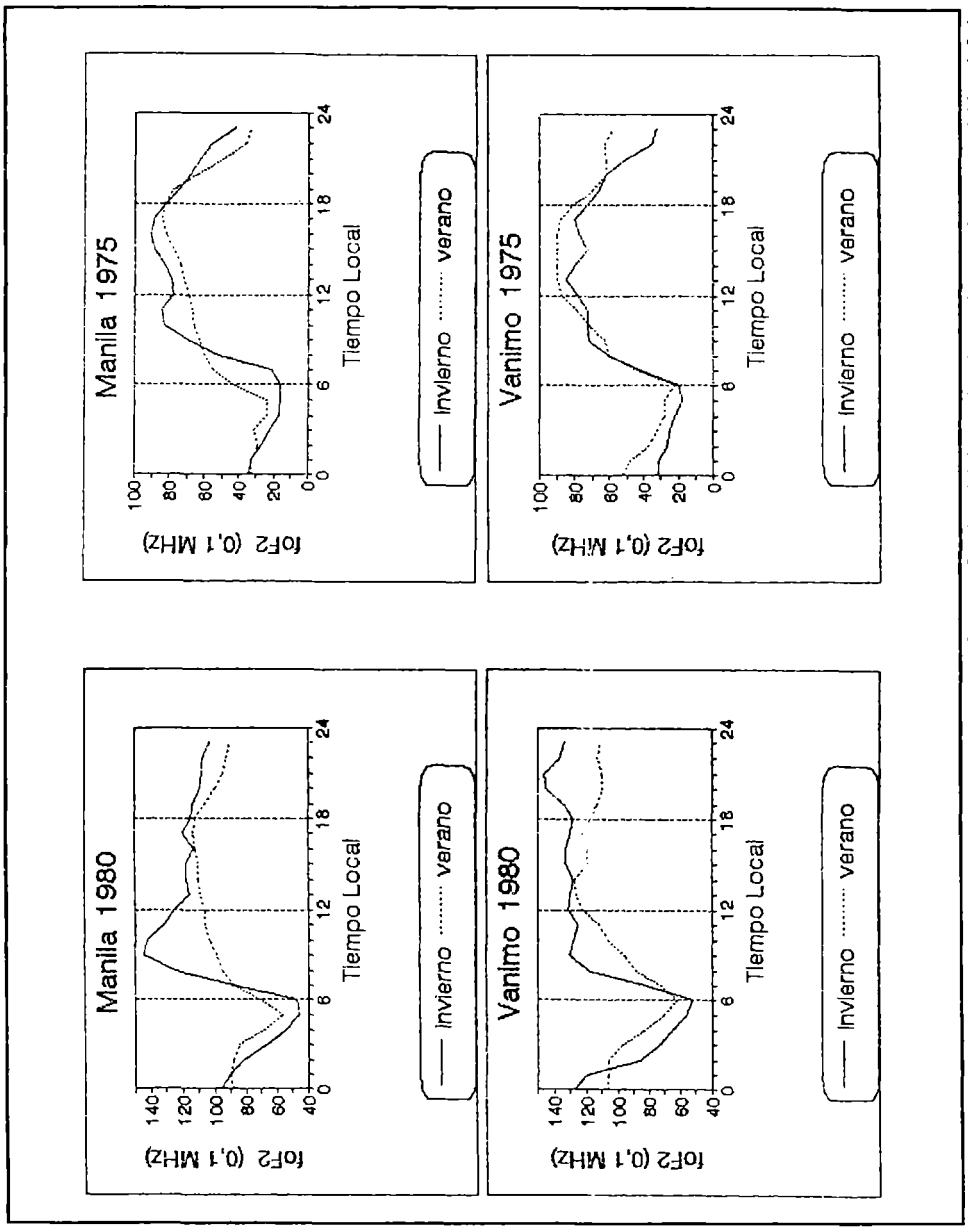

Fig. 5. Medianas mensuales de la frecuencia crítica de la capa F2, foF2, en función del tiempo local para dos estaciones, una del hemisferio norte y otra del hemisferio sur, pero de baja latitud y de longitudes comparables. Tan sólo en Vanimo (HS), para baja actividad solar, no se manifiesta la AI.

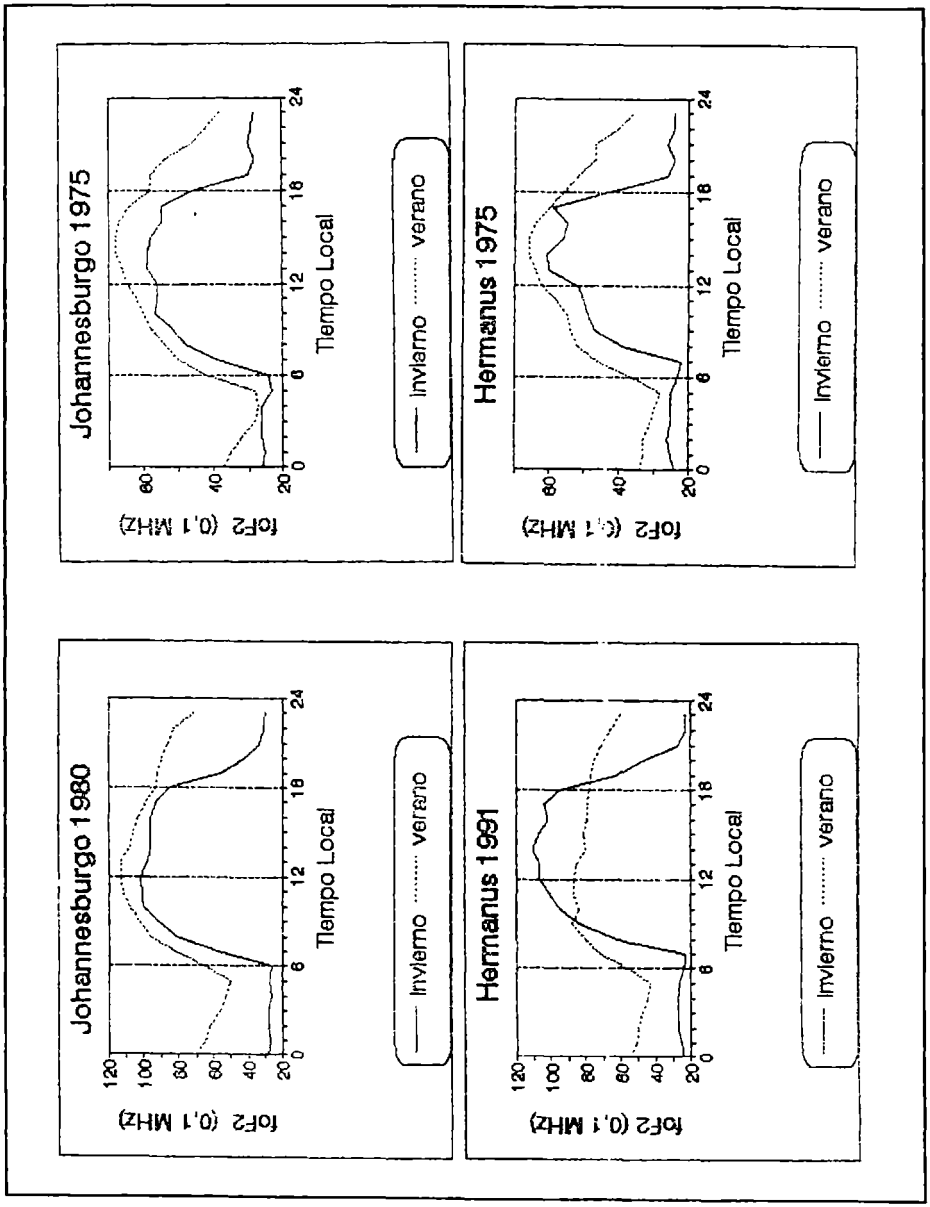

Fig. 6. Medianas mensuales de la frecuencia crítica de la capa F2, foF2, en función del tiempo local para dos estaciones de sudafricanas de baja latitud. Se ha considerado que los meses de julio y enero reflejan el comportamiento del invierno y el verano respectivamente. Los años 1980 y 1991 son de alta actividad solar y el año 1975 de baja. Solo se observa la presencia de la anomalía de invierno para Hermanus, 1991.

TABLA II
Descripción sucinta de la anomalía

Estaciones	Presencia 1980 1975	Hora máx. 1980 1975	Intervalo 1980 1975	Δ foF2 1980 1975
P. Argentino	no no			
Tucumán	no no			
Hermanus(*)	sí no	14	10-18	3,1
	no no			
Johannesb.	sí no	10	08-18	2,1
Canberra	sí no	21	07-02	3,6
Vanimo				
Dourbes	sí sí	12 12	08-17 08-16	5,7 1,0
Wakkanai	sí sí	11 11	08-17 08-16	4,1 1,9
Manila	sí sí	09 10,11	07-01 09-00	5,5 1,7

(*) año 1991

En esta Tabla se señala la presencia o no de la anomalía, en el caso de presentarse durante cuánto tiempo lo hace (intervalo) y cuál es el horario del máximo, siempre teniendo en cuenta la actividad solar. El ΔfoF2 se refiere a la diferencia entre el foF2 del verano y el del invierno. Como se ve, se ha puesto el acento en el estudio de las estaciones del hemisferio sur.

REFERENCIAS

Appleton, E. V. e Ingram, L. J., 1935. Magnetic storms and upper atmospheric ionization, Nature, London 136, 548-549.

Chauhan, N. S., Gurm H. S. y Janve, A. V., 1980. Seasonal difference in ionization and height of F2 layer caused by neutrals at low latitudes, J. Atmosph. Terr. Phys., 47, 265-273.

Duncan, R. A., 1969. F-region seasonal and magnetic-storm behaviour, J. Atmosph. Terr. Phys, 31, 59-70.

King J. W. y Smith, P. A., 1968. The seasonal anomaly in the behaviour of the F2 layer critical frecuency, J. Atmosph. Terr. Phys., 30, 1707-1713.

Kirby, S. S., Berkner L.V. y Stuart, D. M. , 1934. Proc. Inst. Eng., 22, 481.

Martinez Pulido, A., 1989. Study of the south hemisphere F2 region winter anomaly, Rev. de

Geofísica, España, 45, 211-216.
Mao-Fou Wu y Newell, R. E., 1972. Computer simulation of the F region seasonal anomaly, J. Atmosph. Terr. Physics, 34, 1635-1646.
Rawer, K., 1986. Ionospheric modelling during past decades, Indian Journal of Radio & Space Physics, 15, 217-234.
Rishbeth, H., 1989. Basic physics of the ionosphere; a tutorial review, College on theoretical and experimental radio propagation science. International Centre for Theoretical Physics, Trieste.

GEOACTA, 22,59-73,1997

ABSOLUTE PALAEORECONSTRUCTIONS OF CONTINENTS BASED ON PALAEOMAGNETIC POLES AND VIRTUAL GEOMAGNETIC POLES?

Haroldo Vizan and Carlos Alberto Vasquez
Lab. de Paleomagnetismo Daniel Valencio. CONICET. Universidad de Buenos Aires.
Depto de Ciencias Geológicas. Fac. de Cs. Ex. y Nat. Pabellón II. Ciudad Universitaria.
1428 Nuñez. Buenos Aires.

ABSTRACT

Transitional Jurassic and Early Cretaceous Virtual Geomagnetic Poles (VGPs) repositioned according to absolute palaeoreconstructions, define two paths similar to those for reversals of the last 12 Myr. These paths roughly coincide with the regions of the present core mantle boundary (CMB) that lie below regions of the lower-mantle with fast seismic wave velocities. A statistical test applied to the population of Jurassic-Early Cretaceous transitional VGPs identifies two antipodal bands (105/137° E-285/317° E). Mantle convection and geoid models suggest that the present topographic temperature pattern over the CMB has persisted since the Late Paleozoic. Hotspot tracks are alternative tools to make absolute reconstructions, but they are not applicable to Late Paleozoic times due to lack of hotspot framework for those times. Absolute reconstructions of South America for the Late Permian based on a mean palaeomagnetic pole and on the position of the bands defined by transitional and oblique VGPs are presented. These reconstructions are compared with an alternative obtained by a different method.

RESUMEN

Polos geomagnéticos (PGVs) transicionales del Jurásico y Cretácico Inferior reconstituidos de acuerdo a paleoreconstrucciones absolutas, definen dos caminos similares a los de reversiones de los últimos 12 m.a. Estos caminos aproximadamente coinciden con zonas del límite manto núcleo (LMN) actual que se encuentran debajo de regiones de la base del manto con rápidas velocidades de ondas sísmicas. A través de modelos de geoide y convección se ha sugerido que el actual patrón de geoide y convección se ha sugerido que el actual patrón de topografía térmica en el LMN ha perdurado desde el Paleozoico Tardío. Para el Jurásico y Cretácico inferior un análisis estadístico aplicado a una población de PGVs transicionales de ese lapso definió dos bandas antípodas (105/137° E - 285/317° E). Las trazas de puntos calientes han sido empleadas como herramientas alternativas para efectuar reconstrucciones absolutas, pero ellas no son aplicables para el Paleozoico Tardío dada la carencia de grillas confiables de puntos calientes con esa edad. En este trabajo se presentan reconstrucciones absolutas de América del Sur para el Pérmico Tardío basadas en un polo paleomagnético promedio y en la posición de las bandas definidas por PGVs transicionales y oblicuos. Estas reconstrucciones son comparadas con una reconstrucción alternativa obtenida por un método diferente.

1. INTRODUCTION

Within the field of Paleomagnetismo there are three branches that, up too now, have practically evolved independently, (i) applications to geodynamics and tectonics; (ii) magnetostratigraphy and (iii) studies of the geomagnetic field (GMF) behaviour. Anyway there are some few papers that integrate evidence from the three branches (i.e., Livermore *et al.*, 1984; Courtillot and Besse, 1987; Besse and Courtillot, 1991).

The support given by Paleomagnetismo to geodynamics and stratigraphy has been singular. Both latitudinal reconstructions of continental plates and accurate stratigraphical correlations have been possible from palaeomagnetic and magnetostratigraphic studies. Paleomagnetismo is also the only tool that geomagnetists have for studying one intriguing process of the GMF: the polarity transitions. At the present time, it is controversial whether transitional virtual geomagnetic poles (VGPs) occurred along preferred longitudinal paths. For example, Gurary (1988), Clement (1991) and Tric *et al.* (1991), have observed that transitional VGP paths of different reversals for the last 12 Myr, are mainly distributed within two preferred and practically antipodal bands: one of them along the Americas and the other over Australia and Asia. Laj *et al.* (1991) suggested that these transitional paths would reflect a geomagnetic phenomenum related with regions of fast seismic wave propagation (and then, low temperature) in the lower mantle. However, this suggestion was happened by several possible flaws: 1) statistical errors (Valet *et al.*, 1992), 2) dependence of the VGP paths with the geographic locations of the sampling sites (Egbert, 1992; McFadden *et al.*, 1993), 3) transitional paths could be an artifact due to processes involved in the acquisition of the magnetic remanences by sediments (Langerais *et al.*, 1992; Quidelleur and Valet, 1994). These three arguments have been rejected by recent contributions: Laj *et al.* (1992) observed that there is no statistical errors in the determination of the preferred transitional paths. Zhu *et al.* (1994) demonstrated that the longitudes of the VGP reversal paths are independent of the longitudes of the sampling sites.

Hoffman (1992) and Brown *et al.* (1994) have observed transitional VGPs derived from Cenozoic volcanic sequences and show that they are distributed in patches located within the longitudinal bands considered by Laj *et al.* (1991). Vizán *et al.* (1993; 1994) have observed that preferred paths occur for Late Paleozoic-Mesozoic polarity transitions and that those are quite similar to the Late Cenozoic paths. On the basis of a model of reversals that considers the features of the GMF in historical and present times (Gubbins and Coe, 1993 and Gubbins, 1994), Vizán and Van Zele (1994) analysed the magnetic directions of the reversal recorded in the Stormberg Lavas (van Zijl *et al.*, 1962) of Jurassic age. They found that this reversal could have been driven by similar conditions to those that drive the Late Cenozoic polarity transitions. According to this model the structure of the GMF should be strongly non-dipolar during a reversal so that the

transitional paths of VGPs of a same reversal recorded in different localities, would be confined in similar longitudinal bands but each path would have a different longitude.

The palaeomagnetic methodology used in the analysis of the reversals is different to that applied in geodynamics and tectonics. When palaeomagnetism is used to make palaeoreconstructions of continents, remanence directional data must be averaged for a geologic time spaning over 10.000 years according to the axial, geocentric and dipolar field hypothesis (i.e., Valencio, 1980). Apparent polar wander paths (APWP) not only provide information about the past movements of continental plates but also about true polar wander (TPW): the movement of the whole Earth with respect to the rotational axis (see Andrews, 1985; Cox and Hart, 1986; Courtillot and Besse, 1987; Besse and Courtillot, 1991). Another way of making palaeoreconstructions is by referring the continent positions to a hotspot framework, which is interpreted to belong to D" layer in the lower mantle (e.g. Stacey and Loper, 1983). Therefore, frameworks or tracks of hot spots and palaeomagnetic poles (PPs) can be used in conjunction to make absolute reconstructions of the palaeolatitudinal and palaeolongitudinal positions of the continents.

Hotspot framework can be identified from Jurassic to present times (Morgan, 1983; among others). For times before 200 Ma, there are fewer hot spots so that, only few tracks can be recognized (Zonenshain *et al.*, 1985). Thus, reconstructions based on hot spots older than the Lower Jurassic, have greater uncertainty.

In this paper, we describe a method of making absolute reconstructions of the continents for the Late Permian based only on palaeomagnetic data. This method is a two step process consisting in, first a latitudinal reconstruction of the continent using PPs and then a longitudinal reconstruction based on the preferred transitional VGP paths.

2. HYPOTHESIS AND METHOD

Vizán *et al.* (1994) defined two preferred longitudinal transitional VGP bands for the Lower Jurassic-Early Cretaceous based on the application of the Raleigh test to a population with a von Mises distribution (see Davis, 1986) defined by mean longitudes (θ) of 121-301° E, with an interval of uncertainty ($\Delta\theta$) of 16° for a 5% significance level. This defines two antipodal bands between: 105-137° E and 285-317° E longitude (Fig.1). The VGPs defining these bands were previously rotated according to the hotspot framework of Morgan (1983) and subsequently by TPW.

These VGP bands coincide with the lows of the residual geoid, i.e. the regions of the CMB of fast seismic waves (Vizán *et al.*, 1993; 1994). Different authors (Anderson, 1982; Chase and Sprowl, 1983; Hager *et al.*, 1985; Gurnis, 1988; 1993; among others) have suggested that the pattern of the residual geoid and the topography of the present CMB were determined by the mantle insulation and the thermal blanketing caused by the super continent Pangaea which existed in the Middle Carboniferous (Lefort and Van der

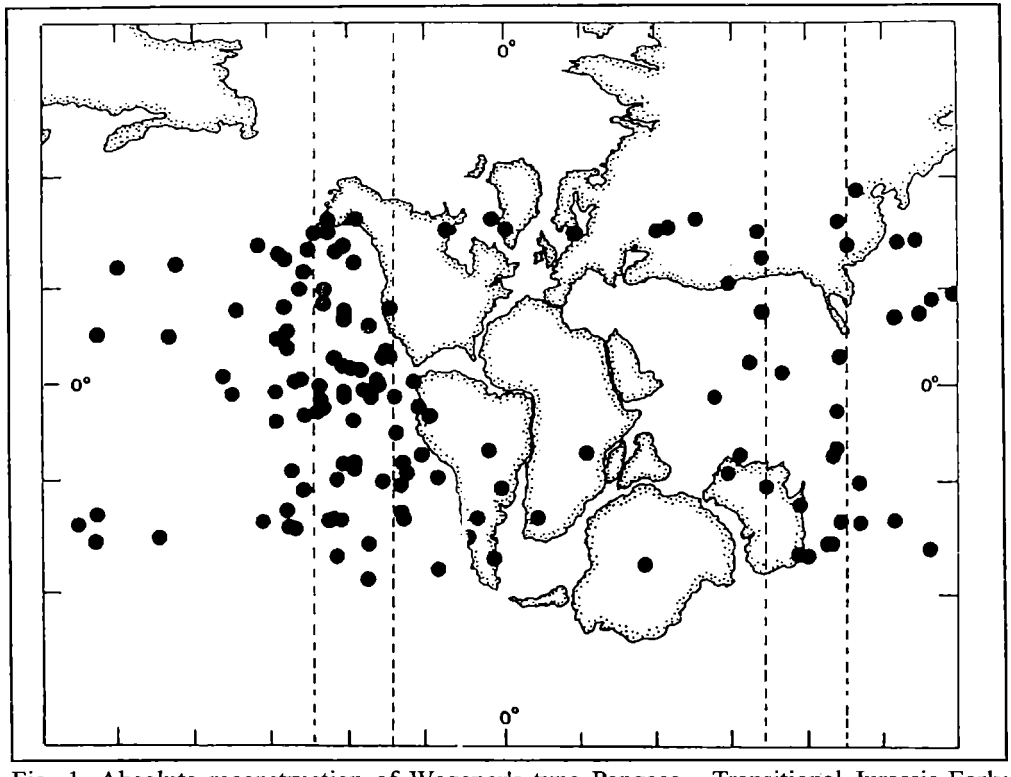

Fig. 1. Absolute reconstruction of Wegener's type Pangaea. Transitional Jurassic-Early Cretaceous VGPs (little black circles) and preferred longitudinal bands (dashed lines).

Voo, 1981; Veevers, 1991; among others). Therefore, it is possible to suggest that the pattern of the present CMB has existed since the Late Permian. It follows that, the preferred Jurassic-Early Cretaceous transitional VGP bands can be used to define a reference frame to make longitudinal reconstructions of continents for Pre-Jurassic times (i.e. Late Permian-Triassic). Jurassic and Early Cretaceous VGPs of stable polarity palaeomagnetic data of South America and Antarctica were found preferentially distributed along the same preferred longitudes of transitional VGPs (see Lanza and Zanella, 1993; Vizán *et al.*, 1993). If GMF conditions during the Late Permian were similar to those during the Jurassic - Early Cretaceous, it is possible that also elongated VGPs populations of Late Permian and Triassic sequences can be used to make longitudinal palaeoreconstructions of continents for these times. In our proposal (Fig. 2), a latitudinal reconstruction is made as a first step, by rotating the PP of the geologic

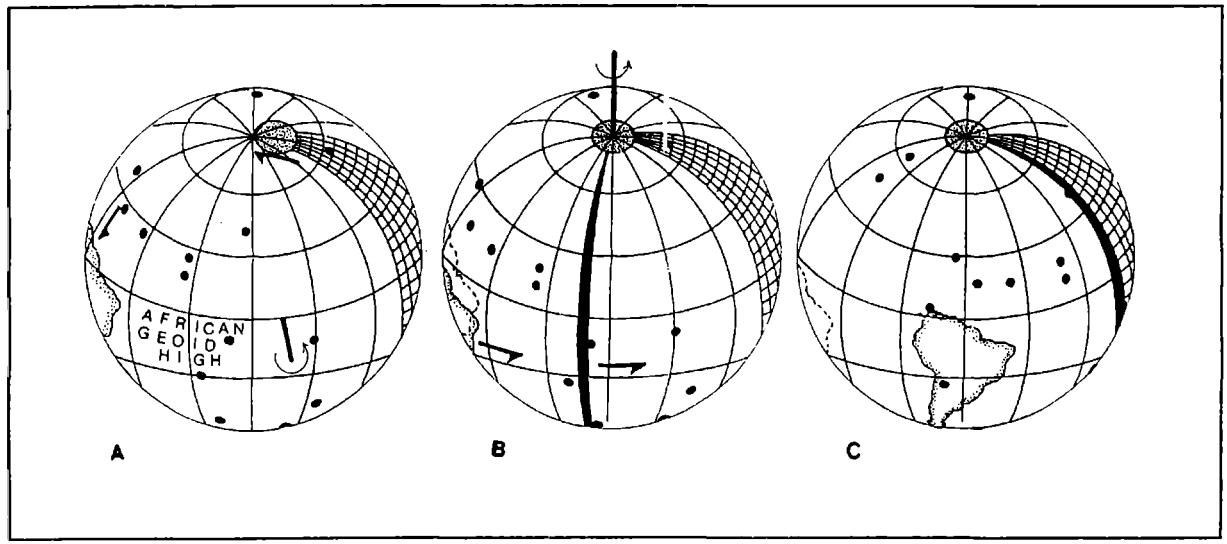

Fig. 2. Absolute reconstruction on the basis of palaeomagnetic data. Dotted circle: Late Permian mean palaeomagnetic pole (MPP) for South America. Squared longitudinal band: preferred longitudes of Jurassic-Early Cretaceous VGPs. Little black circles: VGPs of the Illawarra Zone, recorded in the upper section of Late Permian Paganzo Group. Black longitudinal band: statistically defined mean longitude. A) Latitudinal reconstruction using the MPP: the pivot is perpendicular to the great circle that contains MPP and the Earth rotation axis. The arrows indicate the sense of movement. B) Longitudinal reconstruction using the VGPs: the pivot coincides with the axis of rotation. C) Absolute reconstruction of South America after the rotations showed in A and B. The geographic position of the continent in the previous step is shown in dashed lines.

sequence being analysed through the great circle that contains the axis of rotation of the Earth and the PP or a coeval mean palaeomagnetic pole (MPP) for the continent (Fig. 2a). In other words, a pivot located on the equator is used to rotate the PP or the MPP, as well as all the VGPs and the continent itself, from their original positions to the Earth rotation axis. Thus, both the palaeomagnetic data and the continent are referred to the axis of rotation of the Earth. The rotated VGPs are statistically analysed in the same way as the preferred Jurassic-Early Cretaceous bands. It is important to point out here that if the longitudinal rotation of the continent is made using only the transitional VGPs (between 50° N and 50° S respect to the axis of rotation), the statistical values of a population will change according to the latitudinal rotation: i.e., a different number of VGPs with different geographic coordinates will be located between the mentioned parallels.

The applied statistics defines the mean longitude of the population of VGPs (Fig. 2b) and its intervals of uncertainty. The longitudinal rotation is made through a pivot at the Earth rotation axis until the mean longitude coincides with one of the Jurassic-Early Cretaceous bands (Fig. 2c). In Permian and Triassic sequences this rotation must be applied toward the African geoid high, or in the contrary sense of the drift of the plate. The same rotation is applied to the continent to obtained its longitudinal reconstruction (Fig. 2c). This analysis is illustrated with real palaeomagnetic data in Fig. 2. The position of the MPP on the northern hemisphere over the Jurassic-Early Cretaceous band (Fig. 2a), **does not** mean that it is related with this band, therefore this band **must not** be latitudinally rotated. The plotted VGPs belong to the Illawarra Zone recorded in the upper section of the Paganzo Group (Valencio *et al.*, 1977). The black meridional band is that defined by these VGPs. Its rotation up to 105°E meridian permits the best matching of South American reconstruction with an absolute reconstruction of this continent for 250 Ma obtained on the basis of hot spots (see below).

3. DISCUSSION AND POSSIBLE APPLICATIONS

In order to test the reliability of the absolute palaeomagnetic reconstructions, we compare it with a reconstruction of South America for 25O Ma ago based on the hotspot framework defined by Morgan (1983), from 200 Ma to present, and a hotspot track recorded in Siberia from 280 Ma to 130 Ma (Zonenshain *et al.*, 1985). To make the absolute reconstruction of reference (Ref) we considered two movements: 1) the movement of South America respect to the hot spots and 2) the TPW of this continent from 250 Ma to present. We obtained the pivot Phs (Table 1) to determine the position of South America with respect to the hot spots for the Late Permian by rotating South America to European coordinates according to Bullard *et al.* (1965), and then, adjusting both continents to the hotspot framework for 200 Ma (Morgan, 1983). The continents were then rotated again about the Siberian pivot (with its coordinates referred to 200 Ma)

TABLE 1: Pivots or Euler Poles to make the reconstructions.

Name	Geog.Coordinates Lat.(°)	Long.(°)	Angle of rotation	Movement of South America that is involved
Phs	51.5	8.5	83	referred to hot spots (250 Ma).
Pref	81.3	67.9	66.4	absolute (250 Ma).
Plat	0	215	-9.5	latitudinal (MPP Table 2).
Plon C	-90	0	-73	longitudinal (Corumbatai VGPs).
Plon P	-90	0	-87.7	longitudinal (Paganzo VGPs).
Plon CP	-90	0	-85	longitudinal (VGPs Cor.& Pag.).
Plon ob	-90	0	-79	longitudinal (oblique VGPs).
Pab C	82	71.5	73	absolute (VGPs Cor.).
Pab P	83	79	88	absolute (VGPs Pag.).
Pab CP	83	77.5	85.4	absolute (VGPs Cor.& Pag.).
Pab ob	82.5	74.5	79.5	absolute (oblique VGPs).

Latitude N (S) is positive (negative), longitude E (O) is positive (negative), clockwise (counterclockwise) rotation is negative (positive). The oblique VGPs for calculate the pivot Pab ob belong to Corumbatai Formation and Paganzo Group.

until the positions that they would have respect to the hot spots for 250 Ma. Previously, we calculated the possible amount of movement involved from 200 Ma to 250 Ma according to Zonenshain *et al.* (1985).

To correct the South American movement due to the TPW, we obtained a MPP for the Late Permian by averaging four reliable PP of that age from this continent (Table 2). The reliability criteria considered in the selection of the PPs are the following: 1) Reported test of the stability of the remanence applying AF or thermal cleaning in the original papers; 2) Interval of uncertainty (A_{95})<= 16; 3) Stratigraphic ages defined with an uncertainty lesser than a geologic period. The MPP was obtained using the statistics of Fisher (1953). The geographic coordinates (with South America in its present position) and statistical parameters for the calculated MPP are: Lat.= 80.5° S, Long.= 305° E, N= 4, R= 3.972, A_{95}= 9°, K= 106.35. This MPP was considered as the best estimator of the Earth rotational axis position respect to South America in the Late Permian.

We referred this MPP to the hot spots for 250 Ma through a rotation about Phs. The coordinates of the MPP after the rotation are: Lat.= 45.4° S, Long.= 121.4° E. According

TABLE 2: Late Permian plaeomagnetic poles of South America

Geologic sequence or locality	Age Geol.	Age Rad.	Pole position Long.(°E)	Pole position Lat.(°S)	A_{95} (°)	Ref.
Q.del Pimiento	Ps	263±5 Ma	282	81	12	Creer et al.,1971
Choique Mahuida	Ps	254±10 Ma	344	75	15	Conti and Rapalini,1991.
Paganzo G.	Ps	266±7 Ma*	249	78	3	Valencio et al., 1977.
Corumbatai F.	Ps-Tr		294	86	14	Valencio et al., 1975.

Mean Palaeomagnetic Pole (MPP): N= 4, Long.= 305° E, Lat.= 80.5° S, K= 106.

*The radimetric age of Paganzo G. belong to a volcanic level near the base of the section. The upper part of this section spans the boundary between Kiaman Magnetic Interval and Illawara Zone dated at 250 Ma (Harland et al., 1990).

to that, a possible TPW of about 45° must have occurred since the Late Permian. To make MPP, already referred to the hot spots, to coincide with the Earth rotation axis, we had to define a new pivot which, by definition, is perpendicular to the great circle that contain the MPP and the Earth rotation axis (Lat.= 0°, Long.= 31.4° E, clockwise rotational angle= 44.6°). So, this pivot was combined with Phs (Pref in Table 1) to make the Ref. The Ref is shown in figures 4 and 5 with dashed lines.

To perform the absolute palaeomagnetic reconstruction of South America, the latitudinal position of the continent was obtained rotating the MPP to the Earth rotation axis about the pivot Plat (Table 1). The VGPs used in the longitudinal movements, were also rotated about this pivot.

The longitudinal movement of South America was obtained using only the VGPs of Corumbatai Formation (Valencio *et al.*, 1975) and Paganzo Group (Valencio *et al.*, 1977) . The 4 VGPs of Quebrada del Pimiento (Creer *et al.*, 1971) and the 8 VGPs of Choique Mahuida (Conti and Rapalini, 1991) were not used, because they are not enough to accurately define a VGP band. Anyway, it is worth note that the VGP population of Choique Mahuida have a preferred distribution similar to those of Corumbatai Formation and Paganzo Group (see Table 3 and Fig. 3).

The VGPs populations of the latter sequences are formed by a significative numbers of VGPs (Table 3 and Fig. 3b and 3c). Therefore, they were employed to determine the longitudinal rotation of South America. The VGPs of Corumbatai Formation and Paganzo Group were analysed according to the Raleigh test. Combined VGPs of both sequences

TABLE 3: Mean longitudes and intervals of uncertainties for Choique Mahuida Formation, Corumbatai Formation and Paganzo Group (von Mises' distributions).

VGP Populations	N° of VGPs	Mean longitude ($\bar{\theta}$) (°E)	Interval of uncertainty	Rm
1. C. Mahuida F.	8	16	89° (10%)	0.258
2. Corumbatai F.	17	32	44° (5%)	0.415
3. Paganzo G.	168	17	20° (5%)	0.19
4. Cor.F.& Pag. G.	185	20	28° (5%)	0.209
5. Oblique	35	26	41° (10%)	0.257

The population 5 belongs to oblique VGPs of Corumbatai F. and Paganzo G. together. The values of Rm and θ of populations 2,3 and 4 belong to the 5% confidence level. The values of these parameters for the populations 1 and 5 belong to the 10% confidence level. All values of Rm pass the Rayleigh test. The values of Rm for the populations 1 and 5 that belong to the 5% confidence level do not pass the Rayleigh test.

were also analysed with the same test, considering the whole VGP population or only the oblique or transitional VGPs. The mean longitudes of the VGP populations of the different PPs are very similar (Table 3 and Fig. 3). These mean longitudes are also similar to those observed in 8 populations of Jurassic VGPs from South America (Vizán *et al.*, 1993).

The populations of the Corumbatai Formation, the Paganzo Group and both combined pass the Raleigh test with a 5% level of significance. The other analysed populations, pass this test with a 10% level of significance. To make longitudinal reconstructions of South America, the mean longitudes obtained for the Late Permian VGPs were rotated about a pivot at the Earth rotation axis until it coincided with the Jurassic-Early Cretaceous longitudinal band defined by the meridians 105-137° E. In the same way, South America was longitudinally rotated. The best fits with the Ref were obtained when the longitudinal movements were done up to the 105° E meridian (Figs. 4 and 5).

The main deficit of the palaeomagnetic absolute reconstructions here showed, are the intervals of uncertainties due to the scarce number of transitional and oblique VGPs (Table 3). Anyway, two palaeomagnetic reconstructions and the Ref are similar. The best fit with the Ref is undoubtedly obtained with the data of the Corumbatai Formation (Fig. 4a). When the VGPs of both the Corumbatai and Paganzo Formations are considered together, the best fit is obtained with the oblique or transitional VGPs (Fig. 5b).

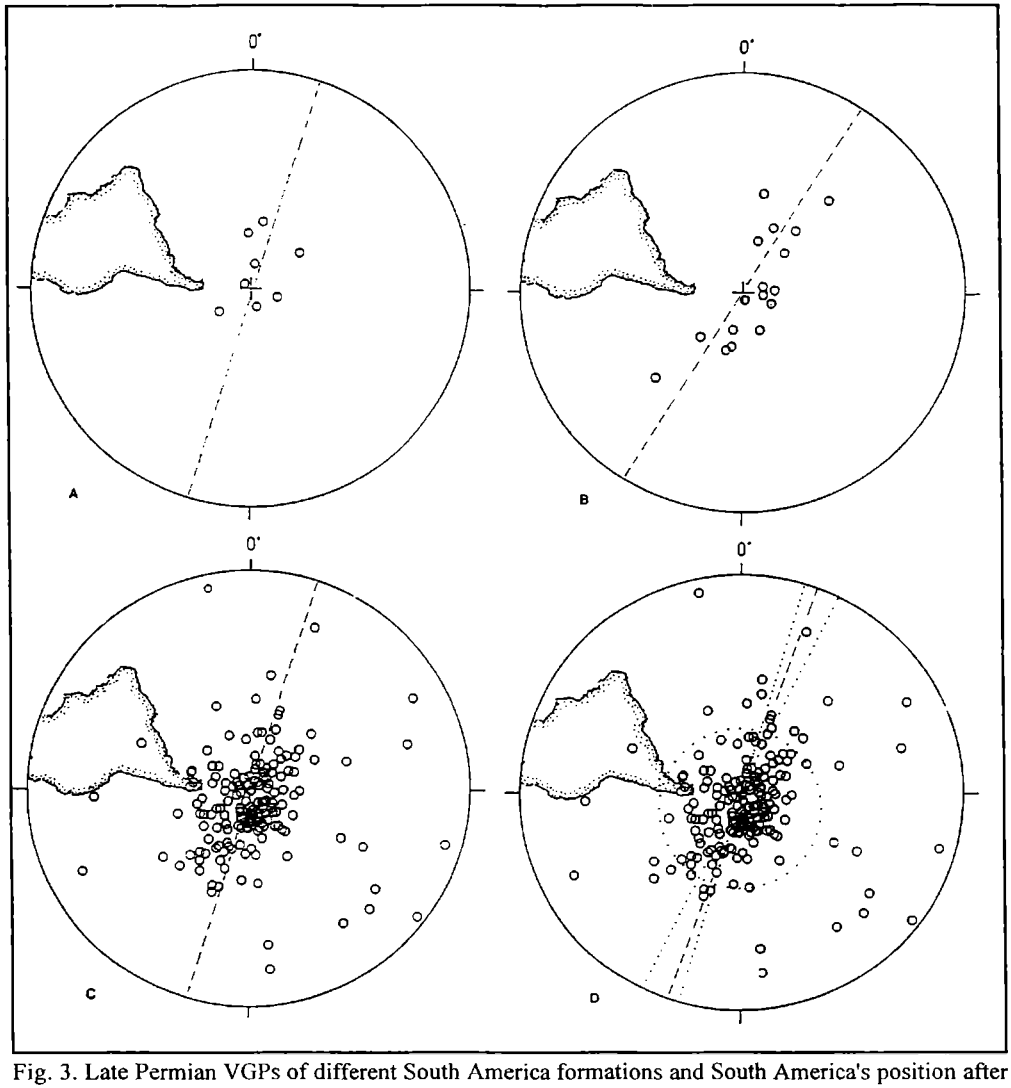

Fig. 3. Late Permian VGPs of different South America formations and South America's position after a latitudinal palaeoreconstruction, plotted in stereographic projections. The south geographic pole is at the center of the projections. The VGPs are only plotted in the southern hemisphere. In dashed lines: mean longitudes of VGPs. A) Choique Mahuida Formation. B) Corumbatai Formation. C) Paganzo Group. D) Corumbatai Formation plus Paganzo Group. Large dotted circle: window of 40° about the MPP. The mean longitudes corresponding to the VGPs of only stable polarities from each geologic formation are depicted in dotted lines.

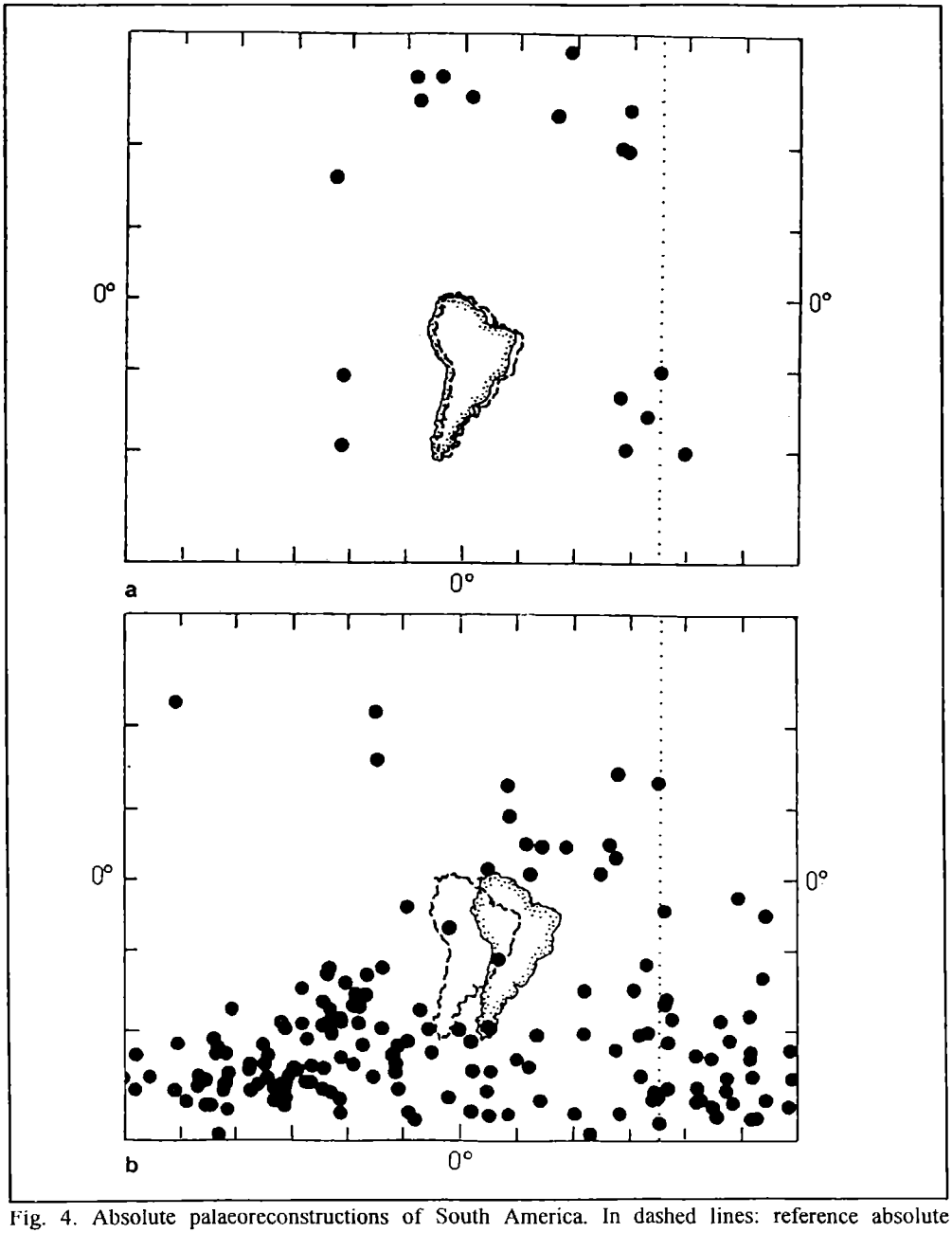

Fig. 4. Absolute palaeoreconstructions of South America. In dashed lines: reference absolute reconstruction. In dotted lines: 105°E meridian. A) Reconstruction using the VGPs of the Corumbatai Formation (pivot Pab C of table 2). B) Reconstruction using the VGPs of the Paganzo Group (pivot Pab P of Table 1).

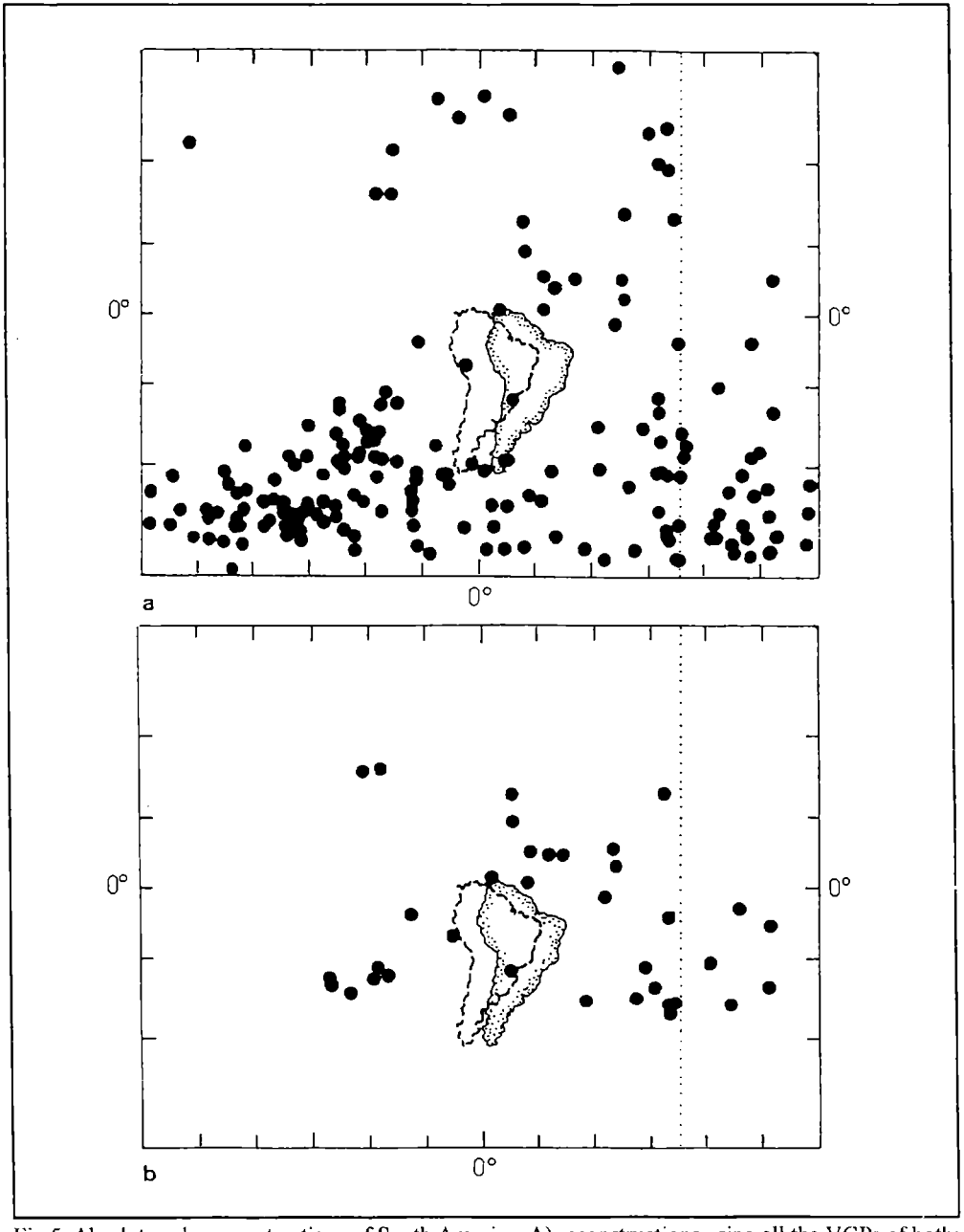

Fig.5. Absolute paleoreconstructions of South America. A) reconstructions using all the VGPs of both: the Corumbatai formation and the Paganzo Group (pivot Pab CP of Table 2). B) reconstruction using only the transitional or oblique VGPs of both sequences (Pivot Pab ob). See Fig. 4 for more information.

4. CONCLUSION

A methodology that allows possible absolute palaeomagnetic reconstructions is designed and appraised. This methodology was used in palaeoreconstructions of South America for the Late Permian, considering VGPs of two geologic formations of this age to determine the longitudinal position of this continent. The similitude between these absolute palaeomagnetic reconstructions and another obtained by a different way is quite encouraging.

Acknowledgments

We wish to thank the Consejo Nacional de Investigaciones Científicas y Técnicas and the Universidad de Buenos Aires for supporting our investigations. Special thanks to Dr. K. Creer and Dr. A. Rapalini who improved our original manuscript.

REFERENCES

Anderson, D. L., 1982. Hotspots, polar wander, Mesozoic convection and the geoid. Nature, 297, 391-393.

Andrews, J.A., 1985. True polar wander: An analysis of Cenozoic and Mesozoic palaeomagnetic poles. Journal of Geophysical Research, 90, 7737-7750.

Besse, J. and V. Courtillot, 1991. Revised and Synthetic apparent polar wander path of the African, Eurasian, North American and Indian plates, and true polar wander since 200 Ma. Journal of Geophysical Research, 96, 4029-4050.

Bullard, E.C., J.E. Everett, and A.G. Smith, 1965. The Fit of Continents around the Atlantic. Philosophical Transactions of the Royal Society, 258, 41-51.

Brown L., J. Pickens, and B. Singer, 1994. Matuyama-Brunhes transition recorded in lava flows of the Chilean Andes: Evidence for dipolar fields during reversals.Geology, 22, 299-302.

Clement, B.M., 1991. Geographical distribution of transitional VGPs: Evidence for non-zonal equatorial symmetry during the Matuyama-Brunhes geomagnetic reversal.Earth and Planetary Science Letters, 104, 48-58.

Conti,C. and A.E. Rapalini, 1990. Paleomagnetismo de la Formación Choique Mahuida, aflorante en la sierra homónima, provincia de La Pampa, República Argentina, XI Congreso Geológico Argentino, San Juan, Actas II, 235-238.

Courtillot, V. and J. Besse,1987. Magnetic Field Reversals, Polar Wander, and Core-Mantle Coupling. Science, 237, 1140- 1147.

Cox, A.V. and B.R., Hart, 1986. Plate tectonics: How it Works. Editorial Blackwell, Palo Alto, 389 pp.

Creer, K.M., J.G. Mitchell and D.A. Valencio, 1971. Evidence for a Normal Geomagnetic Field Polarity Event at 263 ± 5 m.y. bp within the Late Palaeozoic Reversed Interval. Nature Physical Science, 233, 87-89.

Chase, C.G. and D.R. Sprowl, 1983. The modern geoid and ancient plate boundaries.Earth

Planetary Science Letters, 62, 314-320.
Davis, J.C., 1986. Statistics and Data Analysis in Geology. John Wiley (Ed.), New York.
Egbert, G., 1992. Sampling bias in VGP longitudes. Geophysical Research Letters, 19, 2353-2356.
Fisher, R. A., 1953. Dispersion on a sphere. Royal Society of London Proceedings, 217, 295-306.
Gubbins, D. and R.S. Coe, 1993. Longitudinally confined geomagnetic reversal paths from non-dipolar transitions field. Nature, 362, 51-53.
Gubbins, D., 1994. Geomagnetic polarity reversals: a connection with secular variation and core-mantle interaction ? Reviews of Geophysics, 32, 61-83.
Gurary, G.Z., 1988. Geomagnetic field during reversals in the Late Cenozoic. Academy of Sciences of the USSR, Moscow, 207 pp.
Gurnis, M., 1988. Large Scale mantle convection and the aggregation and dispersal of supercontinents. Nature, 332, 695-699.
Gurnis, M., 1993. Phanerozoic marine inundation of continents driven by dynamic topography above subducting slabs. Nature, 364, 589-593.
Hager, B.H., R.W. Clayton, M. Richards, R. Comer and A. Dziewonski, 1985. Lower mantle heterogeneity, dynamic topography and the geoid. Nature, 313, 541-545.
Harland,W.B., R.L. Armstrong, A.V. Cox, L.E. Craig, A.G. Smith and D.G., Smith, 1990. A geologic time scale 1989. Cambridge University Press, United Kingdom, 263 pp.
Hoffman, K.A., 1992. Dipolar reversal states of the geomagnetic field and core-mantle dynamics. Nature, 359, 789-794.
Laj, C., A. Mazaud, R. Weecks, M. Fuller, and E. Herrero-Bervera, 1991. Geomagnetic reversal paths. Nature, 351, 447.
Laj, C., A. Mazaud, R. Weecks, M. Fuller and E. Herrero-Bervera, E., 1992. Geomagnetic reversal paths. Nature, 359, 111-112.
Langereis C. G., A. A. M. Van Hoff and P. Rochette, 1992. Longitudinal confinement of geomagnetic reversal paths as a possible sedimentary artifact. Nature, 358, 226-230.
Lanza, R. and E. Zanella, 1993. Palaeomagnetic of the Ferrar dolerite in the northern Prince Albert Mountains (Victoria Land, Antartica). Geophysical Journal International, 114, 501-511.
Lefort J. P. and R. Van der Voo, 1981. A Kinematic model for the collision and complete suturing between Gondwanaland and Laurassia in the Carboniferous. The Journal of Geology, 5, (89), 537-550.
Livermore, R. A., F. J. Vine and A.G. Smith, 1984. Plate motions and the geomagnetic field, II, Jurassic to Tertiary. Geophysical Journal Royal Astronomical Society, 79, 939-961.
McFadden, P.L., C.E. Barton and R.T. Merrill, 1993. Do virtual geomagnetic poles follow preferred paths during geomagnetic reversals ? Nature, 361, 342-344.
Morgan, W.J., 1983. Hotspot tracks and the early rifting of the Atlantic. Tectonophysics, 94, 123-139.
Quidelleur, X. and J. P. Valet, 1994. Paleomagnetic records of excursions and reversals: possible biases caused by magnetization artefacts. Physics of the Earth and Planetary Interiors, 82, 27-48.
Stacey, F. D. and D. F. Loper, 1983. The thermal boundary layer interpretation of D" and its role as a plume source. Physics of the Earth Planetary Interiors, 33, 45-55.
Tric, E., C. Laj, J.P. Valet, P. Tucholka, M. Paterne and F. Guichard, 1991. The Blake geomagnetic

event: transition geometry, dynamical characteristics and geomagnetic significance. Earth and Planetary Science Letters, 102, 1-13.

Valencio, D. A., 1980. El magnetismo de las rocas. Editorial Universitaria de Buenos Aires, Temas, Buenos Aires, 351 pp.

Valencio, D. A., A. Rocha Campos and I. G. Pacca, 1975. Palaeomgnetism of some sedimentary rocks of the Tubarao and Passa Dois Groups from the Paraná basin.Revista Brasileira de Geociencias, 5, 186-197.

Valencio, D. A., J. F. Vilas and J. E. Mendía, 1977. Palaeomagnteism of a sequence of red beds of the middle and upper sections of Paganzo Group (Argentina) and the correlation of Upper Palaeozoic-Lower Mesozoic rocks. Geophysical Journal of the Royal astronomical Society, 51, 59-74.

Valet, J. P., P. Tucholka, V. Courtillot and L. Meynadier, 1992. Paleomagnetic constraints on the geometry of the geomagnetic field during reversal. Nature, 356, 400-407.

Van Zijl, J. S. V., L. W. Graham, and A. L. Hales, 1962. The Paleomagnetism of the Stormberg lavas II. The behaviour of the Magnetic field during a reversal.Geophysical Journal Royal astronomical Society, 7, 169-182.

Veevers, J. J., 1989. Middle-Late Triassic (230 ± 5 Ma) singularity in stratigraphic and magmatic history of the Pangean heat anomaly. Geology, 18, 784-787.

Vizán, H., M. Mena, and J. F. Vilas, 1993. Pangea, the geoid, and the paths of virtual geomagnetic poles during polarity reversals. Journal of South America Earth Sciences, 6, 253-266.

Vizán, H., R. Somoza, M. J. Orgeira, C. Vázquez and M. Mena, J. F. Vilas, 1994. Late Palaeozoic-Mesozoic geomagnetic reversal paths and core mantle boundary. Geophysical Journal International, 117, 819-826.

Vizán, H. and M. A. Van Zele, 1995. Analysis of a Lower Jurassic Geomagnetic reversal based on a model that relates transitional fields with variations of flux on the core surface. Studia Geophysica et Geodaetica, 39, 177-188.

Zhu, R., C. Laj, and A. Mazaud, 1994. The Matuyama-Brunhes and Upper Jaramillo transitions recorded in a Loess Section at Weinan, North-Central China. Earth and Planetary Science Letters, 125, 143-158.

Zonenshain, L. P., M. I. Kuzmin and M. V. Kononov, 1985. Absolute reconstructions of the Paleozoic oceans. Earth and Planetary Science Letters, 74, 103-116.

GEOACTA, 22, 74-90, 1997

VARIABILITY AND MOTION OF THE BRAZIL-MALVINAS FRONT

Alejandro A. Bianchi[1] and Silvia L. Garzoli[2]
[1]Departamento Oceanografía, Servicio de Hidrografía Naval
Av. Montes de Oca 2124, 1271 Buenos Aires, Argentina
[1]Lamont-Doherty Earth Observatory of the Columbia University
Palisades, NY 10964, USA

ABSTRACT

The temporal evolution of the thermal field associated with frontal motions in the South Western Atlantic is studied. The analysis is based on data collected with an array of inverted echo sounders (IES) deployed during the Confluence Program (1988-1990) at the Brazil/Malvinas Confluence. The travel time series obtained with the IES are scaled to mean temperatures of the upper 500 m (T_{500}) of the ocean and series of T_{500} horizontal distributions are constructed. A description of the evolution of the thermal field, emphasizing the frontal motions and some meso-scale features, is presented. Three well-defined northward penetrations of the Malvinas current with fairly variable periods of permanence (15-60 days) and mean frontal motion velocities of 0.2 m/s are observed. Cross-correlation of the T_{500} time series analysis leads to a plausible explanation of some features of the observed variability. Comparison with previous results in the area indicate a marked interannual variability and sources of variability are discussed.

RESUMEN

Se estudia la evolución temporal del campo de isotermas asociados con movimientos frontales en el océano Atlántico Sudoccidental. El análisis está basado en datos obtenidos de ecosondas invertidos (IES) fondeados durante la ejecución del Programa Confluencia (1988-1990) en la confluencia de las corrientes de Malvinas y Brasil. Las series de tiempo obtenidas con los IES fueron estandarizados con las temperaturas medias de los primeros 500 m (T_{500}) del océano y de esta forma se obtuvo la distribución horizontal de T_{500}. Se presenta una descripción de la evolución del campo térmico en relación con los movimientos frontales y las características de mesoescala de esa zona. Se observaron tres penetraciones bien definidas de la corriente de Malvinas con períodos variables de permanencia (15 -60 días) y velocidades del frente de 0.2 m/s. Del análisis de la correlación cruzada de la serie de T_{500} se obtiene una posible explicación de la variabilidad observada. La comparación con resultados previos indican una variabilidad interanual. Se discuten las fuentes de variabilidad.

1. INTRODUCTION

The most prominent feature of the upper circulation of the Western South Atlantic is the encounter of two boundary currents at the Brazil/Malvinas Confluence in the area of the Argentine Basin (Brennecke, 1921; Deacon, 1937). The Brazil Current flows poleward along the continental slope of South America. Between 35° and 3° S, this current converges with the Malvinas Current that flows northward along the continental margin, causing a sharp thermohaline front (Roden, 1986; Gordon, 1989). The Brazil Current is the western limb of the anticyclonic South Atlantic Subtropical Gyre while the Malvinas Current originates as a branch of the Antarctic Circumpolar Current (Deacon, 1933; Sverdrup *et al.*, 1942) downstream of the Drake Passage. After the encounter, both currents turn seaward, with the poleward momentum flux of the Brazil Current usually dominating (Gordon, 1981). Then, the Brazil Current executes an anticyclonic turn to the north, establishing a quasi-stationary meander of warm subtropical upper waters (Gordon and Greengrove, 1986), with its mean axis location along 53° W. Westward of this feature, a cyclonic trough of cold subantarctic water is enclosed by the Malvinas Current and its return.

High variability characterizes this region in a wide time and space range associated with strong baroclinicity due to the high horizontal density gradients. A large mesoscale variability related to the meandering nature of the Confluence area has been observed by satellite infrared imagery (Legeckis and Gordon, 1982; Olson *et al.*, 1988), surface drifting buoys (Piola *et al.*, 1987; Figueroa and Olson, 1989) and satellite altimetry (Cheney *et al.*,1983; Zlotnicki and Fu, 1990).

The subtropical upper water carried by the Brazil Current is characterized by temperatures higher than 10° C (up to 26° C in the surface layer during summer) and salinities higher than 35 (up to 36), while the subantarctic water carried by the Malvinas Current has temperatures lower than 10° C and salinities lower than 34.3 (Reid *et al.*, 1977; Bianchi *et al.*, 1993).

Dynamic height time series and a simple model assuming a mean profile of the 8 to 10° C isotherms across the front, were used to study frontal motions in the Confluence area. These time series are derived from a pilot experiment with inverted echo sounders (IES) moored during 16 months from 1984 to 1986 (Garzoli and Bianchi, 1987; Garzoli and Garraffo, 1989). Infrared satellite sensors were used to monitor sea surface temperature and to study temporal variations of the separation of Brazil and Malvinas Currents from 1984 to 1987 (Olson *et al.*, 1988). Both types of measurements provided information on the time-space variability of the front and demonstrated the importance of a regional survey based on long-term continuous observations. On these basis, an international (Argentine, French and U.S.A.) effort was initiated in 1988 to perform a high-resolution study of the frontal region: the Confluence Program (Confluence

Principal Investigators, 1990). As part of the Confluence Program, an array of 10 IES was deployed in November 1988 from R.V. Puerto Deseado and recovered in February 1990 from R.V. Le Suroit.

The IES data were analysed in terms of dynamic heights and geostrophic velocities and an estimate of the geostrophic transports associated to the main flows was obtained by Garzoli (1993). One of the main results of the study is that the large surface temperature variability (Olson et al, 1988) is also present in the dynamic height field of the surface relative to 1000 m. Most of this variability is due to the eddies generated between the two main flows and to the change in latitude where separation of the Brazil Current occurs. This in turn, is associated with a large frontal variability.

The objective of this paper is to analyse IES data to further study and quantify the frontal motions. In section 2, the data and methods used are presented. In section 3, a description of some features of the variability of the thermal field, due to the front location, is given. In section 4, association of pulses of Malvinas and Brazil Currents is studied using cross-correlation analysis. Finally, local dynamics of the area and time-space variability are discussed on the basis of the new results.

2. DATA AND METHODS

The location of the IES Confluence deployments (Garzoli, 1993) is shown in Fig. 1. Coordinates, depth of the moorings, and dates of deployment and recovery are given in Table 1. Hydrographic data (CTD and XBT) were obtained during the three Confluence cruises (Confluence Principal Investigators, 1990). The hydrographic information obtained during the first two cruises (Charo *et al.*, 1991), was used to scale the observed travel time (TT) to various oceanographic parameters.

2.1 Calibration to T_{500}

The travel time (TT) of an acoustic signal in sea water is a function of sound velocity, c:

$$TT = -2 \int dz/c(T,S,P)$$

TT is a function of the temperature (T), salinity (S) and pressure (P), a quantity directly related to the vertical structure of the temperature in the water column. In the Confluence area, where large changes in the depth of the thermocline are associated with frontal displacements, the variability in the TT record mainly represents the thermal variability of the upper layer. Therefore, the temperature averaged over the upper 500 m of the ocean (T_{500}), is directly related to the TT.

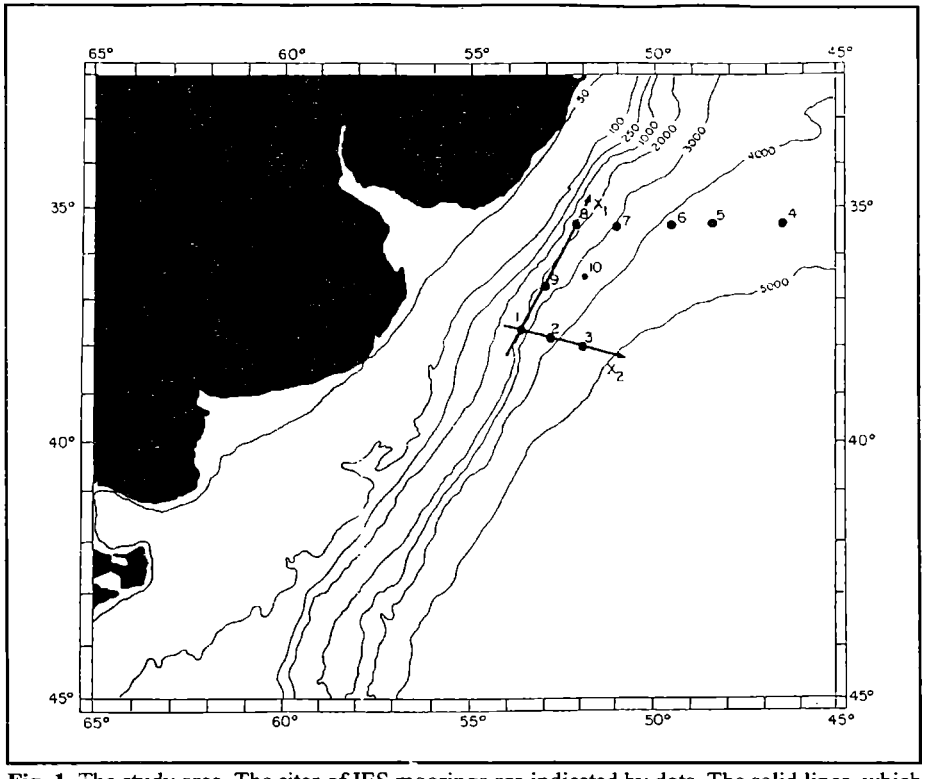

Fig. 1. The study area. The sites of IES moorings are indicated by dots. The solid lines, which were used to measure the frontal motions, indicate the axes along and normal the continental margin.

The CTD data collected during the first two cruises were used to calculate both parameters, TT and T_{500}. A linear regression fit of T_{500} as a function of travel time yields to the relation:

$$T_{500}\ (°C) = 0.622\ TT\ (ms)$$

with a coefficient of determination $R^2 = 0.999$ and a standard error of the estimate of 0.118° C. This relation is used to calculate time series of T_{500}. The absolute value of T_{500} is then determined by adjusting the records to the vertically averaged values of temperature of the upper 500 m obtained from the CTD stations over the IES moorings in November 1988 and September 1989 cruises. In some cases (IES 8 and 10), additional data from XBT casts of February 1990 are used.

Differences between the values of T_{500} obtained from the CTD and IES data vary

TABLE I

IES Site #	Latitude	Longitude	Depth (m)	Deployment Date	Recovery Date
1	37°37.64'S	53°34.11'W	2852	11/14/88	02/23/90
2	37°48.10'S	52°45.20'W	3804	11/04/88	02/23/90
3	37°57.42'S	51°53.47'W	4346	11/05/88	02/24/90
6	35°22.90'S	49°30.40'W	4247	11/10/88	02/18/90
7	35°21.89'S	51°00.40'W	3018	11/10/88	02/17/90
8	35°27.39'S	52°16.94'W	1327	11/12/88	02/17/90
9	36°39.54'S	53°00.39'W	2231	11/13/88	02/21/90
10	36°29.56'S	51°52.35'W	3307	11/12/88	02/21/90

between 0.01° C and 1.2° C, with a mean value of 0.6° C and a standard error of 0.4° C. Examples of the resulting T_{500} series are given in Fig.2 (shown as the result of a 10-day running mean averages). The temperature differences between subantarctic and subtropical waters in the upper layer are of 11 to 14° C. Therefore, thermal variability in the area is one order of magnitude higher than the temperature estimate error. T_{500} changes of more than 10° C are observed for periods of 10-15 days at different moorings. Temperature changes of this magnitude, that occur in relatively short time, can only be explained by frontal motions and by eddies passing over the IES mooring sites. At IES stations 1, 2, 3 and 9 the wide range of thermal variability, more than 15° C in periods of 2 to 3 months, is essentially due to frontal motions. Local seasonal variability observed in the T_{500} series from summer to winter averages 2° C, never exceeding 4° C. This range is confirmed by historical CTD observations (Piola and García, 1993).

2.2 Horizontal Temperature distributions

A generalization of minimum-curvature giddying algorithms (Smith and Wessel,1990) was used to obtain instantaneous pictures of the integrated temperature distribution based on IES data. The minimum-curvature surface approximates the shape by a thin plate flexed to pass through the data points (for an analogy in elastic plate flexure). A grid with continuous curvature splines in tension and contouring programs is used to build a series of horizontal distributions of T_{500} using daily averages of the T_{500} series. Records obtained at IES stations 4 and 5 are excluded of the analysis because their locations induce extrapolation errors, specially in the area southward of these sites, where no data are available (see Fig.1). Computer contours accurately represent "freehand drawing" thermal distributions for different oceanographic conditions.

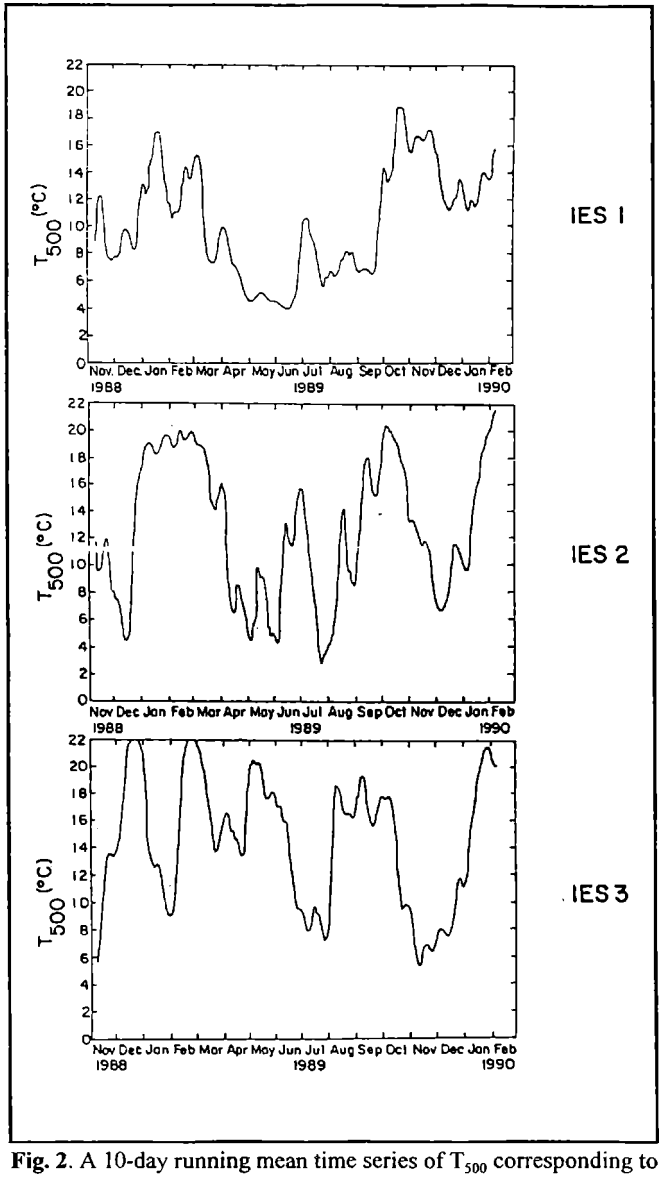

Fig. 2. A 10-day running mean time series of T_{500} corresponding to the first leg of IES (1,2 and 3) of the array.

2.3 Location of the front

Bianchi *et al.* (1993) estimated horizontal temperature gradients in the upper layer

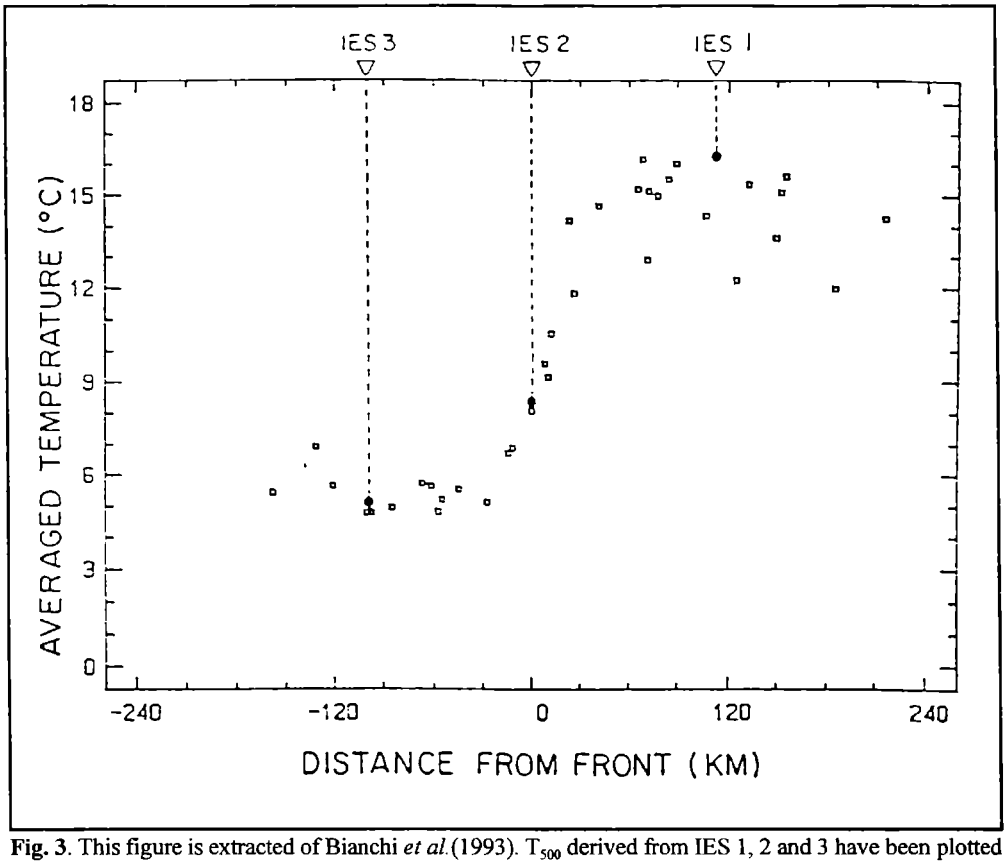

Fig. 3. This figure is extracted of Bianchi *et al.* (1993). T_{500} derived from IES 1, 2 and 3 have been plotted for a situation (December 22 of 1988) in which the temperature at the IES 2 site is the T_{500} representative of the front location (8.5° C). The figure shows the distribution of the vertically averaged temperatures (from hydrographic data) for the upper 500 m vs. distance to the front. The figure was constructed aligning individual profiles according to distance of the front. Large dots indicate T_{500} obtained from the IES sites for a situation in which the front was coincident with IES # 2.

of the Brazil-Malvinas Confluence based on the following scheme: the location of the front was defined where the 10° C isotherm is at 200 m depth (see Garzoli and Bianchi, 1987). Using a data set of the region (hydrographic cruises PD-02-84, OA-04-85, PD-02-88, and Confluence 1988 and 1989), different synoptic realizations of the front were obtained in front coordinates, i.e., shifted to align the front location of each section. The mean temperatures of the upper 500 m of the water column are calculated and plotted as function of the distance to the front (Fig. 3, adapted from Bianchi et al, 1993). IES temperatures agree well with CTD observations available in the area. Similar situations are obtained for other instants of the record (see Fig. 2) in which the front is located at

IES 2. Low values of T_{500} (generally about 4 to 5° C) correspond to subantarctic water and high values of T_{500} (generally higher than 15 °C) correspond to subtropical waters. In a band of 100 km (-50 to 50 km) T_{500} abruptly increases across the frontal region. Variability due to the mesoscale processes and the meandering nature of the front produce some T_{500} values lower than 12° C, at more than 100 km east. The location of the front is defined where the 8.5° C contour of T_{500} is observed. This criterion leads to similar results the 10° C isotherm at 200 m depth obtained in other analyses (Bianchi *et al.*, 1993).

In the pilot experiment (1984-1986) only front zonal displacement were resolved due to the geometry of the reduced array of IES deployed. The present array allows the detection of both, zonal as well as meridional front displacements. Then, this method permits to obtain the location of the front, by the analysis of horizontal distributions of vertically averaged temperatures in a larger array distributed zonally and also meridionally. This method avoids ambiguities and is more accurate than ones used in previous work (Garzoli and Bianchi, 1987; Garzoli and Garraffo, 1989).

3. VARIABILITY OF THE THERMAL FIELD AND FRONTAL MOTIONS

Based on the thermal field evolution, the frontal motions were investigated. Some features of the thermal field will be presented, emphasizing the frontal location related to local dynamic variability. It will be indicated, when possible, displacements of cold or warm eddies in the area. A more quantitative description is then given based on two time series of the frontal motion.

Four "snapshots" of the time series have been selected to depict particular features of the thermal field (Fig. 4). These snapshots were selected after inspection of the 91 5-day block averaged maps in order to represent oceanographic situations typical of the region. The infrared images collected by a satellite of NOAA (Olson & Podestá, personal communication) were visually compared with the T_{500} maps. Although the imagery is showing the skin temperature of the sea, and in most cases, the agreement with T_{500} is very good.

The thermal front is clearly depicted by the close meridional isotherms in December 22, 1988 (Fig. 4a). Due to the giddying scale and the smoothing techniques applied to the data, real gradients are probably are higher than the ones shown in the figure. The estimated cross-front horizontal temperature gradient, leads to an order of magnitude of 1 x 10-4 °C/m. This value is of the same order of magnitude as the estimates presented by Bianchi *et al.* (1993) based on hydrographic data. In December 22 of 1988 the front location reached 36° S , a latitude lower than the mean one for that time of the year (Olson et al, 1988). This anomaly was obviously observed in the geostrophic velocity field (Garzoli, 1993). The local wind forcing appears to be responsible of this northward penetration of the front (Garzoli and Giulivi, 1994).

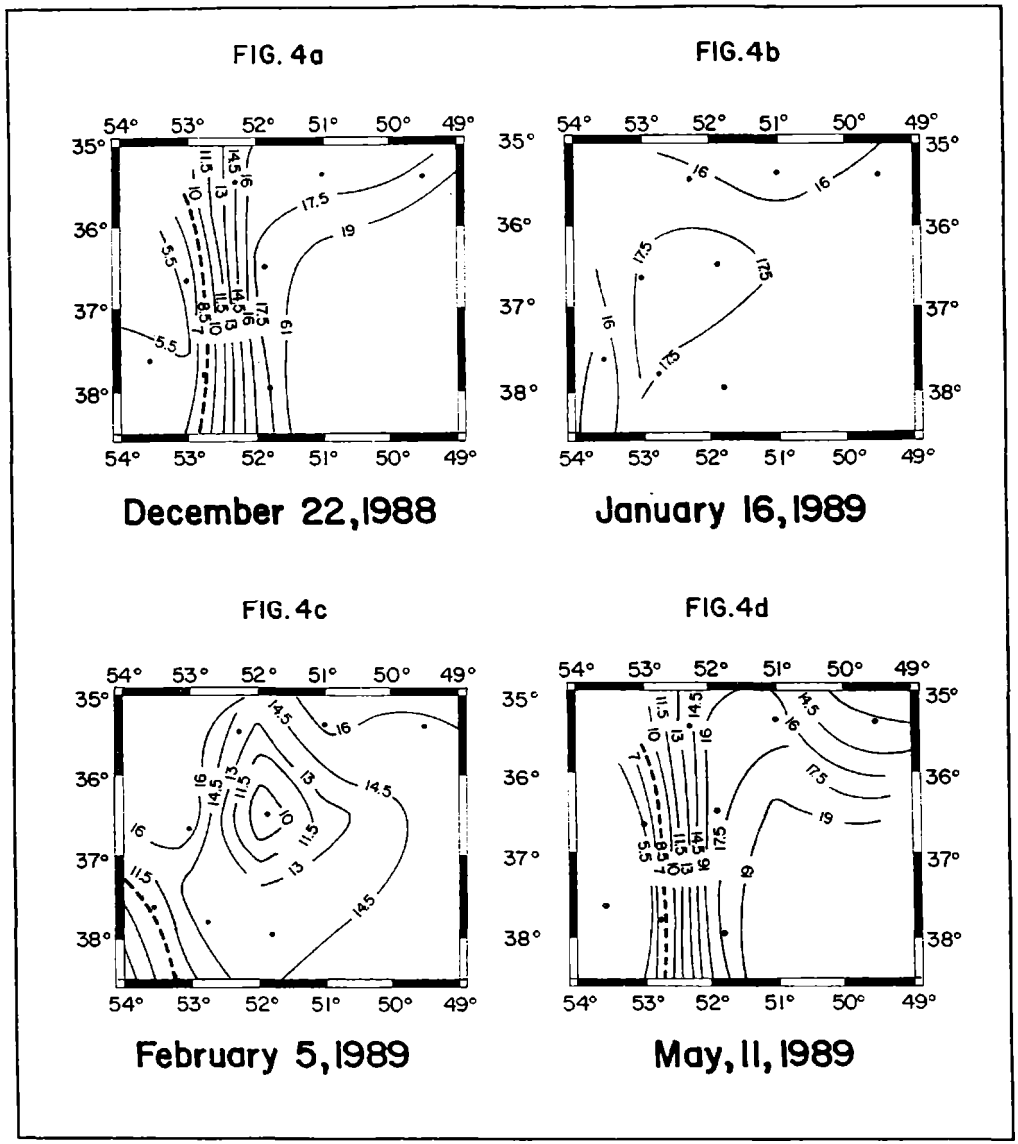

Fig. 4. Averaged temperatures of the upper 500 m contours for the study area. Maps are chronologically sorted. The 8.5° C contour(dashed) represents the location of the thermal front.

One month later, (January 16,1989, Fig. 4b) the front is no longer observed in the area. Most of the region is occupied by warm water preceding typical southern hemisphere summer conditions. The front has probably migrated southward, according to what it is expected to be the summer situation. This condition is confirmed by satellite

imagery. A warm core of temperature higher than 17.5° C dominates the central part of the study region.

A situation showing a large-scale cold-core eddy of about 300 km of diameter centered at 52° W and 36° S is observed on April 6, 1989 (Fig. 4c). Malvinas water is found at 38° S and between 54-53° W (southwest corner of the map). Evidence of this cyclonic mesoscale feature is found in the geostrophic velocity field relative to 1000 dbar (Garzoli, 1993). Satellite imagery does not confirm the presence of the cold-core eddy. This is an example of a particular situation in which sea surface temperature does not represent the oceanographic conditions of the upper layer. Probably, due to large temperature differences between the sea and the atmosphere during the summer, air-sea heat fluxes increase and a thin, warm, stable surface layer develops, masking the cold eddy. An example of a similar situation is seen from hydrographic data in March 1986. At that time, a warm mixed layer over subantarctic waters was masking the presence of the front in the surface field for at least 80 km (Garzoli and Garraffo, 1989). Similar conditions have been recently observed at sea in the same region during a cruise performed at the end of March 1993 and 1994 (Piola, personal communication). In late April 1989, the observed cold eddy re-coalesced with the Malvinas waters. The eddy shedding and re-coalescing process are clearly depicted in a film made to represent the time evolution of the thermal field.

West of 53° W, maximum northward penetration of the Malvinas Current beyond 36°S is observed in mid May 1989 (Fig. 4d). The warmer waters of the area are centered in the southeast corner and maximum thermal gradients are present in a meridional band, between 52 and 53° W.

3.1 Frontal motion

According to the definition given in section 2.3, the front location is assumed to be at T_{500} = 8.5 °C. On the basis of this definition, a subset of 91 horizontal T_{500} distribution maps (one every 5 days) are used to quantify the position of the front. The location of IES 1 is used as the origin of the coordinates system. Distances to the front (to the 8.5° C isotherm) are measured over each map in two directions (see Fig. 1): along the continental slope, X_1 (in a line going from IES 1 to 8) and almost normal to the continental slope, X_2 (in a line from IES 1 to 3). Time series of the distances from the front to IES 1 are displayed in Fig. 5. Gaps in the series correspond to periods during which the front did not intersect one of the two axes. Peaks in Fig. 5 are associated to northward and eastward penetrations of the Malvinas Current.

Three northward penetrations of Malvinas Current are observed (Fig. 5a) for November-December 1988, May-June 1989 and August-September 1989. In less than ten days the front migrates about 200 km to the north. The mean front displacement velocity

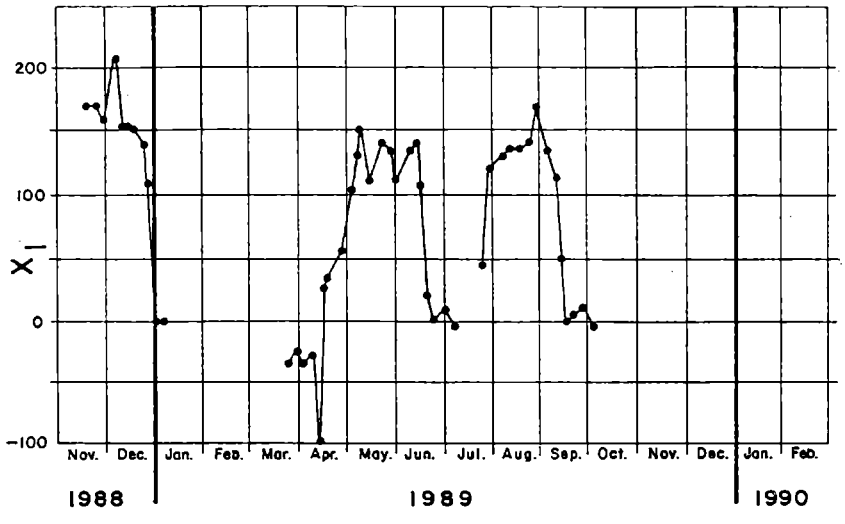

FIG. 5a

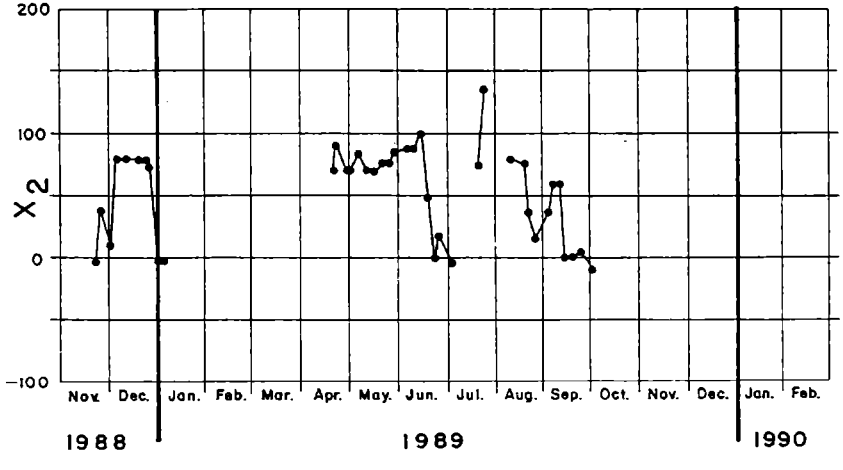

FIG. 5b

Fig. 5. Time series of the location of the front. a) along the slope, positive northward; b) normal to the slope, positive eastward.

is 0.2 m/s. The duration of the northward penetrations vary from 15 to 60 days.

The full extent of the along-slope penetrations of the Malvinas Current can not be estimated because subantarctic waters are repeatedly advected southward from the study area. The cold waters retreat as fast as they penetrate (5 to 10 days). During the summer of 1989 (January through March), in part of July 1989 and from mid-October to the end of the record (February 1990) subantarctic waters are displaced south of the domain of interest by pulses of warm subtropical waters (Brazil Current). Similar frontal behaviour is observed in Fig. 5b. It is reasonable to associate broadening areas covered by subantarctic waters to northward penetrations of Malvinas Current. Therefore, motions of the front in the eastward direction are related with northward penetrations of the Malvinas Current. According to density distributions and sea surface temperatures (Piola and García, 1993), Malvinas, as a boundary current, flows in a band of about 100 km.

4. SOURCES OF VARIABILITY

Sea surface temperature distributions suggest cyclical displacements of the Currents along the continental slope at semi annual and annual periods, although considerable interannual variability is present in the signal (Olson *et al.*, 1988). Similar frontal motion periods were derived from an array of 3 IES moorings in a zonal section at 38°S, at the same location of the southern leg of the data set presented here (Garzoli and Garraffo, 1989).

The late austral summer situations are very similar in 1989 and 1990. In the austral winter 1989, Malvinas water is observed during all the period except for 15-20 days of July 1989, because subtropical waters were present in the region. This feature, associated with a southward extension of Brazil Current during winter, suggests that seasonality is not the most important source of variability in the area. Unfortunately, the length of the record is too short to resolve annual fluctuations.

The inspection of the 91 T_{500} maps reveals that penetrations of relatively cold waters along the western boundary of the area, occur with penetration of warm waters in the eastern boundary. The enhancement of zonal temperature gradients suggests that instability processes are associated to the increased amplitude of the frontal variability. Thus, pulses in the Malvinas Current along the continental slope are associated to pulses of Brazil Current offshore. In order to further investigate this hypothesis, cross-correlation estimates were made between 5-day block averaged T_{500} time series of the western and eastern IES sites for the three sections (Fig.6).

For lags of 20-30 days, all the cross-correlations are negative and significatively different from 0, with the eastern series lagging behind the western series. Thus, when cold waters reach the western sites, warm water is present offshore 20 to 30 days later. This suggest that a Malvinas northward pulse enhances the baroclinicity of the

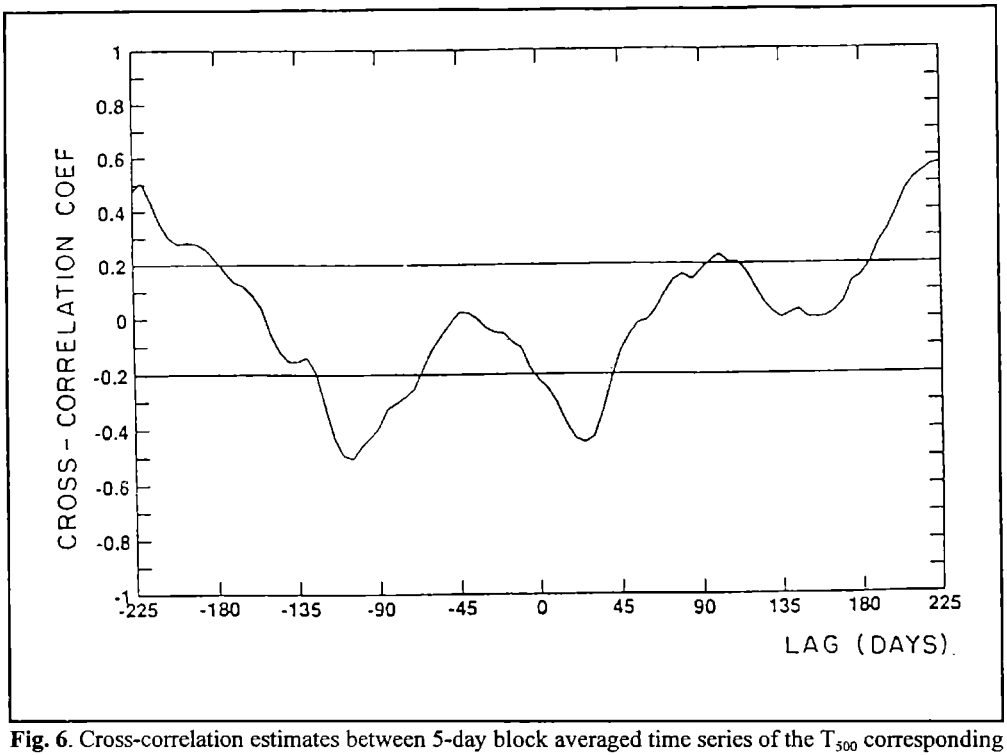

Fig. 6. Cross-correlation estimates between 5-day block averaged time series of the T_{500} corresponding to the IES 1 and 3. The record corresponding to IES 3 is lagging behind the corresponding to IES 1.

geostrophic jet. Significative correlation is also observed at periods centered at -110 days (Fig. 6) for the southern section. There are no significative correlation at this period for the other two sections. This time scale may be associated with the meridional motion of the front location and it is probably only observed in the southern border of the area because during most of the record, the front did not reach the central and northern IES sections.

Garzoli and Giulivi (1994) attempted to explain the observed frontal displacements in terms of the atmospheric forcing. They conclude that the main source of variability of the frontal location is the local wind forcing. In addition to the seasonal cycle in the latitude of separation of the Brazil current from the coast, a marked interannual variability was driven by wind forced pulses south of the Confluence. The "anomalous" northward penetration of the Malvinas Current during November 1988 and the southward extension of the Brazil Current during austral winter 1989 can be explained by these causes.

On the other hands, Gordon (personal communication) suggests that pulses of the

Brazil Current may be tied with eddies detached from the Agulhas Current that are then transported to the northwest. Once in the pathway of the South Atlantic subtropical gyre, the eddies would reinforce the Brazil Current.

Data from Geosat altimeter (Gordon and Haxby, 1990) reveals numerous transient anticyclonic Indian Ocean eddies penetrating into the South Atlantic subtropical gyre. Olson *et al.* (1988) suggested that variations in the Brazil-Malvinas Confluence might be driven by changes in the Malvinas Current forced by variability in the Antarctic Circumpolar Current (ACC). Besides, Campos (1988) suggests that the apparent intensification of Malvinas Current in the western part of the study area associated with southward penetrations of Brazil Current offshore should be related with overshooting of Rossby waves in the Confluence area.

The Brazil Current separation from the coast is determined where it meats the Malvinas Current. The latter could be affected by fluctuations of the ACC at the Drake Passage or by the forcing of winds in the Southern Ocean. Matano (1994) suggested that meridional migrations of the Subtropical Convergence, which are tightly associated with the North-South displacements of the Brazil-Malvinas Confluence, could control the thermohaline properties of the Atlantic Ocean. However, Garzoli and Giulivi (1994) did not observe a significant correlation between wind-forced pulses in the ACC and anomalous northward penetration of the Malvinas Current. Simultaneous monitoring of the variability in both regions (ACC and Brazil-Malvinas Confluence) is necessary to further understand this process.

5. SUMMARY AND CONCLUSIONS

It has been showed that the original method implemented to calibrate IES TT records in terms of T_{500} is an useful tool to monitor the evolution of the variability of the ocean upper layer in a frontal region. The main features of the mean upper ocean thermal field during the record period are evident in the different kind of representations used in this study.

In most cases, T_{500} maps are in good agreement with the satellite imagery showing sea surface temperature (excluding some mesoscale features that could not be resolved by images that represent the skin temperature of the ocean). Estimates of cross-front horizontal gradients derived from T_{500} maps are confirmed by hydrography data.

Northward penetrations of the Malvinas Current or southward extensions of the Brazil Current are also clearly observed. Mean front displacement velocities and the duration of currents penetrations are obtained from time series inspections. In other words, this study allows to have a first order approximation to space and time range scales of frontal motion. Cross-correlation analysis of time series showed that when Malvinas cold waters reach the IES western sites of the array, warm water appears 20/30

days after in the eastern sites. This fact induces an enhancement of horizontal temperature gradients and reinforce the baroclinicity of the frontal geostrophic jet.

This study has shown that the strong variability of the Brazil- Malvinas System is not dominated by the annual or semi-annual cycle. The larger component of the observed variability in the time-frame covered by the IES array is forced by local winds as was shown by Garzoli and Giulivi (1994) in a companion paper. Probably, the intense cross-frontal mixing processes in the area (Bianchi *et al.*, 1993) are important in the relaxation and dissipation of the front after it has been intensified by horizontal advection. This hypothesis is matter of study of ongoing research in the region (Piola & Bianchi, 1992).

Acknowledgements

The authors are indebted to the crews on board BOARA Puerto Deseado, BIP Oca Balda and R/V Le Suroit, for different stages of field work. To the authorities of Servicio de Hidrografía Naval (SIHN) and Instituto de Investigación y Desarrollo Pesquero(INIDEP) from Argentina, for their support during the preparation and logistics of the cruises. To the government of Uruguay who granted permission to work in territorial waters. To Alberto Piola for his careful reading and useful comments on the manuscript. D. Olson, G. Podestá and O. Brown kindly provided the processed images for the present study. M. Charo and A. P. Osiroff were responsible of hydrographic data processing. M. Macció was in charge of the IES from preparation for deployment to recovery. He was assisted during the cruises by M. Ferrario. The IES data processing and computer programming was performed by A. Martino. Silvia Damiani prepared the final figures. The field work was supported by NSF through grant OCE-87-11529, by SIHN and CNRS (French National Research Council). Data collection and analysis were partially supported by NSF grants OCE-87-11529 and OCE-91-02541. The satellite images were collected by the Servicio Meteorológico Nacional (SMN) of Argentina and processed at the University of Miami under NSF grant OCE-91-02112. A grant from the TINKER Foundation, a grant of the International Division of the NSF, INT-89-14536, and Consejo Nacional de Investigaciones Científicas y Técnicas, supported part of the cooperative work between the authors.

REFERENCES

Bianchi, A. A., C. F. Giulivi and A. R. Piola. Mixing in the Brazil/Malvinas Confluence. Deep-Sea Research I, 40, pp 1345-1358, 1993.

Brennecke, W. Die ozeanographischen Arbeiten del Deutschen Antarktischen Expedition, 1911-1912. Aus dem Archiv der Deutschen seewarte. 39:1, 216 pp,1921.

Campos, E.J. D. Stationary Rossby waves in the western boundary current extensions. Doctoral dissertation, University of Miami, 115 pp, 1988.

Charo M., A. P. Osiroff, A. A. Bianchi and A. R. Piola. Datos Físico-Químicos, CTD y XBT. Campañas Oceanográficas: Puerto Deseado 02-88, Confluencia 88 y Confluencia 89. Informe Técnico N° 59/91. Servicio de Hidrografía Naval, 450 pp, 1991.

Cheney, R. E., J. G Marsh and B. D. Beckley . Global mesoscale variability from collinear tracks of Seasat altimeter data. Journal of Geophysical Research, 88, pp 4343-4354, 1983.

Confluence Principal Investigators. Confluence 1988-1990. An Intensive Study of the Southwestern Atlantic. EOS, Transactions, American Geophysical Union, 71, No 41, pp 1131-1133 and 1137, 1990.

Deacon, G.E.R. A General Account of the Hydrology of the South Atlantic Ocean. Discovery Reports, 7, 171-238, 1933.

Deacon, G.E.R. The Hydrology of the Southern Ocean. Discovery Reports, 15, 1-124, 1937

Figueroa, H. A. and D. B. Olson. Lagrangian statistics in the South Atlantic as derived from SOS and FGGE drifters. Journal of Geophysical Research, 47, 525-546, 1989.

Garzoli, S. L. Geostrophic Velocity and Transport Variability in the Brasil/Malvinas Confluence. Deep-Sea Research, 40, 1379-1404 , 1993.

Garzoli, S. L. and A. A. Bianchi (1987). Time-space variability of the local dynamics of the Brazil-Malvinas Confluence as revealed by inverted echo sounders. Journal of Geophysical Research, 92, 1914-1922.

Garzoli, S.L. and Z. Garraffo. Transports, Frontal Motions and Eddies at the Brazil-Malvinas Confluence. Deep-Sea Research, 37, 1053-1074, 1989.

Garzoli, S.L. and C. F. Giulivi. What Forces the Variability of the South Western Atlantic Boundary Currents? Deep-Sea Research, 41, 1527-1550, 1994.

Gordon, A. L. South Atlantic Thermocline Ventilation. Deep-Sea Research, 28, 1239-1264, 1981.

Gordon A. L. Brazil-Malvinas Confluence-1984. Deep-Sea Research, 36, 359-384, 1989.

Gordon A.L. and C. L. Greengrove. Geostrophic Circulation of the Brazil-Falkland Confluence. Deep-Sea Research, 33, 573- 585, 1986.

Gordon, A.L. and W. Haxby. Agulhas Eddies Invade the South Atlantic: Evidence from GEOSAT Altimeter and Shipboard Conductivity-Temperature-Depth Survey. Journal of Geophysical Research, 95, 3117-3125, 1990.

Legeckis, R. and A. Gordon. Satellite observations of the Brazil and Falkland Currents 1975 to 1976 and 1978. Deep-Sea Research, 29, 375-401, 1982.

Matano, R. P., M. G. Schlax and D. Chelton. Seasonal Variability in the Southwestern Atlantic. Journal of Geophysical Research, Journal of Geophysical Research 98, 18027-18036, 1993.

Olson, D., G. Podestá, R. H. Evans and O. Brown. Temporal variations in the separation of Brazil and Malvinas Currents. Deep-Sea Research, 35, 1971-1990, 1988.

Piola, A. R. y Bianchi, A. A. AR8: Southwest Atlantic Boundary Currents, WOCE Newsletter 12, International Project Office at Natural Environmental Research Council, IOS, Deacon Lab., pp 14-16, 1992.

Piola, A. R., H. A. Figueroa and A. A. Bianchi. Some aspects of the surface circulation South of 20° S revealed by First GARP Global Experiment Drifters. Journal of Geophysical Research, 92, 5101-5114, 1987.

Piola, A. R. and O.A. García. Atlas oceanográfico de la Cuenca Argentina Occidental y Plataforma Continental lindera. Servicio de Hidrografía Naval, Buenos Aires, 1993, 246 pp.

Reid J. L., W. D. Nowlin Jr. and W. C. Patzert. On the characteristics and circulation of the Southwestern Atlantic Ocean. Journal of Physical Oceanography, 7, 62-91, 1977.

Roden, G. I. Thermohaline fronts and baroclinic flow in the Argentine Basin during the Austral Spring of 1984. Journal of Geophysical Research, 91, 5075-5093, 1986.
Smith, W. H. F. and P. Wessell. Giddying with continuous curvature splines in tension. Geophysics, 55, No. 3, pp 293-305, 1990.
Sverdrup, H. U., M. W. Johnson and R. H. Fleming (1942). The Oceans. Their Physics, Chemistry and General Biology, Prentice Hall, Englewood Cliffs, New Jersey, 1087pp.
Zlotnicki, V. L. L. Fu. Seasonal Variability in Global Sea level Observed with Geosat Altimetry. Journal of Geophysical Research, 94, 17959-17971, 1990.

GEOACTA, 22, 91-102,1997

THE ANDEAN ELEVATION IN ARGENTINA-CHILE AT 39° SOUTH LATITUDE FROM GRAVITY DATA

María Cristina Pacino
Instituto de Física Rosario (IFIR), Fac. de Cs Ex., Ingeniería y Agrimensura
Univ. Nac. de Rosario, Av. Pellegrini 250, (2000) Rosario, Argentina

ABSTRACT

In this paper, we analyze an E-W gravity section at 39° South latitude. It extends from the western Chilean trench, across the Andean belt, into Argentina, and reaches the Atlantic Ocean. The minimum Bouguer anomalies, in the order of -90 mGal, are located in coincidence with the maximum Andean altitudes, while the largest values, of about +230 mGal, are located offshore, in the Pacific Ocean.

We present simple crustal models, among others considering the possible gravity influence of the subduction system Nazca Plate - Southamerican Plate. Isostatic models that combine the Airy and Pratt's hypothesis are also detailed. Orogenic Shortenings were also calculated by using the topographic areas above the sea level and the crustal root below the assumed "normal" crustal thickness for different models.

RESUMEN

En este trabajo se analiza una sección gravimétrica Este-Oeste, centrada aproximadamente en 39° de latitud Sur, que se extiende desde la fosa Chilena hasta el Océano Atlántico atravesando el cinturón Andino. Las mínimas anomalías de Bouguer, del orden de -90 mGal, se ubican en coincidencia con las máximas altitudes andinas, mientras que los valores máximos, de unos +230 mGal, se hallan costa afuera, en el Océano Pacífico.

Se analizan modelos de corteza simple considerando la posible influencia del sistema de subducción Placa de Nazca - Placa Sudamericana y se presentan también modelos isostáticos que combinan las hipótesis de Airy y Pratt. Se calcularon valores de acortamiento con expresiones que involucran las áreas emergidas y las raíces corticales debajo del espesor cortical asumido como normal en los diferentes modelos.

1. INTRODUCTION

The analysed section is referred to a previous study at this latitude (Diez Rodriguez and Introcaso, 1986), incorporating gravity anomalies both in the Pacific and Atlantic ocean sectors and altimetric satellital data (Fig. 1).

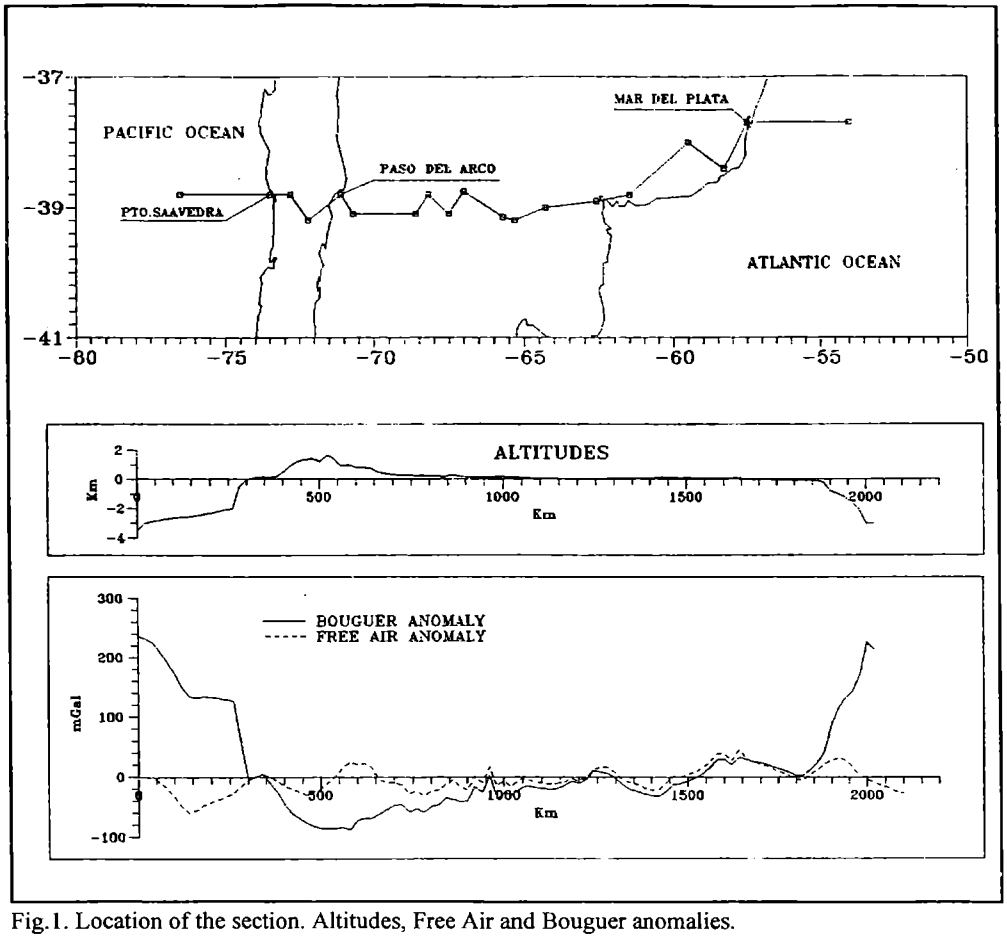

Fig.1. Location of the section. Altitudes, Free Air and Bouguer anomalies.

The continental section crosses several geological provinces in Argentina and Chile: Cordillera de la Costa, Central Valley of Chile, Cordillera de los Andes, Neuquén Basin, northwestern section of the Colorado Basin, Interserrana Bonaerense Basin and the southern border of Tandilia.

According to previous studies, we could obtain the following crustal characteristics: thicknesses and isostatic equilibrium. Moreover, from this gravity study, as well as from previous works (Introcaso and Pacino, 1988; Pacino and Introcaso, 1989), we have found that the wavelength and amplitude of regional Bouguer anomalies beneath the Andean chain, are principally controlled by crustal roots. With the areas of this crustal root, we also calculated Orogenic Shortenings. These shortenings require significant compressive

stresses to explain the Andean uplift.

According to Chinn and Isacks (1983), depths of shallow earthquakes in the eastern Andes of South America range between 9 and 36 km, indicating that both the upper and middle crust are seismically active; about 75% of the events occurred in the upper 25 km. Furthermore, the focal mechanisms indicate that the crust of the eastern side of the Andean Cordillera is in a state of east-west compression oriented nearly parallel to the direction of convergence between the Nazca and South American plates. The depths, the orientations of the earthquake nodal planes, and the close relationships to Quaternary tectonics imply basement - involved crustal shortening.

Furthermore, Froidevaux and Ricard (1987) pointed out that south of 27° South (or north of 14° South), the entire Andean Belt is in compression. We will see later that this state of compression is required to justify the shortenings proposed for the Andes at this latitude.

2. DATA BASES USED

The gravity profile analysed was based on the following measurements and data base:

- In Argentina, altitudes and gravity values were obtained from the Instituto Geográfico Militar (I.G.M.). They used La Coste and Romberg G 145 and G 146 gravimeters, which were checked at the "Gravimeter Control Line" of Santa Fe. The maximum mean-square error of one isolated observation was ±0.02 mGal. The gravity values were corrected for tidal effects. The mean-square error of single observations was ±0.02 mGal to ±0.03 mGal. The altitudes of stations were obtained using high precision levelling (1 mm/km).
- In the continental Chilean sector we used altimetric and gravity data from Dragicevic (1970). These values were obtained from Departamento de Geofísica y Geodesia (Universidad de Chile) and Empresa Nacional de Petròleo (Chile), operating both with Worden gravimeters. The errors CIERRE in the gravity circuits were in the order of 0.2 to 0.3 mGal for 2 to 3 hours periods. The gravity values were corrected for tidal effects. The altitudes and location of stations were mainly obtained by means of taquimetric polygonal.
- In both, the Pacific and Atlantic Oceans, depths' data from DBDB5 satellital file and Free Air anomalies from Bowin et al. (1981) were used. Free Air anomalies and ocean depths' values were compared with data from Fisher and Raitt (1962), Hayes (1966), Scholl et al. (1970), and Woollard and Daugherty (1970).

All gravity values are in the IGSN-1971 System. The fundamental gravity values for Argentina and Chile are: 979690.03 mGal (Miguelete, Buenos Aires) and 979416.70 mGal (Santiago, Div. de Geofísica, Universidad de Chile), respectively. The gravity networks of Argentina and Chile are connected from modern measurements by air-tie

repeated measurements between Mendoza Airport and Santiago Airport. New gravity values in IGSN-1971 are: 979217.2±0.019 mGal and 979444.1±0.015 mGal, respectively (Becker et al., 1986). The profile, which exceeds 2000 km length, shows minimum Bouguer anomalies of about -90 mGal in coincidence with the largest Andean altitudes, while maximum values of +230 mGal are located offshore, in the Pacific Ocean (Fig. 1).

3. CALCULATION OF GRAVITY ANOMALIES

In the continental sector, the anomalies were calculated by using the classical expressions:

$FAA = Go - Gt + FAC$

$BA = G0 - Gt + FAC - BC$

where:

FAA: Free Air Anomaly

BA: Bouguer Anomaly

Go: Observed value related to Miguelete's fundamental value (979690.03 mGal)

Gt: Theoretic value (1971 System)

FAC: Free Air Correction

$FAC = (0.30855 + 0.00022 \cos 2\Phi)\, h - 0.072\, (h/1000) \cos \Phi$

With Φ: latitude and h: height in meters

BC: Simple Bouguer Correction

$BC = 0.0419\, \sigma\, h$

With σ= 2.67 g/cm3 and h: height in meters a.s.l.

Bowin et al. (1981) pointed out that free-air anomalies at sea and Bouguer anomalies inland present different features. Therefore, in preparing the gravimetric models, free-air anomalies were transformed into Bouguer anomalies by replacing the sea water (σ=1.03 g/cm3) by materials of 2.9 g/cm3 density, which is the assumed crustal density (Introcaso et al., 1992; Introcaso and Pacino, 1988).

4. ISOSTATIC BEHAVIOUR

The isostatic balance of the section was analysed in two ways: (a) by means of a thickened crust in the Airy concept (Fig. 2A) and (b) by means of a thermal root in the upper mantle, according to Pratt's hypothesis (Fig. 2B). The isostatic anomalies in the Airy concept were calculated by defining 2D "roots" beneath a normal crust (T = 33 km) in the Andes and foreland, and 2D "antiroots" in the oceanic sectors, based on the well-known expressions:

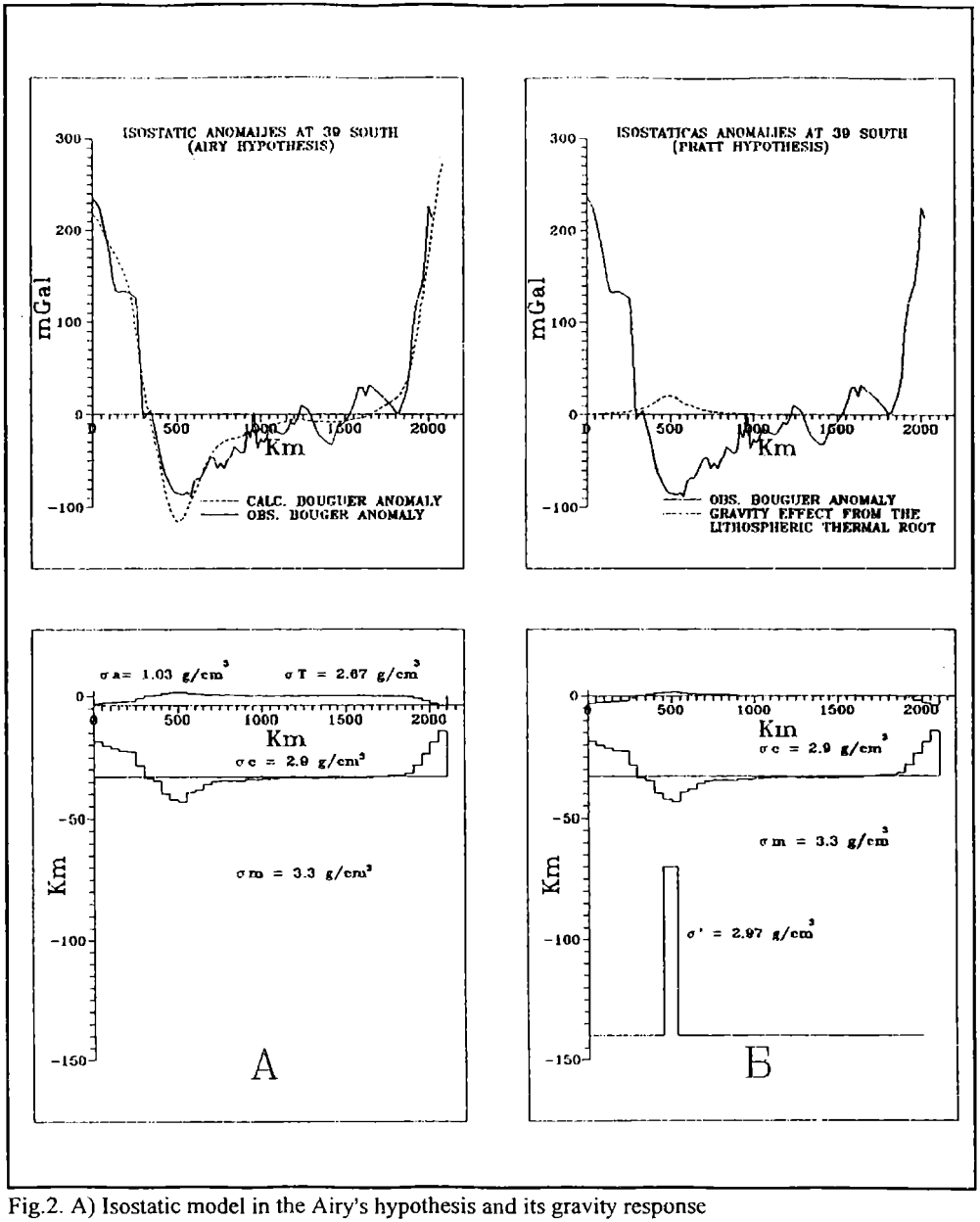

Fig.2. A) Isostatic model in the Airy's hypothesis and its gravity response
B) Isostatic model in the Pratt's hypothesis and its gravity response

$$\Delta R = \frac{\sigma c \, h}{\Delta \sigma}$$

and

$$\Delta R' = \frac{\sigma c - \sigma a}{\Delta \sigma} ha$$

(See Woollard (1969) among many others). With:

Δ R: "root" beneath the normal bottom of the crust

Δ R': "antiroot" above the normal bottom of the crust

σ c: exposed crustal density (2.67 g/cm3)

$\Delta \sigma$: density contrast between lower crust and upper mantle (-0.4 g/cm3)

h: mean altitudes from the averaged topography in 50 km wide E-W segments

ha: mean ocean depths from the averaged depths in 50 km wide E-W segments

The -0.4 g/cm3 value adopted as density difference between the crust and the upper mantle replaces, as an average value, the values proposed by other investigators (Talwani et al., 1959; Grow and Bowin, 1975; Woollard, 1969; Dragicevic, 1970). Based on previous works (Bullen, 1963; Woollard, 1969; Introcaso and Pacino, 1988; among others) we adopted T=33 km as normal crustal thickness. Furthermore, Andean gravity-seismic models at other latitudes (Introcaso and Pacino, 1988; Introcaso et al., 1992) confirm this assumption. It is convenient to point out that Woollard (1969) states that the model adopted is not critical in evaluating isostasy.

On the other hand, to locate the "thermal lithospheric root," we used as a reference, the top of the subducted Nazca Plate. Part of this surface, with constant dip of 25° located between nearly 70 and 140 km depths (Froidevaux and Isacks, 1984; Isacks, 1988), defines the slope of both flanks of the hot anomalous body. Its longitudinal extension, from 33°S to 50°S is quite coincident with the distribution of Quaternary volcanism, and its width (80 km), uniform from top to bottom, corresponds to the strip of highest altitudes. A deficit of density $\Delta\sigma' = 0.03$ g/cm3 was assumed, according to Introcaso et al.(1995, unpublished).

The results suggest that the studied section essentially respond to an Airy's isostatic model, with little positive and negative anomalies that, in a great part, could be justified locally considering inhomogeneities in the upper crust in the different crossed geological provinces. The model with a lithospheric thermal root gives no more than 20 mGal in its maximum and has a short longitudinal extension, but it must be considered attending to the important manifestations of active volcanism south of 33° South latitude and the detected heat flows (Muñoz et al., 1990).

5. GRAVITY MODELS

It has been analysed the possible gravimetric influence from the subducted plate, a wedge of asthenospheric materials between the Nazca and Southamerican plates, two "roots" in the intermediate and lower crust in the continental sector and "antiroots" in the lower crust in both oceans. In this way, a simple one-layer crustal model shows maximum depth for the continental crust of about 43 km. This value could vary in no more than 10% incorporating the other referred gravity effects. Thus, as a simplification, a one layer crustal model is shown in Fig. 3 together with its gravity response and the observed gravity data.

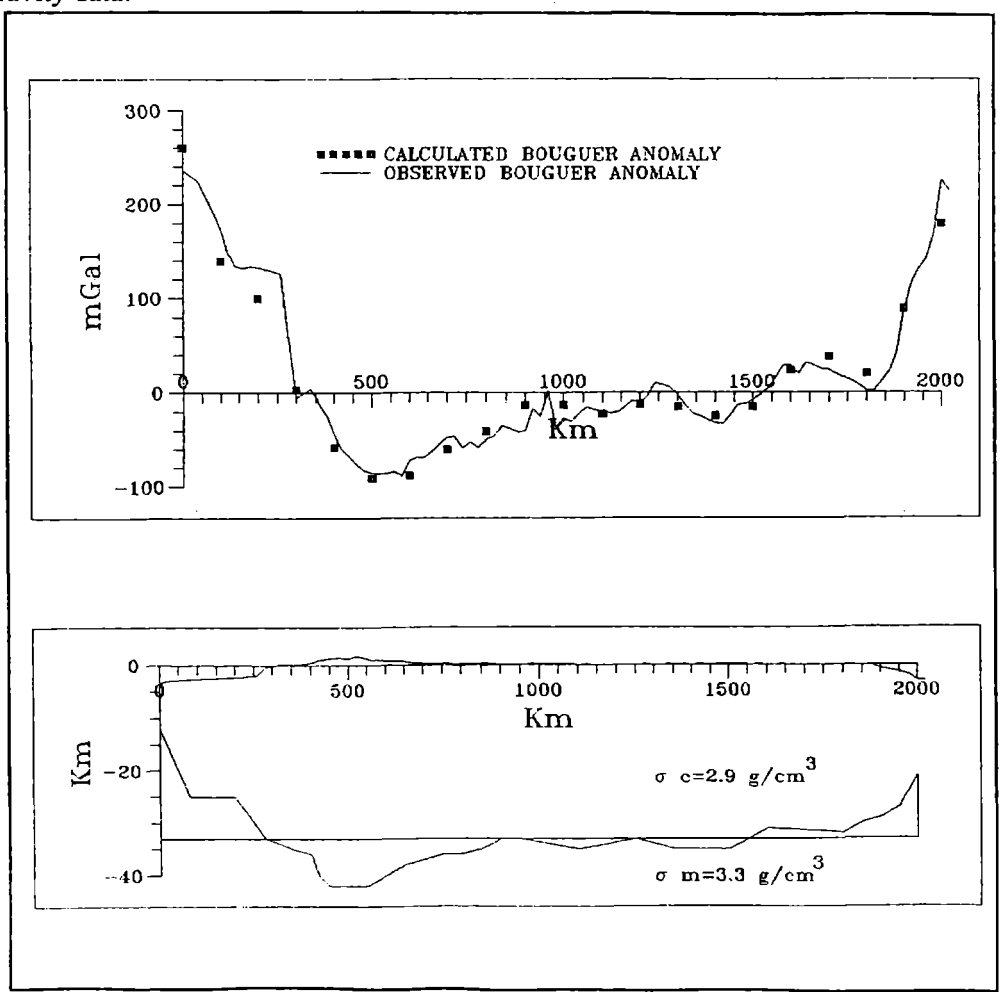

Fig. 3. One layer crustal model and its gravity response.

The regional anomaly was obtained using the filtering method proposed by Pacino and Introcaso (1987). In this method, the observed Bouguer anomalies are continued to different elevations until short wavelengths disappear. Then, they are inverted from there (for example with Talwani et al.'s (1959) method) to obtain the model. Finally, from the model so defined, the direct method calculated the gravity at the topographic level. This gravity must conform to a suitable regional anomaly when it is compared with the observed anomaly.

The residual anomaly from the difference between the observed and calculated Bouguer anomaly, which have been studied by several investigators, could not be due to grow or decreasing of the crustal thickness. In this way, the positive residual anomaly in the Pacific Ocean at different latitudes has been entailed to differences in density and phase changes in the upper part of the subducted Nazca plate (Grow and Bowin, 1975; Introcaso and Pacino, 1988; Pacino and Introcaso, 1989). The negative residual anomaly in the Chilean sector, in the order of -20 mGal, has been interpreted by Dragicevic et al. (1970) as local and superficial anomalies. A similar interpretation was given by Diez Rodriguez and Introcaso (1986) for the negative residual anomaly at the Neuquen basin.

In the northwestern sector of the Colorado basin we can see a positive residual anomaly of about +30 mGal. It could be justified through the addition of asthenospheric materials in high lithospheric levels, according to Introcaso and Ramos (1984), who gave this interpretation for the Salado basin, northwards of Buenos Aires province with wide recognized similarities.

At the Interserrana Bonaerense basin, we found a residual anomaly of about -30 mGal that could be justified by means of a -0.07 g/cm3 density contrast between the Paleozoic sediments and the crystalline basement (Diez Rodriguez and Introcaso, 1986), according to the seismic waves velocity pointed out by Zambrano (1972). Finally, we found a positive residual anomaly at Tandilia, near the Atlantic Ocean. These ranges, with low altitudes, represent the oldest basement in Argentina. The positive anomaly there could be entailed to the uppermost part of the structure (Introcaso, 1982), since the mass' excess would be supported by a crust without modifying its thickness.

Again, and according to the results obtained in previous studies for different Andean sections (Introcaso and Pacino, 1988; Pacino and Introcaso, 1989), it was proved that the observed Bouguer anomaly is mainly controlled by the Mohorovicic discontinuity and the subcrustal gravimetric effects are smaller than was supposed, or they cancel each other out.

6. SHORTENINGS

It has been previously proposed that the build-up of the Central Andes was partially or almost totally caused by orogenic shortenings (Suarez et al., 1983; Isacks, 1988;

Introcaso et al., 1992). Thus, values of orogenic shortening were calculated from the topographic areas above the sea level, and the areas of crustal roots beneath the assumed "normal" crustal thickness obtained from different models.

Following Isacks (1988) and assuming isostatic equilibrium, the shortening value found at 39° S is 66 km. On the other hand, considering the "root" from the inversion of gravity data and according to Introcaso et al. (1992), the shortening value reaches 72 km. It is well known that the magmatic activity in coincidence with the main altitudes beneath the Central Andes would support the idea of a thermal root (Froidevaux and Isacks, 1984), although a thermal anomaly may justify only a part of a mountain build up (Froidevaux and Ricard, 1988).

There exists consents in affirming that shortening would be the principle responsible of the Andean elevations, although it could also be explained by the proper combination of other mechanisms (Isacks, 1988; Introcaso et al., 1992). South of 33° South latitude, similar conditions -but of less signification- like those between 13° and 27° South latitudes are also present. We can mention the heat flow detected by Muñoz (1987, 1991) and Muñoz et al. (1990) and the important occurrences of active volcanism pointed out by Casertano (1963), Barazangi and Isacks (1976), Jensen (1984), Hickey et al. (1989), among many others. Furthermore, the Nazca Plate, with a flat - subduction style in the segment between 27°S and 33°S latitudes, deeps again 25°-30° in the southern segment, similar to the Central Andes segment. Based on that, it is reasonable to assume a similar mechanism of vertical uplift acting south of 33°S latitude.

Thus, we considered the present Andean altitudes in the study section as produced by both mechanisms, lithospheric heating and crustal shortening. Assuming that the lithospheric heating could cause a maximum elevation of 0.64 km (Introcaso, 1993), and considering then a ductile distribution for this mass upon the 300 km width of the Neuquén Cordillera, we found that only 0.17 km of the present altitudes could be due to thermal uplift.

Considering both mechanisms acting together, the compressive shortening and the lithospheric heating, the gravity model in Fig. 4 was obtained. In this model, the observed Bouguer anomaly is justified by a crustal thickening reaching a maximum depth of about 41 km (instead of the 43 km maximum depth obtained for the Moho discontinuity in the simple one layer gravity model of Fig. 3), and in a minor part by the lithospheric thermal root.

7. CONCLUSIONS

A preliminary isostatic analysis would suggest that the section essentially responds to an Airy´s isostatic model showing, as a whole, a reasonable isostatic equilibrium. From gravity data, the maximum thickness for the continental crust at 39° South latitude was

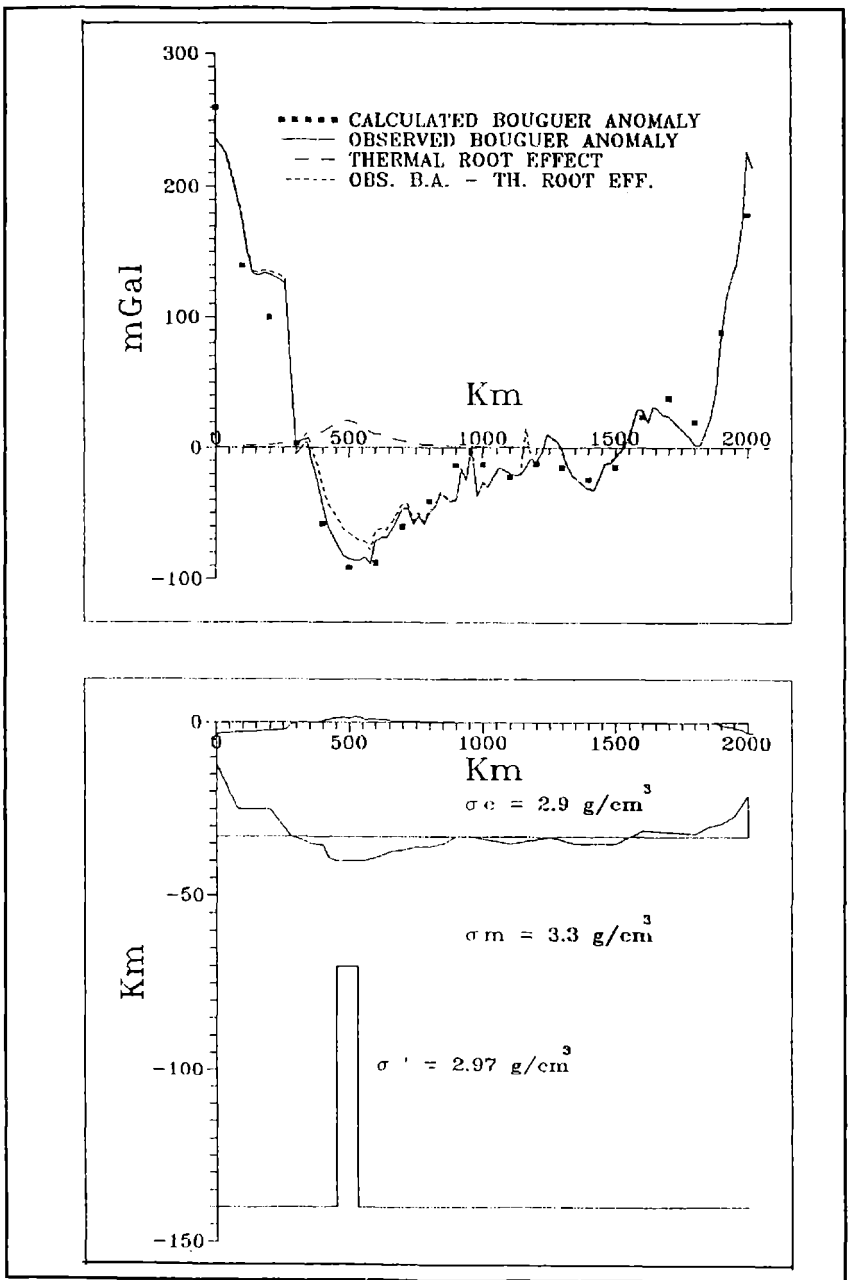

Fig.4. Crust and upper mantle model which justifies the observed Bouguer anomaly by means of a crustal thickening and a thermal lithospheric root.

located beneath the Andean axes, at 43 km depth, while the minimum thickness for the ocean crust at that latitude, with 12 km depth, would be located 300 km offshore, in the Pacific ocean. Considering lithospheric heating to partially explain the Andean uplift, combined with compressive shortening, the maximum crustal depth would be diminished in about 2 km with respect to the one layer crustal model. Bouguer anomalies could be then justified by both, crustal thickening and a lithospheric thermal root. The calculated orogenic shortening for all the crustal models is in the order of 70 km.

Acknowledgements.

This work was partially supported by CONICET (Consejo Nacional de Investigaciones Científicas y Técnicas de Argentina -Grant: PID-BID 214) and by Facultad de Ciencias Exactas, Ingeniería y Agrimensura (U.N.R.): Res 239/92.

REFERENCES

Barazangi, M. and Isacks, B. L., 1976. Spatial distribution of earthquakes and subduction of the Nazca Plate beneath South America. Geology, 4: 686-692.

Becker, M., Gao, X. M., and Groten, E., 1986. First results of precise gravity measurements on the A-B-C profile. Tectonophys., 130: 33-47.

Bowin, C., Warsi, W. and Milligan, J., 1981. Free Air Gravity Anomaly Atlas of the World. Woods Hole Oceanographic Institution, 38 pp.

Bullen, K. E., 1963. An introduction to the theory of seismology (Third Ed.). Cambridge University Press, 381 pp.

Casertano, L., 1963. Catalogue of the active volcanoes and solfatara fields of the Chilean continent. Catalogue of the active volcanoes of the world including solfatara fields. International Volcanological Association, Part XV: 55 pp.

Chinn, D. S. and Isacks, B. L., 1983. Accurate source depths and focal mechanisms of shallow earthquakes in western South America and in the New Hebrides island arc. Tectonics, 2 (6): 529-563.

Diez Rodriguez, A. and Introcaso, A., 1986. Perfil transcontinental sudamericano en el paralelo 39° S. Geoacta, 13 (2): 179-201.

Dragicevic, M., 1970. Carta gravimétrica de los Andes Meridiona-les e interpretación de las anomalías de gravedad en Chile Central. Publ. de la Universidad Nacional de Chile, 42 pp.

Fisher, R. L. and Raitt, R. W., 1962. Topography and structure of the Perú - Chile trench. Deep-sea Res., 9: 423-443.

Introcaso, A., 1991. El comportamiento isostático de los Andes Argentino - Chilenos. II Congr. Soc. Bras. de Geof., Actas I: 160-164.

Introcaso, A., 1993. Anomalous upper mantle beneath the Central Andes. Isostasy and Andean uplift. Actas II International Symposium on Andean Geodynamics (Oxford): 13-16.

Introcaso, A. and Pacino, M. C., 1988. Gravity Andean Model Associated with Subduction near

24° 25´ South Latitude. Rev. Geofis., 44: 29-44.
Introcaso, A., Pacino, M. C. and Fraga, H., 1992. Gravity, Isostasy and Andean Crustal Shortening Between Latitudes 30° and 35° S. Tectonophys., 204: 31-48.
Introcaso, A. and Ramos, V., 1984. La cuenca del Salado: un modelo de evolución aulacogénica. IX Congr. Geol. Arg., Actas III: 27-46.
Isacks, B. L., 1988. Uplift of the Central Andean Plateau and Bending of the Bolivian Orocline. J. Geophys. Res., 93 (B4): 3211-3231.
Jensen, O. L., 1984. Andean tectonics related to geometry of subducted Nazca Plate: Discussion and reply. Geol. Soc. of Am. Bull., 95: 877-880.
Muñoz, M., Fournier, H., MamanI, M., Febrer, J., Borzotta, E. and Maidana, A., 1990. A comparative study of results obtained in magnetotelluric deep soundings in Villarrica active volcano zone (Chile) with gravity investigations, distribution of earthquake foci, heat flow empirical relationships, isotopic geochemistry Sr/Sr and SB systematics. Phys. of the Earth and Planet. Interiors, 60: 195-211.
Pacino, M. C. and introcaso, A., 1987. Regional Anomaly Determina-tion using the upwards-continuation method. Bull. Geofis. Teór. ed Appl., XXIX (114): 113-122.
Pacino, M. C. and Introcaso, A., 1989. Modelo gravimétrico sobre el sistema de subducción Placa de Nazca - Placa Sudamericana en la latitud 33° Sur. V Congr. Geol. Chileno, Actas II: F77-F90.
Scholl, D., Christensen, M., Von Huene, R. and Marlow, M., 1970. Perú - Chile trench sediments and sea-floor spreading. Geol. Soc. of Am. Bull., 81: 1339-1360.
Talwani, M., Worzel, J. L. and Landisman, M., 1959. Rapid gravity computations for two dimensional bodies with application to the Mendocino Submarine fracture zone. J. Geophys. Res., 64 (11): 49-58.
Woollard, G. P., 1969. Regional variations in gravity. In: The Earth´s Crust and Upper Mantle. Pembroke J. Hart Edit. Geophys. Monogr., A.G.U., 13: 320-341.
Woollard, G. P. and Daugherty, K. I., 1970. Collection processing and geophysical analysis of gravity and magnetic data: Gravity gradients associated with sea-floor topography. Aeronautical Chart and Information Center U.S.A.F., 269 pp.
Zambrano, J., 1972. Las cuencas sedimentarias en la plataforma continental argentina. Petrotécnica, XXI (4): 26-37.

GEOACTA, 22, 103-121, 1997

SPECTRAL DECOMPOSITION OF A LONG ROSSBY WAVE AFTER REFLECTION ON AN EQUATORIAL WESTERN BOUNDARY

Alejandro Camerlengo and Mónica Ines Demmler
Faculty of Marine Sciences, Universiti Pertanian Malaysia Terengganu
Mengabang Telipot, 21030 Kuala Terengganu, Malaysia

ABSTRACT

This study addresses the evolution of a single Rossby wave in the wavenumber space. Due to its simplicity, as compared to the reflection at the equatorial eastern boundary, the analytical and numerical problem of the reflection of the long Rossby wave at the western boundary is chosen. The main results of this investigation are:
1) the solution in the wavenumber space is similar to the one in the original wave pattern field, although their physical interpretation is completely different;
2) the interpretation of the spectrum is fairly more simple than the analysis of the original wave pattern field.

RESUMEN

Este trabajo estudia la evolución de una onda de Rossby en el espacio del nu'mero de onda. La reflexión de ondas en la frontera oeste es mucho más sencilla de tratar que la reflexión en la frontera este. Por lo tanto, se consideran las soluciones analíticas como numéricas de la reflexión de una onda larga de Rossby en la frontera oeste ecuatorial. Los resultados más significativos de esta investigación son:
1) la solución en el espacio del nu'mero de onda es similar a la solución en el espacio de ondas original. No obstante, la interpretación física de las soluciones es radicalmente diferente,
2) la interpretación en el campo espectral es mucho más sencilla que el ana'lisis del campo de ondas en el espacio original.

1. INTRODUCTION

Spectral decomposition is particularly useful in wave problems. If a given wave field is characterized by several wave patterns, it is difficult to analyze a particular wave pattern alone. By contrast, in the wavenumber space, a wave is represented by a single point and the presence of simultaneous waves can be easily detected. Therefore, the study of a wave pattern by means of spectral decomposition represents a powerful tool, useful to analyze conditions whenever several waves are interacting among themselves. For this reason, the study of the reflection-diffraction process of waves is chosen. Our particular

concern is the mechanism by which one single wave may generate others.

The aim of this investigation is to study the time-evolution of an initial wave pattern in the wavenumber space. This study represents the first of such an attempt. An analytical study is made to predict the numerical results. Several numerical models of equatorial basin are available. The model of Camerlengo & O' Brien (1980) is selected to illustrate reflection effects on the flow pattern and the spectrum, at a meridional boundary.

The group velocity may be defined as C_g = d (frequency) / d (wavenumber). The frequency is represented by $\tilde{\omega}$. Due to the particular nondimension used in Camerlengo and O' Brien (1980), the wavenumber is represented by α m, where α is the horizontal aspect ratio. According to Pedlosky (1979) and Moore & Philander (1977), it follows that:

$$\partial E / \partial t + C_g \partial E / \partial x = 0, \qquad (1)$$

where E represents the energy density. Therefore, the group velocity represents the speed at which the wave energy propagates. In Figure 1, the group velocity is represented by the slope of the curves.

Moore (1968) analyzed the complexity of the reflection of equatorial waves at the eastern boundary. The reflection, at the eastern boundary, of an incoming Kelvin wave, depends on the frequency. If the frequency is greater than 1.755, the reflected field consists both of a finite number, Z, of inertia gravity waves, with real wavenumber, and an infinite number of modes p > Z (where p represents the reflected wave mode), with complex wavenumber. The latter case represents a coastally trapped Kelvin wave front, moving in a poleward direction, along the eastern boundary (Cane and Sarachik, 1976). The number Z is given by:

$$Z = \text{integer}\ \{\tilde{\omega}^2 + 1/(2\tilde{\omega})^2 - 1\}/2 + 1 \qquad (2)$$

On the other hand, if the frequency of the incoming Kelvin wave is lesser than 0.288 (the maximun frequency for Rossby waves), the reflected field consists both of a finite number , Z, of westward group velocity long Rossby waves, and an infinite number p > Z (with complex wavenumber) of coastally trapped Kelvin waves, travelling in a poleward direction, along the eastern boundary (Clarke, 1983). The Rossby radius of deformation is proportional y^{-1} . Its width decreases with latitude. The amplitude of the coastal Kelvin wave is proportional to $y^{1/2}$. Thus, the amplitude of the coastally trapped Kelvin wave increases with increasing latitude. A poleward loss of energy follows quite naturally (Clarke, 1983; Moore, 1968).

The long Rossby wave has a westward phase speed of C/(2p + 1), where C represents the phase speed of the Kelvin wave. The most rapid Rossby wave travels at 1/3 the speed of the Kelvin wave, at approximately 50 cms/sec. Therefore, the Rossby wave tends to

travel faster closer to the Equator (Philander, 1990).

If the frequency of the incoming Kelvin wave is in the range between 0,288 and 1.755, there will be no equatorial waves reflected at the eastern boundary. Such a frequency corresponds to a time period ranging from a week to a month (Fig. 1).

The reflection at the eastern boundary of an incoming eastward group velocity inertia gravity wave consists of a finite number of westward group velocity inertia gravity waves p = P, P + 1, P + 2, P - Z + 1 (where P represents the incoming wave mode), and an infinite number of modes p > Z, trapped along the eastern boundary.

On the other hand, the reflection process at the western boundary is fairly simple. Assume an incoming westward group velocity Rossby (eastward group velocity inertia gravity) wave. The reflection process at the western boundary consists of a finite number of short wavelength eastward group velocity Rossby (short wavelength westward group velocity inertia gravity) waves (p < P) and a short wavelength Yanai wave (if P is even) or an equatorial Kelvin wave (if P is odd). In short, the incident Rossby wave reflects a finite number of short Rossby waves plus a Kelvin wave or a Yanai wave. The zonal wavenumber of the reflected waves are all real, so that the reflection does not involve coastally trapped waves (Moore & Philander, 1977).

The short Rossby waves are much slower than the long Rossby waves. The short Rossby waves are prone to dissipation. They do not tend to propagate far offshore before being dissipated. Thus, energy tends to accumulate close to the western boundaries (Philander, 1990).

2. MODEL EQUATIONS

The non-dimensional form of the governing equations are:

$$\partial u/\partial t = y v - \alpha \partial h/\partial x + A(\alpha^2 \partial^2 u/\partial x^2 + \partial^2 u/\partial y^2) \quad (3a)$$

$$\partial v/\partial t = - y u - \alpha \partial h/\partial y + A(\alpha^2 \partial^2 v/\partial x^2 + \partial^2 v/\partial y^2) \quad (3b)$$

$$\partial h/\partial t = - (\alpha \partial u/\partial x + \partial v/\partial y) \quad (3c)$$

For specific details about the model, finite difference formulation, boundary conditions and nondimensional parameters, the reader is referred to Camerlengo and O' Brien (1980).

3. ANALYTICAL SOLUTION

Lateral friction is difficult to take into account in an analytical analysis. Furthermore, it may mask the reflection processes. Therefore, it is assumed that A is zero in the analytical approach. Moreover, the numerical computations are made with an extremely

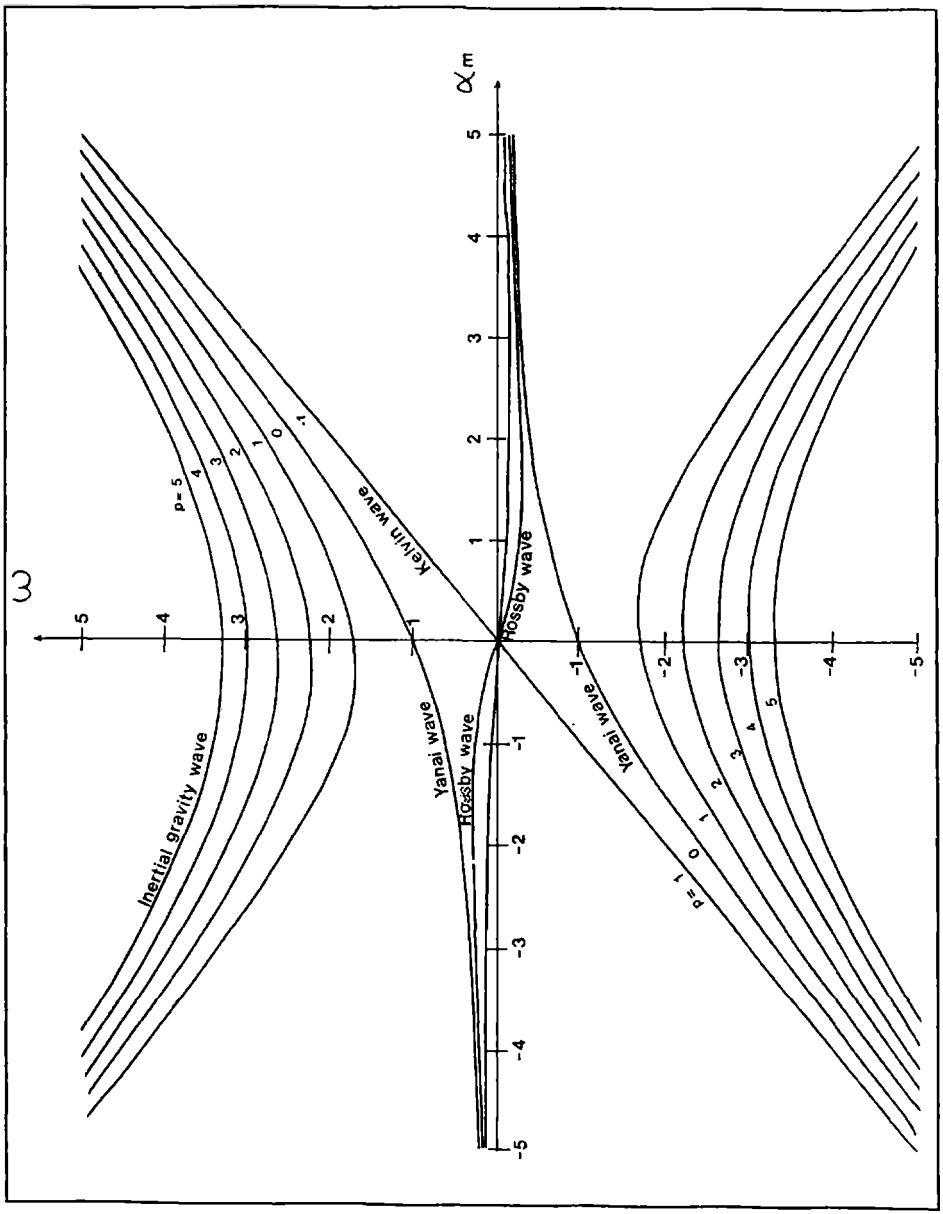

Fig. 1. Dispersion relation of equatorial waves, following Cane and Sarachik (1976).

small value of A.

To simplify the mathematical treatment of the problem, the external forcing is set to be zero in the analytical model. The coordinate y is allowed to vary between - ∞ to + ∞. Upon reflection, the processes of refraction and diffraction take place. The frequency remains constant. Therefore, both the incident and the reflected waves must have the same angular frequency, ϖ. A solution the form:

$$u = u_0 (x,y) \exp (- i \varpi t) \quad (4a)$$
$$v = v_0 (x,y) \exp (- i \varpi t) \quad (4b)$$
$$h = h_0 (x,y) \exp (- i \varpi t) \quad (4c)$$

is sought, where the frequency, ϖ, is given by the incident initial wave.

A solution is sought in the spectral domain. For this purpose, the Fourier transforms of the amplitudes u_0, v_0 and h_0 are introduced. Let:

$$U (m,n) = (1/2\pi) \int_{-\infty}^{+\infty} \int u_0 (x,y) \exp[- i (m x + n y)] \, d x \, d y \quad (5a)$$

$$V (m,n) = (1/2\pi) \int_{-\infty}^{+\infty} \int v_0 (x,y) \exp[- i (m x + n y)] \, d x \, d y \quad (5b)$$

$$H (m,n) = (1/2\pi) \int_{-\infty}^{+\infty} \int h_0 (x,y) \exp[- i (m x + n y)] \, d x \, d y \quad (5c)$$

Using the relation (4) and taking the Fourier transform of the system of equations (3), it yields:

$$\varpi U = - \partial V / \partial n + \alpha m H \quad (6a)$$
$$\varpi V = \partial U / \partial n + n H \quad (6b)$$
$$\varpi H = \alpha m U + n V \quad (6c)$$

The set of equations (6) is solved. A solution in terms of the Hermite function emerges, in the same fashion as the solution of the non-Fourier transformed equations (Moore, 1968). This mathematical peculiarity is due to the fact that the Hermite functions are transformed into themselves by means of the Fourier transform. However, in spite of the similarity of the obtained solution with the previous solution, the physical meaning of the

obtained solution is substantially different.

From equations (6a) and (6c) it is obtained:

$$(\tilde{\omega}^2 - \alpha^2 m^2) U = - \tilde{\omega} \partial V/\partial n + \alpha m n V \quad (7)$$

$$(\tilde{\omega}^2 - \alpha^2 m^2) H = - \alpha m \partial V/\partial n + \tilde{\omega} n V \quad (8)$$

Replacing U and H in (6b), it yields a single equation for V:

$$\partial^2 V/\partial n^2 + (\tilde{\omega}^2 - \alpha^2 m^2 - (\alpha m/\tilde{\omega}) - n^2) V = 0 \quad (9)$$

If $\tilde{\omega}^2 - \alpha^2 m^2 - (\alpha m/\tilde{\omega})$ is an odd integer, the solutions of (9) are bounded as $n \to \infty$. Thus,

$$\tilde{\omega}^2 - \alpha^2 m^2 - (\alpha m/\tilde{\omega}) = 2p + 1, \quad p = 0, 1, \ldots\ldots \quad (10)$$

or

$$\tilde{\omega}^3 - (\alpha^2 m^2 + 2p + 1)\tilde{\omega} - \alpha m = 0 \quad (11)$$

This equation represents the dispersion relation previously obtained by Moore (1968). It follows naturally, from Figs. 1 and 2, that for a given value of $\tilde{\omega}$, three real roots, for all real values of m, are obtained. Moreover, for V = 0, one more solution is possible. Namely that:

$$\tilde{\omega} = \alpha m \qquad U = H = \Psi_o(n) = c \exp(-n^2/2),$$

where c is a constant. The solution corresponds to the non-dispersive Kelvin wave propagating in the eastward direction. In the general case, the V-solution is a Hermite function of order p:

$$V_p = \Psi_p(n) = [H_p(n) \exp(-n^2/2)] / \{2^p p! (\pi)^{1/2}\}^{1/2}$$

where $H_p(n)$ is the Hermite polynomial of degree p (Moore and Philander, 1977). Whenever p = 0, one solution is $\tilde{\omega} = -\alpha m$. This solution is rejected due to the fact that leads to unbounded values of U and H, for larger values of n (Matsuno, 1966; Moore and Philander, 1977).

The other possible solution is represented by the mixed Rossby-gravity wave (Yanai wave). This wave is antisymmetric in V, about the Equator. Because of the fact that in Camerlengo and O' Brien (1980)' s model, symmetric boundary conditions are placed at its southern boundary (along the equator), the Yanai wave cannot be properly resolved.

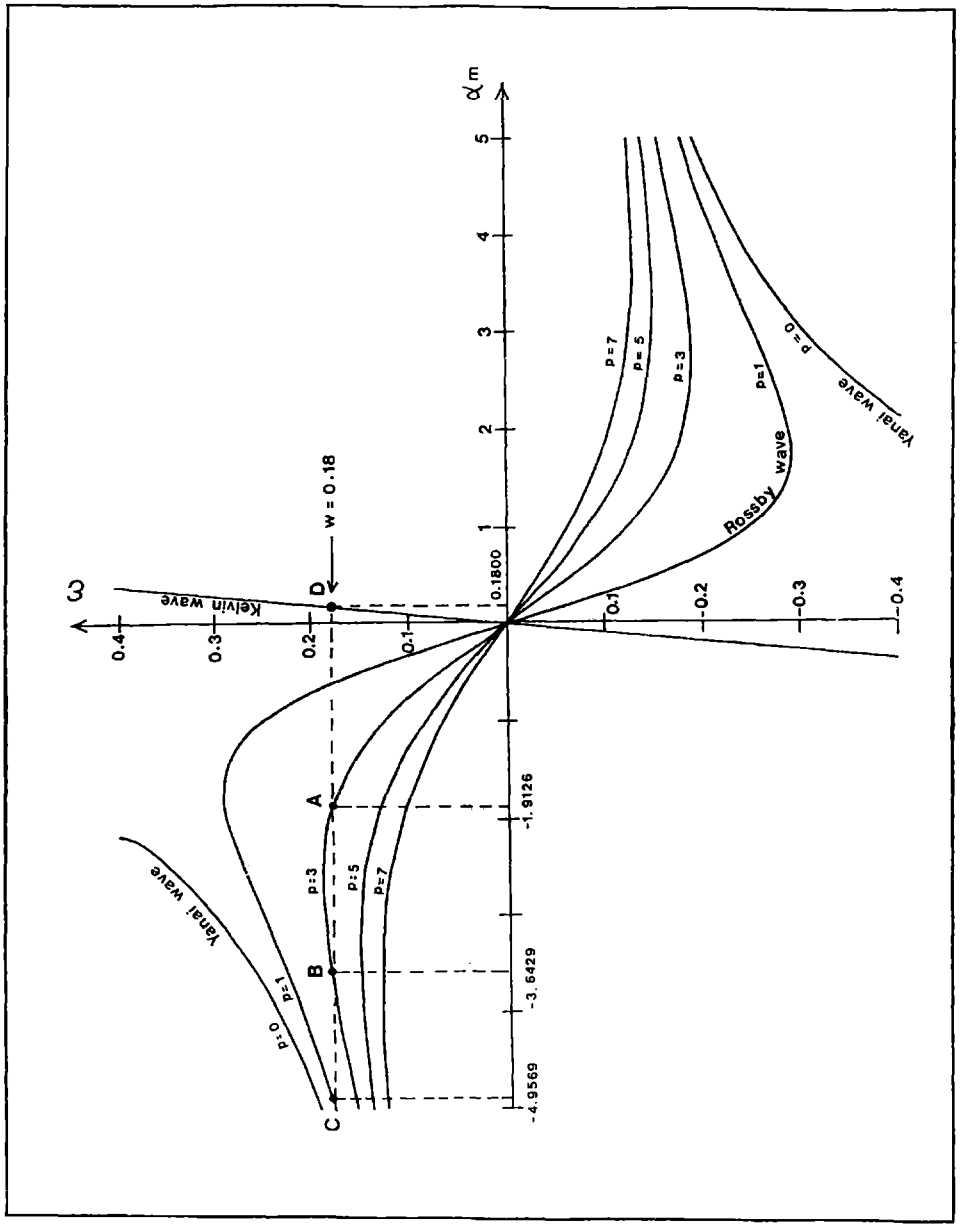

Fig. 2. Dispersion relation of the lowest modes of the Rossby wave. Point A representsthe initial condition. That is, the long wavelength positive group velocity Rossby wave. Points B and C represent the reflected short wavelength Rossby waves of order p = 3 and p = 1, respectively. Point D represents the reflected eastward Kelvin wave.

Whenever $p \geq 1$, the dispersion relation (11) yields:

$$\alpha m = (1/2\,\tilde{\omega})\,\{ -1 \pm [\,1 + 4\,\tilde{\omega}^2\,(\tilde{\omega}^2 - 2p + 1)\,]^{1/2}\} \qquad (12)$$

where the positive (negative) sign represents the Rossby (inertia-gravity) waves. Following Moore and Philander (1977), the general solution is:

$$Vp\,(n) = \Psi_p\,(n) \qquad (13)$$

$$U_p\,(n) = \imath\{[\,2(p+1)\,]^{1/2}/(\tilde{\omega} - \alpha m)\}\,\psi_{p+1}\,(n) - \{[\,2p\,]^{1/2}/(\tilde{\omega} + \alpha m)\}\psi_{p-1}\,(n)]/2 \qquad (14)$$

$$H_p\,(n) = \imath\{[\,2(p+1)\,]^{1/2}/(\tilde{\omega} - \alpha m)\}\,\psi_{p+1}\,(n) + \{[\,2p\,]^{1/2}/(\tilde{\omega} + \alpha m)\}\psi_{p-1}\,(n)]/2 \qquad (15)$$

Because of the fact that the value of $\tilde{\omega}$ is imposed, the values of m are quantified by the discrete values of p through the dispersion relation (11). Therefore, the complete Fourier transforms U, V and H are combinations of the above solutions and the Dirac functions. The values of m are given by $\tilde{\omega}$ and p, respectively. For example, the zonal velocity transform can be written as:

$$U(m,n,\tilde{\omega}) =$$

$$\Big[\sum_{p=1}^{\infty} A_p\,\imath\{[\,2(p+1)\,]^{1/2}/(\tilde{\omega} - \alpha m_{p,1})\}\,\psi_{p+1}\,(n) - \{[\,2p\,]^{1/2}/(\tilde{\omega} + \alpha m_{p,1})\}\psi_{p-1}\,(n)]/2\Big]*$$

$$*[\delta\,(m - m_{p,1})] \qquad +$$

$$\Big[\sum_{p=1}^{\infty} B_p\,\imath\{[\,2(p+1)\,]^{1/2}/(\tilde{\omega} - \alpha m_{p,2})\}\,\psi_{p+1}\,(n) - \{[\,2p\,]^{1/2}/(\tilde{\omega} + \alpha m_{p,2})\}\psi_{p-1}\,(n)]/2\Big]*$$

$$*[\delta\,(m - m_{p,2})] + D\,\psi_o\,(n) \qquad (16)$$

where the coefficients A_p, B_p and D are introduced to get the most general solution. The last term represent the possible Kelvin wave. The terms $m_{p,1}$ and $m_{p,2}$ represent the roots of the dispersion relation (12).

The condition u = 0 is imposed to study the reflection at the western boundary. In terms of the spectrum, this constrain requires that:

$$u = (1/2\pi) \int_{-\infty}^{+\infty}\int U\,(m,n,\tilde{\omega})\,\exp\,(i\,n\,y)\,d\,m\,d\,n = 0 \qquad \text{for any y}$$

or

$$\int_{-\infty}^{+\infty} U(m,n,\tilde{\omega})\, dm = 0 \qquad \text{for any } n.$$

Because of the Dirac functions, this condition becomes a discrete sum over the set of possible wavenumbers:

$$\sum_{im} U_i(m_i,n,\tilde{\omega}) = 0$$

Considering a single incoming long Rossby wave, with negative group velocity, C_g, characterized by the frequency $\tilde{\omega}$, the mode of order p and the wavenumber m, there is always another short Rossby wave with the same frequency $\tilde{\omega}$, the same order p, but with negative group velocity. The values of $\tilde{\omega} = 0.18$ and $p = 3$ are chosen arbitrarily. In Fig. 2, the dispersion diagram, the incoming (outgoing) wave is represented by point A (B). The spectrum corresponding to point A has an n-structure of the form:

$$U_A(n) \alpha \; [(8)^{1/2}/(\tilde{\omega} - \alpha m_A)]\, \psi_4(n) - [(6)^{1/2}/(\tilde{\omega} + \alpha m_A)]\, \psi_2(n), \qquad (17)$$

with $\alpha m_A = -1.9126$; while the point B is:

$$U_B(n) \alpha \; [(8)^{1/2}/(\tilde{\omega} - \alpha m_B)]\, \psi_4(n) - [(6)^{1/2}/(\tilde{\omega} + \alpha m_B)]\, \psi_2(n), \qquad (18)$$

with $\alpha m_B = -3.6429$.

By adding a suitable multiple of U_B, the $\psi_4(n)$ part of U_A may be cancelled. This leaves a part proportional to $\psi_2(n)$ which, in turn, may be cancelled by the wave with the same frequency, positive group velocity and a north-south structure characterized by $p = 1$: point C (Fig. 2). By doing so, a U field proportional to $\psi_o(n)$ is left. This U field may be cancelled by a Kelvin wave; which, in turn, has the appropriate north-south structure $\psi_o(n)$. The Kelvin wave always has a positive group velocity.

Upon choosing $A_3 = 1$, for the incoming wave, the complete set of waves after reflection, is:

$$U = [\,0.6758\,\psi_4(n) + 0.7069\,\psi_2(n)\,]\,\delta(m + 1.9126/\alpha) \;\Leftarrow \text{incoming wave: A}$$

$$+ [\,-0.6758\,\psi_4(n) - 0.6461\,\psi_2(n)\,]\,\delta(m + 3.6429/\alpha) \;\Leftarrow \text{wave: B}$$

$$-[\;0.0608\,\psi_2(n) + 0.0462\,\psi_0(n)\,]\,\delta(m + 4.9569/\alpha) \;\Leftarrow \text{wave: C}$$

$$+ 0.04620\,\psi_0(n)\,\delta(m - 0.18/\alpha) \;\Leftarrow \text{Kelvin wave: D}$$

4. NUMERICAL RESULTS

An external body force (wind, in our case) generates a set of different waves (a wave packet). Upon reflection at the western boundary, the forcing can lead to a very complex flow and spectrum patterns. Therefore, the external body force is chosen to be zero. The model equations, the finite difference formulation and the model geometry are essentially the same as in Camerlengo and O' Brien (1980). However, the initialization being used in our numerical simulation differs. The initial condition is chosen to be a single long Rossby wave, with negative group velocity (Fig. 3a). Only one single mode is specified. In doing so, the scattering process is clearly observed. The boundary condition, $u = 0$, at the western boundary, is responsible for the wave scattering in the east-west direction. This long Rossby wave transports energy from east to west. The mode of this wave is selected in such a way that it only generates three reflected waves: two short Rossby waves and a Kelvin wave (Fig. 2). All of the reflected waves have positive group velocity (Moore and Philander, 1977; Clarke, 1983).

The Fourier transform of the initial condition of the u field is represented in Fig. 3b. The non-linear coefficients introduced by the β-effect are responsible for the wave scattering in the north-south direction. This effect appears in the analytical study. Furthermore, due to the β-effect, the non-constant coefficients y u and y v, in the system of equations (3), lead to the partial derivatives $\partial V / \partial n$ and $\partial U / \partial n$ in the system of equations (6). Because of the existence of these two terms, no single wave is observed in the y-direction. In turn, these two terms scatter energy in a continuum n-spectrum.

The Fourier transform of initial zonal velocity field exhibits almost two complete wavelengths. Its north-south structure shows the structure of a typical Hermite function. The Fourier transform of the u initial field is relatively simple. This is the particular advantage in dealing with spectral analysis. Following Jenkins and Watts (1968), the Fourier transform pattern has a double symmetry. Taking into consideration equation (17), this is what is to be expected, as we are dealing with Fourier transform, that correspond to the same wavenumber. This wavenumber is chosen to be $\alpha m = - 1.9126$ (Fig. 3b).

The Rossby wave propagates in a westward direction. Because of the fact that the Rossby wave has dispersive characteristics, there is an increasing distortion in the non dimensional zonal velocity field, as time evolves (Figs. 4a, 5a and 6a). Due to the small frictional effect and the lack of wave generation at the eastern boundary, some noise is detected in the numerical simulation. This is clearly observed in the intensification of the extreme values of the nondimensional zonal velocity field, in the eastern half of the basin, at nondimensional time 6.4 (Fig. 4a). Taking into consideration the initial field, numerical noise is clearly detected around the Equator (southern boundary), at nondimensional time 15.0 (Fig. s 3a and 5a). The distortion of the initial Rossby wave and the numerical noise

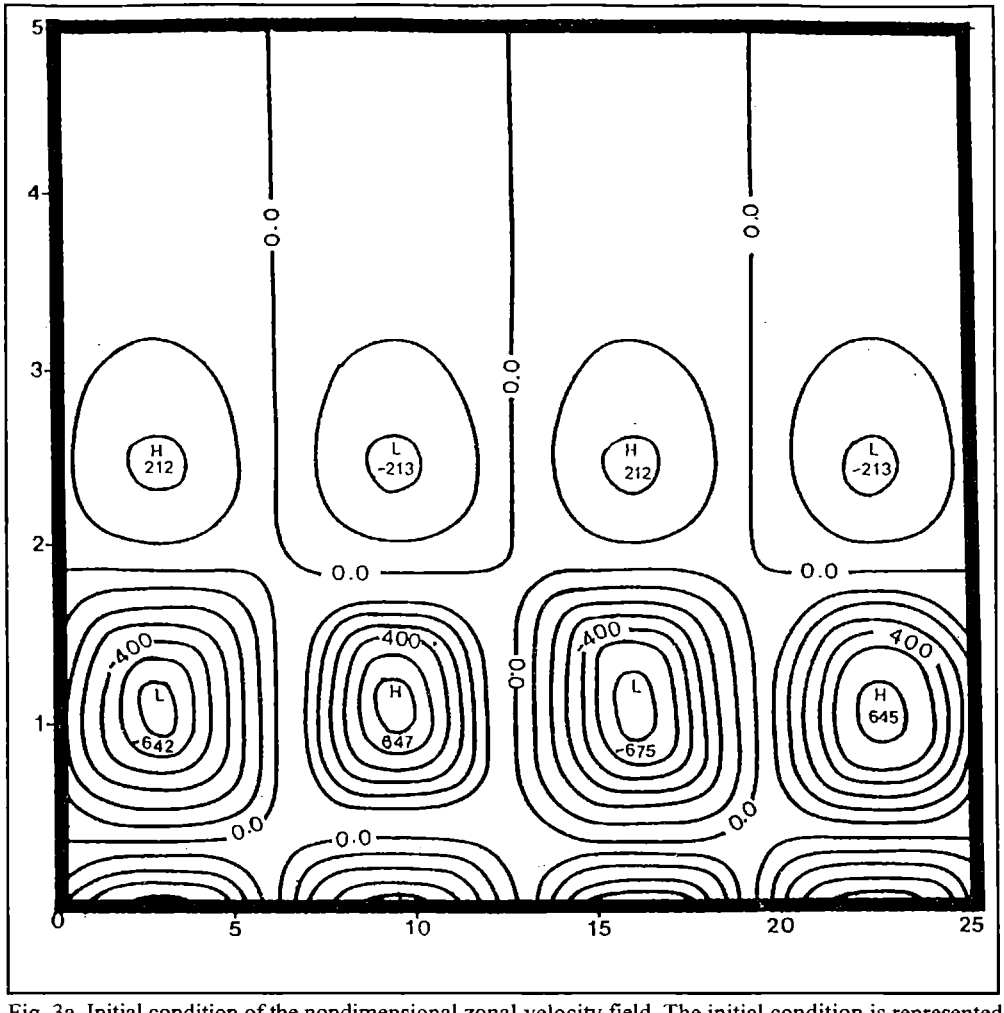

Fig. 3a. Initial condition of the nondimensional zonal velocity field. The initial condition is represented by a single Rossby wave. Following Camerlengo and O' Brien (1980), the abscissa extends 25 nondimensional internal radii of deformation along the Equator, while the meridional boundary extends 5 nondimensional radii of deformation in the north-south direction, respectively.

around the southern boundary, at nondimensional time 19.8, is clearly visible (Figs. 3a and 6a). The nondimensional unit of time, in Camerlengo and O' Brien (1980), is approximately 1.8 days. As expected, the westward propagation of the initial Rossby wave, is rather slow (Figs. 3a and 6a).

In the real world, long (negative group velocity) Rossby waves reflect at the western boundary of the basin as short Rossby waves. They do not tend to propagate far offshore

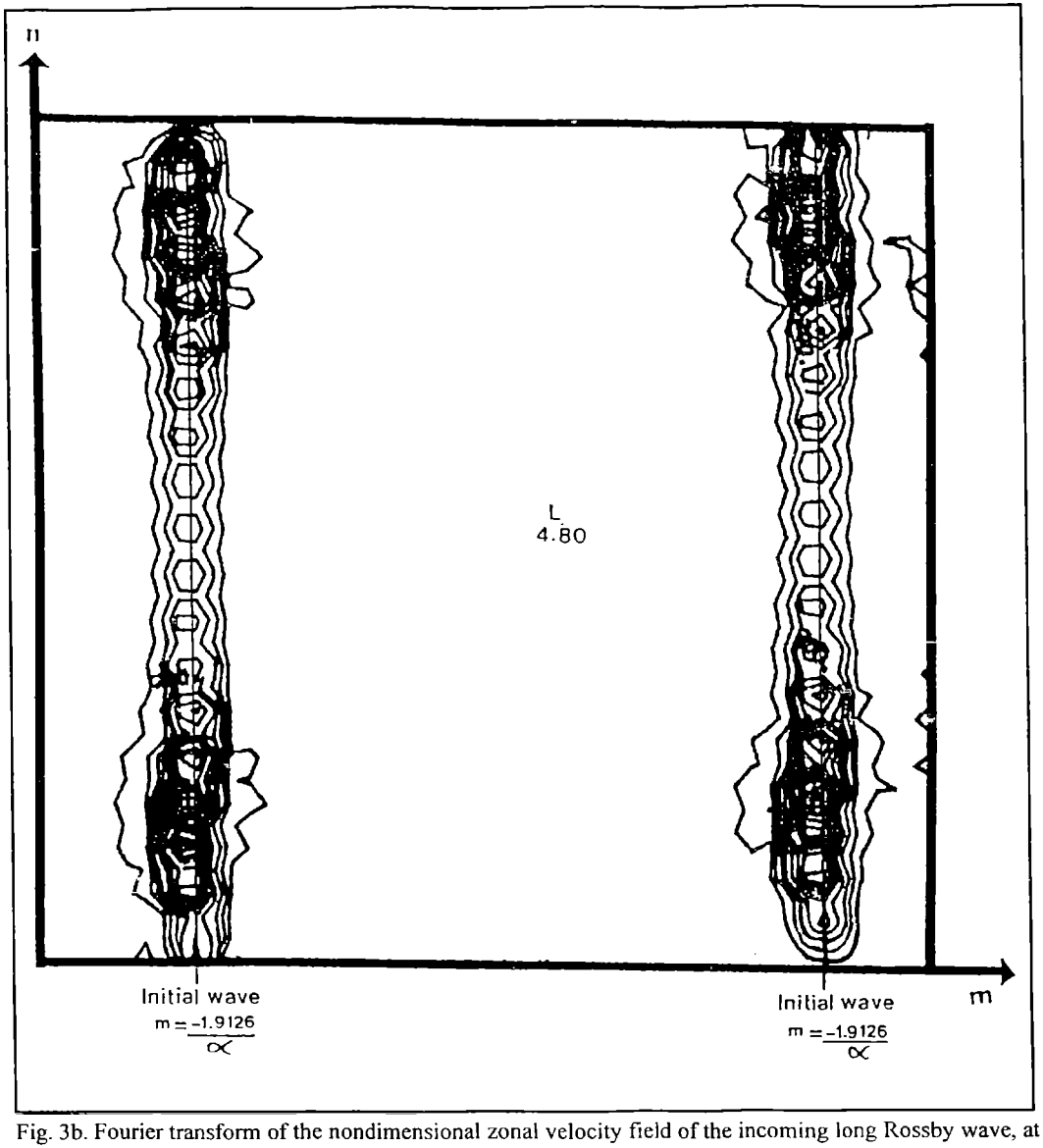

Fig. 3b. Fourier transform of the nondimensional zonal velocity field of the incoming long Rossby wave, at nondimensional time zero (point A of Fig. 2).

before being dissipated. Therefore, energy tends to accumulate close to the western boundary (Philander, 1990). This is what happens, in our experiences, in spite of the extremely small value of A being chosen (Fig. 6b). Due to the particular choice of the

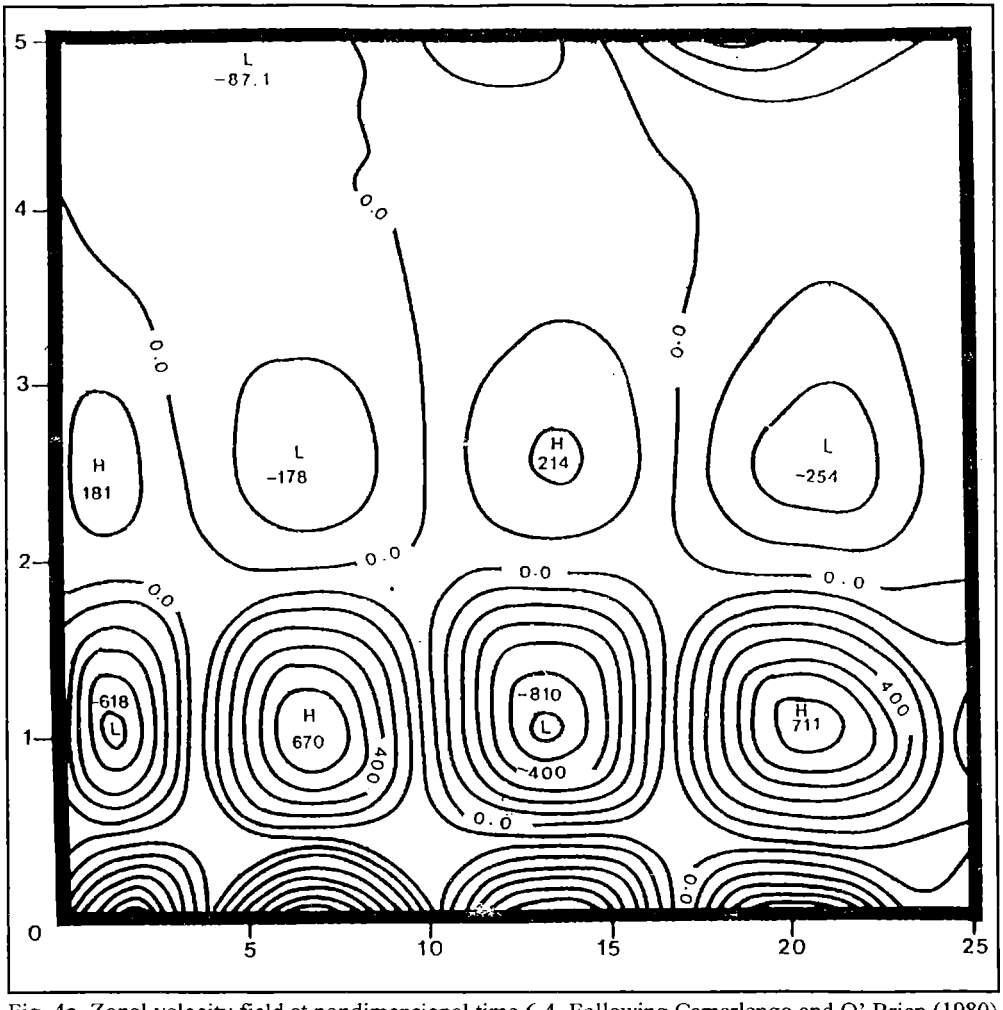

Fig. 4a. Zonal velocity field at nondimensional time 6.4. Following Camerlengo and O' Brien (1980), the abscissa extends 25 nondimensional internal radii of deformation along the Equator, while the meridional boundary extends 5 nondimensional radii of deformation in the north-south direction, respectively.

initial condition, almost the total amount of energy is retained in the initial wave. Only a relatively small percentage of the total amount of energy is propagated eastward, by the Kelvin wave (Figs. 4b, 5b and 6b).

The results of the Fourier transform nondimensional zonal velocity field shows that the identification of the initial wave, the two reflected short Rossby wave and the Kelvin wave, is much easier than in the original non-Fourier transform field.

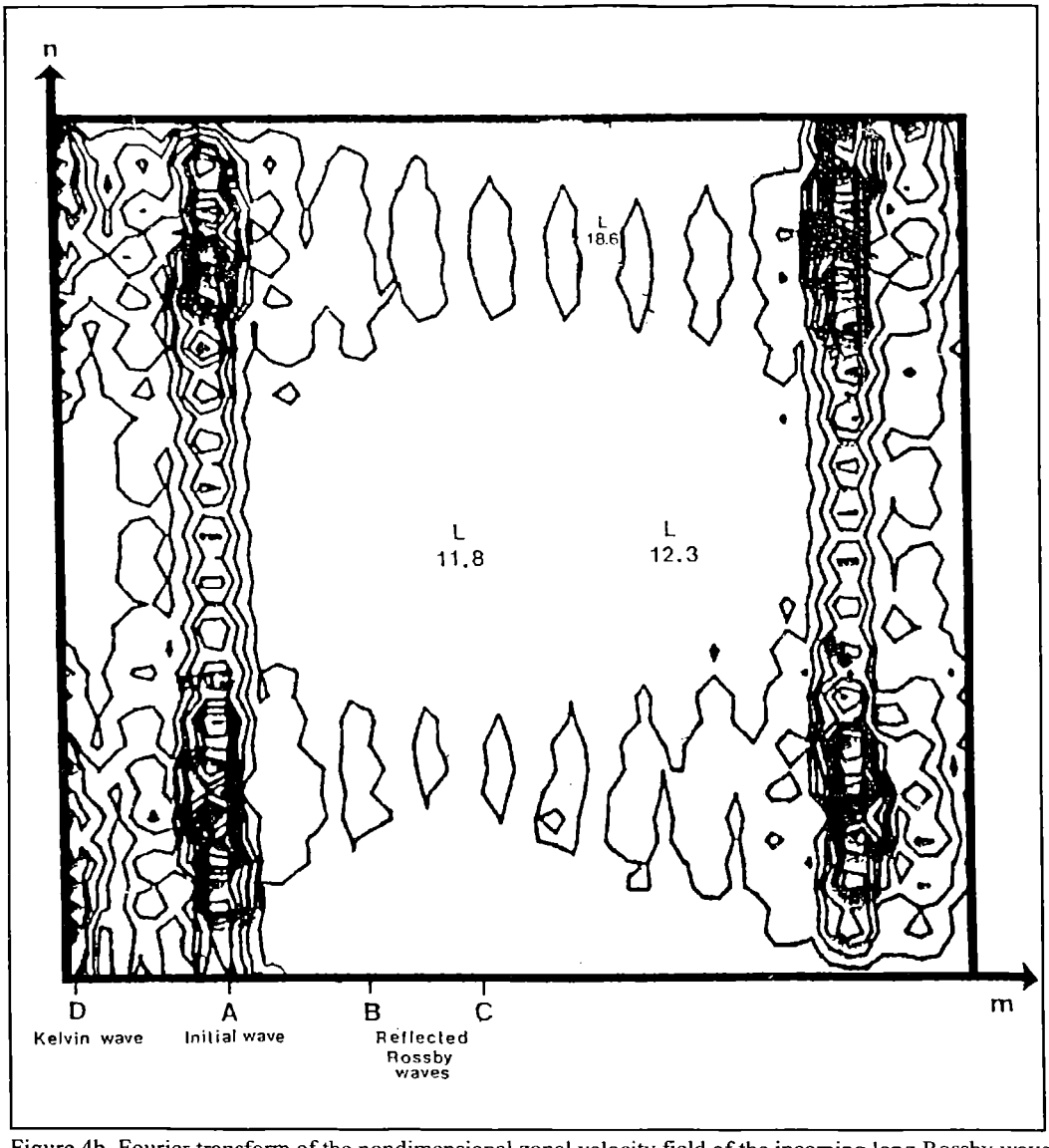

Figure 4b. Fourier transform of the nondimensional zonal velocity field of the incoming long Rossby wave (point A), the reflected short Rossby waves (points B and C) and the reflected Kelvin wave (point D), at nondimensional time 6.4.

5. CONCLUSIONS

This investigation studies the evolution of an initial long Rossby wave in the

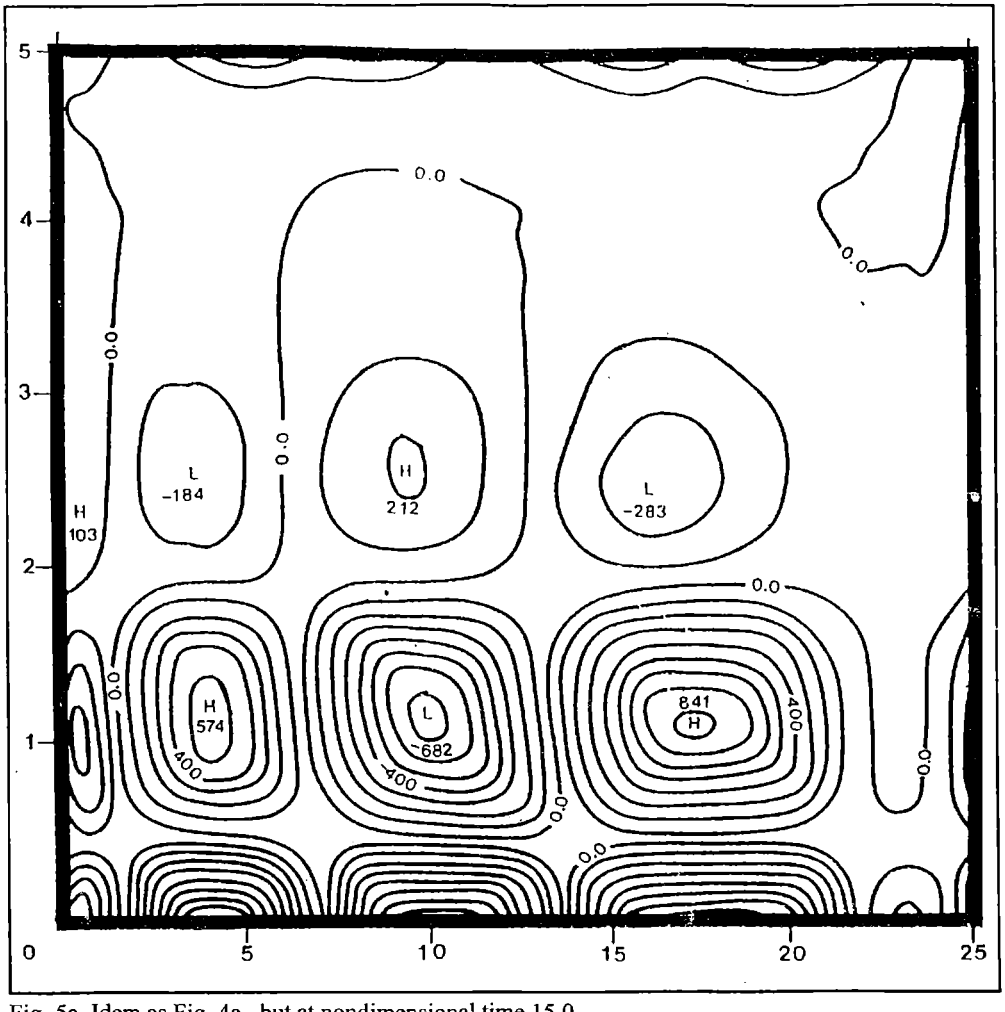

Fig. 5a. Idem as Fig. 4a., but at nondimensional time 15.0.

wavenumber space. A numerical model is used to study the reflection of the initial wave, at a meridional boundary. Due to its simplicity, as compared to the eastern boundary, the western boundary is chosen as the meridional boundary. An analytical study, to better understand the results of the numerical simulation, is also conducted.

The main conclusions of this study can be summarized as follows:

1) The solutions of the Fourier transform inviscid, unforced model equations, leads to a solution in terms of the Hermite function. Following Moore and Philander (1977) and Matsuno (1966), these solutions are similar to the solutions of the non-Fourier

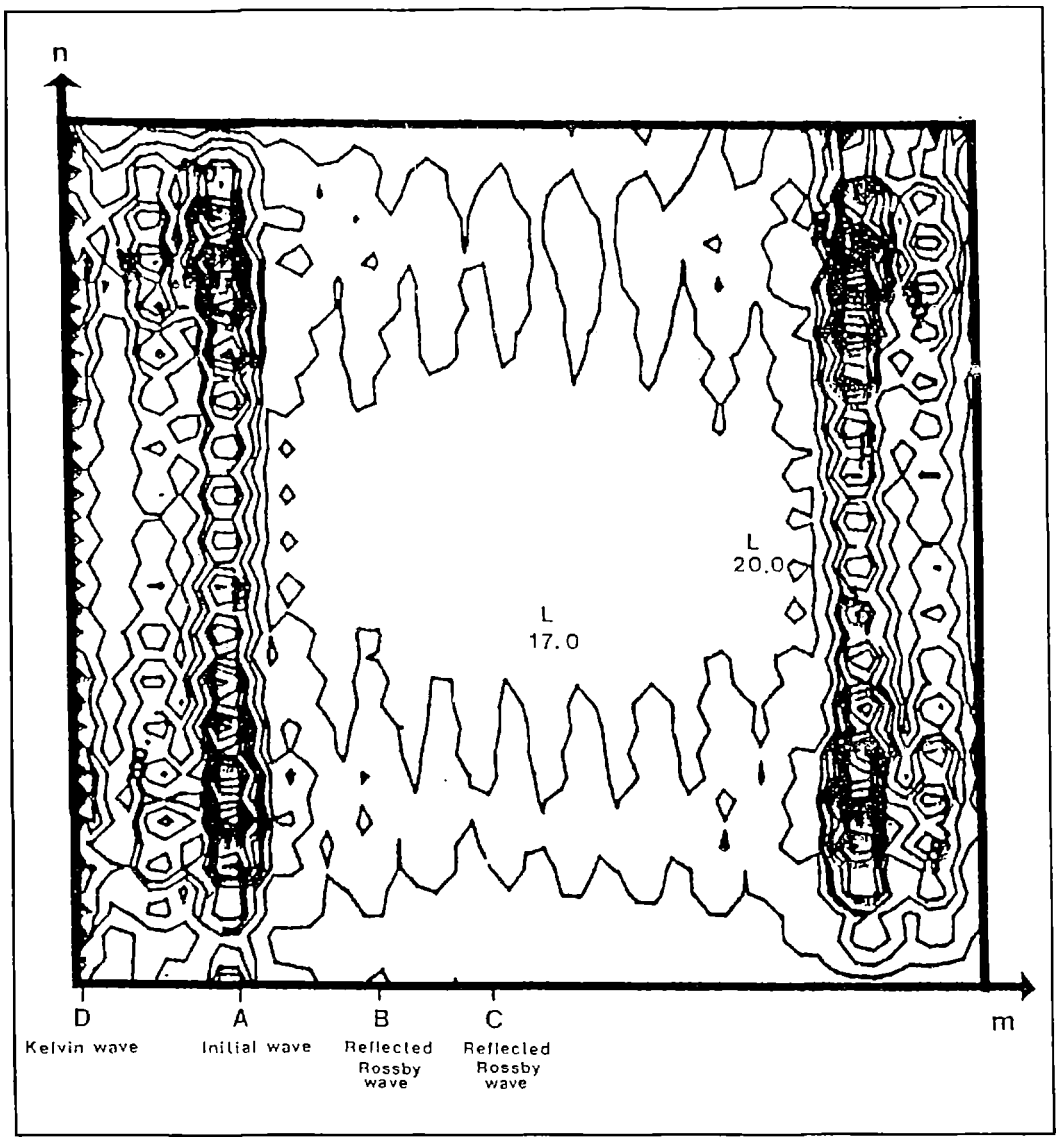

Fig. 5b. Idem as Fig. 4b., but at nondimensional time 15.0.

transformed equations. However, as shown in this study, the physical interpretation of the solutions of the Fourier transform model are completely different, from the solutions of the non-Fourier transform model.

2) Following the derivation of equation (17), the Fourier transform pattern of the initial

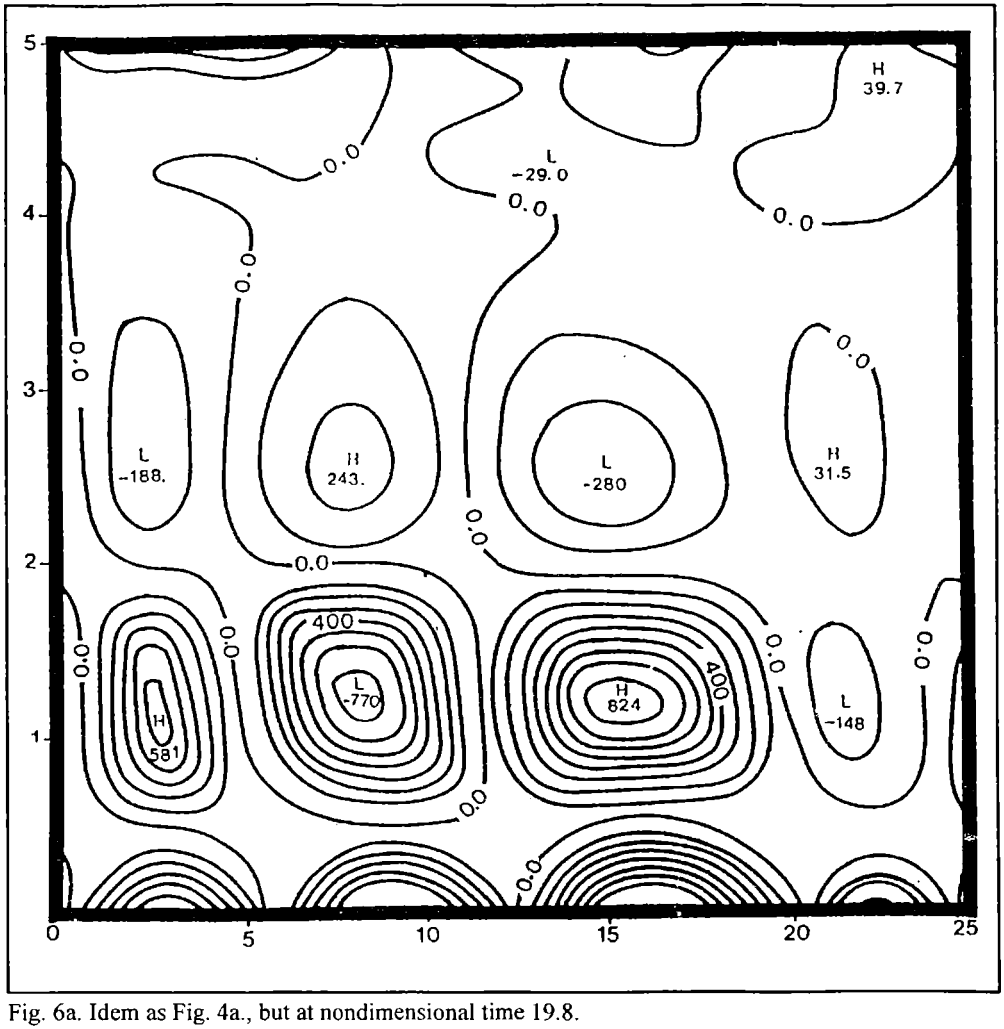

Fig. 6a. Idem as Fig. 4a., but at nondimensional time 19.8.

non-dimensional u field, exhibits a double symmetry. This double symmetry corresponds to the same wavenumber (Fig. 3b).

3) As shown in the analytical study, the non-linear coefficients introduced by the β-effect are responsible for the wave scattering in the north-south direction. As a consequence of this, no single wave is observed in the y-direction. The two non-linear coefficients are responsible for the scattering of energy in a continuum n-spectrum (Fig. 3b).

This study represents the first attempt to study the reflection of the an initial wave pattern in the wavenumber space. It is also shown that the interpretation of waves in the

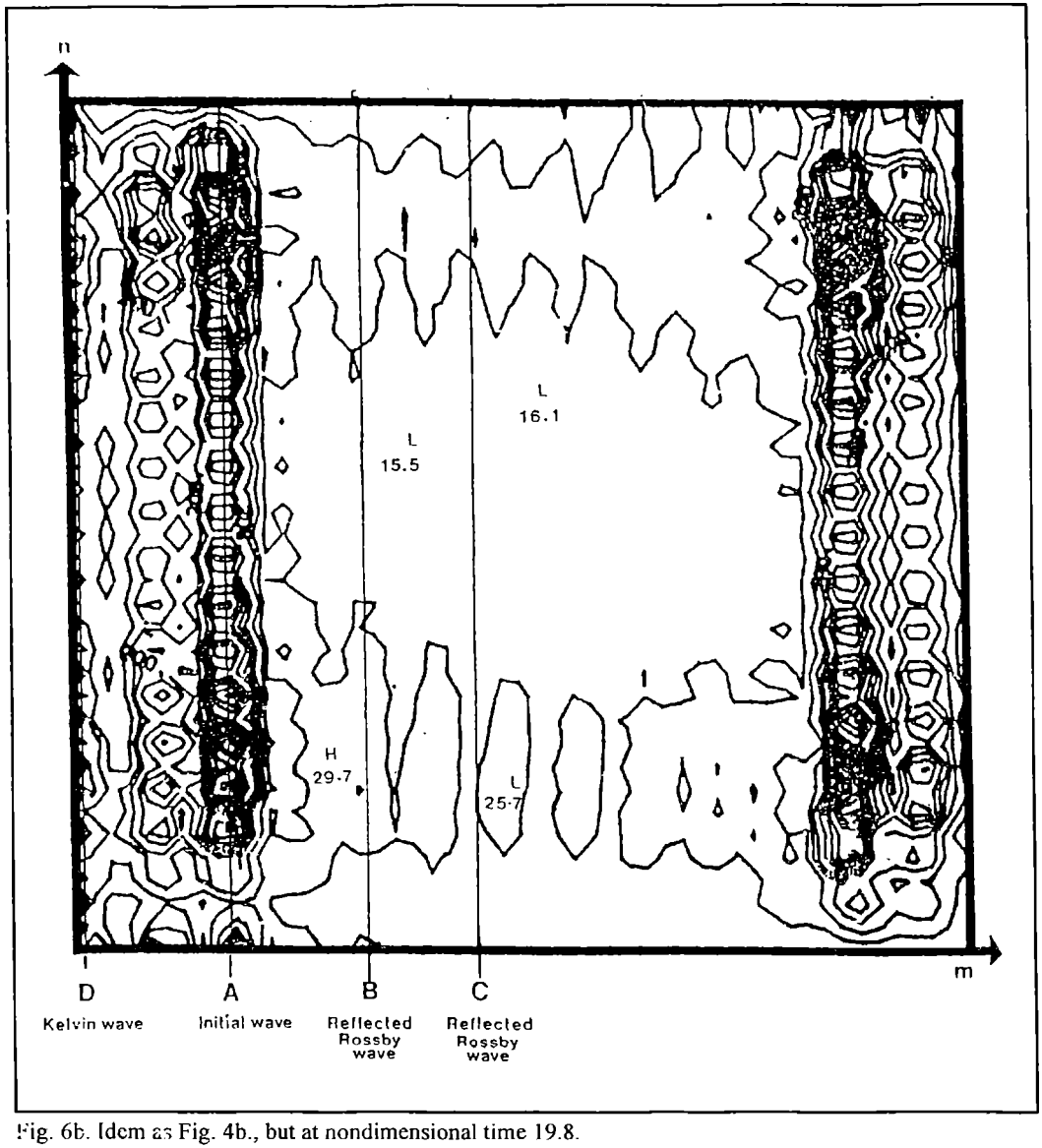

Fig. 6b. Idem as Fig. 4b., but at nondimensional time 19.8.

spectrum is relatively easier than on the original field.

Acknowledgements

This investigation was supported by a short grant of Universiti Pertanian Malaysia. The authors gratefully acknowledge this support. Comments made by an anonymous referee contributed to make this a much better manuscript. The authors would also like to express their deep gratitude.

REFERENCES

Camerlengo, A. L. and J. J. O' Brien, 1980. Open boundary conditions in rotating fields. *J. Comp. Phys.*, 35, 12-35.

Cane, M. and E. S. Sarachik, 1976. Forced baroclinic ocean motions. I. The linear equatorial unbounded case. *J. Mar. Res.*, 34, 629-665.

Clarke, A. J., 1983. The reflection of equatorial waves from oceanic boundaries. *J. Phys. Oceanogr.*, 13(7), 1193-1207.

Jenkins, G. W. and D. G. Watts, 1968. Spectral analysis and its applications. *Holden- Day*, 525 pages.

Matsuno, T., 1966. Quasi-geostrophic motions in an equatorial are. *J. Meteor. Soc. Jap.*, 44, 25-43.

Moore, D. W., 1968. Planetary-gravity waves in an equatorial ocean. Ph. D. thesis, Harvard University, Cambridge, Massachuset, 200 pages.

Moore, D. W. and S. G. H. Philander, 1977. Modelling of the tropical oceanic circulation. The Sea. Vol. 6. E. D. Goldberg, Ed. Wiley, 319-361.

Philander, S. G. H., 1990. El Niño, La Niña and the Southern Oscillation. Academic Press, 289 pages.

GEOACTA, 22, 122-133, 1997

GEOMAGNETISM AS AN INDEPENDENT SCIENCE

Luiz Muniz Barreto
Instituto de Geofisica de UNAM,México, Observatorio Nacional,Brasil

ABSTRACT

At its beginning, Geomagnetism was involved into a mystical atmosphere. Neckham and Norman´s experiments, and the practical use of the compass by Columbus had no significance to disconnect it from a mysterious understanding. In spite of the magnificent Gilbert´s treatise, the general belief about Geomagnetism remained enigmatic. Gauss´creative methods to measure the Earth´s Magnetism were the most important step to place geomagnetic phenomena into the frame of physical rational sciences. Many of those phenomena continued to be considered as low atmospheric events, and they were treated as meteorological ones. In 1851, Liais proved that a typical geomagnetic phenomena, the aurora borealis, occurs far from the "meteorological atmosphere", but his results were only recognized in our century, when IATME, and latter, IAGA were created. The influence of Geomagnetism as a seed of great scientific programs (e. g. the 1st. and the 2nd. Polar Years, and the IGY) puts Geomagnetism in its proper place as an independent science.

RESUMEN

En su principio el Geomagnetismo estuvo envuelto en una atmósfera mística. Los experimentos de Neckham y Norman y el uso práctico de la brújula por Colón no fueron suficientes para separar esa incipiente ciencia de una significación misteriosa. A pesar de la publicación del magnífico tratado de Gilbert, el entendimiento general sobre el Geomagnetismo fue enigmático. Los métodos originales creados por Gauss para medir el Magnetismo Terrestre fueron los pasos más importantes para poner sus fenómenos en el esquema de las ciencias físicas. No obstante ese éxito, muchos de aquellos fenómenos continuaron en ser considerados como eventos de la baja atmósfera y por eso, ellos eran tratados como perteneciendo a la Meteorología. En 1851, Liais probó que un fenómeno típico del Geomagnetismo, la aurora boreal, ocurre mucho más arriba de la "atmósfera meteorológica", pero sus conclusiones sólo fueron reconocidas en nuestro siglo, cuando la IATME y después, la IAGA ya existían. La influencia del Geomagnetismo, como la semilla creadora de grandes programas científicos (por ejemplo, el Año Geofísico Internacional) ha proporcionado a esa ciencia su lugar propio como una ciencia independente.

1. PREHISTORICAL PERIOD

In spite of its prominent place in the history of science, Geomagnetism was

involved into a mystical atmosphere, from its beginnings up to recent times. Certainly, that unhappy childhood provoked many wrong interpretations of its phenomena and an inconvenient placement in the frame of Science. It is well known that the Chinese civilization used a magnet on land and nautical orientation. According to Needhm (1962) the earliest quotation about the compass´use was made in 1088 AD. by Shen Kua. On the other hand, the first European reference to a compass was made by Alexander Nekham in 1190. It is possible that the Marco Polo imaginative descriptions of the technology in China had contributed to the practical use of the magnetic stone properties. These characteristics were also discovered some centuries before from the strange characteristics of the loadstone as it was quoted by Plinius (Malin, 1987).

Since there are no clear written documents about a widespread use of the compass, it is possible to call "Prehistoric Period" the time before the Great Navigation. For this reason, some speculative statements about the use of the compass could be proposed to explain some nautical success occurred during that crucial historical period (May 1956). Vicking´s trips to America and the initial Portuguese discoveries could be connected to the use of the compass. A fortunate coincidence joined the two intrepid nations. Eric of Pomerania was married with Philippa, a cousin of Enrique o Navigator (Henry the Navigator), the great founder of the Sagres School (Barreto, 1987).

If we give a look to a Portugal map, we could see Sagres promontory as a veritable caravel prow pointing out to the Atlantic Ocean. At that defiant place, the Infante Dom Enrique founded a scientific center, where astronomers, geographers, cartographers and navigators from various countries prepared one of the most audacious adventures of the mankind. The opportune coincidence of a linkage between Sagres and the Vickings made very probable the assumption that one or more Portuguese sailors joined the Vicking during their heroic trip to Greenland. In spite of the lack of written documents, the use of the compass on Navigation by Sagres' scholars should be considered as very possible.

As a consequence of the economical and political importance of the navigation and discoveries, it is easy to understand the scarcity of clear historical references about the navigational techniques. Geography and Cartography were classified subjects, and Portugal used the experience from Sagres to expand its power over the new lands. The "variation of the needle variation" or, in modern language, the "declination change with the geographic position", was a common method to obtain longitudes, and it was well known in Sagres. It is conceivable that the scholars from Sagres knew that in the 15th Century the isogonic lines were close to the meridians direction in the Southern Atlantic, but they had somewhere an Eastern-Western direction in the Northern Atlantic. This old regional peculiarity of the geomagnetic field could be a strong reason to underestimate the distance between Europe and the Unknowing Continent,

America, and a very probable argument for the Portuguese choice of a Transafrican route to India and the refusal of the Columbus´project by the Lisbon Crown (Barreto, 1991).

A historical injustice was learned some years ago in primary school books:" Brazil was discovered by a fortuitous error of the Cabral´s fleet". The Admiral Pedro Alvarez Cabral organized his expedition to India with the best requirements of his time by using Sagres knowledge of the Southern Atlantic, including a rough estimate of the isogonic lines (Barreto, 1987). It was a routine task of Portuguese sailors to measure the magnetic declination during their voyages. Sometimes, a crude isogonic chart was traced, and the famous Castro´s magnetic chart of the Indian Ocean is a typical example (Chapman and Bartels, 1940). In fact, Castro´s work represents the end of the "Prehistorical Period" because, after it, there are confident documents. Among them, the notable Halley´s Atlantic Chart (Halley, 1693). The History of Geomagnetism was born.

2. FROM CASTRO TO GILBERT

The Great Navigation represents one of the most remarkable periods of the History of Mankind. Sometimes, it is compared to the Space Age, but we must consider it as an heroic one, in spite of its limited terrestrial proportions. It occurred before the advent of the scientific method with its technological consequences. The unknowing oceanic dangers, with the fantastical monsters was more terrific than the present space with its known perils.

In the 15th and 16th centuries, a great lot of mystic explanations were used to interpret natural phenomena. Old and grotesque superstitions were considered as absolute truths. The main scientific goals were the same from the Middle Age, the search for the "philosopher stone", the "long-life elixir" and the official use of mendacious astrological predictions. Even though those risible interpretations were common in all scientific branches, with respect to the Earth´s Magnetism they persisted until the last century, in spite of some notable discoveries and experimental activities, and the importance of the practical use of the compass. There are written documents about that persistent wrong interpretations. Old books on Physics show crude explanations of the geomagnetic phenomena.

In fact, it is necessary to find out the reasons for this long-lived kind of sorcerous thinking, from which Mathematics, Mechanics and some subjects of Physics had escaped. Perhaps the influence of great men, such as Copernicus, Galileo, Kepler, Newton and Leibnitz could explain that good riddance. Strugles among intellectual groups, during and after the Renaissance, caused the birth of the Reformation, the Catholic Counter-Reformation, the Absolutism and the consequent fall of the

Feudalism. As an effect of those quarrels, many times warlike and bloody discords, a new scientific thinking was born. The search to explain Nature by general laws substituted the old beliefs on traditional unexplained credulities.

To achieve such generalization, new and powerful mathematical methods were created. It was the beginning of the Natural Determinism and the birth of the Scientific Method. Since then, a primordial attention was given to experience and the analysis of its results by means of predictable observed events. Now, a scientist auscultate the Nature to obtain its answers, and human laws were not capriciously imposed to it.

Notwithstanding the greatness of that intellectual revolution and its practical consequences was not a sufficient reason to consider the Terrestrial Magnetism as a real rational science. In fact, the use of the compass was a kind of a practical technique to help sailors. Castro's and other similar magnetic charts were a sort of a "portolano", a practical navigation guide. The famous Halley's charts had different characteristics. They were the result of scientifically made observations. The Halley great work was a consequence of another notable advancement, the admirable "De Magnet", published by William Gilbert hundred years before. That publication constitutes a gratifying exception in the Geomagnetism beginning. Actually it could be considered as the first ever scientific textbook (Malin, 1987). The newcomer Scientific Method was the guide in De Magnet pages.

Geomagnetism was not treated as a hidden force with an inexplicable origin and then, its study had surpassed the low level of a mere navigation aid. It was the result of many years of careful experiments (Gilbert, 1600) by using a modern scientific approach.

3. A PIVOTAL NAVIGATION TOOL

Although Gilbert'treatise had given to Geomagnetism a new scientific reputability, the compass'use persisted as its most known aspect. The Great Navigation period was succeeded by the epoch of the new lands conquest. More and more magnetic charts were produced by the pioneers, Portugal and Spain, as well by other European countries, mainly by British navigators. It is interesting to notice that Portuguese and Spanish nautical interests were not connected to a scientific study of that important nautical aid. On the other hand, England became the main source of the studies on the Terrestrial Magnetism. Speculative activities about the origin of the Terrestrial Magnetism and experimental enquires had their high point in Gilbert's treatise.

The discovery of magnetic inclination by Norman, in 1581, was followed by the first isoclinic chart prepared by Whiston in 1721. One of the most impressive contributions in that period was the discovery that declination and inclination suffered time changes in a quasi-regular way. Gunter, in 1584, by comparing his declination

values with those ones obtained 40 years before by Borough, concluded that a sensible change had occurred. Those contribution and many others came from British scientists. The British Admiralty perceived the necessity of such activities, and its support was fundamental to improve Geomagnetism. The determination of longitudes was one of the most serious problems on Geography and Cartography in the 16th to the 19th centuries. It is probable that the Spanish accordance to sign with Portugal the Tordesillas Treaty was the result of a lack of knowledge about longitude determination. Portugal gained some millions of square miles and, in consequence, Brazil has today its great area.

Some astronomical methods were used as a complement of declination and inclination measurements to estimate the longitude. The astronomical determination of latitude was not a problem, but for the longitude, there were many puzzling questions. The observations of Moon hide, and the Jupiter´satellites eclipses were not satisfactory procedures. They depended on clear skies, correct astronomical predictions, and a reasonable time-keeping. On the other hand, longitude determination by declination measurements was a function of well elaborated isogonic charts.

In spite of some substantial scientific accomplishments and the elimination of many mystical aspects, the Geomagnetism continued to be considered as a complement of nautical techniques. In fact, the general magnetic phenomena were not well understood, and its relationships with the new discovered Electricity was also an incoming subject. It is possible that an unexpected question was placed to the 19th Century scientists: "What is the Science in which field the Terrestrial Magnetism could be included?" An independent science was out of order. Its subjects were so narrow and peculiar, that it was impossible to conceive such status. On the other hand, Meteorology presented, since the early days of the last Century, an extraordinary development and good scientific procedures. For these reasons, it was a natural choice to place the "Terrestrial Magnetism" and the so called "Atmospheric Electricity" into the limits of the Meteorology.

4. A NEW SCIENCE IS BORN: GAUSS

One of the Lord Kelvin´best statements was his lapidary phrase about the importance of a quantitative consideration of natural phenomena. The advancements of the Terrestrial Magnetism until the third decade of the last century had produced a considerable amount of information about a scientific nameless entity, today called "geomagnetic field". At a specific point of the Earth´s surface, and at a definite instant, the values of two different things were obtained: the declination and the inclination of a magnetic needle.Both are angles. Those values represented a kind of deviation from a "normal" position of the needle, in fact only qualitative concepts, a sort of peculiar

characteristic of that unknown entity, at those place and instant. In that epoch, vectorial concepts were not well understood. Declination and inclination gave only the direction of the undefined vector B, the "geomagnetic field". Its numerical and modular value, the "intensity", remained undefined.

The experiments made by Humboldt in South America in the 18th Century, showed that there was a relationship between the oscillation of a magnetic needle and the strength of the magnetic effects (Malin, 1987). Carl Friedrich Gauss, one of the greatest names on Science, could be considered as the Father of the Scientific Geomagnetism. The multiplicity of his activities and the penetrating wisdom of his works are present in many scientific fields. Gauss had an extraordinary aesthetic sense and the perfection of his works will maintain his discovered truths alive, through centuries.

In a spontaneous and crude comparison between two great fields of the human mental creation, Science and Music, Gauss could be understood as the J. S. Bach of the Science. Gauss settled the frame of the scientific theories, as Bach established the frame of the Music. First of all, Gauss studied the best measuring instruments to analyse a natural event, taking into account the precision and the errors of the measuring method. It was the "first movement" of his symphony, an "adagio maestoso". Secondly, he obtained a large series of measures, by using a carefully chosen method. It was the second movement, certainly a "largo".

The third movement, in "crescendo" was the establishment of a general theory of the studied phenomenon. Finally, the last movement, an "allegro cantabile" was the experimental test of the theory. The best "Gauss symphony" was the creation of the methods for geomagnetic measurements. The establishment of a rational system of coherent units called for Gauss' attention. He intended to apply the basic idea of the Metric System, created few years ago, toa new physical entity, the "magnetic intensity". For this reason, Gauss called "absolute" the result of a measurement in which only the units of length, time and weight were used to define a final value. In fact, a measure cannot be "absolute", but Gauss used that expression for a lack of a better one.

Around 1832, Gauss and Weber (Malin, 1987) created the famous *deflections-oscillations method* to measure the modulus of the horizontal component of the geomagnetic field. In fine, the vector B had been completely defined by three independent components, D, I, and H. To compose the *second movement*, perhaps the most beautiful of his *symphony*, Gauss analysed a great lot of measures, in order to obtain the most probable value. To perform this part of his *opus*, Gauss created the *mean squares method*, one of the best *melodic themes* even created on Science.

The *Gaussian forth movement* was the construction of simple but very precise instruments, the fibre suspended magnetometers, in order to check his theory. The high

quality of such devices is the reason why they are used up-to-now at many magnetic observatories. Kelvin´statement had been adopted: a new Science was born.

Gauss was aware of the strong necessity to study the new science in a worldwide scale. For many other sciences, such aspect was not important but in this case as well that one of the Meteorology, an earthly consideration is crucial. We must remember that the existing communication means in the first part of the 19th Century were very precarious. Today, scientists could perform a cooperative research in an on-line way but, in Gauss epoch, a letter was the unique process to communicate a result or an important question. The worldwide use of the telegraph was not established.

In order to attenuate such bad condition, Gauus created in 1834 the Göttingen Verein (Fukushima, 1994), usually called the Magnetic Union. From the historical point of view, the Göttingen Verein could be considered as the direct ancestor of the actual IAGA and, in a broader sense, the first scientific union.

For the first time, in spite of its newness, Geomagnetism presented its precursory influence. Although the notable event is not generally recognized , since then Geomagnetism was an independent science.

5. GEOMAGNETISM AND METEOROLOGY

Up to the end of the 19th Century the Earth´sciences were considered as an additional consequence of astronomical studies or, in some cases, as the complement of astronomical researches. It was the case of Geodesy, the basis of a reference frame for Astronomy. When a natural event could be linked to the Earth crust, it was naturally connected to Geology. It was the case of Seismology. Geomagnetic phenomena were difficult to be classified.

On that time, Electricity was a fast developing science and its practical applications began to be present to change the Civilization. After Benjamin Franklin´s famous experiment on lightning rods, the Atmospheric Electricity becomes a very important scientific subject. Its connection with meteorological phenomena was an obvious reason to its inclusion in that discipline. On the other hand, the initial discoveries on Electromagnetism settled a natural assembly between Electricity and Magnetism.

It is easy to understand the simple solution that was found to place geomagnetic studies into the frame of a well studied science, the Meteorology. For this reason, in the second part of the 19th Century the scientific centers, mainly at the principal European astronomical observatories, a department or service on "Meteorology, Terrestrial Magnetism and Electricity" was created (Flamarion, 1911).

An interesting occurrence on this matter is slightly known by the History Science (Barreto, 1995): the influence of Emmanuel Liais to understand Geomagnetism as an

independent science. Emmanuel Liais is most known as a classical astronomer, a skilful producer of precise instruments, and a courageous explorer.

Liais was born at Cherbourg, France, in 1826 and, since his early years he demonstrated an extraordinary ability on exact sciences, mainly on their experimental aspects. In 1852, Liais visited the Paris Observatory and he caused a vivid impression on Arago, the old and respected Director (Liais, 1853 I). One of the last Arago's wills was the promise to nominate Liais as a Paris Observatory astronomer.

After Arago's death, Le Verrier, a national name in France, was appointed as the Director of Paris Observatory. He maintained Arago's promise, and in 1854, Liais was nominated Assistant-Astronomer. Only three years latter he rode to the status of Titular-Astronomer, and received the title of Chevalier de la Legion d'Honour (Ancellin, 1986). That fast professional ascent was due to an intense and original scientific work that was recognized by Le Verrier, who was parsimonious on explicit quotations about his colleagues (Barreto, 1995).

After a friendly beginning, step by step, Liais and Le Verrier relationships were been deteriorate, because the differences and similarities between those two great men were conspicuous (Barreto, 1995). In spite of the historical interest of that quarrel, a detailed analysis of it cannot be presented here (Ancellin, 1986; Flamarion, 1911; Barreto, 1995; Morize, 1927). We must be restricted to Liais activities on the Terrestrial Magnetism.

Few years latter his appointment to Paris Observatory, Liais was the Head of the Meteorological Division. In 1885, he presented to Le Verrier a detailed project to reorganize that Division. The use of the telegraph on meteorological forecasts was a revolutionary improvement to increase the percentage of exactitude. In spite of a small interest from Le Verrier, in 1858 Liais finished the complete reorganization of the French Meteorology. Besides his great efforts to improve meteorological activities, Liais started a scientific research on Geomagnetism with an intuitive tendency to split it from Meteorology. His work to install original variometers with photographic records is not well known. The first photographic *variographs* were introduced by Brooke and Ronalds in 1847 (Malin, 1987) but their continuous operation for many years was due to Liais improvement of a special driving device (Ancellin, 1986).

Notwithstanding the importance of such activities on Terrestrial Magnetism, his principal result on this discipline was obtained few years before his arrival at Paris. In three articles (Liais, 1851, 1852, 1853 II) he proposed and applied an observational method to measure the height of the Polar Aurora, to prove that such phenomenon occurs above the atmospheric regions were meteorological events took place.

The discord between Liais and Le Verrier arrived at an unsupportable point, and Lias'permanence at Paris Observatory becomes impossible. For this reason, he accepted a friendly invitation from the Brazilian Emperor, Pedro the Second to be the

Director of the Imperial Observatory of Brazil. In his second country Liais and his wife, Margarita, performed many difficult and important scientific activities (Ancellin, 1986; Barreto, 1987; Liais, 1881; Liais, 1888). However, his last scientific effort had been unsuccessful. He intended to repeat in Brazil his work on Geomagnetism, and he tried to install at Rio de Janeiro the first magnetic observatory in Latin-America. The story of Liais struggle against the stupid bureaucracy and the hypocritical envy from some politicians is a real historical learning for us, because such drama is alive today with other players (Barreto, 1995). Defeated by his enemies, he returned to France and becomes a politician, as the "Maire" of Cherbourg. Liais´proof that a typical geomagnetic phenomenon, the polar aurora, occurs far from the meteorological level was only recognized many years latter.

On the other hand, Gauss´work was fruitful. The Göttingen Verein becomes the nucleus of a new sort of scientific stations, the first network of magnetic permanent stations. 50 magnetic observatories, now independent from their previous meteorological tasks, formed that scientific network (Malin, 1987). Humboldt published six reports of the Magnetic Union (1830-1841), a pioneer result. He stimulated E. Sabine to install permanent stations in the British Colonies, on behalf of the Royal Society. A remarkable result was obtained in India: the installation of an observatory at Colaba in 1841. In 1906 that observatory was moved to Alibagh. Today, we wonder of more than 150 years of continuous recording , thereby one of four selected observatories which can claim this honour (Indian Institute of Geomagnetism, 1991).

It would be possible to consider that extensive distribution of permanent magnetic stations was a sufficient reason to a general acceptance of the importance of Geomagnetism. In the same way that many specific geomagnetic researches were been developed, from a narrow but general point of view, the Geomagnetism maintained its restricted characteristic of a particular activity to help navigation.

It was necessary the accomplishment of international scientific campaign, that had been motivated by the geomagnetic phenomena, to obtain an unquestionable understanding that Geomagnetism is the unique science with a natural and accessible laboratory, the Earth, to study a fundamental property of the Universe the Magnetic Field.

6. THE FIRST AND THE SECOND POLAR YEARS. THE IGY

The close association between Geomagnetism and Aeronomy, that was only a conventional bond until recent times, was indeed a very useful one to develop geomagnetic researches. Aldredge (1981) explained in a very clear way, the painful process to create a new and independent science. Fukushima´description (1994) about

this subject is also very instructive.

In 1873, the International Meteorological Organization (IMO) was created and a special *Commission of Terrestrial Magnetism and Atmospheric Electricity* was one of its parts. That Commission formalized an International Polar Year Commission to plan the *First International Polar Year* to be executed in 1892 to 1893. One of the most important objectives of that first international scientific campaign was the study of polar aurora and simultaneous ground level geomagnetic observations. Around twenty papers about those observations had been published (Robin, 1958). It was the first general acceptance of the necessity of a global study of geomagnetic phenomena.

After the inspired Balfour Stewart's article in the Encyclopaedia Britannica (1878 edition), the attention on external electromagnetic events received an increasing consideration. Such interest became larger after the invention and development of radio-waves propagation. The study of the Kennelly-Heaviside layer, involved many groups of radio-engineers and physicists. It was the beginning of the ionospheric studies. In opposition to the effect of dissociating linked disciplines, an interesting phenomenon occurred from the necessity of a multidisciplinary researches of natural events. Truly global scientific associations were created as a consequence of that necessity. Their names suffered changes as it was explained by Aldredge (1981) and Fukushina (1994).

The International Council of Scientific Unions (ICSU, 1976) brought together twelve academies and twelve scientific unions. One of those unions was the International Union of Geodesy and Geophysics (IUGG). Under the IUGG organization, the International Association of Terrestrial Magnetism and Electricity (IATME) was in charge of the geomagnetic studies.

One of the most important IATME realizations was the Second International Polar Year (1932-1933), an improved version of the First Polar Year. Now, many new scientific subjects were included, such as the study of airglow, rapid magnetic variations, Earth currents and radio propagation.

An unusual return to the discussions about an overlap of interests between IATME and the IAM (International Association of Meteorology) took place. In fact, it was difficult to define the real limits of the Atmosphere. However, I guess that an etymological interpretation could be used to solve such intricate question. Meteor comes from the Classical Greece, and it means all known phenomena up to the discovery of the Ionospheric Physics, whose main characteristics are electromagnetic ones.

On the other hand, it is impossible to disconnect ionospheric and magnetospheric events from their association with the Earth's magnetic field, as it is measured from the surface of our planet. Many vivid discussions about this controversy occurred at successive IUGG Meetings. Fukushima (1994), and Aldredge (1981) gave interesting

reports about them. Finally, Chapman closed the dispute with a happy thought by creating the neologism *Aeronomy*.

According him: *Aeronomy signifies that part of the Science of the high atmosphere wich is not usually considered by meteorologists*. There is a curious anecdote about Chapman's proposal. After the approval of his suggestion at the IUGG 1954 Assembly, Chapman was questioned about his neologism, and he answered: *Do you know the meaning of Aeronomy ? No? I do not know too.*

The IAGA (International Association of Geomagnetism and Aeronomy) was born, to substitute IATME functions. An interesting question was placed about the words *Geomagnetism* and *Aeronomy*. The word Geomagnetism was also suggested by Chapman (1938). His etymological arguments were irrefutable, and they are skilfully improved by Fukushima (1994). Since 1951, at the Brussels IUGG Assembly, the idea of a 3rd. International Polar Year gained support from the various IUGG branches. However, a broader campaign was necessary. A worldwide coverage of geophysical phenomena was imposed by the development of new disciplines and a sensible improvement of communications on Science. The International Geophysical Year (IGY) was approved by ICSU to be executed in the period July 1957 to December 1958 (Robin, 1956).

The IGY was the greatest scientific effort even made by Mankind. For its results and consequences, it could be considered as a turning point in the History of Science. If we consider that sixty seven counties and more than 30,000 scientists were involved on its programs, it is possible to understand its magnitude.

A personal remembrance from IGY publications is alive in my memory. After the IGY campaign, I was charged to organize all related papers and reports. I remember the smile of the late Lelio Gama, Director of the National Observatory of Brazil, when he said: "It will be a good opportunity to learn Geophysics". A large room was plenty of books and papers. Some months were spent to finish my task.

All branches of Geophysics presented a real jump on their development. The Space Age was born with the Sputnik and the Explorer. The Van Allen radiation belts were discovered. A new scientific landscape was visible. Our Science, the Geomagnetism, grew-up to its actual high scientific level. If we make a statistical survey about the number of magnetic observatories in operation, it is possible to understand such explosive development (Malin, 1987).

Unfortunately, the number of active observatories in 1958, about 200, had been drastically reduced. Many important permanent stations had been closed, such as Easter Island and Paramaribo observatories. Cheerfully, the quality of the remaining stations has grown, and new observatories are planned to be installed.

We must be very confident on a bright future for our Geomagnetism, an Independent Science.

REFERENCES

Alldredge, L. R., 1981. Evolution of the IAGA organization. IAGA News, no. 20.
Ancellin, J., 1986. Un homme de Science du XIX Siecle: l'astronome Emmanuel Liais. Imp. Ocep. Cherbourg.
Barreto, L. M., 1987. Observatorio Nacional: 160 años de Historian. Acad. Bras. de Ciencias. Rio de Janeiro.
Barreto, L. M., 1988. Secular Variation and Geomagnetic Normal Field Modelling in Brazil. Deuts. Hydrogr. Zeitsch. N° 4.
Barreto, L. M., 1991. Geomagnetism in Brazil. Presented at the IAGA General Assembly. Vienna.
Barreto, L. M., 1995. Emmanuel Liais: a scientist of two continents. Accepted for publication in GEOACTA, AAGG, Buenos Aires.
Chapman, S., 1938. Geomagnetism or Terrestrial Magnetism. J. Geophys. Res. 43.
Chapman, S. and Bartels, J., 1940. Geomagnetism. Oxford and Clarendon Press.
Flamarion, C., 1911. Mémoires biographiques et philosophiques d'un astronome. Paris.
Fukushina, N., 1994. Some topics and historical episodes in Geomagnetism and Aeronomy. J. Geophys. Res. Vol.99, A-10.
Gilbert, W., 1600. De Magnet. English translation. Basic Books, published in 1958.
Halley, E., 1693. Phil. Trans. R. Soc. of London, N° 17.
ICSU, 1976. ICSU Organization and Activities. Paris.
Indian Institute of Geomagnetism, 1991-150 years of Geomagnetism. Bombay.
Liais, E., 1851. Sur la hauter des aurores boreales: méthode pour determiner cette hauter. Ann. Acad. Sc. Nat. de Cherbourg.
Liais, E., 1852. Mémoire sur un bolide observé dans le Department de la Manche. Ann. Acad. Sc. Nat. de Cherbourg.
Liais, E., 1853 I. Influence de la Mer sur les climats. Ann. Acad. Sc. Nat. de Cherbourg.
Liais, E., 1853 II. Observations sur une aurore boreale. Ann. Acad. Sc. Nat. de Cherbourg.
Liais, E., 1881. L'Espace Céleste. Garnier -Fr 2eme. ed. Paris.
Liais, E., 1888. Annales de l'Imperial Observatoire. Rio de Janeiro.
Malin, S. , 1987. Historical Introduction to Geomagnetism. In "Geomagnetism", Vol I, J. A. Jacobs (Ed). Academic Press.
May, W. E., 1956. Compass. In "Encyclopaedia Britannica", London, 167 to 175.
Morize, H., 1987. Observatorio Astronómico: um século de Historian. CNPq. Rio de Janeiro.
Needham, J., 1962. Science and Civilization in China. Vol. 4 part 1. Cambridge Univ.Press.
Robin, G., 1956. Why an International Geophysical Year. Geographical Magazine, Vol.28, N ° 12.

GEOACTA, 22, 134-143, 1997

RESPONSE OF THE OCEAN MIXED LAYER, OFF THE EAST COAST OF PENINSULAR MALAYSIA, DURING THE NORTH-EAST AND SOUTH-WEST MONSOONS

Mohd Nasir Saadon and Alejandro Camerlengo
University College (UPM), Mengabang Telipot, 21030 Kuala Terengganu - Malaysia

ABSTRACT

The behaviour of the mixed layer, off Kuala Terengganu, during the north-east and south-west monsoons is addressed. Temperature and salinity profiles, for both seasons, are analysed. The results are quite conclusive. In the mixed layer, temperature and salinity have different characteristics during each season, being lower during the north-east monsoon. The depth of the mixed layer is shallower during the south-west monsoon. Two distinctive water masses are detected during both seasons.

RESUMEN

Se estudia la respuesta de la capa de mezcla del océano a la influencia de los monzones del Noreste y del Sudoeste, en la costa este de la península Malaya. Para ello se analizan los perfiles verticales de temperatura y salinidad en ambas estaciones monzónicas. Los resultados son concluyentes. Durante el Monzón del Noreste la temperatura y la salinidad de la capa de mezcla son menores y la profundidad de la capa mezcla es mayor que durante el Monzón del Sudoeste. Se distinguen dos masas de agua de distintas características durante las diferentes estaciones monzónicas.

1. INTRODUCTION

The ocean boundary layer can be considered as an intermediate zone between the deep ocean and the atmosphere. The ocean boundary layer extends from the sea surface to a depth ranging between 10 and 150 meters. Sometimes, the depth of the mixed layer is compared with the depth of the Ekman layer. This comparison is not correct, due to the fact that the Ekman layer depth depends on the wind speed at the time of the observation. On the other hand, the mixed layer depth depends on the past history of the wind (Pond & Pickard, 1978).

Vertical exchange processes between the ocean and the atmosphere, as well as vertical mixing within the upper layers of the ocean, will affect local conditions more effectively than horizontal processes. Usually the upper ocean layers are treated as being

homogeneous along the horizontal plane. Therefore, the horizontal derivatives are neglected in one-dimensional models of the mixed layer. Thus, only changes in the vertical are taken into account in such models (Niiler and Krauss, 1977). This effect has been taken into consideration in one-dimensional numerical models of the ocean mixed layer (Schopf and Cane, 1983).

The aim of this investigation is to gain some understanding of the behaviour of the mixed layer, off the east coast of Peninsular Malaysia, during both monsoon seasons. For this purpose, both the temperature and the salinity profiles, during the period ranging from October 26 to October 30, 1995, are analysed (Saadon and Yasin, 1994). Our results are compared with the results of Lokman *et al.* (1986). The mentioned authors studied the temperature and salinity profiles during a typical South-west monsoon season.

2. CLIMATOLOGY OF THE AREA

The weather pattern of the east coast of Peninsular Malaysia is greatly influenced by the monsoons. In the winter seasons, the air mass over Asia is cooler than over the surrounding areas. A high pressure system is enhanced. During the same period, November through March, the air mass over Australia is warmer than over the surrounding areas. The natural consequence is a low pressure system over Australia. A result of the combined effect of these two pressure systems is a north-easterly wind over the South China Sea. This weather system is characteristic of the north-east monsoon season.

Conversely, during the southern hemisphere winter, a high and a low pressure system over Australia and Asia, respectively, are enhanced. During May through September, these two pressure systems will produce a south-westerly wind over the South-east Asian region. This system is called the south-west monsoon season. Cloudless skies over the eastern coast of Peninsula Malaysia are observed during this period.

Two transitional periods (usually occurring in April and October, respectively) are observed between the two monsoon seasons. These transitional periods have a duration, ranging from four to seven weeks. Heavy rainfall in the east coast of Peninsular Malaysia is usually associated to the north-east monsoon. The east coast is considered the wet belt of Peninsular Malaysia, with an annual rainfall of 2800 mm. Maximum precipitation usually occurs during the months of November and December (Chua, 1984).

3. MATERIALS AND METHODS

A cruise was conducted from October 26 to October 30, 1993. The research vessel used for the cruise was the KL. PAUS, owned by the Malaysian Department of Fisheries.

The area covered by this study was about 61,600 km^2 (Fig. 1). Temperature and salinity were measured with an Inter-ocean S4-CTD. The CTD was deployed at 33 sampling stations. However, only 12 stations were considered in our study because they were in the same study area as presented by Lokman *et al.* (1986).

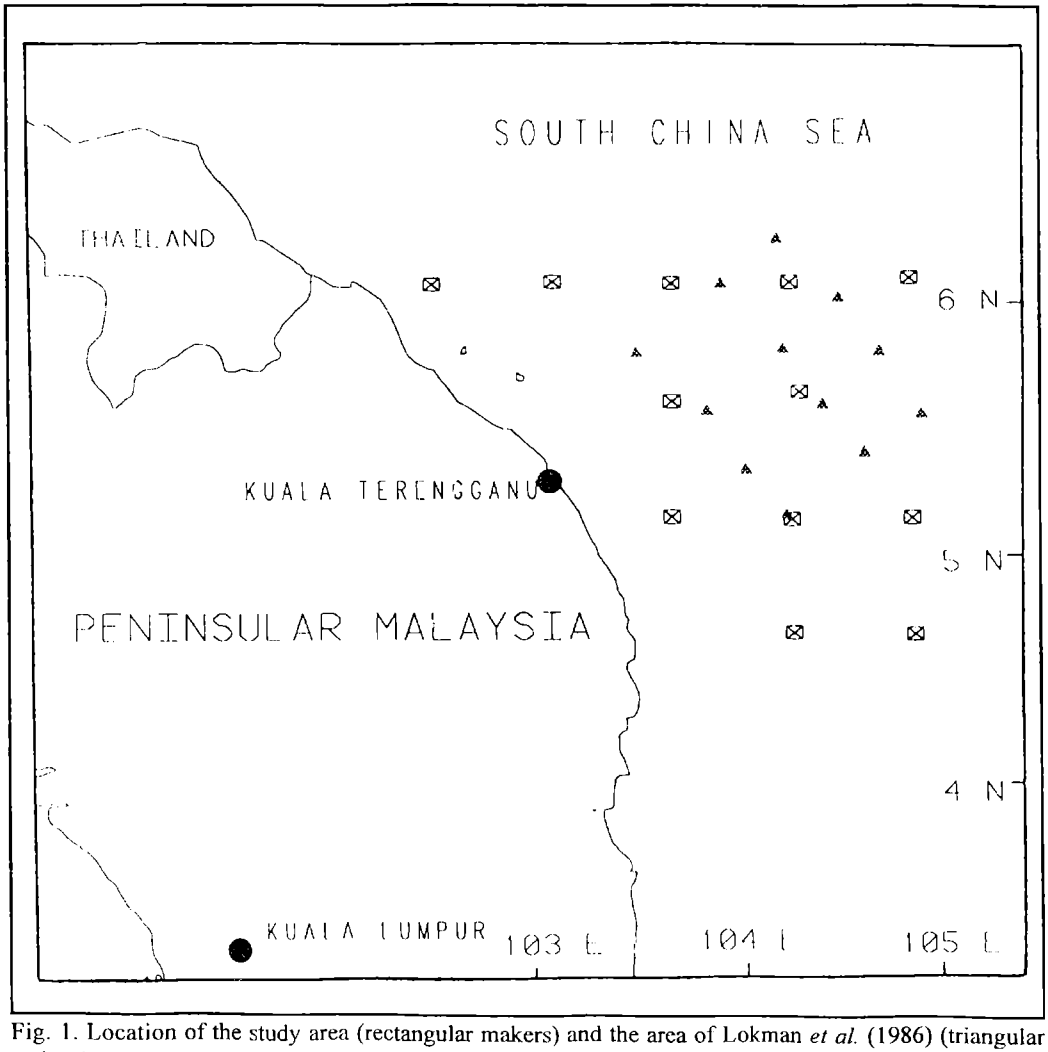

Fig. 1. Location of the study area (rectangular makers) and the area of Lokman *et al.* (1986) (triangular makers).

4. DISCUSSION AND CONCLUSIONS

In extratropical latitudes, the distributions of atmospheric wind forcing are very similar all year round. However, the intensity of the wind is greater in winter than during any other time of the year (Elsberry and Camp, 1978; Elsberry and Raney, 1978).

The source of mechanical energy is proportional to the cubic power of the friction velocity. Due to the strong wind forcing during the passage of a winter storm, an upward heat flux from the ocean to the atmosphere results. Mechanical mixing is enhanced. As a consequence of the upward heat flux, the thermocline deepens. Therefore, the depth of the mixed layer increases. Due to the entrainment from the lower layers of the sea, the cooling effect continues for approximately a week, at the wake of the storm's passage (Camerlengo, 1982).

In summer, the forcing due to atmospheric wind is weaker than in winter. Consequently, the entrainment at the base of oceanic boundary layer is almost nonexistent. As a direct consequence of the stabilising effect of the surface heating, the mixed layer becomes shallower (Elsberry and Camp, 1978; Elsberry and Raney, 1978).

In the South China Sea, the intensity of the monsoons has to be taken into consideration. Due to the fact that the north-east monsoon has stronger winds than the south-west monsoon, it is expected that greater masses of water should be entrained from the lower layers of the ocean. Therefore, the depth of the mixed layer should be greater and slightly cooler, during the north-east monsoon.

In his linear theory of the ocean's response to the displacement of a hurricane, Geisler (1970) showed the existence of inertia gravity waves at the wake of the cyclone's path. This result was confirmed by the observational study at the wake of hurricane Eloise in 1975 (Black and Whitee, 1976), and by numerical simulation (Chang and Anthes, 1978).

Geisler's theory (1970) forecasted, that very far at the rear of the storm, after the dispersion of the inertia gravity waves, the motion will be geostrophically balanced. Due to the absence of external forcing, the kinetic energy of the ocean is rapidly redistributed. Camerlengo (1982) showed that the e-folding time scale of dissipation of kinetic energy after the storm's passage, is of ten days. In the absence of any external atmospheric forcing, the kinetic energy in the ocean is rapidly redistributed. A shorter e-folding time scale would be expected if vertical mixing has been taken into consideration, in that study.

Due to overcast skies during the north-east monsoon season, the mean monthly air temperature drops by one or two degrees Celsius. During this same period, the sea surface temperature (SST) charts by Zainal (1993) and Morgan and Valencia (1983) shows a decrease of one degree Celsius, as compared to the south-west monsoon season.

All along the eastern coastline, the combined effect of freshwater discharge from rivers and heavy precipitation affects the salinity pattern. In effect, Zainal (1993) reported lower salinity water masses, all along the eastern coast of the Peninsular Malaysia. This lower salinity water mass is a natural consequence of freshwater discharge (from rivers), due to heavier precipitation in this area.

During the north-east monsoon the water mass tends to pile up against the western boundary of the South China Sea. Sea levels are higher than at any other time of the year. Due to the combined effects of geostrophy and coastal geometry the water masses tend to flow equatorwards, in a counterclockwise circulation, further reducing the salinity pattern in the area under consideration (Chua, 1984; Morgan and Valencia, 1983; Wyrtki, 1961).

Winds are stronger during the north-east monsoon (Wyrtki, 1961). These stronger winds will generate higher waves in the shallower areas of the east coast. Anon (1991) reported that during this same period, maximum wind wave heights range from three to four meters along the east coast. During the south-west monsoon, a depression of the free surface elevation at the western boundary of the South China Sea is recorded. Due to geostrophy and coastal geometry the water masses flow poleward along the east coast of Peninsular Malaysia into the Gulf of Thailand in a clockwise circulation (Chua, 1984; Morgan and Valencia, 1983; Wyrtki, 1961).

Temperature profiles of the 12 stations gathered in this investigation and in Lokman *et al.* (1986) are shown in Fig. 2. It can be readily seen that the temperature, in the mixed layer during the north-east monsoon season, ranges from 29.3 to 29.8 °C. However, for the south-west monsoon season, the temperature of mixed layer is usually greater than 30°C.

During the north-east monsoon season, skies are usually overcast. Heavy precipitation do occur within this period. Warming of the ocean surface by solar radiation is dramatically reduced. Stronger north-east winds enhances evaporation. All these factors combined explain the decrease in temperature of the mixed layer.

For the reasons explained above, the depth of the mixed layer is greater during the north-east monsoon (Fig. 2). Salinity profiles, for both seasons are shown in Fig 3. It can readily be observed that salinity values for the north-east monsoon season are lower than in its south-west counterpart. This is due to heavier precipitation and freshwater discharge from rivers along the east coast of Peninsular Malaysia and the Gulf of Thailand, which occurs during the north-east monsoon season.

During the south-west monsoon season, the halocline layer is well defined in most of the stations. This is not the case for the stations sampled during the north-east monsoon season. Fig. 4 shows the T-S diagrams for both seasons. The existence of two different water masses, for both seasons, along the east coast of Peninsular Malaysia, is clearly established.

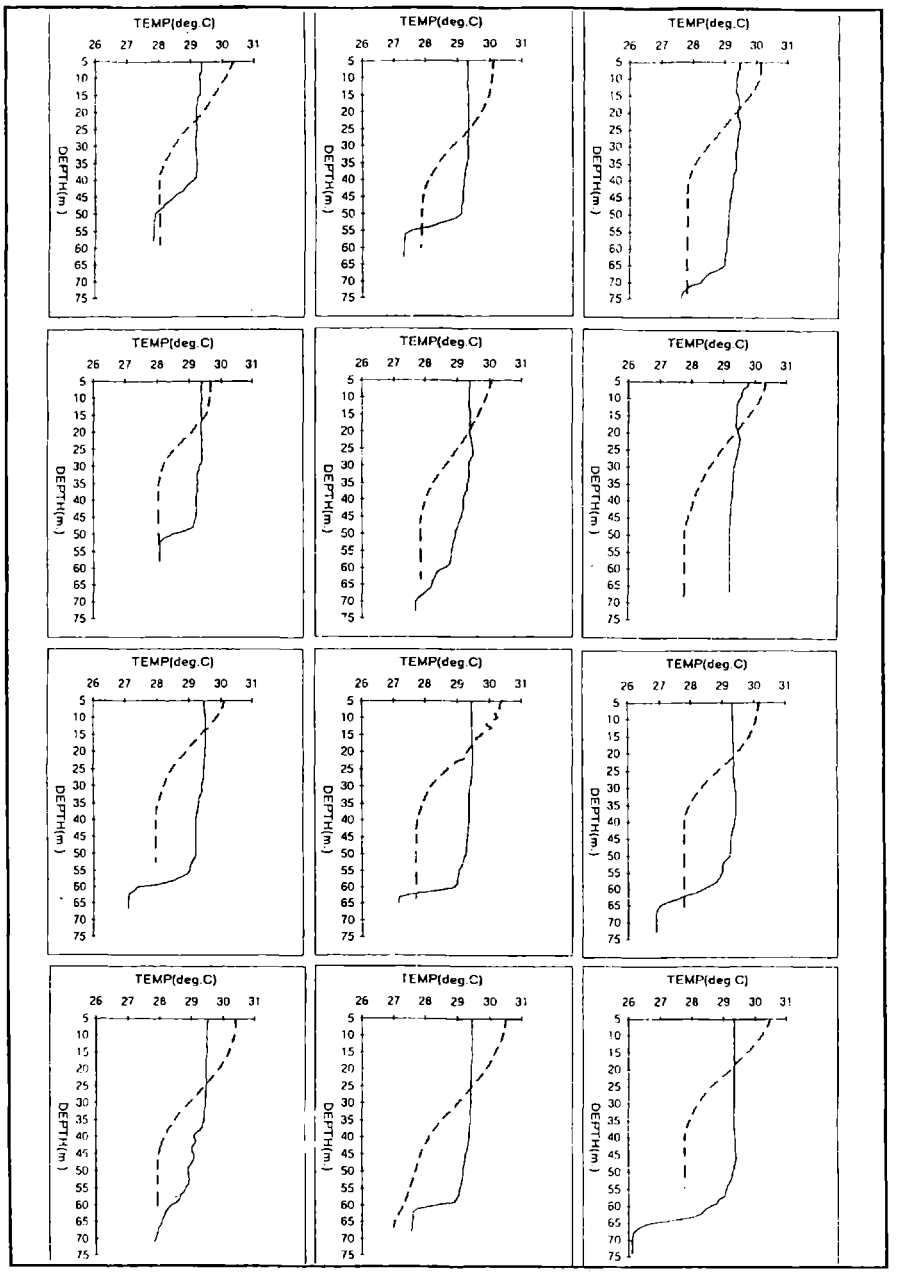

Figure: 2. Temperature profiles of 12 stations during the north-east (solid lines) and the south-west (broken lines) monsoon seasons. The stations represented in the figure, for both monsoon seasons, are not in the same location but they are in a very close proximity.

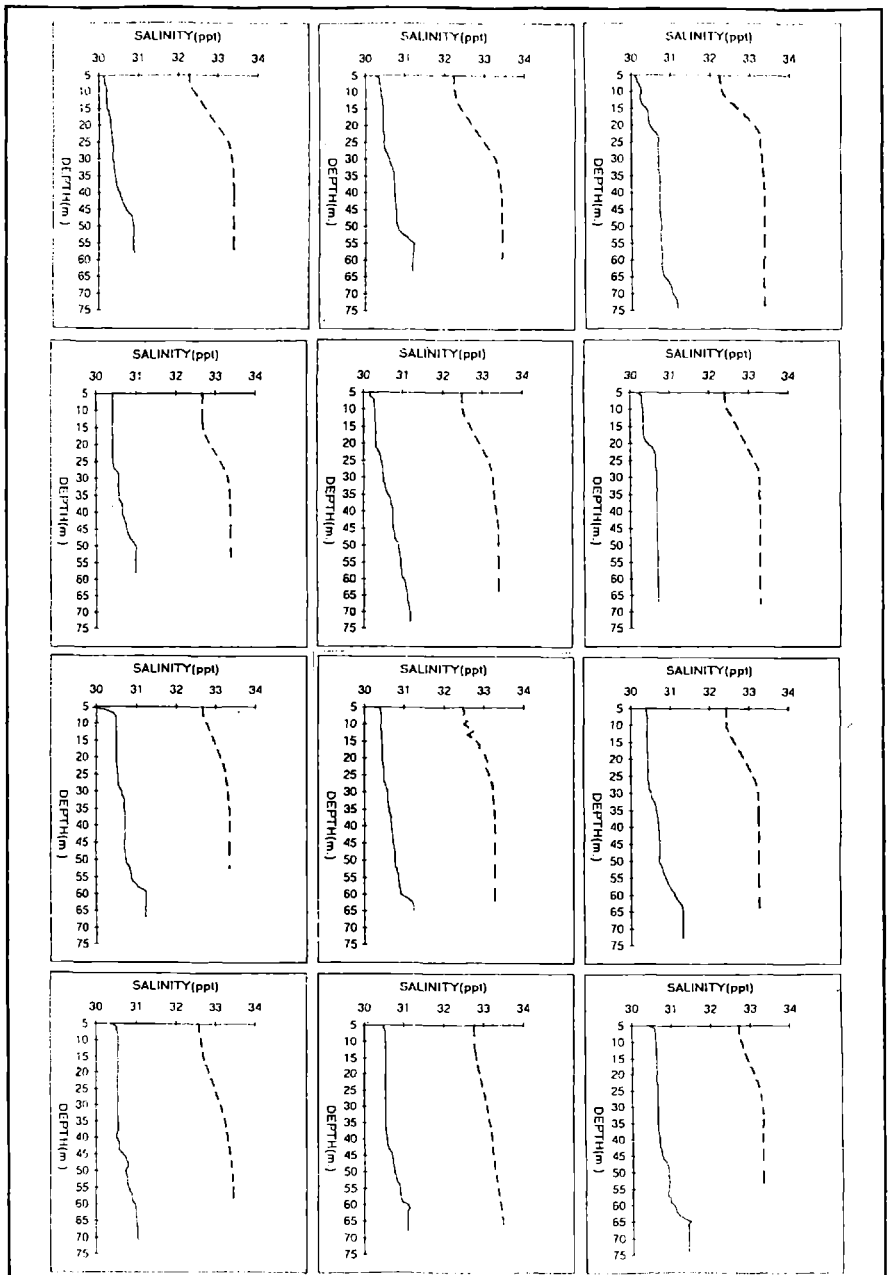

Figure: 3. Salinity profiles of 12 stations during the northeast (solid lines) and the south-west (broken lines) monsoon seasons. The stations represented in the figure, for both monsoon seasons, are not in the same location but they are in a very close proximity.

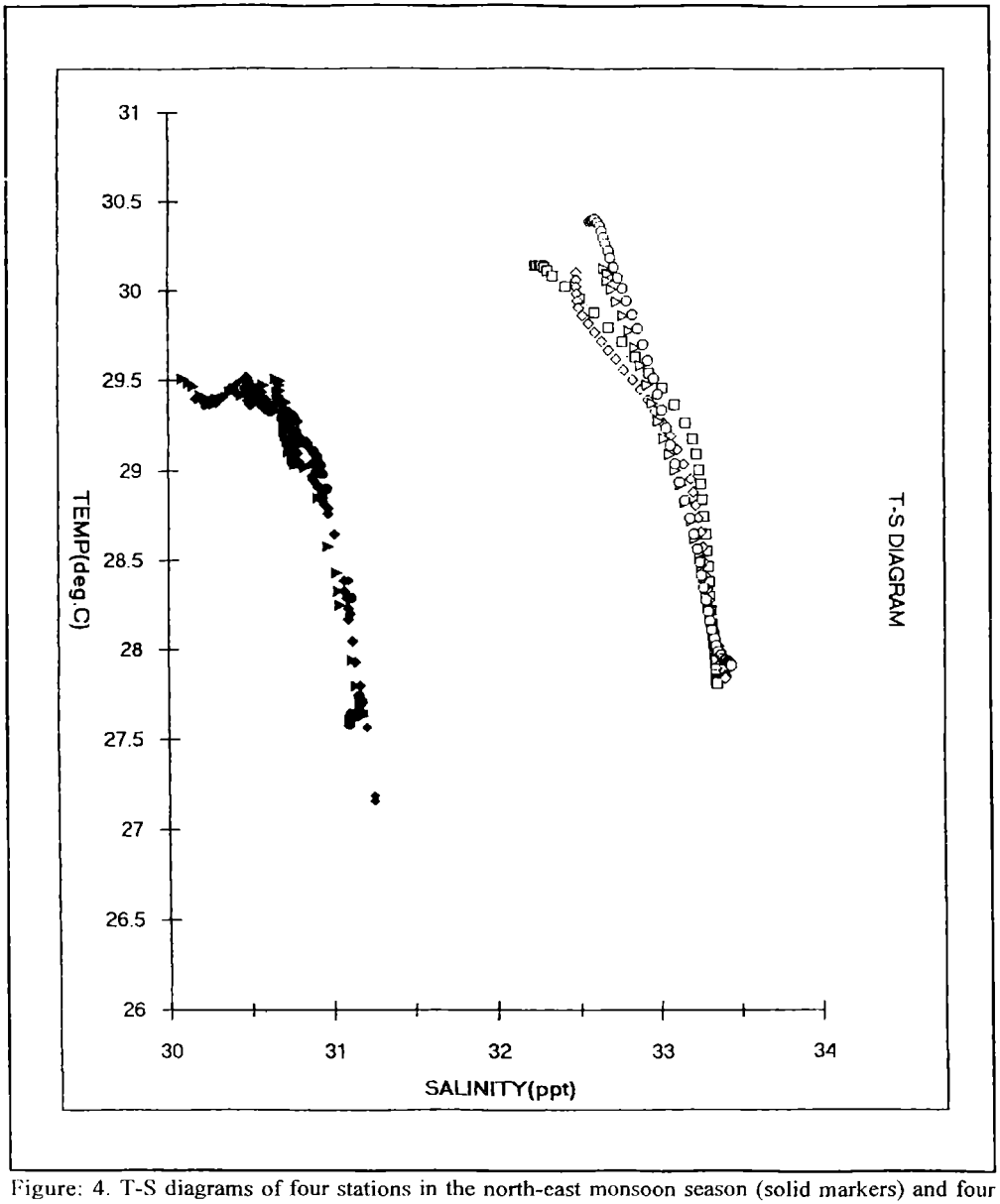

Figure: 4. T-S diagrams of four stations in the north-east monsoon season (solid markers) and four stations in the south-west monsoon season (empty markers).

Acknowledgments

This study was financed by the Malaysian Department of Fisheries and Universiti Pertanian Malaysia. The equipment, as well as the technical staff needed for this study was provided by the Faculty of Fisheries and Marine Science, UPM. The authors gratefully acknowledge their support.

REFERENCES

Anon, 1991: Monthly Summary of Marine Meteorological Observations. Year 1991. Issued under the authority of the Director General. Malaysian Meteorological Service. Petaling Jaya, 48 pp.

Black, P.G. and G. Whitee, 1976: The Effect of Hurricane Eloise on the Gulf of Mexico. Proc. Second Conf. Ocean-Atmosphere Interaction, Seattle, Amer. Meteor. Soc. (Abstract in Bull. Amer. Meteor. Soc., 57, 139).

Camerlengo, A. L., 1982: Large-scale Response of the Pacific Subarctic Front to Momentum Transfer: A numerical Study. J. Phys. Ocean., 12, 1106-1121.

Chang, S.W. and R. A. Anthes, 1978: Numerical Simulations of the Ocean's Non-linear, Baroclinic Response to Translating Cyclones. J. Phys. Ocean., 8, 468-480.

Chua, T. E., 1984: Physical Environments of the East Coast of Peninsular Malaysia. Chua T.E. and J.K. Charles (eds.). Penerbit Univ. Sains Malaysia, Penang. Pages 1-10.

Elsberry, R. L. and N. T. Camp, 1978: Oceanic Thermal Response to Strong Atmospheric Forcing, J. Phys. Ocean., 8, 206-214.

Elsberry, R.L. and S. D. Raney, 1978: Sea Surface Temperature Response to Variations in Atmospheric Wind Forcing, J. Phys. Ocean., 8, 881-887.

Geisler, J. E., 1970: Linear Theory of the Response of a Two-layer Ocean to a Moving Hurricane. Geophys. Fluid Dyn., 1, 249-272.

Lokman, H., R. Yacoob and N. A. M. Shazili, 1986: Some Measurements of Temperature and Salinity on a Portion of the South China Sea. In: Ekspedisi Matahari ' 85. A Study on the Offshore Waters of the Malaysian EEZ. A.K.M.
Mohsin, M.I. Mohamed and M.A. Ambak (eds.). Faculty of Fisheries and Marine Science, UPM. Occasional Publication No. 3, 49-79.

Morgan, J.R. and M.J. Valencia, 1983: The Natural Environment Setting. In: Atlas for Marine Policy in South-east Asian Seas. J.R. Morgan and M.J. Valencia (eds.). University of California Press, 4-17.

Niiler, P.P. and E.B. Krauss, 1977: One-dimensional Models of the Upper Ocean.
Modelling and Prediction of the Upper Layers of the Ocean. E.B. Krauss (ed.). Pergamon Press, 143-172.

Pond, S. and G.L. Pickard, 1978: Introductory Dynamical Oceanography. Pergamon Press, 241 pages.

Saadon, M.N. and A.H. Yasin, 1994: Temperature and Salinity Profile Variations in the East Coast of Peninsular Malaysia during the North-east Monsoon, Third IOC-WESTPAC International Symposium. Bali, Indonesia, 22-26 Nov.

Schopf, P.S. and M. Cane, 1983: On Equatorial Dynamics, Mixed Layer Physics and Sea Surface Temperature, J. Phys. Ocean., 13, 917-935.

Wyrtki, K., 1961: Physical Oceanography of the South-east Asian Waters. In: Naga Report Volume 2. Univ. of California. Scripps Institution of Oceanography. California, 195 pp.
Zainal, A., 1993: Seasonal Variation in the Hydrography of the South China Sea. M.Sc. Thesis. Univ. College of North Wales. Bangor, Wales, 103 pp.

GEOACTA 22, 144-154, 1997

SEA LEVEL CHARACTERISTICS IN PUERTO QUEQUÉN

María Cintia Piccolo[1,2] and Gerardo M. E. Perillo[1,3]

[1]Instituto Argentino de Oceanografía, Casilla de Correo N° 107, 8000 Bahía Blanca

[2]Depto de Geografía, Universidad Nacional del Sur, 12 de Octubre y San Juan, Bahía Blanca.

[3]Depto de Geología, Universidad Nacional del Sur, San Juan 670, 8000 Bahía Blanca.

ABSTRACT

Sea level observations at the mouth of the Quequén Grande river, Puerto Quequén station, are used to study the sea level variation in different time scales: tidal and subtidal fluctuations, sea level variation and seiches in the estuary. Four tidal constituents are found to be the most active in Puerto Quequén, with M_2 being the most important. At subtidal frequencies, the sea level variations are primarily forced by atmospheric forcing on the adjacent shelf. Spectral analysis evidenced atmospheric forcing into the estuary at macro, synoptic and local scale.

RESUMEN

Se estudian las fluctuaciones mareales y submareales, las variaciones del nivel del mar y los seiches en el estuario del río Quequén Grande mediante observaciones del nivel de mar en la estación mareográfica de Puerto Quequén, Cuatro componentes astronómicas son las más activas en el estuario, siendo M_2 la más importante. Las fluctuaciones submareales son originadas primariamente por fluctuaciones en el nivel del mar generadas por el forzamiento atmosférico en la plataforma continental interior adyacente al estuario. El análisis espectral de las variaciones del nivel del mar muestra evidencia de forzamiento atmosférico en escala local, sinóptica y macroescala.

1. INTRODUCTION

Water level variations are known to occur in response to a variety of forces, including the periodic astronomical forces of the Earth-Moon-Sun system, the aperiodic or periodic meteorological forces, and dynamic or thermodynamic forces associated with the motion or properties of seawater. The relative magnitude of these forces are highly variable both in space and time. Therefore, sea level variations have been extensively studied in different time scales.

Many authors have analyzed the large scales tidal features ranging from yearly to monthly values (ie; Balay, 1958; Hicks and Shofnos, 1965; Hicks, 1968; Church, 1980; D'Onofrio *et al*, 1981; Seim, 1987; Bongers and Wyrtki, 1987; Woodworth *et al*, 1991) and they proved that every place presents its own and particular variability. On the other hand, subtidal sea level variations have been extensively examined for evidence of wind-driven coastal circulation and the seasonal variation of oceanic circulation (ie., Wang, 1979; Chao and Pietrafesa, 1980; Schwing, 1989).

In coastal areas, especially those with a relatively small astronomical tide, meteorological forces can play a significant and sometimes dominant role in creating water level variations over time scales ranging from a few hours to several days. This is especially true in estuaries or semi-enclosed coastal bays, where the constricting effects of narrow channels and shallow water serve both to damp progressive tidal waves of astronomical origin and to amplify meteorological effects (Smith, 1974). Storm surges are one of the major processes that have been extensively studied in those environments (i.e., Proudman, 1955; Provis and Radok, 1979; Murty and El-Sabh, 1981).

Little is known about the tides and sea level variations in the Quequén river estuary. The estuary is situated in the SE of the Buenos Aires province (38° 33' S - 58° 43' W), Argentina. In the mouth of the estuary is located the Quequén harbor. The harbor is a very active commercial and industrial site, where many of the main products of Argentina are exported. The knowledge of the circulation and dynamics of the area is useful. However, few works have been performed on the subject.

Lanfredi *et al.* (1988) have studied the variations of the mean sea level in Puerto Quequén. They analyzed 64 years of hourly tidal heights and obtained the long term trend of 16.09 cm/100 yr. The mean tidal range in Puerto Quequén is 0.8866 m. The most important astronomical components are the M_2, O_1 and K_1 (Piccolo et al., 1995). The objective of the present study is to describe and analyze the characteristics of the sea level in the Quequén Grande estuary in different time scales.

2. METHODOLOGY

The tidal data were supplied by Dirección Nacional de Construcciones Portuarias and Vías Navegables of Puerto Quequén, Argentina. The data consisted of daily, monthly and hourly values, in different periods that are mentioned along the present work. Five years (1989-1993) of hourly data were use to calculate the astronomical tides by the methods of Godin (1972) and Foreman (1978).

Non tidal sea level variations were calculated for the period 1989-1993. For operational purposes, storm surges are defined as the difference between the recorded water level and the predicted astronomical tide. This traditional method of subtracting the

astronomical tide from the observed water level and treating the residue as storm surge assumes that tide and surge are linearly additive and there is no nonlinear interaction (Murty and El-Sabh, 1981). This form of nontidal sea level fluctuation were calculated from the study period with the purpose of determine its magnitude in the estuary. Standard statistical analysis were performed with the surge information.

Averaging of hourly sea level values over the study period permitted the calculation of monthly mean sea level. Lanfredi *et al* (1988) presented the monthly and annual mean sea level in Puerto Quequén from 1918 to 1982. The data was completed and analyzed with new information. Spectral analysis was performed using the Fast Fourier Transform technique.

3. RESULTS AND DISCUSSION

3.1 General characteristics

Considering the last twenty years, the mean annual value of the tide in Quequén Grande estuary is 0.88 m. However, the former value changes if a longer period is considered. For the period 1918-1994, the mean annual tide is 0.97 m. Fig. 1 shows the spectral analysis of the hourly data for all 1993. The main harmonic tidal constituents are the M_2, K_1 and O_1. The shallow water constituent, M_4, is also significant.

The harmonic constituents of a particular location are called tidal constants, however it is known that they change from year to year. Restricting the analysis to the period 1989-1993 and to the three main constants, in Table 1 is shown their change in amplitude and phase. An important change in amplitude and phase is found during the

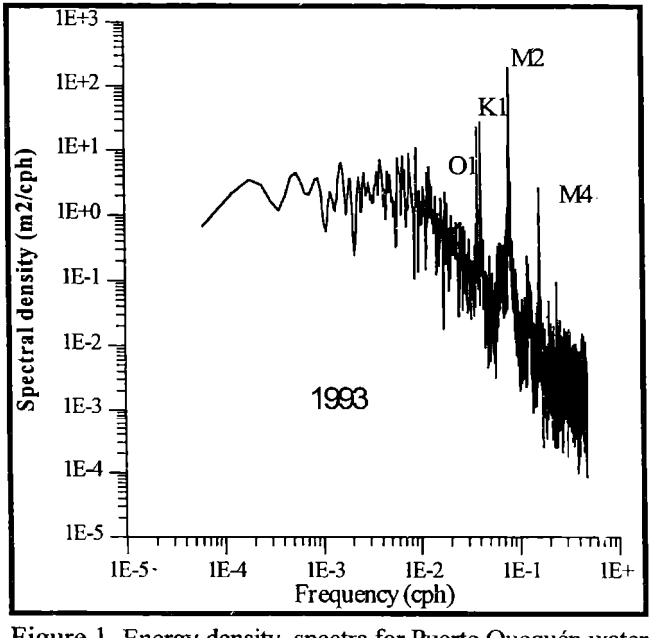

Figure 1. Energy density spectra for Puerto Quequén water level.

study period for all the astronomical constituents. The observed annual variations are significant according to the results presented in Pugh and Faull (1982). Therefore, a more complete study should be made taking decades or centuries to analyze the trends in the tidal constants, but that is beyond the purpose of the present work. An example of the sea level variation during June 1992 is presented in Figure 2. An important semidiurnal inequality is present in the record.

Year	M_2		K_1		O_1	
	A (m)	G (°)	A (m)	G (°)	A (m)	G (°)
1989	0.438	178	0.174	74.73	0.176	3.66
1990	0.439	75.13	0.173	72.21	0.169	265
1991	0.44	333	0.161	69.46	0.164	168.8
1992	0.401	248.9	0.143	257.6	0.137	265.8
1993	0.363	165.2	0.145	78.71	0.137	3.44

Table 1. Amplitude and local phase angles for the principal diurnal and semi-diurnal tidal constituents at Puerto Quequén.

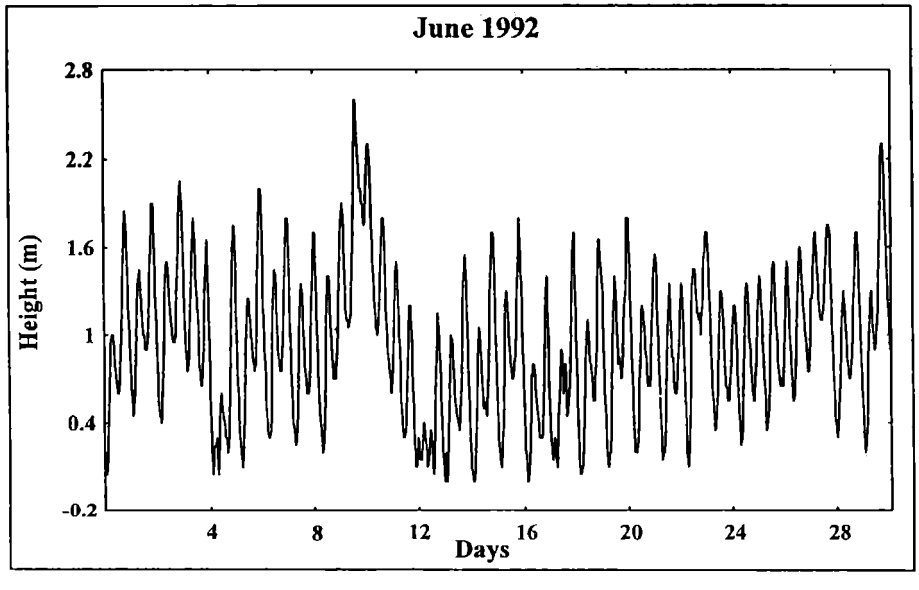

Figura 2. Example of a monthly sea level record.

The semi-diurnal, diurnal or mixed nature of the tide is defined by the ratio of the principal diurnal and semidiurnal constituents: $F = (O_1+K_1)/(M_2+S_2)$. The magnitude of this ratio at Puerto Quequén is 0.68, indicating that the tide is a predominantly semi-diurnal, mixed tide.

Yearly maximum tides were analyzed for the period 1958-1994. The highest values were registered in 1962 and 1979 with 3.10 m. However, in 1975 the maximum tide reached the value of 2.30 m.

3.2 Time variance

The seasonal departures from the annual mean differ considerably from one year to the next, due largely to anomalies in weather (atmosphere and ocean). Table 2 shows the

Month	Mean (cm)	Minimum departure	Maximum departure	SD
January	4.7	-7	16	5.2
February	6.5	-9	19	5.3
March	4.4	-13	17	6.2
April	5.3	-12	28	7.2
May	3.9	-20	17	6.4
June	2.4	-11	24	6.7
July	-3	-34	9	6.7
August	-6.3	-21	8	5.9
September	-10.5	-28	6	5.9
October	-7.1	-20	7	5.1
November	-2.2	-21	16	5.6
December	2.2	-15	15	5.9

Table 2. Standard deviation per year for each month.

standard deviation, SD, of a monthly departure from the annual average, taken year by year, based on the procedure by Patullo et al. (1955). The study period was 76 years.

There is a significant seasonal variation. From January to June the monthly values were greater than the annual one. On the contrary from July to November the monthly values were smaller. The standard deviation calculated for the Quequén Grande estuary is smallest in October and greatest in April. According to Patullo et al. (1955) the April SD for La Plata, Buenos Aires and Montevideo are 8.0, 6.3 and 6.2 respectively. Therefore, the calculated standard deviations are similar to the ones calculated for the Río de la Plata estuary. Both estuaries are located in the Buenos Aires province and they present similar tidal ranges.

3.3 Low Frequency Perturbations of the Tide

In many harbors is common to find a series of oscillations superimposed to the normal astronomical tidal record; however, their presence is observed only a small percentage of the time. In the case of Puerto Quequén Tide Gage records (Fig. 3) these oscillations are practically continuous having amplitudes of few tens of a meter. In certain occasions the oscillations become strongly enhanced reaching amplitudes up to 1.5 m within 5 to 20 minutes. Such significant changes in water level occurring within short times induce rapid modifications in the harbor depth affecting the navigation in it. In fact, this analysis was initiated due to two major incidents that happened in March and May, 1992 in which two loaded cargo vessels were leaving the harbor when events of 1.2 and 1.5 m, respectively, produced that their hulls touched the bottom. Fortunately there were no damages nor injuries because the vessels were relatively small compared with the ones that operate there normally.

Balay (1961) and Inman et al. (1962) have mentioned the occurrence of typical oscillations in tidal records both in Quequén and Mar del Plata (in two nearby tide stations), both places are separated by 124 km. In the latter article the authors tried unsuccessfully to correlate the fluctuations to edge wave propagating along the broad Argentine continental shelf. Also, the sampling rate employed by them was 5 minutes; therefore, they were looking for large scale processes beyond the resonance period of small harbors.

Balay (1961) commented about a storm surge that produced the flooding of all downtown Mar del Plata beaches causing panic and damage on the tourist that were on the beach January 21, 1954. Similar events repeated several times in the last decades. Those that have been reported in the press were associated to very good weather conditions on the coast that helped large concentrations of beach goers. In all cases the tourist were surprised because no previous warning was possible. According to Balay (1961) these events can be related to rapid changes on the atmospheric pressure over the

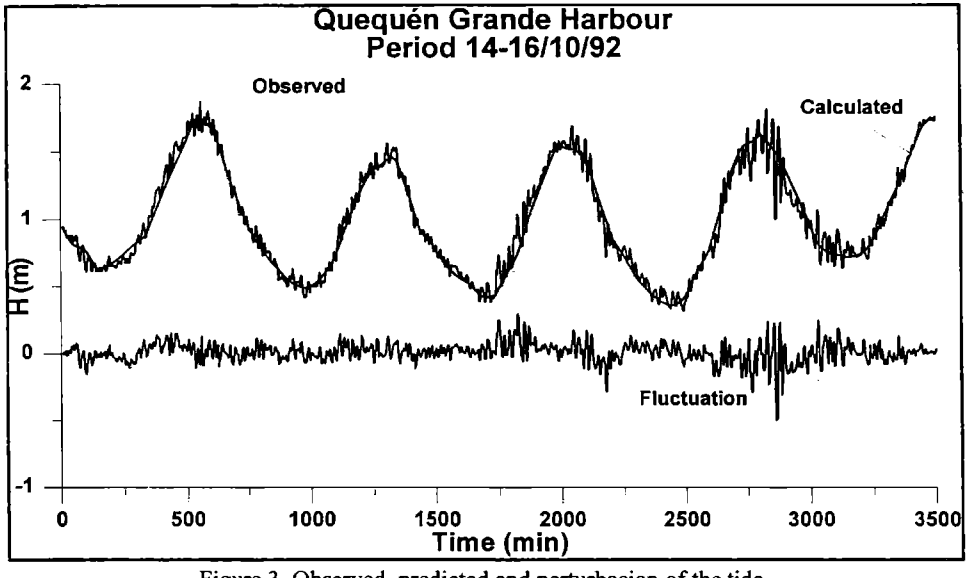

Figure 3. Observed, predicted and perturbacion of the tide .

shelf. In the present case we have analyzed a total of 20 100-hr tidal records from the Quequén tidal station which is located some 1000 m from the mouth of the harbor.

All records were digitized at approximately 1 min intervals. Since the resulting data file presented unequal time intervals, the sampled data was interpolated using the Stinoman method (Perillo and Piccolo, 1991) and resampled to $\Delta t = 1$ min. The record for October, 1992 is shown in Fig. 3. The actual tidal curve estimated by sampling every hour was interpolated with the same method at also 1 min interval and subtracted from the original record. The resulting perturbation record is also shown in Fig. 3.

Spectral analysis using FFT of these records (i.e., Fig. 4) show that energy peaks appear at periods 25, 6.5, 5.2, 4.3, 3.4 and 3 min. Also the high frequency part of the spectra is proportional to $f^{5/3}$. These periods cannot be correlated to atmospheric forcing since there were no meteorological data available for that period. An automatic weather station was installed at only 500 m of the tidal gage only in August 1995.

To establish if the periods could be related to the normal resonance of the harbor. For an open basin with the characteristics of the Quequén harbor, Sorensen (1978) proposed a classical expression for the resonant period (T_n)

$$T_n = \frac{4L}{(2k + 1)\sqrt{gd}} \qquad (1)$$

where L is the length of the harbor, g is the acceleration of gravity, d is water depth and k represents the oscillation mode of the basin, being k = 0 the free oscillation mode and higher values the forced ones. Considering that the harbor has a length of almost 2000 m and the water depth is quite homogeneous in 12 m due to the dredging, T_n results in 12.3 min.

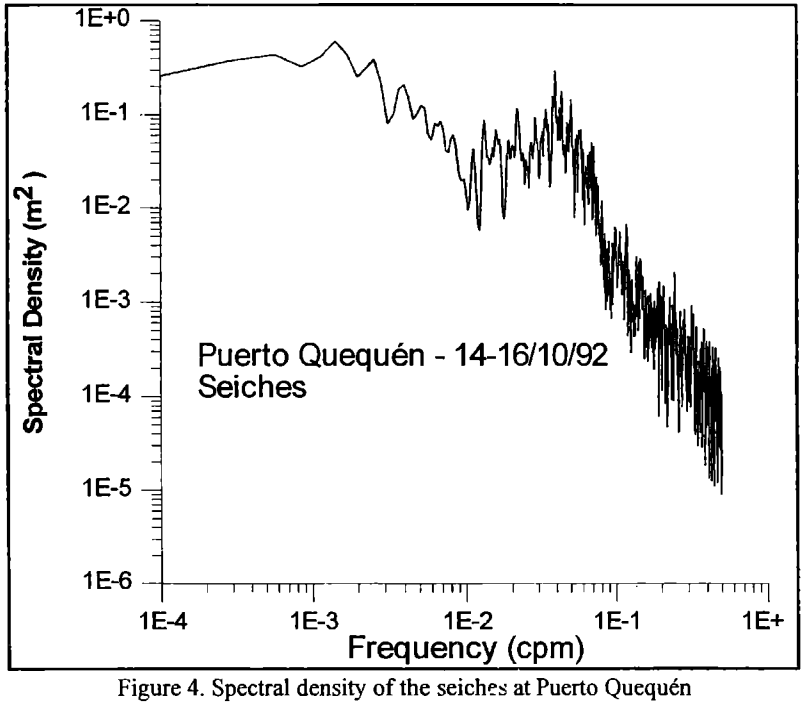

Figure 4. Spectral density of the seiches at Puerto Quequén

In addition to the standing wave mode represented by eq. (1), a basin of the characteristics of Quequén harbor can resonate in the Helmholtz mode, which is analogous to the acoustic resonator by the same name. In this case, the water surface in all the basin moves up and down uniformly, while the water at the inlet oscillates in and out (Sorensen, 1978). The period of the Helmholtz resonance is estimated by

$$T_H = \sqrt{\frac{(L_c + L_c')A_b}{gA_c}} \quad (2)$$

where A_b and A_c are respectively the areas of the basin and the inlet cross-section, L_c is the length of the inlet channel and L_c' is an additional length to account for the water mass outside of each end of the channel that is involved in the resonant oscillation. Sorensen (1978) gives the following expression for the estimation of L_c'

$$L_c' = -\frac{W}{\pi} \ln\left(\frac{\pi W}{\sqrt{gd_c}T_H}\right) \quad (3)$$

where W and d_c are the channel width and depth. Assuming that the width of the channel is 200 m, its depth is 12 m, the area of basin 1.6 10^6 m^2 and the channel cross-section area is 2400 m^2, estimation of T_H and L_c' must be made by an iteration procedure that results in T_H = 2.2 min and L_c' = 51.9 m.

Although there are some peaks at periods similar to those calculated for the normal oscillation and the Helmholtz resonance for the harbor in the spectra, they are small in comparison with those indicated before. The lack of meteorological data preclude some correlations with the atmospheric forcing that may give some light to these behavior. Another possible source for harbor oscillation is the effect induced by waves which are important at the mouth. However,

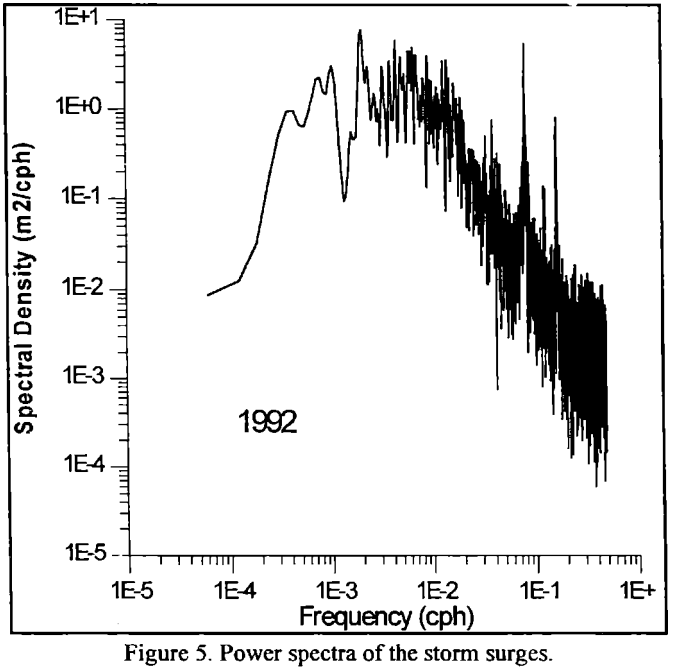

Figure 5. Power spectra of the storm surges.

there is no data available at the presetn time to assess their influence.

3.3 Storm Surges

Hourly departures of observed tides from predicted ones, storm surges, presented maximum values of 1.5 m and -1.66 m in the period 1989-1994. Figure 5 shows the power spectrum for 1992. Significant energy peaks are found in 2 month, 21 days, 10 d, 5.6 d and 12 hs. These periods indicate that the fluctuations are produced by meteorological process in macro, sinoptic and microescales. The 10 days peak corresponds to the frequency of storm passage for the study zone and the 5.6 d characterizes the sinopticscale. These periods are typical of high and mid latitudes. The 12 hs peak corresponds to the local wind circulation, the sea breeze. Therefore, the sea level variations of the Quequén river estuary is due mostly to the effect of the meteorological forcing.

4. CONCLUSION

Sea level and its fluctuations have interested man for many centuries. Historical sea level time-series data are unique among marine data sources. Sea level records include not only periodic fluctuations due to astronomical tides but also nontidal, low frequency fluctuations resulting from various oceanic and atmospheric processes.

Analysis of 5 years of hourly sea levels indicates that the nontidal sea level variations are large compared with the normal tide range in Quequén harbour. The meteorological processes are important in determine the sea level variations in the different time scales.

Acknowledgments

To the Dirección Nacional de Direcciones Portuarias y Vías Navegables, and specially to Sr Hugo Giménez for his useful collaboration in the meteorological and tidal information. This work had the support for CONICET, Universidad Nacional del Sur and the Economic European Community.

REFERENCES

Balay, M., 1958. Variations saisonnieres du niveau moyen de la Mer Argentine. Revue Hydrographique International 35, 117-145.

Balay, M.A., 1961. El Río de la Plata entre la atmósfera y el mar. Servicio de Hidrografía Naval H621, Buenos Aires, 153pp

Bongers, T. and Wyrtki, K., 1987. Sea level at Tahiti. A Minimum of Variability. J. Phys. Ocean. 17 (1), 164-168.

Chao, S and Pietrafesa, L. J., 1980. The subtidal response of sea level to atmospheric forcing in the Carolina Capes. J. Phys. Ocean., 10(8), 1246-1255.
Church, J.A., 1980. The relationship between mean sea level and steric height at Sydney. Report 124. CSIRO. Div. of Fisheries and Oceanography, Australia, 9 pp.
D'Onofrio, E.E., Frutos, H.C. y Balay, C.E., 1981. Nivel medio del mar en el litoral argentino. Servicio de Hidrografía Naval., Buenos Aires, 64 pp.
Foreman, M.G.G., 1978. Manual for Tidal current analysis and prediction. Pacific Marine Science Report 78-6. Institute of Ocean Sciences, Patricia bay, Victoria, B.C., 70 pp.
Godin, G., 1972. The analysis of tides. University of Toronto Press, Toronto, 345 pp.
Hicks, S. D., 1968. Long period variations in secular sea level trends. Shore and Beach, 36 (1), 32-36.
Hicks, S.D. and Shofnos, W., 1965. Yearly sea level variations for the United States. J. of the Hydraulics Div., Proc. Of the Am. Soc. Civil Engineers, 23-28.
Inman, D.L., Munk, W. and Balay, M., 1962. Spectra of low frequency ocean waves along the Argentine shelf. Deep Sea Res. 8:155-164.
Lanfredi, N. W., D'Onofrio, E. E. y Mazio, C. A., 1988. Variations of the mean sea level in the southwest Atlantic Ocean. Continental Shelf research, 3 (11), 1211-1220.
Murty, T. S and El-Sabh, M. I., 1981. Interaction between storm surges and tides in shallow waters. Marine Geodesy, 5(1), 19-33.
Perillo, G.M.E. y Piccolo, M.C., 1991. An interpolation method for estuarine and oceanographic data. Computers & Geosciences 17(6), 820-826.
Piccolo, M.C., Perillo G.M.E. y Marcos, A., 1995. Estudio de mareas en Puerto Quequén, Argentina.VI Congreso Latinoamericano de Ciencias del Mar, Mar del Plata, Argentina, (Abstract).
Proudman, J., 1955. The propagation of tide and surge in an estuary. Proceedings of the Royal Society of London, ser. A, 233, 407-417.
Provis, D. G., and Radok, R., 1979. Sea-level oscillations along the Australian coast. Austr. J. Mar. Freshwater Res., 30, 295-301.
Pugh, D.T. and Faull, H.E., 1982. Tides, surges and sea level trends. In Shoreline Protection. Thomas Telford ltd. London, 45-55.
Schwing, F. B., 1989. Subtidal response of the scotian Shelf bottom pressure field to meteorological forcing. Atmosphere-Ocean, 27 (1), 157-180.
Seim, H. E., Kjerfve, B. and Sneed, J. E., 1987. Tides of Mississippi Sound and the adjacent continental shelf. Estuarine, Coastal and Shelf Science 25, 143-146.
Smith, N.P., 1974. Intracoastal tides of Corpus Christi bay. Contributions in Marine Science, 18, 205-219.
Sorensen, R.M., 1978. Basic coastal engineering. John Wiley & Sons, New York, 227 pp.
Wang, D-P., 1979. Subtidal sea level variation in the Chesapeake bay and relations to atmospheric forcing. J. Phys. Ocean., 9(2), 413-421.
Woodworth, P. L., Shaw, s. M. and Blackman, D.L., 1991. Secular trends in mean tidal range around the British isles and along the adjacent European coastline. Geophys. J. Int. 104, 593-609.

GEOACTA, 22, 155-164, 1997

STABILITY CONDITION FOR ARAKAWA' S *B* GRID

Alejandro L. Camerlengo and Monica I. Demmler
Faculty of Fisheries and Marine Science Center, Universiti Pertanian Malaysia Terengganu, Mengabang Telipot, 21030 Kuala Terengganu - Malaysia

ABSTRACT

Most models that demand a coarse grid resolution use Arakawa' s B grid. Using this particular grid, it is shown that the CFL condition, for the fastest travelling wave, is twice the value than for both the non-staggered and the staggered C grid, respectively.

RESUMEN

La mayoría de los modelos que requieren poca resolución horizontal utilizan la grilla B de Arakawa. Mediante la técnica de estabilidad lineal, demostraremos que la condición de estabilidad para la onda de gravedad es el doble de la requerida para las grillas A y C de Arakawa. La onda de gravedad es la de mayor velocidad de propagación en el modelo de aguas someras.

1. INTRODUCTION

Bryan (1969), Gill and Bryan (1971), build up their numerical models, employing Arakawa' s B lattice, where the free surface elevation is evaluated at the center of the grid, while both velocity components, u and v, are evaluated at the four corners of the grid (Fig. 1). In computing both, the Coriolis and the nonlinear terms, quite an amount of averaging is omitted.

The theoretical analysis of Mesinger and Arakawa (1976) strongly suggests that grid C produce better numerical simulations than grid B. This situation holds true as long as the gridpoint resolution is smaller than the Rossby radius of deformation. The reverse is also true. Whenever the Rossby radius of deformation is smaller than the gridpoint size, grid B gives better numerical simulations than grid C (Bryan, 1989; page 473). Most numerical models that demand a coarse-grid resolution are designed using the B grid (Semtner, 1986).

The aim of this study is to gain some understanding as to why lattice B works better for numerical models with coarse-grid resolution. Following the pioneering work of

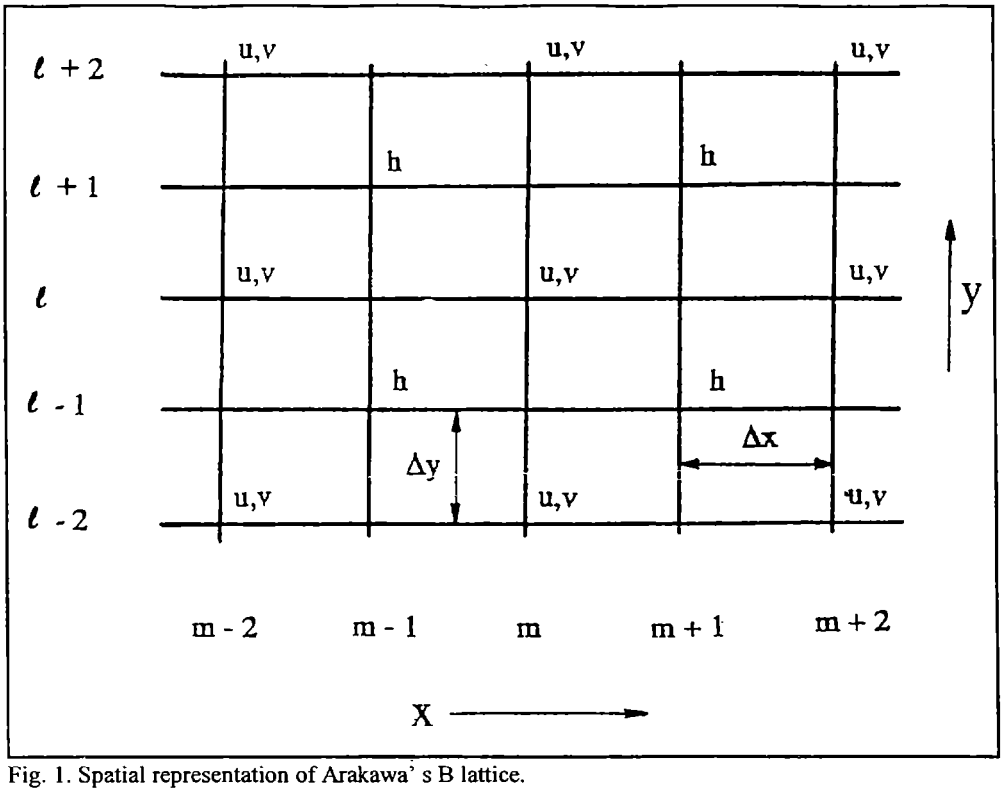

Fig. 1. Spatial representation of Arakawa' s B lattice.

O'Brien (1986) on stability conditions, a series of analytical studies is conducted. For this purpose, the linear stability technique developed by von Neumann is used (Charney et al., 1950,.

In our analysis, we choose to index all the gridpoints and consider the distance between grid points as Δx and Δy; where Δx and Δy, represent the gridpoint resolution in the east-west and north south directions, respectively (Fig. 1). Other investigators choose to call the distance between the same variable as the grid resolution. Our indexation makes the interpretation of the stability results more interesting. The same indexation criterion was followed by O' Brien (1986) and O' Brien & Inoue (1982) (Fig. 2). The results are quite conclusive. It is shown that the stability condition for the gravity (fastest travelling) wave is twice the value than for the non-staggered and the C grids, respectively (Mesinger & Arakawa, 1976; O' Brien, 1986; O' Brien & Inoue, 1982).

2. THE PROBLEM

The general stability condition of the finite difference scheme is determined by the

general condition (Mesinger & Arakawa, 1976):

$$C \Delta t / \Delta x \leq O(1)$$

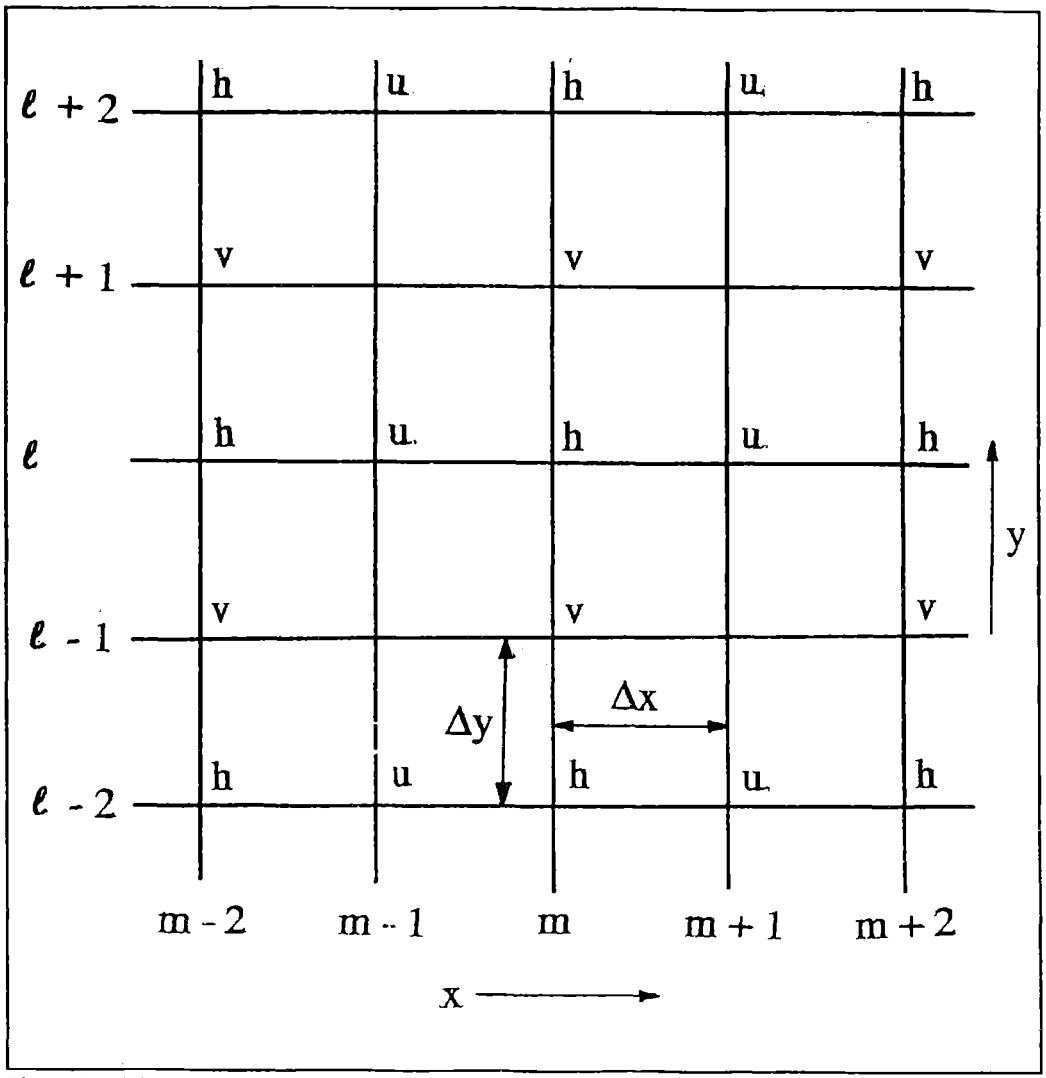

Fig. 2. Spatial representation of Arakawa' s C lattice.

3. STABILITY ANALYSIS

3.1. Analysis for the one - dimensional gravity wave

Consider the following set of partial differential equations:

$$\partial u / \partial t = - g \, \partial h / \partial x$$
$$\partial h / \partial t = - H \, \partial u / \partial x, \qquad (1)$$

where g represents the earth' s gravity acceleration; u and v, the velocity components in the east-west and north-south directions, respectively; h, the free-surface elevation; and H the mean sea level depth.

A second order, centered in space and time finite difference scheme is employed. It is obtained:

$$u^{n+1}_{m,l} = u^{n-1}_{m,l} - (g\gamma/2)[(h^{n}_{m+1,l+1} + h^{n}_{m+1,l-1}) - (h^{n}_{m-1,l+1} + h^{n}_{m-1,l-1})]$$
$$h^{n+1}_{m+1,l+1} = h^{n-1}_{m+1,l+1} - (H\gamma/2) [(u^{n}_{m+2,l+2} + u^{n}_{m+2,l}) - (u^{n}_{m,l+2} + u^{n}_{m,l})] \qquad (2)$$

where the superscript *n*, stands for time level; the subscripts *(m,l)*, the mesh of discrete points in the x and y directions, respectively; Δ x and Δ y, the gridpoint resolution in the x and y directions, respectively; γ is equal to Δ t / Δ x, and Δ t represents the time step increment (Fig.1).

Define $C^2 = g H$, θ ($= \mu \Delta x$) and σ ($= \nu \Delta y$), where μ and ν, are the east-west and north-south wavenumbers, respectively. It is convenient to define Q = (u,v,h). Assume:

$$Q^{n}_{m,l} = Q_n \exp (i m \mu \Delta x) \exp (i l \nu \Delta y) \qquad (3)$$

Upon substitution of equation (3) into the set of equations (2), yields:

$$u_{n+1} = u_{n-1} - \gamma g (2 i \sin \theta \cos \sigma) h_n$$
$$h_{n+1} = h_{n-1} - \gamma H (2 i \sin \theta \cos \sigma) u_n \qquad (4)$$

It is convenient to define an amplification factor, Z, such that:

$$Q_{n+2} = Z Q_n \qquad (5)$$

In doing so, equations (4) may be rewritten as:

$$L_1 u_n + L_2 h_n = 0$$
$$L_1 h_n + L_3 u_n = 0 \qquad (6)$$

The operators L_1, L_2 and L_3 are defined as:

$$L_1 = Z^{1/2} - Z^{-1/2}$$
$$L_2 = 2 i g \gamma \sin\theta \cos\sigma$$
$$L_3 = 2 i H \gamma \sin\theta \cos\sigma \qquad (7)$$

The homogeneous set of equations (6) is solved by letting:

$$L_1^2 - L_2 L_3 = 0. \qquad (8)$$

A second order equation for Z is obtained. Namely:

$$Z^2 - 2 (1 - 2 C^2 \gamma^2 \sin^2\theta \cos^2\sigma) Z + 1 = 0. \qquad (9)$$

Two complex conjugate solutions are obtained

$$Z_- = G - i (1 - G^2)^{1/2}$$
$$Z_+ = G + i (1 - G^2)^{1/2} \qquad (10)$$

where

$$G = 1 - 2 (C \gamma \sin\theta \cos\sigma)^2 \qquad (11)$$

To have a stable (neutral) condition the absolute value of Z should be less (equal) than (to) one. Otherwise, the finite difference scheme under consideration will be unstable. In multiplying the two solutions yields:

$$| Z |^2 = Z_+ Z_- = 1 \qquad (12)$$

Therefore, if the term under the radical sign, $1 - G^2$, is positive, then the absolute value of the amplification factor will be equal to one. This instance will hold certain if, and only if:

$$(C \gamma \sin\theta \cos\sigma)^2 \leq 1. \qquad (13)$$

Given the fact that the absolute value of the sine and the cosine is less or equal to unity, and recalling the definition of γ, it follows that:

$$C \Delta t / \Delta x \leq 1, \qquad (14)$$

which is the classical C-F-L condition for computational stability.

3.2. Stability analysis for the inertial gravity wave

Let us consider the following set of partial differential equations:

$$\begin{aligned} \partial u / \partial t &= f v - g \, \partial h / \partial x \\ \partial v / \partial t &= - f u \\ \partial h / \partial t &= - H \, \partial u / \partial x, \end{aligned} \qquad (15)$$

Upon using the same finite difference scheme as above yields:

$$\begin{aligned} u_{n+1} &= u_{n-1} + 2 f \Delta t \, v_n - \gamma g (2 i \sin \theta \cos \sigma) h_n \\ v_{n+1} &= v_{n-1} - 2 f \Delta t \, u_n \\ h_{n+1} &= h_{n-1} - \gamma H (2 i \sin \theta \cos \sigma) u_n \end{aligned} \qquad (16)$$

Equations (16) may then be rewritten as:

$$\begin{aligned} L_1 u_n - L_4 v_n + L_2 h_n &= 0 \\ L_1 v_n + L_4 u_n &= 0 \\ L_1 h_n + L_3 u_n &= 0 \end{aligned} \qquad (17)$$

where $L_4 = 2 f \Delta t$.

Following the same procedure as above yields:

$$Z^2 - 2 (1 - 2 C^2 \gamma^2 \sin^2 \theta \cos^2 \sigma - 2 (f \Delta t)^2) Z + 1 = 0. \qquad (18)$$

The two complex conjugate solutions are:

$$\begin{aligned} Z_- &= G - i (1 - G^2)^{1/2} \\ Z_+ &= G + i (1 - G^2)^{1/2} \end{aligned} \qquad (19)$$

where the value of G has changed. It is:

$$G = 1 - 2(f\Delta t)^2 - 2(C\gamma \sin\theta \cos\sigma)^2 \qquad (20)$$

In multiplying the two complex conjugate solutions, as in the previous case, we will arrive to a neutral stability condition, provided that the term under the radical sign, $1 - G^2$, is positive. This will require that:

$$(f\Delta t)^2 + (C\gamma \sin\theta \cos\sigma)^2 \leq 1 \qquad (21)$$

Thus, this is the same stability condition as the one for the unstaggered grid case (O' Brien, 1986; page 177):

$$C\gamma \leq [1 - (f\Delta t)^2]^{1/2} \qquad (22)$$

3.3. Stability condition for a two dimensional flow

Let us consider the following set of equations:

$$\begin{aligned} \partial u/\partial t &= fv - g\,\partial h/\partial x \\ \partial v/\partial t &= -fu - g\,\partial h/\partial y \\ \partial h/\partial t &= -H(\partial u/\partial x + \partial v/\partial y) \end{aligned} \qquad (23)$$

In using a centered in space and time finite differencing scheme, yields:

$$\begin{aligned} u_{n+1} &= u_{n-1} + 2f\Delta t\, v_n - 2i\gamma g \sin\theta \cos\sigma\, h_n \\ v_{n+1} &= v_{n-1} - 2f\Delta t\, u_n - 2i\eta g \cos\theta \sin\sigma\, h_n \\ h_{n+1} &= h_{n-1} - 2i\gamma H \sin\theta \cos\sigma\, u_n - 2i\eta H \cos\theta \sin\sigma\, v_n \end{aligned} \qquad (24)$$

where η is equal to $\Delta t / \Delta y$. This system of equations, 24, may be rewritten as:

$$\begin{aligned} L_1 u_n - L_4 v_n + L_2 h_n &= 0 \\ L_1 v_n + L_4 u_n + L_5 h_n &= 0 \\ L_1 h_n + L_3 u_n + L_6 v_n &= 0 \end{aligned} \qquad (25)$$

where

$$\begin{aligned} L_5 &= 2i\, g\eta \sin\sigma \cos\theta \\ L_6 &= 2i H\eta \sin\sigma \cos\theta \end{aligned} \qquad (26)$$

For this set of equations to have unique solution, it follows that:

$$L_1 (L_1^2 - L_2 L_3 - L_5 L_6 + L_4^2) = 0 \qquad (27)$$

Following the same procedure as in the two previous cases, yields:

$$Z^2 - 2 \psi Z + 1 = 0 \qquad (28)$$

where

$$\psi = 1 - \{ 2 (f \Delta t)^2 + 2 C^2 (\gamma^2 \sin^2 \theta \cos^2 \sigma + \eta^2 \sin^2 \sigma \cos^2 \theta) \} \qquad (29)$$

As before, a neutral stability condition will be obtained if:

$$(f \Delta t)^2 + C^2 (\gamma^2 \sin^2 \theta \cos^2 \sigma + \eta^2 \sin^2 \sigma \cos^2 \theta) \leq 1 \qquad (30)$$

Several cases are considered:

a) For $L_x = 2 \Delta x$ (4 Δx) and $L_y = 2 \Delta y$ (4 Δy) , i. e., $\theta = \sigma = \pi$ ($=\pi/2$), where L_x and L_y are the wavelengths in the x and y directions, respectively, yields:

$$| f \Delta t | \leq 1 \qquad \text{for stability} \qquad (31)$$

This same result holds for very long waves. Namely for $\theta = \sigma = 0$.

b) For $L_x = 8 \Delta x$ and $L_y = 8 \Delta y$, i. e., $\theta = \sigma = \pi / 4$, yields:

$$(f \Delta t)^2 + C^2 (\gamma^2 + \eta^2) \leq 1 \qquad (32)$$

If $\Delta x = \Delta y = \Delta$, yields:

$$C \Delta t / \Delta \leq \{ 2 (1 - (f \Delta t)^2) \}^{1/2} \qquad (33)$$

Following O' Brien (1986), the CFL condition for the 2 D gravity wave for the unstaggered grid, is:

$$C \Delta t / \Delta \leq \{ (1 - (f \Delta t)^2)/2 \}^{1/2} \qquad (34)$$

This same result is obtained, for the C grid, using this same type of indexation (O' Brien & Inoue, 1982). Without considering the Coriolis parameter, Mesinger and Arakawa

(1976, page 52) show that the stability criterion for the 2 D dimensional gravity wave, for the unstaggered grid, is:

$$C \Delta t / \Delta \leq \{1/2\}^{1/2} \tag{35}$$

which is similar to O' Brien (1986) and O' Brien & Inoue (1982). Therefore, the CFL condition for the B grid, is less restrictive. The stability condition for the gravity wave is twice the value of the stability condition of both the unstaggered grid and grid C.

In their reduced gravity model, Adamec & O' Brien (1978) used a $\Delta t = 10^4$ sec. The product $f \Delta t$ could be of order one. Therefore, the CFL condition, for the reduced gravity models, could easily be violated, if caution is not taken care.

4. CONCLUSIONS

Stability conditions of a series of problems, for the staggered lattice B, leading to the shallow water wave equations are considered. Comparison with stability conditions with both the unstaggered grid and the staggered grid C are made (Mesinger & Arakawa, 1976; O' Brien, 1986; O' Brien & Inoue, 1982). It is shown that the stability condition is double the value than for the other two grids (equations (33) through (35)) This represents a clear improvement of Mesinger and Arakawa' s (1976) solutions.

Therefore, numerical models that require a coarse-grid resolution are designed using the B lattice. In doing so, more accurate solutions, for a coarse grid resolution, are obtained.

Acknowledgments

This study was supported by Universiti Pertanian Malaysia under contract No. 50213-94-05. The authors gratefully acknowledge this support. Corrections made by an anonymous reviewer contributed in the improvement of this paper. The authors gratefully acknowledge this contribution.

REFERENCES

Adamec, D. & J. J. O' Brien, 1978. The seasonal upwelling in the Gulf of Guinea due to remote forcing. J. Phys. Oceanogr., 8, 1050-1060.

Bryan, K., 1969. A numerical method for the study of the circulation of the world ocean. J. Comp. Phys, 4, 347-376.

Bryan, K., 1989. Oceanic circulation models. combining data and dynamics. NATO ASI series. Kluwer Academic Publishers, London, 465-500.

Charney, J. G., R. Fjortoft and J. von Neumann, 1950. Numerical integration of the barotropic

vorticity equations. Tellus, **2**, 237-254.
Gill, A. & K. Bryan, 1971. Effects of geometry on the circulation of the three-dimensional southern hemisphere ocean. Deep Sea Res., **18**, 685-721.
Mesinger, F. and A. Arakawa, 1976. Numerical methods used in atmospheric models. GARP Publications Series, No. 17, World Meteorological Organization, Geneve, Switzerland, 64 pages.
O' Brien J. J. & M. Inoue, 1982. A note on the CFL condition for the shallow water wave equations (unpublished manuscript), 15 pages.
O' Brien, J. J., 1986. Advanced Physical Oceanographic Numerical Modeling. D. Reidel Publishing Co., 174 - 181.
Semtner, A. J., 1986. History and methodology of modeling the circulation of the world ocean. Advanced Physical Oceanographic Numerical Modeling. D. Reidel Publishing Co., 23-32.

GEOACTA, 22, 165-184, 1997

MEJORAMIENTO EN EL AJUSTE ORBITAL DE SATELITES GPS

A. Meza [1,2], J.C. Usandivaras[1] and C. Brunini[1]
[1] Facultad de Ciencias Astronómicas y Geofísicas, La Plata.
[2] Comisión Nacional de Investigación Científicas y Tecnológicas.

ABSTRACT

En the lastest years, GPS has showed up to be a powerful tool in both scientific and technological aspects. Most of its applications require the highest precision of the system and to achieve it we must enhace our knowledge of the satellite orbits. In this work we describe the classical methos of orbital fit and we analyse the different accelerations that take part in it, showing that the actual accuracy is constrained by the solar radiation pressure effect: this fact is confirmed by the analysis of the residuals or our fit. We discuss the actual methods and propose a new treatment of the problem. In order to reach this stage we studied SPR and we develop the necessary formulae through a detailed analysis of the geometry of the problem.

RESUMEN

En los últimos años el sistema GPS se ha impuesto como herramienta tanto en trabajos científicos como tecnológicos. Muchas de las aplicaciones demandan de la máxima precisión del sistema y para lograrla debemos mejorar las órbitas satelitales. En el trabajo describimos el método clásico de ajuste orbital y analizamos las componentes de aceleraciones intervinientes, mostrando que la precisión actual se ve limitada por el efecto de presión de radiación solar (P.R.S.); hecho que confirmamos con el análisis de los residuos de nuestro ajuste. Discutimos los métodos actuales en uso y proponemos un nuevo tratamiento. Para poder llegar a esta ultima etapa abordamos el fenómeno de la P.R.S. y desarrollamos las fórmulas necesarias a través de un detallado análisis de la geometría del problema.

1. INTRODUCCION

El sistema G.P.S. (Global Position System) es hoy en día la herramienta de posicionamiento mas potente y muy probablemente será la empleada en los próximos tiempos. Su valiosa utilidad está relacionada con la alta precisión con que trabaja el sistema y esta a su vez depende de la precisión con que se conocen las órbitas de los satélites. Para realizar el cálculo preciso es necesario un modelo completo de fuerzas que actúan sobre el satélite. Teniendo en cuenta el tipo de satélite que integran el

sistema G.P.S., de órbitas casi circulares y a aproximadamente 20200 km. sobre la tierra, las fuerzas intervinientes serán: la atracción gravitatoria de la tierra (que nos bastará debido a su altura con unos pocos armónicos esféricos), la atracción gravitatoria del sol y de la luna, la presión de radiación solar (P.R.S.) y en menor magnitud términos relativistas.

De las fuerzas consideradas la presión de radiación solar no encuentra todavía un modelo satisfactorio y debido a su falta de resolución no se puede realizar aún un análisis detallado de las que actúan con menor magnitud. La posición del satélite se obtiene integrando numéricamente las ecuaciones de movimiento. El software de cálculo y ajuste orbital utilizado fue desarrollado en la Facultad de Ciencias Astronómicas y Geofísicas de la U.N.L.P. (Perdomo y del Cogliano, 1992). El programa básicamente evalúa las fuerzas involucradas en el ajuste a partir de las condiciones iniciales (coordenadas y velocidad para una época determinada) y de los parámetros que aparecen en el modelo de fuerzas, luego avanzo un paso de integración evaluando coordenadas y velocidades para un tiempo posterior (integración numérica); el proceso se reitera hasta obtener una serie de posiciones y velocidades calculadas a lo largo del período requerido. Las posiciones calculadas junto con las posiciones observadas nos dan las diferencias *O - C* que se minimizan utilizando por ejemplo el método de mínimos cuadrados.

Teniendo en cuenta que la presión de radiación solar fija el límite de la precisión con que se pueden calcular en la actualidad las efemérides satelitarias es entonces el objetivo de este trabajo mejorar la resolución de dicho efecto sobre las órbitas G.P.S.

2. ANALISIS DE LOS METODOS EMPLEADOS PARA EL CALCULO DEL EFECTO DE LA PRESION DE RADIACION SOLAR.

2.1. Modelo numérico

Según Fliegel et al. (1985) la aceleración debida al efecto directo de la presión de radiación solar consta de dos componentes, la componente principal $d\vec{a}_1$ que está en la dirección opuesta al sol y otra componente $d\vec{a}_2$ más pequeña que actúa a lo largo del eje $\vec{e}_2$ del satélite (eje ortogonal al vector que apunta en la dirección opuesta al sol y al de las antenas, el cual está dirigido nominalmente hacia el centro de la tierra).

La componente principal es usualmente modelada por:

$$d\vec{a}_1 = \nu k \rho_S^2 \frac{\vec{\rho} - \vec{\rho}_S}{\left|\vec{\rho} - \vec{\rho}_s\right|^3}$$

donde ρ es la posición geocéntrica del satélite y ρ_s es la posición geocéntrica del sol; ν depende linealmente de la constante de radiación solar Φ, de un facto C_r que define las propiedades de reflectividad del satélite y de la relación masa área efectiva del satélite: k es un factor de eclipse el cual vale cero cuando el satélite está en el cono de sombra de la tierra y vale uno cuando el satélite está iluminado por el sol; para la penumbra k tiene un valor entre cero y uno. El modelado es extremadamente difícil ya que el factor Φ varía impredeciblemente a lo largo del año y un único valor de C_r no es adecuado para el satélite, también se tiene que si bien la masa es bien conocida, la forma irregular del satélite no nos permite una determinación exacta de la relación masa área efectiva. La componente $\vec{da_2}$ llamada y-bias, es causada principalmente por una combinación del desalineamiento de los paneles solares y de la radiación térmica a lo largo del eje $\vec{e_2}$; esta componente puede permanecer constante por varias semanas y es dos órdenes de magnitud mas pequeña que el término principal.

Por otra parte para realizar un tratamiento numérico del problema, Beutler et al. (1986) describen el modelo de presión de radiación solar como:

$$\vec{a} = k(-p_0\vec{e}_0 + p_2\vec{e}_2)$$

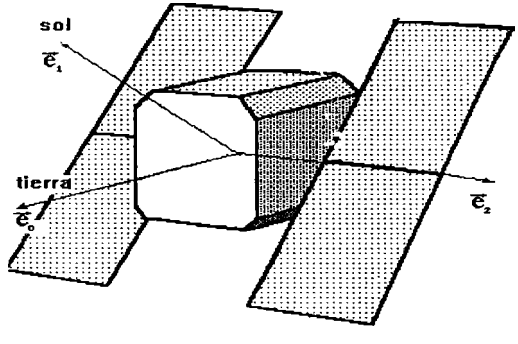

Figura 1

donde:

$\vec{e}_0$: vector unitario al sol

$\vec{e}_1$: vector unitario en la dirección del eje de las antenas

$\vec{e}_2$: vector unitario en la dirección del eje de los paneles

p_0 : magnitud en la dirección del sol

p_2 : magnitud en la dirección del eje de los paneles solares

Los valores definitivos de p_0 y p_2 deben ser determinados por un proceso de mejoramiento orbital, usando observaciones de GPS durante varios días. Es decir, Beutler propone un análisis determinista del efecto de la PRS, considerando constantes los parámetros del modelo, aunque sus valores definitivos son incógnitas en el ajuste orbital.

Este tratamiento tiene la ventaja de emplear poco tiempo computacional ya que puede evaluarse rápidamente en cada paso de integración orbital. Para los coeficientes p_0 y p_2 se adoptan valores teóricos a priori:

$p_0 = 10^{-7}$ m/s^2 y $p_2 = 0$ m/s^2 y se determinan correcciones Δp_0 y Δp_2 mediante el proceso de mejoramiento orbital ya descrito.

2.2. Prueba del modelo numérico

Con la intención de mostrar la importancia de la presión de radiación solar en el modelo de fuerzas estudiamos el comportamiento de los residuos sobre cada una de las componentes (radial, normal y tangencial) a lo largo del período de integración de 96 horas (arbitrariamente elegimos el satélite PRN3). La Fig. 2 muestra lo que ocurre cuando no se incluye la P.R.S. en el modelo de fuerzas; vemos que la componente tangencial lleva la parte mas significativa de tal efecto, es decir es la que tiene mayor amplitud. Observamos también un período de 12 horas en las variaciones de los residuos el cual coincide con la revolución orbital del satélite. Finalmente tenemos que la componente normal no promedia en cero, es decir su valor medio se encuentra desplazado hacia un valor negativo.

Comparando la Fig. 2 con lo obtenido teniendo en cuenta en el modelo de fuerzas de la P.R.S. sólo el término en $\vec{e}_0$, es decir en $\vec{a} = p_0 \vec{e}_0$ (Fig. 3), observamos que la amplitud para la componente radial y tangencial disminuyen notablemente, si bien para esta última aparece una fuerte componente de baja frecuencia, mientras que para

la normal aparece un desplazamiento en valor medio, es decir que con esta corrección, al igual que en otras componentes, la normal promedia en cero. Si el programa de integración trabaja ahora con ocho parámetros libres Δx, Δy, Δz, $\Delta \dot{x}$, $\Delta \dot{y}$, $\Delta \dot{z}$, p_0 y p_2 (Fig. 4), las amplitudes en las componentes radial y tangencial disminuyen notablemente.

El ajuste final fue hecho para cuatro días con un error medio cuadrático de 1,78 metros y las máximas diferencias son menores que cinco metros. El programa converge rápidamente con solo tres iteraciones. Los valores obtenidos de los coeficientes del modelo de presión son:

$$p_0 = 0{,}821\,10^{-7} \pm 0{,}002\,10^{-7}\ \frac{m}{s^2}$$

$$p_2 = -0{,}640\,10^{-9} \pm 0{,}001\,10^{-9}\ \frac{m}{s^2}$$

Se observa de los resultados obtenidos que a pesar que el comportamiento de los residuos mejora notablemente siguen aún *correlacionados*; es decir el modelo no es lo suficientemente bueno. En los residuos aparece sumado, al ruido observación, una señal.

3. MODELO ANALITICO

3.1. Análisis geométrico de la presión de radiación solar (P.R.S.)

Debemos abordar el problema de otra manera y es por ello que analizaremos más en detalle el efecto P.R.S.; estudiaremos su modelo físico para poder aplicar un método estadístico sobre el problema. Existe un efecto directo de la radiación solar sobre el satélite. Esta aceleración neta resultante es producto de la interacción (por absorción, reflexión y difusión) de la luz solar con cada elemento de la superficie de la nave, debido a que cada fotón lleva una cantidad de momento (energía dividida por la velocidad de la luz) que puede recombinarse durante la interacción con la superficie de un sólido.

Se llama a cada elemento pequeño de la superficie del satélite *dA* y a la fracción de la luz incidente que es absorbida, reflejada y difundida α, σ, δ, respectivamente.

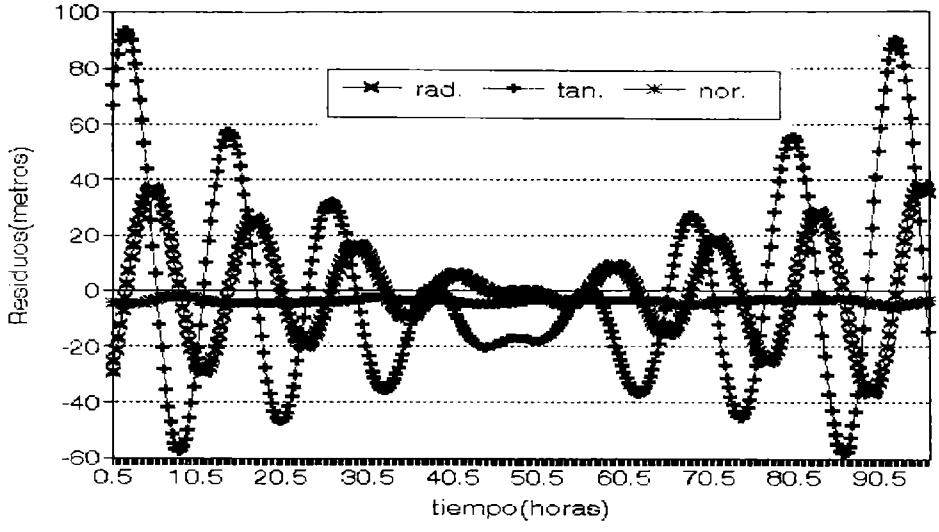

Comportamiento de los residuos en la dirección R,T,N

cuando en el modelo de fuerza no se incluye el efecto de PRS

Figura 2

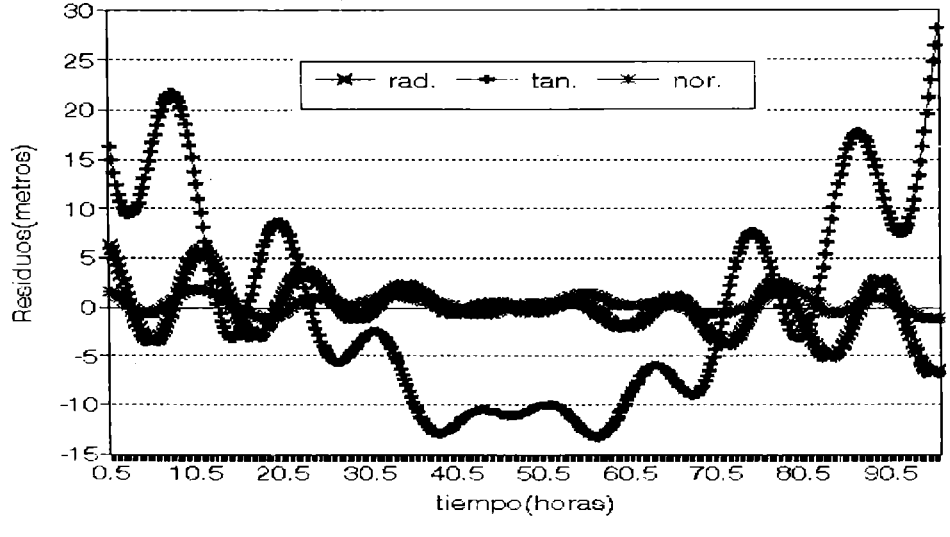

Comportamiento de los residuos cuando solo se tiene en cuenta $\vec{a}_0 = -p_0\vec{e}_0$

Figura3

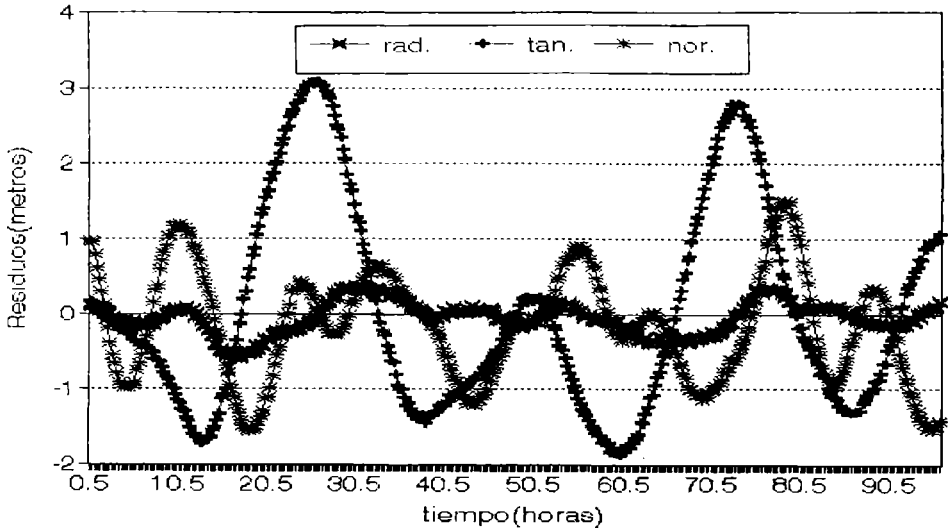

Comportamiento de los residuos, cuando en el modelo de fuerzas se incluye el modelo completo de Beutler (los dos parámetros)

Figura 4

Se considera que:

- La luz absorbida no es remitida.
- Para una dirección dada $\vec{n}$, la luz difundida es proporcional al coseno del ángulo ξ formado entre $\vec{n}$ y $d\vec{A}$ (versor normal al pequeño elemento de superficie dA).
- La reflexión es especular.
- La superficie actúa como una combinación lineal de cuerpo negro, espejo perfecto y difusor Lambert.

Finalmente tenemos (A. Milani, A. M. Nobili y P. Farinella; 1987):

$$F_\alpha = - \frac{k\phi}{c} \int_{A_{eff}} \alpha \cos \xi \, \vec{e}_0 \, d\vec{A}$$

$$\vec{F}_\sigma - \frac{k\phi}{c} \int_{A_{eff}} 2 \sigma \cos^2 \xi \, \vec{n} \, d\vec{A}$$

$$\vec{F}_\delta = - . \frac{k\phi}{c} \int_{A_{eff}} \left(\delta \cos \xi \, \vec{e}_0 + \frac{2}{3} \delta \cos \xi \, \vec{n} \right) d\vec{A}$$

Donde k es el factor de elipse ($0 < k < 1$), el flujo solar y $\vec{e}_s$ el versor que apunta al solar. Como se puede ver para la integración debe tenerse en cuenta cada pequeño elemento de superficie dA y su relación con la dirección de radiación solar en cada momento. Para ello la superficie del satélite debe ser subdividida en superficies planas y cilíndricas; la integración se realizará sobre cada superficie iluminada y finalmente la suma de todas dará la integral sobre el área efectiva de la nave.

La expresión final en forma diferencial es (Milani et.al, 1987):

$$d\vec{F} = k\phi\ (-(1-\sigma)\ \vec{e}_0 + 2(\delta/3 + \sigma\cos\xi)\ \vec{n}\ |\cos\xi|\ dA \quad \text{(I)}$$

En nuestro modelo, dividamos al satélite en ocho zonas (que definiremos mas adelante). Para simplificar el análisis hablaremos de dos modelos:

- En el primero consideramos que el satélite toma la dirección ideal, es decir, los paneles constantemente están dirigidos al sol, las antenas apuntan hacia la tierra y el resto de la nave se mueve sólidamente a las antenas y al eje de los paneles.
- En el segundo tenemos en cuenta el desalineamiento del eje de los paneles.

Para describir el modelo de presión solar es necesario comprender la orientación de las superficies de la nave con respecto al sol. El sistema de coordenadas de la nave se define como sigue (Fig. 5): El eje $\vec{e}_1$ (*-R*) de la nave es positivo a lo largo de las antenas, y por lo tanto dirigida nominalmente hacia el centro de la tierra y el eje $\vec{e}_2$ a lo largo del eje de los paneles.

Existe una rotación o spin alrededor del eje $\vec{e}_1$ y un mecanismo electromecánico es usado para que el eje $\vec{e}_2$ apunte hacia el sol; el movimiento con el que los motores rotan a los paneles alrededor del eje $\vec{e}_3$ está regido de manera tal que los paneles presenten la máxima superficie al sol. Los sensores solares son los encargados del alineamiento de los paneles, y se encuentran ubicados en sus extremos. Uno se usa para activar el control mientras que el otro se utiliza para monitoreo.

3.2. Modelo simplificado del efecto de P.R.S.

Análisis de las áreas en la que dividimos al satélite y su orientación:

A_1 área de los paneles dirigida al sol, $\vec{e}_0$.

A_2 área del cuerpo central del satélite en dirección a la tierra, área de las antenas, $\vec{e}_1$.

A_3 área opuesta a A_2, $-\vec{e}_1$.

Areas laterales del cuerpo central:

a_2 en la dirección $\vec{e}_2$

a_j en la dirección $-\vec{e}_2$

a_1 en la dirección $\vec{e}_3$
a_1 en la dirección $-\vec{e}_3$

A_4 área opuesta a los paneles solares, $\vec{e}_0$ (no interviene en el modelo de fuerzas).

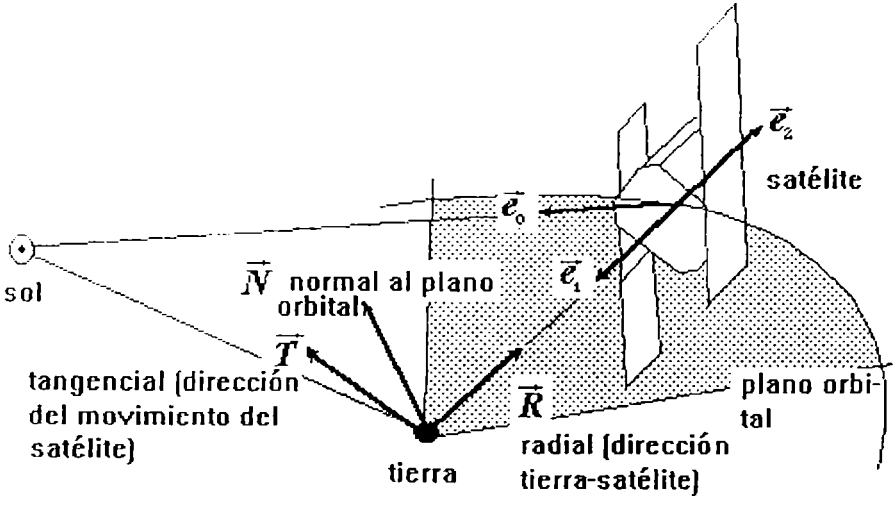

Figura 5

Para el desarrollo analítico que sigue resulta conveniente introducir un punto origen como muestra la Fig. 6, a partir del cual podemos medir el ángulo (f t) que describe la posición del satélite en su órbita. Dicho origen queda definido por el punto "O" donde el plano que contiene al Sol y a la Tierra y es normal a la órbita del satélite corta al plano orbital. Notemos que a los efectos del presente análisis utilizamos elemento orbitales medios para el período considerado.

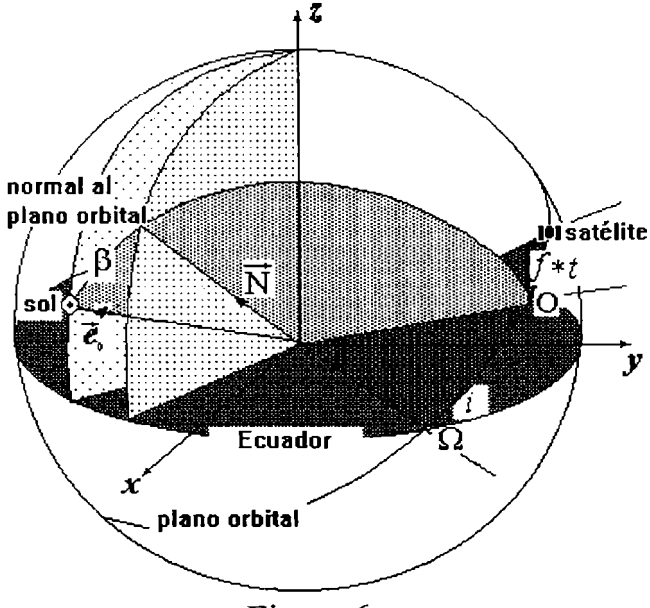

Figura 6

podemos expresar al vector $\vec{e}_0$ en el sistema gaussiano como sigue:

$$-\vec{e}_0 = cos\beta$$
$$-\vec{e}_0 = -\, sen\beta\ cos\, ft$$
$$-\vec{e}_0 = sen\beta\ sen\, ft$$

con $f = \dfrac{\pi}{6\ hs}$ y ft medido a partir del nodo ascendente.

En base a la abstracción realizada sobre la forma del satélite encontramos que las expresiones de las normales a sus caras laterales con las siguientes:

$$\vec{e}_2 = (\vec{R} * \vec{R} * \vec{e}_0))\ \big|\ \vec{R} * (\vec{R} * \vec{e}_0)\big|^{-1}$$
$$\vec{e}_3 = (-\vec{R} * \vec{e}_0) - \big|-\vec{R} * \vec{e}_0\big|^{-1}$$

Reemplazando valores(Meza et al., Practica de la Especialidad, 1994):

$$\vec{e}_2 = (-cos\beta\ \vec{N} - sen\beta\ sen\, ft\ \vec{T})\ (1 - sen\beta^2 cos\, ft^2)^{-1/2}$$

$$\vec{e}_3 = (sen\beta\ sen\, ft\ \vec{N} - cos\beta\ \vec{T})\ (1 - sen\beta^2 cos\, ft^2)^{-1/2}$$

De la expresión diferencial de la fuerza debido al efecto de la radiación solar (ecuación Y), hacemos la siguiente aproximación: en vez de una área diferencial *dA*, tomamos áreas finitas ΔA_i, que constituyen, cada una, las superficies en las que dividimos al satélite; es decir en vez de una integración de los efectos producidos sobre los diferenciales de área, realizamos una suma sobre las zonas de la nave.

Con estas simplificaciones encontramos las expresiones de la fuerza, debida a la P.R.S. sobre la nave. Para todo este procedimiento debemos establecer previamente el sistema de referencia empleado; en esta parte del trabajo es conveniente utilizar el sistema Gaussiano ya que podemos visualizar mejor la geometría del problema.

Teniendo en cuenta lo mencionado anteriormente las expresiones finales de la fuerza en cada una de sus componentes nos queda de la siguiente forma (Meza et al., Práctica de la Especialidad, 1994):

$$F_N = \frac{\phi}{c}(C_{N0} + C_{N1}\, cosft + C_{N2}\, cos\, 2ft + C_{N4}\, cos\, 4ft + \ldots)$$

$$F_R = \frac{\phi}{c}(C_{R1}\, cosft + C_{R2}\, cos2ft + C_{R3}\, cos\, 3ft + \ldots)$$

$$F_T = \frac{\phi}{c}(S_{T1}\, senft + S_{T2}\, sen\, 2ft + S_{T3}\, sen\, 3ft + S_{T5}\, sen\, 5ft + \ldots)$$

Donde los coeficientes dependen del área efectiva, los coeficientes de reflexión, absorción y difusión, el ángulo que forman la normal al plano orbital y la dirección al sol (β).

3.3. Modelo general del efecto de P.R.S.

De acuerdo al diseño, los paneles estarían siempre perfectamente normales a la línea que une al satélite con el sol. Estas condiciones pueden ser violadas por tres razones: los dos ejes de los paneles solares no yacen en una perfecta línea recta, los

sensores no se encuentran perfectamente normales al eje de los paneles y la existencia de desarreglos en el satélite que desvían la actitud de control. En la práctica sin embargo los 3 desalineamientos se reducen a una variación angular que no es superior a 0.02 radianes en torno al eje radial.

Es decir, podemos considerar que cada dirección normal a las áreas, en las que dividimos la nave, está rotada con respecto a su posición ideal, un ángulo en la dirección radial:

$$M_R(\varphi) = \begin{pmatrix} 1 & 0 & -\varphi \\ 0 & 1 & 0 \\ \varphi & 0 & 1 \end{pmatrix}$$

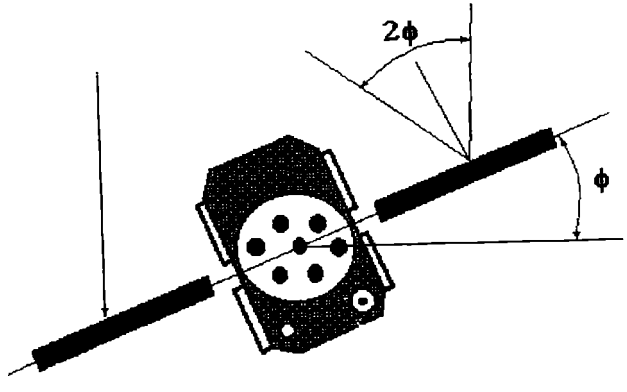

Figura 7

La expresión final de la fuerza ejercida sobre el satélite debido a la P.R.S., toma la siguiente forma (Meza et. al, Practica de la Especialidad):

$$F_N = \frac{\phi}{c}(C_{N0} + C_{N1}\cos ft + C_{N2}\cos 2ft + \ldots) + \varphi\frac{\phi}{c}(S_{N1}\,sen\,ft + C_{N0} + C_{N1}\cos ft + S_{N3}sen\,3ft + \ldots)$$

$$F_R = \frac{\phi}{c}(C_{R1}\cos ft + C_{R2}\cos 2ft + \ldots) + \varphi\frac{\phi}{c}(C_{R1}\cos ft + \ldots)$$

$$F_T = \frac{\phi}{c}(S_{T1}\,sen\,ft + S_{T2}\,sen2ft + S_{T3}\,sen3ft\ldots) + \varphi\frac{\phi}{c}(C_{T0} + S_{T1}\,sen\,ft + C_{T2}\cos 2ft + S_{T3}sen\,3ft + \ldots)$$

Donde los coeficientes dependen del área, los coeficientes de reflexión, difusión y absorción y el ángulo β; como vemos la fuerza está en función directa del valor Φ de (flujo solar).

3.4. Efecto de la P.R.S. sobre las coordenadas en un sistema inercial

Hemos hablado del modelado físico de la aceleración producida por la P.R.S. sobre la nave. Para obtener las expresiones de la variación de las coordenadas debido a dicha fuerza debemos integrar dos veces la aceleración modelada, en un sistema inercial. Por comodidad las fuerzas están expresadas en un sistema con origen en la nave (sist. Gaussiano) por lo tanto no inercial. Para pasar a un sistema inercial optamos por hacer una rotación sobre el plano orbital a un punto fijo, "punto origen" definido anteriormente. Es decir debemos realizar una rotación alrededor del eje normal al plano orbital. Es conveniente aclarar que consideramos constante a la normal al plano orbital, esta aproximación es válida para el tiempo de integración que utilizamos en este ajuste (aproximadamente 4 días).

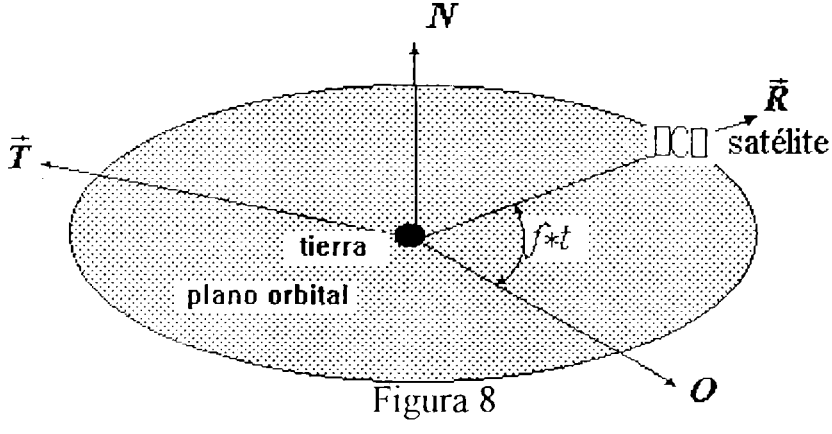

Figura 8

X - Y - Z sistema inercial

$$\begin{pmatrix} F_x \\ F_y \\ F_z \end{pmatrix} = \begin{pmatrix} cos\, ft & senft & 0 \\ -senft & cos\, ft & 0 \\ 0 & 0 & 1 \end{pmatrix} \begin{pmatrix} F_R \\ F_T \\ F_N \end{pmatrix}$$

$$F_x = F_R \cos ft + F_T senft$$

Reemplazando e integrando:

$$X = \frac{\Phi}{c}(X_0^2 t + X_1 t + X_2 + X_3 \cos ft + X_4 cos\ 2ft + X_5 cos\ 3ft + \ldots)$$

$$F_y = -F_R\ sen\, ft + F_T \cos ft$$

Reemplazando e integrando:

$$Y = \frac{\Phi}{c}(Y_1 t + Y_2 + Y_3\ sen\ 2ft + Y_5\ sen\ 3ft + \ldots)$$

$$F_Z = F_N$$

Reemplazando e integrando:

$$Z = \frac{\Phi}{c}(Z_0 t^2 + Z_1 t + Z_2 + Z_3 \cos ft + Z_4 \cos 2ft + \ldots)$$

Donde X_1, X_2, Y_1, Y_2, Z_1 y Z_2 son constante de integración; sus valores dependen de las condiciones iniciales.

3.4.1. Comparación del modelo propuesto con datos externos

Ya se han integrado las fuerzas en un sistema inercial obteniendo una expresión para las coordenadas; por una rotación similar a la anterior podremos pasar

nuevamente a un sistema gaussiano en el que se describe mejor la geometría del problema.

$$\begin{pmatrix} R \\ T \\ N \end{pmatrix} = \begin{pmatrix} cos\,f\,t & -sen\,f\,t & 0 \\ sen\,f\,t & cos\,f\,t & 0 \\ 0 & 0 & 1 \end{pmatrix} \begin{pmatrix} X \\ Y \\ Z \end{pmatrix}$$

Finalmente quedan las siguientes expresiones de las coordenadas en el sistema solidario con la nave:

$$R = R_0^C\, cos\,f\,t + R_1^S\, sen\,f\,f + R_2^C\, cos\,2f\,t + R_3^C\, cos\,3f\,t + \ldots + T.M.$$
$$T = T_0^C\, cos\,f\,t + T_1^S\, sen\,f\,t + T_2^S\, sen\,2f\,t + T_3^S\, sen\,3f\,t + \ldots + T.M$$
$$N = N_0^C + N_1^C\, cos\,f\,t + N_2^C\, cos\,2f\,t + \ldots + T.M$$

Donde T.M. denota los términos en los que el coeficiente que acompaña a la componente periódica varía lineal o cuadráticamente con el tiempo (términos mixtos) y T.S. denota los términos que varían lineal y cuadráticamente con el tiempo.

Una manera de corroborar estas expresiones analíticas con las observaciones es a través del análisis de los residuos (diferencias entre los (*x, y, z*) observados y los (*x, y, z*) calculados en el ajuste). Para que estos residuos representen el efecto de P.R.S., que está presente en los valores observados, obtenemos los valores calculados integrando solamente los efectos gravitacionales terrestre y lunisolar. Estimamos que los efectos de las fuerzas menores (mareas, albedo, etc) son despreciables a los fines de esta comparación. Recordemos que en el caso de incluir en la integración un modelo correcto de la P.R.S. los residuos esperables tendrían carácter aleatorio. Analizamos los residuos con la técnica de Power Spectrum y en líneas generales observamos que las frecuencias con máxima potencia espectral corroboran las frecuencias desprendidas del modelo propuesto.

3.5. Pasaje de coordenadas al sistema terrestre

Una vez que tenemos las expresiones teóricas de las variaciones de las coordenadas debido al efecto de la P.R.S., en el sistema inercial, debemos

pasarlas al sistema en donde se realizan las observaciones, es decir el sistema terrestre.

Para esto debemos realizar las siguientes rotaciones (Fig. 6):

$$M = R(f_t - \Omega)\,R(-i)\,R(-\omega)$$

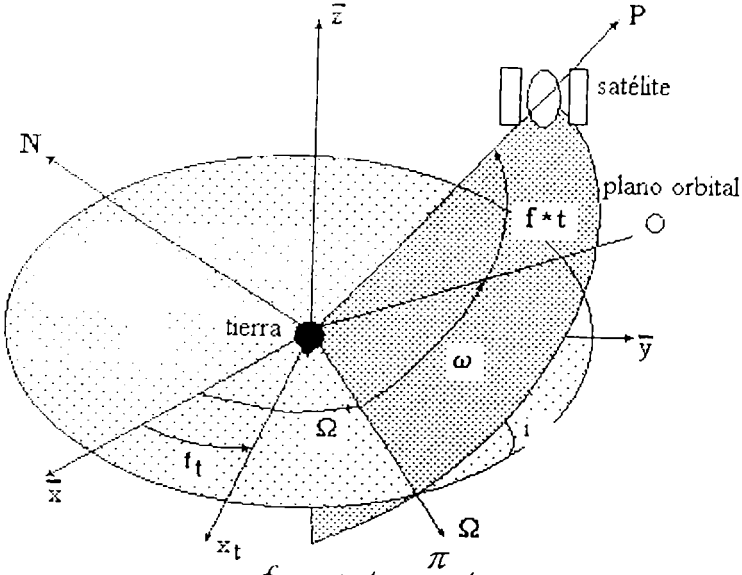

$$f_t = \omega_t t = \frac{\pi}{12} t$$

$$f = \frac{\pi}{6} t$$

donde consideramos que y (inclinación orbital)ω(longitud del perihelio) y Ω (longitud del nodo) son constantes en el período de integración utilizado.

Finalmente tenemos:

$$\begin{pmatrix} \Delta X_T \\ \Delta Y_T \\ \Delta Z_T \end{pmatrix} = M \begin{pmatrix} X \\ Y \\ Z \end{pmatrix}$$

Expresiones finales (Meza et al., Practica de la Especialidad, 1994):

$$\Delta X = \Phi/_C (X^S_{t0} sen(f/_2) + X^C_{t0} cos(f/_2) + X^C_{t1} t cos(f/_2) + X^S_{t1} sen(f/_2) + X^C_{t2} t^2 cos(f/_2$$
$$X^S_{t2} t^2 sen(f/_2) + X^S_{t3} sen(3f/_2) + X^C_{t3} cos(3f/_2) + X^S_{t4} sen(5f/_2) + X^C_{t4} cos(5f/_2) + \ldots$$

$$\Delta Y = \Phi/_C (Y^S_{t0} sen(f/_2) + Y^C_{t0} cos(f/_2) + Y^C_{t1} t cos(f/_2) + Y^S_{t1} sen(f/_2) + Y^C_{t2} t^2 cos(f/_2$$
$$Y^S_{t2} t^2 sen(f/_2) + Y^S_{t3} sen(3f/_2) + Y^C_{t3} cos(3f/_2) + Y^S_{t4} sen(5f/_2) + Y^C_{t4} cos(5f/_2) + \ldots)$$

$$\Delta Z = \Phi/_C (Z^S_{t0} sen(f) + Z_{t2} t^2 + Z_{t2} t + Z_{t3} + \ldots)$$

Donde los coeficientes de los términos precedentes dependen de los valores conocidos ω, Ω, i, β (ángulo formado entre la normal al plano orbital y la dirección del sol), de los coeficientes de reflectividad y de difusión y el área efectiva (estimados por la NASA). Finalmente hemos obtenido las expresiones de la variación de las coordenadas del satélite, debido al efecto de P.R.S., en el sistema terrestre.

4. ANALISIS Y CONCLUSIONES

4.1. Comparación del modelo propuesto con el modelo de Beutler

Del análisis realizado sobre el modelo numérico de Beutler se deduce que las expresiones de la aceleración producido por la P.R.S. en sus dos componentes p_0 y p_2 en el sistema gaussiano son las siguientes:

e_0 :

$$p_{0_N} = cos\,\beta$$
$$p_{0_R} = sen\,\beta\, cos\, f\, t$$
$$p_{0_T} = -\, sen\,\beta\, sen\, f\, t$$

e_2 :

$$p_{2N} = p_{2N1}\, sen\, ft + p_{2N3}\, sen 3ft + p_{2N5}\, sen 5ft + \ldots$$

$$p_{2R} = 0$$

$$p_{2T} = p_{2T0} + p_{2T2}\, cos 2ft + p_{2T4}\, cos 4ft + \ldots$$

Si comparamos estas expresiones con las expresiones de la aceleración (debido al efecto de P.R.S.) obtenidas en nuestros modelos, notamos que los términos principales del modelo extraído en la primera etapa contienen los términos de Beutler para $\vec{p}_0$; mientras que el modelo de la segunda etapa además de contener los términos de Beutler para $\vec{p}_2$ muestra términos cruzados en coseno y seno (para la componente normal y tangencial respectivamente) y términos en coseno para la componente radial, los términos no presentes en el modelo de Beutler son pequeños lo que justifica el buen funcionamiento de este modelo. Sin embargo el modelo propuesto es mas completo y contiene una descripción mas elaborada de la física del problema. Hablando con valores reales, tenemos en la tabla siguiente los ordenes de magnitud de los coeficientes que aparecerían en el desarrollo periódico del efecto, calculado analíticamente:

Sólo la componente $\vec{p}_0$

términos	**comp. normal**	**comp. radial**	**comp. tangencial**
term.indep.	3,020117	-0,62587	0
cos(ft)	0,149767	-4,64385	0
sen(ft)	0	0	5,260699
cos(2ft)	0,105706	-0,62587	0
sen(2ft)	0	0	0,132762
cos(3ft)	0	0,037809	0
sen(3ft)	0	0	0,099187
cos(4ft)	0,008992	0	0
sen(4ft)	0	0	0
cos(5ft)	0	0,004699	0

4.3. Prospectiva

Al principio hablamos de un ajuste orbital, de las condiciones iniciales (coordenadas y velocidades) y de los parámetros del modelo de Beutler (p_0 y p_2), mediante mínimos cuadrados. Allí el modelo de presión de radiación solar era un modelo determinista con parámetros a ajustar. Si bien la amplitud de los residuos disminuye notablemente, después de aplicar el modelo completo de Beutler, no presentan un comportamiento aleatorio sino, por el contrario, aparecen fuertemente correlacionados.

Una vez que tenemos las expresiones del efecto en cada componente (como se encontraron en un ítem anterior) podemos hacer un tratamiento estadístico del problema. Este tratamiento consiste en aplicar el método de colocación por mínimos cuadrados, en el que básicamente se incorpora la información estadística de la señal no modelada, en la matriz de varianza - covarianza a priori que aparece en el ajuste por mínimos cuadrados, dicha matriz se puede calcular con la serie encontrada analíticamente. Analizar, estudiar y aplicar este método en el problema de ajuste orbital es la prospectiva de este trabajo.

Con este método esperamos mejorar la estimación de las incógnitas, especialmente los parámetros del modelo numérico, y garantizar por el estudio de los residuos, el análisis estadístico de la señal de la P.R.S. (no modelable en forma determinista). Además podremos posibilitar el estudio de las fuerzas menores, hoy encubiertas por la P.R.S. que presentan importante información geofísica.

REFERENCIAS

Markus Bath , 1974. Spectral Analysis in Geophisics, Amsterdam - Oxford - New York.

H. Moritz , 1980. Advanced Physical Geodesy, Abacus Press Tunbridge Wells Kent.

H. F. Fliegel, W. A. Fees, W. C. Layton, N. W. Rhodus , 1985. The G.P.S. Radiation Force Modelin proceedings of the First International Symposium on Precise Positioning with the Global Positioning System, Rockville, Maryland. volumen I: pag.:113-119.

G. Beutler, W. Gurtner, M. Rochacher, T. Schildknecht, Y. Bauerisima, 1986. Determination of GPS Orbits using Double Difference Carrier Phase Observations from Regional Networks. Proceed. of the Fourth Int. Geodetic Symp. on Satellite Positioning, Austin, Texas.

A. Milani, A. M. Nobili, P. Farinella, 1987. Non - Gravitational Perturbations and Satellite Geodesy, Adam Hilger, Bristol.

H. F. Fliegel, T. E. Gallini , 1989. Radiation Pressure Models for Block-II G.P.S. Satellites in Proceedings 5th of International Geodetic Symposium on Satellite Positioning, Corbett Center. volumen II. pag: 789-798.

J. Feltens , 1990. The influence of Non-Gravitational Forces on G.P.S.-Satellite Orbits Cahiers du Centre Europeen de Geodynamique et de Seusmologie, Luxembourg. volumen II. pag.: 27-37.
A. Leick , 1994. 2da Edición.. G.P.S. Satellite Surveying, John Wiley & Sons.
R. Perdomo y D. del Cogliano, 1991. Generación de efemérides Satelitarias, Memorias del Congreso de Ciencias de la Tierra, Santiago.
B. Hofmann - Wellenhof, H. Lichtenegger and J. Collins , 1992. Global Positioning System , Theory and Practice, Spinger-Verlag Wien New York.
A. Meza, C. Brunini, J.C. Usandivaras, 1994. Modelo geométrico de la P.R.S., presión de Radiación solar sobre satélites GPS, Práctica de la especialidad, Facultad de Cs. Astronómicas y Geofísicas - La Plata - Argentina.

Normas para los autores

1. Los trabajos deben ser enviados al Editor de GEOACTA, CC. 107 – 8000 Bahía Blanca, Argentina.
3. La presentación de los manuscritos será en castellano o inglés. En ambos casos se hará un resumen en los dos idiomas, sin indentación, colocando en primer lugar el que correspondiera al texto.
4. Se enviarán tres copias del manuscrito, junto con la dirección completa de los autores. La versión final se entregará en diskette 3.5" con procesador Microsoft Word o Word Perfect.
5. Se utilizará papel Carta (21,59 x 27,94). Los márgenes superior, inferior, derecho e izquierdo serán iguales a 4 cm. La letra será Time New Roman, 11 puntos. El resumen, el abstract y las referencias en 10 puntos. El título del trabajo debe ir en mayúscula y en negrilla, los autores y dirección en mayúscula y minúscula, todo irá centrado. Los autores se escribirán en negrilla. Dentro del texto los títulos irán numerados y en mayúsculas, y los subtítulos en mayúscula y minúscula, en ambos casos en negrilla y sobre el margen izquierdo.
6. Las figuras y tablas no excederán los límites de una caja de 15cm x 11cm. Se entregarán en copias listas para su reproducción. Las fotos deberán ser claras y de buen contraste. Las figuras y fotos en colores serán publicadas siempre que el autor asuma los gastos que estas demanden. Se sugiere establecer el lugar donde serán insertados en el texto.
7. Las referencias se detallan en orden alfabético de acuerdo al ejemplo:

REFERENCIAS

Gómez, R.A., 1990. La dinámica costera de la localidad de Monte Hermoso. Geoacta, vol. 3, 133-140.

Lowell Wine, R., 1966. Statistics for Scientist and Engineers. Prentice-Hall, U.K. pp 671.

Hart. B.S., 1995. Delta fornt estuaries. En: Geomorphology and Sedimentology or Estuaries. Perillo G.M.E. (Ed). Elsevier, Amsterdam, 207-226.

GEOACTA, 22, 1997

Isostatic systems -and tectonic mechanisms present in Argentina.
Antonio Introcaso 1
On the dissipation of an upper oceanic front
Alejandro I. Camerlengo and Mónica I. Demmler 20
El calcu!o del agua precipitable y algunas de sus aplicaciones en Argentina
Graciela A. Catuogno e Inés Velasco 30
Aspectos cualitativos en el comportamiento del fof2 en la anomalía de invierno en la región f2 de la ionósfera.
Ana Martínez Pulido 47
Absolute palaeoreconstructions of continents based on palaeomagnetic poles and virtual geomagnetic poles?
Haroldo Vizan and Carlos Alberto Vasquez 59
Variability and motion of the Brazil-Malvinas front
Alejandro A. Bianchi and Silvia L. Garzoli 74
The andean elevation in Argentina-Chile at 39º south latitude from gravity data.
María Cristina Pacino 91
Spectral decomposition of a long Rossby wave after reflection on an equatorial western boundary
Alejandro Camerlengo and Mónica Inés Demmler 103
Geomagnetism as an independent science
Luiz Muniz Barreto 122
Response of the ocean mixed layer, off the east coast of peninsular Malaysia during the north-east and south-west monsoons
Mohd Nasir Saadon and Alejandro Camerlengo 134
Sea level characteristics in Puerto Quequén
María Cintia Piccolo and Gerardo M. E. Perillo 144
Stability condition for Arakawa' s *B* grid
Alejandro I. Camerlengo and Mónica I. Demmler 155
Mejoramiento en el ajuste orbital de satelites GPS
A. Meza , J. C. Usandivaras and C. Brunini 165